Dissertation

submitted to the

Combined Faculty of Mathematics, Engineering and Natural Sciences
of Heidelberg University, Germany

for the degree of

Doctor of Natural Sciences

Put forward by

Christian Will

born in Gießen, Germany

Oral examination: July 06, 2023

Sympathetic Cooling of Trapped Ions Coupled via Image Currents: Simulation and Measurement

Referees: Prof. Dr. Klaus Blaum

Prof. Dr. Markus Oberthaler

Sympathisches Kühlen von gespeicherten Ionen durch Spiegelstromkopplung: Simulation und Messung

Zusammenfassung – Die Fähigkeit, die Temperatur von lasergekühlten Ionen auf Teilchen ohne geeigneten optischen Übergang zu übertragen, ist von erheblichem Interesse für die nächste Generation von Experimenten mit gespeicherten Ionen. Unser Experiment (`BASE-Mainz`) zum Beispiel führt hochpräzise Messungen des magnetischen Moments des Protons in einer Penningfalle durch. Diese Messungen sind aktuell limitiert durch die von null verschiedene Teilchentemperatur von etwa $1\,\mathrm{K}$. Vor kurzem wurde von uns die erste sympathische Kühlung eines einzelnen Protons mithilfe von lasergekühlten Berylliumionen durchgeführt. Hierbei sind beide Teilchenarten in makroskopisch separierten Fallen gespeichert und die Kopplung erfolgt durch Spiegelströme, die mithilfe eines supraleitenden RLC Schwingkreises verstärkt werden. Aufgrund der räumlichen Trennung zwischen Zielion und der laserkühlbaren Spezies kann diese Methode nicht nur auf ein einzelnes Proton angewandt werden, sondern auf beliebige geladene Teilchen und insbesondere auf exotische Teilchen wie Antiprotonen oder hochgeladene Ionen.

Im Zuge dieser Dissertation konnte eine Teilchentemperatur von $(160 \pm 30)\,\mathrm{mK}$ für solch ein sympathisch gekühltes Proton reproduzierbar erreicht werden. Dies stellt eine Verbesserung um einen Faktor 16 zu der bisherigen Rekordmessung von $(2.6 \pm 2.5)\,\mathrm{K}$ dar und ist ein Faktor 55 kleiner als die Umgebungstemperatur. Dieser Erfolg wurde ermöglicht durch zwei bedeutende Entwicklungen: Zum einen wurden numerische Simulationen des gekoppelten Penningfallensystems entwickelt und durchgeführt, die das Verständnis über den Koppel- und Kühlmechanismus erheblich verbessert haben. Zum anderen wurde ein neuer experimenteller Aufbau in Betrieb genommen, der neben anderen Verbesserungen eine dedizierte Falle für Temperaturmessungen umfasst. Zusätzlich wurden mithilfe der Simulationen zukünftige Kühlschemata etabliert, die Temperaturen von $10\,\mathrm{mK}$ und möglicherweise darunter ermöglichen.

Sympathetic Cooling of Trapped Ions Coupled via Image Currents: Simulation and Measurement

Summary – The ability to transfer the temperature of laser cooled ions to species without a suitable optical cooling transition is of vital interest for the next generation of experiments with trapped ions. For example, our experiment (`BASE-Mainz`) performs high-precision Penning-trap measurements of the proton magnetic moment. The currently most precise measurement is limited by the non-zero particle temperature of about $1\,\mathrm{K}$. Recently, we have demonstrated the first sympathetic cooling of a single proton with laser cooled beryllium ions. Here, both species are located in macroscopically separated traps and the coupling is mediated by image currents, which are enhanced via a superconducting RLC circuit. Due to the spatial separation between the target ion and the laser-coolable species, this cooling method can be applied not only to a single proton, but to any charged particle, including exotic particles such as antiprotons or highly-charged ions.

In the course of this thesis, a particle temperature of $(160 \pm 30)\,\mathrm{mK}$ was reproducibly achieved for such a sympathetically cooled proton. This constitutes an improvement by a factor of 16 compared to the previous record of $(2.6 \pm 2.5)\,\mathrm{K}$ and is a factor of 55 below the environment temperature. This accomplishment was enabled by two major advancements: First, numerical simulations of the coupled Penning-trap system were developed and carried out, which significantly progressed the understanding of the coupling and cooling mechanism. Second, a new experimental apparatus was commissioned, which comprises among other upgrades a dedicated temperature measurement trap. In addition, the simulations were employed to establish future cooling schemes that reach temperatures of $10\,\mathrm{mK}$ and possibly below.

Contents

List of Figures

List of Tables

1 | Introduction and motivation

Over the last decades, the preparation of (ultra-)cold particles through laser cooling has probably been the most widely employed technique in the field of atomic, molecular and optical physics [1]. The applications range from precision measurements [2, 3] over quantum gases [4] to quantum computing [5]. However, many species of interest are not amenable to direct laser cooling since they lack a suitable optical transition, although the corresponding measurements would benefit immensely from colder particles. A striking example are tests of CPT invariance in the baryonic sector by high-precision Penning-trap measurements on the proton and antiproton, as conducted by our collaboration BASE (Baryon-Antibaryon Symmetry Experiment). In particular, the measurement of the proton magnetic moment μ_p normalized to the nuclear magneton μ_N [6],

$$\frac{\mu_p}{\mu_N} = 2.792\,847\,344\,62(75)(34), \tag{1.1}$$

is currently limited by the statistical uncertainty. This statistical uncertainty stems from the non-zero particle temperature of about $\gtrsim 1\,\mathrm{K}$ in our trap. Notably, this is only one example and several other experimental programs suffer from similar limitations, e.g. high-precision mass spectrometry [7, 8], antihydrogen synthesis [9, 10, 11], optical spectroscopy of highly-charged ions [2, 12], or high-precision metrology with atomic clocks [13, 14].

Usually, in such cases sympathetic cooling techniques are employed [2, 9, 13, 15, 16], which enable transferring the temperatures of laser-coolable species to a target particle. The established versions of these sympathetic cooling techniques rely on direct ion-ion Coulomb interaction as the mediator of the coupling. As a consequence, in order to achieve sufficiently strong coupling, the two ion species must either be co-trapped in the same potential well [2, 13, 15] or separated by a few hundred micrometers at most [17, 18]. However, both techniques have severe disadvantages for our application: Co-trapping is unfeasible for the antiproton since to this date, a negatively charged laser-coolable ion is an exotic species on its own [19, 20] and therefore not available for routine use. The separation by means of two distinct potential wells requires trap electrodes of comparable dimensions to be built. Besides being a technological challenge, ions in such small traps are also subject to increased systematic frequency shifts such as the image charge shift [21] or stronger heating rates [22]. Nevertheless, it bears mentioning that this approach is currently in development by the collaboration subgroup BASE-Hanover [23].

In contrast, our group, BASE-Mainz, pursues a different approach that relies on coupling the species via image currents instead of direct Coulomb interaction. The original proposals in refs. [24, 25] envisaged coupling by means of a common endcap electrode. However, for feasibility reasons our group has switched to an approach that uses an RLC circuit as mediator of the image currents [26, 27]. This technique allows to place the two species in traps that are separated in space, in our case by several cm. Recently, we have performed a proof-of-principle measurement with this technique, where the axial temperature of a single proton was cooled from $(17.0 \pm 2.4)\,\mathrm{K}$ to $(2.6 \pm 2.5)\,\mathrm{K}$ [27]. However, a particle temperature of $2.6\,\mathrm{K}$ is not yet sufficiently cold to be useful for an improved g-factor measurement of the proton. Hence, a more thorough understanding of the coupling process was required. While the addition of the RLC circuit to the coupled system has enabled this result in the first place, it also severely complicated the system: While previously only two oscillators were coupled (the two ion species), now a third, noise-driven oscillator (the RLC circuit) has to be accounted for in a theoretical description. As a consequence, the major methodical advancement developed in the course of this thesis is a profound understanding of the coupled three-oscillator system. To this end, a sophisticated simulation framework has been developed, which allows simulating the relevant Penning-trap physics from first

principles. These simulations already played a crucial role in supporting the experimental effort to observe the inter-trap coupling between the two particles in the course of the proof-of-principle measurement [27, 28]. Going forward, the simulations were used to study the temperature limit of this method and how the considerable amount of experimental parameters must be adjusted to reach it [28]. In addition, a new experimental apparatus has been commissioned throughout this thesis, which features among other improvements a dedicated temperature measurement trap that allows temperature measurements of a single proton down to a few mK. The simulation work and the improved experimental apparatus culminated in the measurement of axial temperatures of a single, sympathetically cooled proton of $T_z = (160 \pm 30)\,\mathrm{mK}$ in the course of this thesis work. This temperature constitutes a factor of 16 improvement compared to the previous record measurement and is reproducibly achieved. It is a factor of about 55 below the environment temperature of $T_{\mathrm{RLC}} = (8.6 \pm 0.8)\,\mathrm{K}$. In addition, this temperature is within uncertainties exactly the one predicted by the simulations given the experimental parameters. Finally, the simulations were employed to investigate different cooling schemes that can reach even lower temperatures. In particular, by detuning the two ion species in axial frequency from the resonator, the simulations predict that axial proton temperatures of about $10\,\mathrm{mK}$ are achievable. Due to the excellent agreement between experiment and simulation for the on-resonant schemes, this result provides a strong foundation towards proton temperatures of $10\,\mathrm{mK}$ and less.

A striking advantage of the image-current based sympathetic cooling is that it does not impose any requirements on the target particle other than that it needs to carry a charge and that its lifetime is sufficiently long. Consequently, these sympathetic cooling methods are not limited to a proton g-factor measurement but can also be applied to measurements with antiprotons, highly-charged ions, molecular ions or even radioactive species. The relevance of this technique becomes most apparent by the fact that a significant number of Penning-trap experiments have launched a sympathetic cooling program in the last few years: Besides our collaboration, the `ALPHATRAP`-experiment [12] requires sympathetic cooling for g-factor measurements of highly-charged ions and has already demonstrated resonator-mediated coupling [29]. The `PENTATRAP`-experiment [30] has recently founded the new experiment `ELCOTRAP` [31] that will investigate sympathetic cooling of highly-charged ions via electrons stored in a separate trap for improved mass measurements, and the g-factor helium experiment [32] requires sympathetic cooling of the $^3\mathrm{He}^{2+}$ nucleus to measure its g-factor. From a broader perspective, the developments and results presented in this thesis thus pave the way for the next generation of Penning-trap precision measurements.

2 | Theoretical background

The Penning trap is a mature system and its physics has been described in great detail already, see for example refs. [33, 34, 35, 36, 37]. As a result, I will keep this section comparably short and instead direct the reader to the appropriate references. In addition, I emphasize that this and all following sections refer to cryogenic Penning traps that perform measurements with the highest precision on single particles. The particular designs and specifications might be very different from Penning traps that are used in e.g. nuclear physics, where fast cycle times are of utmost importance to perform measurements on short-lived nuclei [38].

2.1   The ideal Penning trap

The idea that leads to a Penning trap is the following: In order to trap charged particles in all three spatial dimensions, it seems a natural choice to employ a magnetic field as then confinement in two dimensions is already provided for. These two dimensions are referred to as radial plane. The confinement in the third and perpendicular dimension is achieved by applying an additional electric field in axial direction. In more quantitative terms, the magnetic field in axial direction

$$\vec{B} = B_0 \vec{e}_z \tag{2.1}$$

is superimposed by a quadrupolar electric potential

$$\phi(\rho, z) = C_2 U_0 (z^2 - \rho^2/2). \tag{2.2}$$

Here, ρ is the radial amplitude $\rho = \sqrt{x^2 + y^2}$, U_0 the applied voltage that is proportional to the potential well depth and C_2 a parameter defined by the geometry of the trap electrodes. Note that in the following, U_0 in terms of a potential well depth should be treated as a positive number while U_0 in terms of a voltage applied to a trap electrode is usually a negative number. In addition, some authors especially in the american literature prefer a similar but different convention where $C_2 \rightarrow \tilde{C}_2/(2d^2)$. Then $\tilde{C}_2$ is a dimensionless parameter and d a characteristic trap length. The most natural way to create a quadrupolar potential is to manufacture electrodes whose surfaces have a hyperbolic contour. A schematic of such a trap is shown in figure 2.1.

The radial component of the electric field stems from Gauss law, i.e. the requirement that $\nabla \vec{E} = 0$. The combined electric field $\vec{E} = -\nabla \phi$ and magnetic field subject the particle to the Lorentz force $\vec{F}_L = q(\vec{E} + \vec{v} \times \vec{B})$, where q is the charge of the particle and $\vec{v}$ its velocity. The resulting coupled differential equations are

$$\ddot{x} - \frac{q}{m} \left(C_2 U_0 x + B_0 \dot{y} \right) = 0 \tag{2.3}$$

$$\ddot{y} - \frac{q}{m} \left(C_2 U_0 y - B_0 \dot{x} \right) = 0 \tag{2.4}$$

$$\ddot{z} + \frac{2q C_2 U_0}{m} z = 0, \tag{2.5}$$

where m is the mass of the particle. The axial direction is decoupled from the radial motions and can immediately be identified as a harmonic oscillator with angular frequency

$$\omega_z = \sqrt{\frac{2q C_2 U_0}{m}}. \tag{2.6}$$

The solution to the radial modes can be obtained by substituting $u = x + iy$. In a purely magnetic field the particle trajectory would be a free cyclotron motion with angular
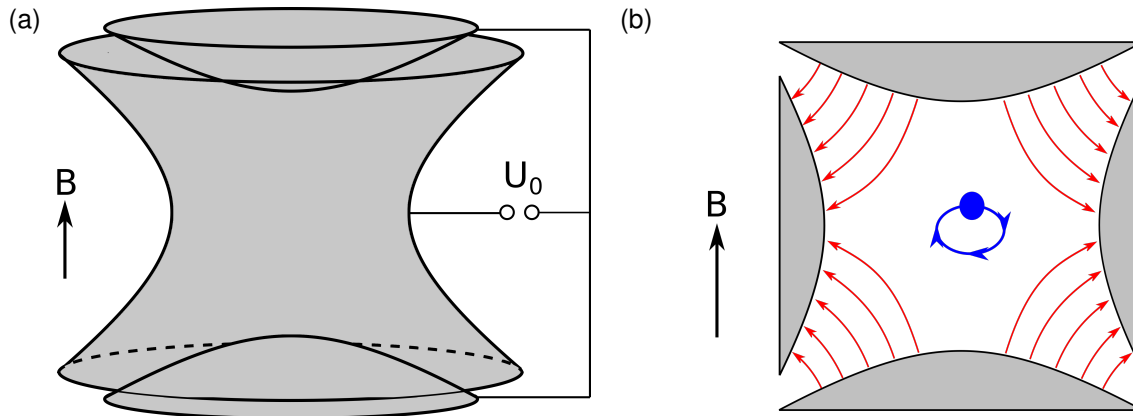
Figure 2.1: A schematic of a hyperbolic Penning trap consisting of two individual endcaps and one ring electrode. The surface geometry and the voltage U_0 between endcaps and ring electrode define the trapping potential. A section view with electrical field lines in red and ion in blue is shown in (b).

frequency $\omega_c = \frac{q}{m} B_0$, however, the radial component of the electric field causes this motion to split up in the modified cyclotron motion with angular frequency

$$\omega_+ = \frac{\omega_c}{2} + \sqrt{\left(\frac{\omega_c}{2}\right)^2 - \frac{\omega_z^2}{2}} \tag{2.7}$$

and the magnetron motion with angular frequency

$$\omega_- = \frac{\omega_c}{2} - \sqrt{\left(\frac{\omega_c}{2}\right)^2 - \frac{\omega_z^2}{2}}. \tag{2.8}$$

The latter is also often referred to as $\vec{E} \times \vec{B}$ drift. A simplified illustration of the individual motions and the full trajectory of a charged particle is shown in figure 2.2. The general solution of the differential equation system writes

$$x(t) = \hat{\rho}_+ \cos(\omega_+ t + \varphi_+) + \hat{\rho}_- \cos(\omega_- t + \varphi_-) \tag{2.9}$$

$$y(t) = -\hat{\rho}_+ \sin(\omega_+ t + \varphi_+) - \hat{\rho}_- \sin(\omega_- t + \varphi_-) \tag{2.10}$$

$$z(t) = \hat{z} \cos(\omega_z t + \varphi_z). \tag{2.11}$$

$\hat{\rho}_\pm$, $\hat{z}$ and $\varphi_\pm$, φ_z are formally the free parameters of the differential equation and can be identified as the motional amplitudes and phases, respectively. The inverse relations for the radial motions are

$$\hat{\rho}_+^2 = \left(y + \frac{\dot{x} - \omega_+ y}{\omega_+ - \omega_-}\right)^2 + \left(x - \frac{\dot{y} + \omega_+ x}{\omega_+ - \omega_-}\right)^2 \tag{2.12}$$

$$\hat{\rho}_-^2 = \left(\frac{\dot{x} - \omega_+ y}{\omega_+ - \omega_-}\right)^2 + \left(\frac{\dot{y} + \omega_+ x}{\omega_+ - \omega_-}\right)^2. \tag{2.13}$$

From equations (2.7, 2.8) a stability criterion can be inferred, namely that the radicand is positive, which is equivalent to $\omega_z < \omega_c/\sqrt{2}$. Intuitively, this can be understood as the force of the electrical field pushing the ion radially outwards being weaker than the force of the magnetic field containing it, compare the electric field lines in figure 2.1 and the electric force in equation (2.3) $\ddot{x} \propto +x$. As a consequence, the motional frequencies in a Penning trap follow the hierarchy $\omega_+ > \omega_z > \omega_-$. This frequency hierarchy is stronger the higher the charge-to-mass ratio of the particle is. From here on, I will continue the
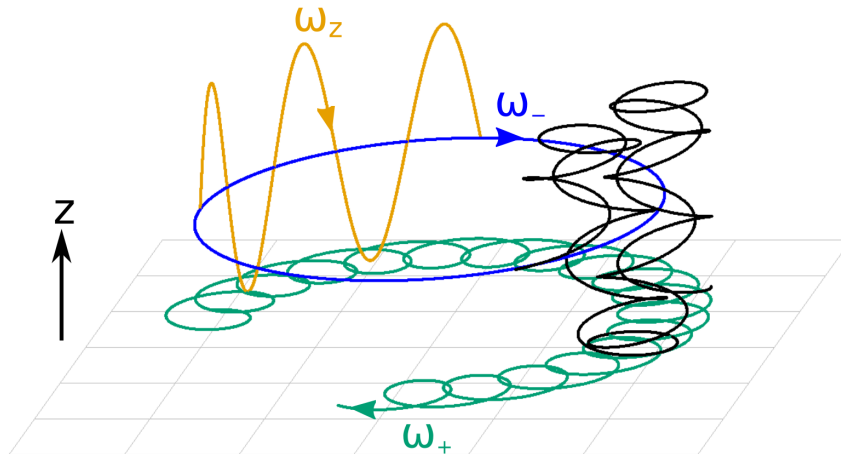
Figure 2.2: Illustration of the individual motions of a charged particle in a Penning trap consisting of the magnetron motion (ω_-), the axial motion (ω_z) and the modified cyclotron motion (ω_+). The combined motion is shown in black. Note that for illustrative purposes the amplitudes and frequencies not necessarily correspond to a real system.

common convention that ω labels the angular frequencies in theoretical calculations and $\nu = \omega/(2\pi)$ labels actual experimental frequencies. In addition, to avoid repeatedly stating the obvious, if not explicitly stated otherwise the subscripts '+, z, -' will from now on refer to the modified cyclotron frequency, the axial frequency and the magnetron frequency, respectively. Similarly, the subscripts 'p' and 'Be' will refer to the proton and beryllium ion(s).

The experimental parameters for the particle-trap combinations used in the course of this thesis are

$$\nu_{+,\mathrm{p}} \approx 29\,\mathrm{MHz} \qquad\qquad \nu_{+,\mathrm{Be}} \approx 3.2\,\mathrm{MHz}$$

$$\nu_{\mathrm{z,p}} \approx 350 - 550\,\mathrm{kHz} \qquad\qquad \nu_{\mathrm{z,Be}} \approx 350 - 550\,\mathrm{kHz}$$

$$\nu_{\text{-,p}} \approx 2 - 9\,\mathrm{kHz} \qquad\qquad \nu_{\text{-,Be}} \approx 18 - 80\,\mathrm{kHz}$$

The fact that $\nu_{\mathrm{z,p}} = \nu_{\mathrm{z,Be}}$ is achieved by applying different trapping voltages and is a necessity of our particle detection method via a fixed-frequency resonator (compare section 2.3).

Throughout this thesis, the energy E_{i} will be referred to as the total energy of the respective oscillator mode i, which can be determined deterministically for every point in time. This includes not only the trapped particles, but also for example the electronic oscillation of the RLC circuit that is employed for particle detection and which will be introduced in section 2.3. In contrast, the term temperature is used to express the average energy over time. Since all oscillators in this thesis have two degrees of freedom, the temperature T is defined as $T_{\mathrm{i}} = \langle E_{\mathrm{i}} \rangle / k_{\mathrm{B}}$ in the following.

The energy associated with each motional mode of the trapped particle can be calculated to

$$E_+ = \frac{1}{2}m\omega_+^2\hat{\rho}_+^2 - \frac{1}{4}m\omega_z^2\hat{\rho}_+^2 \approx \frac{1}{2}m\omega_+^2\hat{\rho}_+^2 \tag{2.14}$$

$$E_- = \frac{1}{2}m\omega_-^2\hat{\rho}_-^2 - \frac{1}{4}m\omega_z^2\hat{\rho}_-^2 \approx -\frac{1}{4}m\omega_z^2\hat{\rho}_-^2 \tag{2.15}$$

$$E_z = \frac{1}{2}m\omega_z^2\hat{z}^2. \tag{2.16}$$

The negative sign of the magnetron energy implies that the magnetron radius increases with decreasing energy, i.e. the motion is metastable. Thus, in the presence of any damping mechanism, energy must constantly be supplied to the magnetron mode in order to keep the particle on a stable magnetron orbit and prevent its loss. This mechanism has direct consequences to laser-cooling of ions in a Penning trap, which will be described in section 2.7.3.

Since all three motional modes are harmonic oscillators, it is possible to describe the energies in quantum mechanical terms,

$$E_+ = \quad \left(n_+ + \frac{1}{2} \right) \hbar\omega_+ \tag{2.17}$$

$$E_- = - \left(n_- + \frac{1}{2} \right) \hbar\omega_- \tag{2.18}$$

$$E_z = \quad \left(n_z + \frac{1}{2} \right) \hbar\omega_z. \tag{2.19}$$

However, even at cryogenic temperatures, the quantum numbers n_+, n_-, n_z are large. For example, a particle with $T_z = 4.2\,\mathrm{K}$ and $\omega_z = 2\pi \times 500\,\mathrm{kHz}$ has an expectation value of $\langle n_z \rangle \approx 176\,000$. Inversely, $\langle n_z \rangle = 1$ corresponds to a temperature of about $35\,\mathrm{\mu K}$.

It can be shown that the quadratic sum of all three motional frequencies yields the free cyclotron frequency [36]:

$$\omega_c^2 = \omega_+^2 + \omega_z^2 + \omega_-^2. \tag{2.20}$$

This relation is known as the invariance theorem and holds true even for small trap imperfections such as a non-zero angle between the magnetic field and the symmetry axis of the trap that defines the electric field. Other relations that can directly be derived from equations (2.7 , 2.8) are

$$\omega_z^2 = 2\omega_+\omega_- \tag{2.21}$$

$$\omega_c = \omega_+ + \omega_-. \tag{2.22}$$

Although these relations only hold true for the ideal Penning trap, they are very useful as an initial estimate when commissioning the trap system after having started a new experimental run (see section 7).

2.2   The real, cylindrical Penning trap

Although historically the first Penning traps were in hyperbolic design (figure 2.1), this design has a few disadvantages. First, the trapping region is a mostly enclosed space that offers no optical access and no possibility to inject ions from an external source without compromising the electrodes and thereby the trapping potential. Second, hyperbolic surfaces are difficult to machine and the real electrodes have consequently comparably large machining tolerances, which imposes a limit on the achievable quality of the trapping potential and resulting harmonicity of the motion of the trapped ion.

The cylindrical open-endcap Penning trap [37] provides a solution to both issues. The standard design consists of 5 electrodes, a central ring electrode surrounded by two correction electrodes and two outermost endcap electrodes. A rendered section image of such a trap is shown in figure 2.3. The electrodes are electrically isolated by sapphire spacers, which have very beneficial properties such as extremely good electrical insulation and thermal conductivity at $4\,\mathrm{K}$, a low dielectric loss tangent, and good mechanical stability.
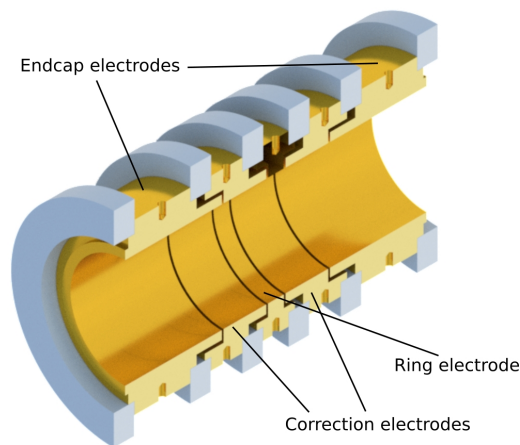
Figure 2.3: Rendered image of a cylindrical open-endcap Penning trap. The electrodes are gold-plated and separated by sapphire spacers. The trapping potential is created by five electrodes, the central ring electrode, two correction electrodes and two endcap electrodes.

2.2.1   Electric potential and electrostatic anharmonicities

Due to the cylinder symmetry, the electric potential of a cylindrical open-endcap Penning trap can be written as a series expansion [37, 39]

$$\phi(\rho = 0, z) = U_0 \sum_{j=0}^{N} C_j z^j. \tag{2.23}$$

The 0th-order is an arbitrary potential offset and thus has no physical implications. The odd coefficients $C_1, C_3, ...$ vanish to a good approximation due to the symmetry of the trap. C_2 corresponds to the desired harmonic potential. Assuming the voltage of the endcaps U_{ec} is at ground potential, a tuning ratio TR can be defined as $TR = U_{ce}/U_r$, where U_{ce} and U_r are the voltages on the correction electrodes and ring electrode, respectively. For clarity, I will follow the common convention to assign the dimensionless unit U for the tuning ratio. It can be shown that to first order, all coefficients C_j are a linear function of TR

$$C_j(TR) = D_j \cdot TR + E_j. \tag{2.24}$$

This implies that an ideal tuning ratio TR_{ideal} exists where $D_4 TR_{ideal} + E_4 = 0$ or $C_4(TR_{ideal}) = 0$. Moreover, when designing a trap, the free parameters are the inner radius r, the axial length of the ring electrode ℓ_r and the length of the correction electrodes ℓ_{ce}. The endcap electrodes are assumed to be sufficiently long such that fringe fields do not affect the potential at the trap center. These degrees of freedom can be used to design the trap such that C_4 and C_6 vanish simultaneously, i.e. $C_4(TR_{ideal}) = C_6(TR_{ideal}) = 0$. Such a trap is called *compensated*. In addition, the trap can be designed *orthogonal*, which means that to first order the tuning ratio does not affect the particle frequency, i.e. $\frac{d\omega_z}{dTR} = 0$ or $D_2 = 0$.

As a final note some traps are designed and manufactured as 7-pole traps [40], which offer additional degrees of freedom regarding geometry and compensation. However, the higher-order compensation is not relevant for this thesis.

Although great effort is put in to tune the trapping potential harmonic, the understanding of anharmonicities is nevertheless crucial. The general case for both electrostatic anharmonicities and magnetic inhomogeneities has been calculated in ref. [41] and I will refrain

from repeating this work in detail. Summarized, the resulting frequency shifts are derived by solving the differential equations with the modified electric or magnetic fields. In general, the motional frequencies then depend on the amplitudes (or energies) of each mode. For example, in the case of constant axial energy E_z, a non-zero C_4 causes the axial frequency to shift by

$$\Delta\nu_z(C_4, E_z) = \frac{3}{2}\frac{C_4}{C_2}\frac{E_z}{4\pi^2 m\nu_z}. \tag{2.25}$$

In the course of this thesis it will be demonstrated that $\Delta\nu_z(C_4)$ is larger by a factor of 2 if the axial energy is not constant but samples a Boltzmann distribution, see section 8. In fact, this factor of 2 was initially discovered in simulations carried out during this thesis work and was first considered a programming error, however, it was subsequently corroborated by a dedicated experimental campaign.

Another frequency shift that will be used throughout this thesis is the axial frequency shift due to non-zero C_4 and non-zero cyclotron energy E_+,

$$\Delta\nu_z(C_4, E_+) = -\frac{3}{4\pi}\frac{C_4}{C_2}\frac{1}{m}\frac{\nu_z}{\nu_+^2}E_+. \tag{2.26}$$

2.2.2   Magnetostatic anharmonicities

The magnetic field homogeneity is one of the most crucial parameters for precision frequency measurements. In an inhomogeneous magnetic field, a particle samples different magnetic field strengths over the course of one axial oscillation, which leads to a broadening of the spin-flip resonance and thus limits the precision of the g-factor measurement. Similar to the electric field, it is convenient to define $z = 0$ as the axial equilibrium position of the ion and describe the magnetic field as a Taylor expansion about this position:

$$B_z(z) = B_0 + B_1 z + B_2 z^2 + B_3 z^3 + ... \tag{2.27}$$

Here B_0 is the desired homogeneous contribution and B_1, B_2, ... the coefficients that define the shape of the inhomogeneity. In general, odd coefficients do not directly give rise to a systematic frequency shift in any oscillation mode of the particle, because the frequency change averages out exactly over one oscillation. However, if the position of the ion is changed by e.g. altering $\hat{\rho}_+$ or the electric trapping potential, the absolute magnetic field and thus the cyclotron frequency changes even with odd coefficients, too. Additionally, the product of two odd coefficients such as $B_1 \cdot B_3$ also causes systematic frequency shifts and must be considered as an even coefficient in this regard.
In contrast, even coefficients directly cause systematic frequency shifts for non-zero particle oscillation amplitudes. Most prominently, the axial frequency shift due to a non-zero B_2 is proportional to ρ_+^2 or the energy in the cyclotron mode E_+,

$$\Delta\nu_z(B_2, E_+) = \frac{B_2}{2B_0}\frac{\nu_+ + \nu_-}{\nu_-}\nu_z\frac{E_+}{4\pi^2 m\nu_+^2}. \tag{2.28}$$

This shift is heavily employed in our experiment and throughout the whole Penning trap community. Traps with deliberate large B_2 serve as temperature measurement traps and spin-state detectors [42, 43, 44]. In fact, all precise temperature measurements in this thesis are conducted using a trap with such a large B_2-coefficient. Note that precise cyclotron frequency measurements must be performed in a different trap with a very homogeneous magnetic field. These diametrical requirements lead to the development of the double-trap method [44, 45, 46], where the particle is shuttled between a precision trap for frequency measurements and an analysis trap for spin-state detection or temperature measurement. The next-generation measurement of the proton's g-factor requires compensation of the
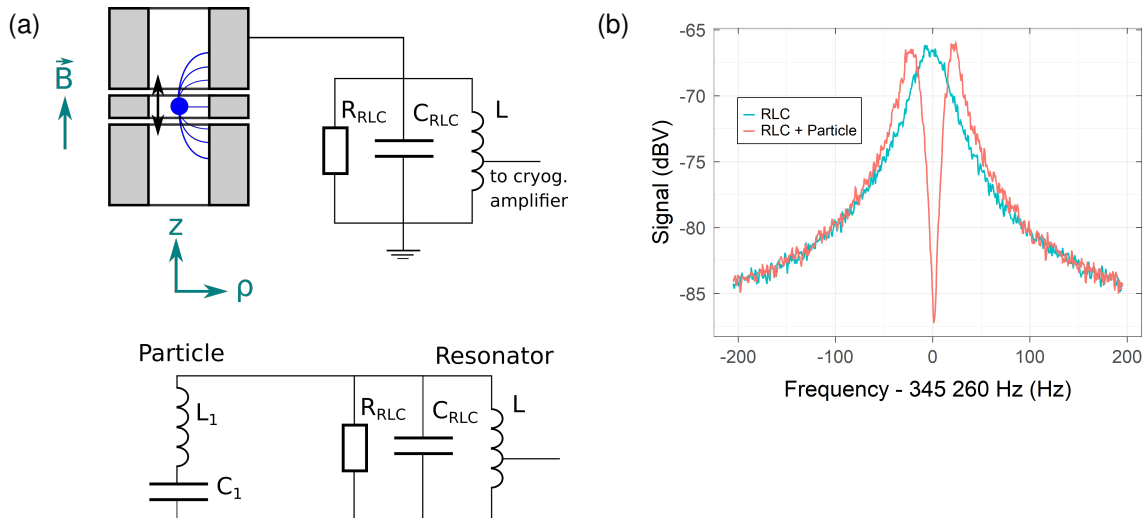
Figure 2.4: Particle detection technique via induced image currents in an RLC circuit. In (a) a schematic of the experimental setup is shown, where the RLC circuit is connected to a trap electrode. The equivalent circuit model which is used to calculate the lineshape in thermal equilibrium is shown in the lower part of the figure. Without a trapped particle, the RLC circuits generates a resonance shown as teal line in (b). With a trapped particle present whose frequency is tuned on resonance, the characteristic dip signal shown as red line is obtained. The dip position corresponds to the axial frequency of the particle and is hence used to measure it. Subfigure (a) is modified from ref. [28].

residual magnetic field inhomogeneities at the location of the precision trap. Therefore part of this thesis is the design of a superconducting shim-coil system, see section 4.1.

2.3 Particle detection and frequency measurements via an RLC circuit

In the following, I will outline the intuitive idea path that leads to detecting the trapped particles via an RLC circuit. While it may seem trivial for a Penning trap expert, I consider briefly outlining it for non-experts worthwhile. After all, almost all measurements that include particles presented in this thesis are performed with this method.

Since Penning traps are used for measurements on single or few particles and in some cases even rare antimatter, a non-destructive particle detection technique is essential. One broadly employed non-destructive technique relies on detecting the image currents of the trapped particle in adjacent electrodes, i.e. an endcap or correction electrode for the axial motion. However, the image current of a trapped particle whose axial mode is thermalized to about $4\,\mathrm{K}$ is on the order of fA and therefore too small to measure it directly. The idea to detect it nevertheless is to measure the voltage drop across a hypothetical resistor with a sufficiently high resistance. However, in reality any real resistor as well as the trap electrode have a certain parasitic parallel capacitance such that the real impedance is much smaller than the nominal resistance for the AC-signal of the particle. To circumvent this, in practice a coil with inductance L is employed instead of a resistor. This coil serves two purposes: First, it constitutes a large impedance for the AC-signal of the particle. Second, the inductance of the coil and the effective capacitance form a LC circuit together. The crux is that close to the resonance frequency of this circuit, the coil shims the capacitance and thus increases the effective impedance. In practice, such an LC circuit also has a damping term usually described by an effective parallel resistance R_{RLC}. A schematic setup is shown in figure 2.4(a). Note that the terms RLC circuit, LC circuit, resonator and (image-current) detector are used synonymously throughout the Penning trap community.

To quantify these thoughts, consider the impedance of the parallel RLC circuit. The individual impedances are

$$Z_{\mathrm{R}} = R_{\mathrm{RLC}}, \qquad Z_{\mathrm{C}} = \frac{1}{i\omega C_{\mathrm{RLC}}}, \qquad Z_{\mathrm{L}} = i\omega L \qquad (2.29)$$

for the resistance, the capacitance and the inductance, respectively. Note that later different resistances and capacitances will be introduced and in order to avoid confusion, the impedances are labelled already here explicitly with a subscript. The total impedance of the parallel RLC circuit is

$$Z_{\mathrm{RLC}}(\omega) = \frac{1}{\frac{1}{Z_{\mathrm{R}}} + \frac{1}{Z_{\mathrm{C}}} + \frac{1}{Z_{\mathrm{L}}}} \qquad (2.30)$$

$$= \frac{\omega^2 \Delta\omega_0^2 R_{\mathrm{RLC}}}{\omega^2 \Delta\omega_0^2 + \left(\omega^2 - \omega_0^2\right)^2} - i\frac{\omega\Delta\omega_0 R_{\mathrm{RLC}}(\omega^2 - \omega_0^2)}{\omega^2 \Delta\omega_0^2 + \left(\omega^2 - \omega_0^2\right)^2}. \qquad (2.31)$$

In the last step the eigenfrequency of the circuit $\omega_0^2 = 1/(LC_{\mathrm{RLC}})$ and the damping rate $\Delta\omega_0 = 1/(R_{\mathrm{RLC}}C_{\mathrm{RLC}})$ has been introduced.

The next key element towards a particle signal is the thermal Johnson-Nyquist noise. This noise should not be considered an experimental imperfection, but rather a desired fundamental ingredient. It is a direct consequence of the fluctuation-dissipation theorem that states, in a simplified form, that any dissipative element (resistor) is inevitably also a source of fluctuation (noise). In the case of a resistor R, the mean squared voltage $\langle u_{\mathrm{th}}^2\rangle$ is given by

$$\langle u_{\mathrm{th}}^2\rangle = 4k_{\mathrm{B}}TR\Delta f, \qquad (2.32)$$

where T is the temperature of the resistor and Δf the bandwidth with which the noise is recorded. It can be shown that R in equation (2.32) can be replaced by the dissipative part of any circuit [47], i.e. the real part of the impedance, yielding

$$\langle u_{\mathrm{th}}^2(\omega)\rangle = 4k_{\mathrm{B}}T\Re\left(Z_{\mathrm{RLC}}(\omega)\right)\Delta f \qquad (2.33)$$

$$= 4k_{\mathrm{B}}T\Delta f \cdot \frac{\omega^2 \Delta\omega_0^2 R_{\mathrm{RLC}}}{\omega^2 \Delta\omega_0^2 + \left(\omega^2 - \omega_0^2\right)^2}. \qquad (2.34)$$

As a result, equation (2.34) defines the lineshape of the resonator, that is the scaling of the noise with frequency.
An alternative but equivalent way of deriving the lineshape is to model the RLC circuit as a reactive component. Here, the noisy resistance is modelled as a noiseless resistance with a current source in parallel that has a spectral current density of

$$\langle i_{\mathrm{th}}^2\rangle = \frac{4k_{\mathrm{B}}T\Delta f}{R_{\mathrm{RLC}}}. \qquad (2.35)$$

This current then incoherently drives the RLC circuit, which inherently oscillates due to the LC-part and damps itself due to the resistance. The same resonance is obtained for both cases. This model is used in the simulation developed in the course of this thesis, see section 6.
A measured example of such a lineshape is shown in figure 2.4 as blue line. The damping rate $\Delta\omega_0$ can be identified as the full-width at half maximum in linear scale or the 3 dB-width in logarithmic scale. Besides, it is convenient to introduce a quality factor $Q = \omega_0/\Delta\omega_0 = R_{\mathrm{RLC}}/(\omega_0 L)$. In practice, significant effort is put in to maximize the quality factor of these circuits, see for example [48, 49, 50].

Next, the lineshape of the resonator coupled to a trapped ion is derived. The following calculations assume that the axial motion is detected, however, the concepts are applicable

to the cyclotron or magnetron motion as well. Again, I will only briefly summarize the derivation, more details can be found in [33]. The ion with mass m and charge q induces an image current [33, 51]

$$I_\text{ind} = \frac{q}{D}\dot{z} \tag{2.36}$$

in the electrode that is connected to the resonator. D is an effective ion-electrode distance and for typical axial amplitudes constant. Similarly, a voltage U_el on the electrode subjects the ion to a force [33]

$$F_\text{el} = \frac{q}{D}U_\text{el} \tag{2.37}$$

in axial direction. The equation of motion is then modified to

$$\ddot{z} + \omega_\text{z}^2 z = F_\text{el}/m. \tag{2.38}$$

While this relation holds generally true, it is of particular interest if F_el stems from the accumulated image charges. Substituting $\ddot{z} \to \dot{I}\frac{D}{q}$ as well as $z \to \int \dot{z}dt = \int \frac{D}{q}Idt$ yields the differential equation

$$\underbrace{m\frac{D^2}{q^2}}_{=l_1}\dot{I} + \underbrace{m\frac{D^2}{q^2}\omega_\text{z}^2}_{=1/c_1}\int I dt = U_\text{el}. \tag{2.39}$$

The structure of this equation is the one of a series LC-circuit and therefore suggests to introduce an inductance l_1 and capacitance c_1 in series to the detection circuit, as shown in figure 2.4(a). To finally obtain the lineshape of the particle signal, it is hence necessary to calculate the impedance of the resulting circuit, i.e. of the detector circuit and particle circuit in parallel,

$$Z_\text{RLC+ion}(\omega) = \frac{1}{\frac{1}{Z_\text{RLC}} + \frac{1}{Z_\text{ion}}} \tag{2.40}$$

$$= \frac{4R_\text{RLC}\left(\frac{\omega-\omega_1}{\Delta\omega_1}\right)^2 - i\left[8R_\text{RLC}\frac{\omega-\omega_0}{\Delta\omega_0}(\frac{\omega-\omega_1}{\Delta\omega_1})^2 - 2R_\text{RLC}\frac{\omega-\omega_1}{\Delta\omega_1}\right]}{4\left(\frac{\omega-\omega_1}{\Delta\omega_1}\right)^2 + \left[4\frac{\omega-\omega_0}{\Delta\omega_0}\frac{\omega-\omega_1}{\Delta\omega_1} - 1\right]^2}. \tag{2.41}$$

Here the particle frequency $\omega_1 \equiv \omega_\text{z} = \sqrt{\frac{1}{l_1 c_1}}$ was introduced. At $\omega = \omega_1$ the real part of the impedance vanishes and the characteristic dip spectrum is obtained. An example for an on-resonance dip ($\omega_0 = \omega_1$) is shown as red line in figure 2.4(b). If more than one ion is in the trap, the dip width $\Delta\omega_1$ can be utilized to count the number of ions in the trap down to the single particle level. It can be calculated to be [33]

$$\Delta\omega_1 = \frac{R_\text{RLC}}{m}\frac{q^2}{D^2}N, \tag{2.42}$$

where N is the number of ions in the trap, provided they are of the same species. The center-of-mass motion of the cloud can be treated as an effective ion with mass Nm and charge Nq.

In order to fit an experimentally recorded dip with the theoretical lineshape, several scaling factors have to be taken into account. Quantitative treatments can be found in refs. [52, 53, 54, 55]. First, in practice not the voltage across the full coil is measured but rather after e.g. 80% of the windings, referred to as tap and already indicated in figure 2.4. This allows to optimize the SNR and Q-factor relative to each other in presence of an amplifier with finite input resistance. Second, the coupling capacitance between coil tap and amplifier input combined with the parasitic input capacitance of the amplifier give rise to an additional coupling factor. Third, amplifiers at the cryogenic and room-temperature stage not only introduce an amplification factor, they also have an equivalent input noise

that defines the noise floor of the spectrum. As a result, the function that is used to fit a single dip is [53]

$$\langle u_{\text{th, exp}}^2(\nu) \rangle = n_0 + n_1 \frac{4 \left(\frac{\nu - \nu_1}{\Delta \nu_1} \right)^2}{4 \left(\frac{\nu - \nu_1}{\Delta \nu_1} \right)^2 + \left(4 \frac{\nu - \nu_0}{\Delta \nu_0} \frac{\nu - \nu_1}{\Delta \nu_1} - 1 \right)^2} \tag{2.43}$$

where n_0 is an effective noise floor and n_1 a measure of the SNR containing all scaling factors. For completeness, $\nu_{0/1} = \omega_{0/1}/(2\pi)$ are the resonator/particle frequencies, and $\Delta \nu_{0/1} = \Delta \omega_{0/1}/(2\pi)$ are the resonator/particle (dip) widths.

2.4   Radiofrequency drives and sideband coupling

The manipulation of the motion of trapped ions by means of radiofrequency drives is one of the key elements for virtually all measurements conducted in Penning traps. In general, the excitations are applied either via one of the trapping electrodes or via small coils placed in direct vicinity of the traps.

2.4.1   Monopolar or parametric excitation

A monopolar or parametric excitation changes by definition the trapping potential of the ion. Hence it can be introduced via any trap electrode including the endcaps. The drive strength at the position of the ion can be described by the electric field

$$E_z = \frac{E_{\text{mono}}}{d} \cos(\omega_{\text{RF}} t + \phi_{\text{RF}}) z, \tag{2.44}$$

where ω_{RF} and ϕ_{RF} are the frequency and phase of the drive, respectively. E_{mono} is the electric field amplitude and d is a characteristic length defined by the distance of the electrode to the ion as well as the geometry of the electrode. In the absence of further forces, the equation of motion for the trapped particle is then

$$\ddot{z} + \left(\omega_z^2 - \frac{q E_{\text{mono}}}{md} \cos(\omega_{\text{RF}} t + \phi_{\text{RF}}) \right) z = 0. \tag{2.45}$$

In this form the modulation of the trapping potential is directly visible. It can be shown that at $\omega_{\text{RF}} = 2\omega_{\text{z}}$ the ion is resonantly excited. A brief and incomplete explanation can be derived via Fourier components: Assuming $z(t) = A\cos(\omega_z t) + B\sin(\omega_z t)$, the drive is equivalent to an external force with frequency components

$$\cos(2\omega_{\text{z}} t)\left(A\cos(\omega_z t) + B\sin(\omega_z t) \right) \propto A\cos(\omega_z t) - B\sin(\omega_z t). \tag{2.46}$$

Thus, in contrast to a drive at $\omega_{\text{RF}} = 1\omega_{\text{z}}$, the parametric excitation excites both the sin- and cos-component of the undisturbed motion of the ion.

The resonance feature is regularly utilized when initially debugging a system. For example, sweeping the ring voltage while applying a parametric excitation at constant frequency is equivalent to recording a mass spectrum, allowing to determine the composition of an ion cloud composed of different species. Furthermore, it is helpful when searching a particle in a trap where the ring voltage and tuning ratio differ from the ideal values e.g. due to patch potentials.

2.4.2   Dipolar excitation

A dipolar excitation has by definition an electric field of type

$$E_{x,z} = E_{di} \cos(\omega_{RF} + \phi_{RF}),\tag{2.47}$$

where E_{di} is the constant electric field amplitude. The dipole excitation can coherently excite all three eigenmotions of an ion in the trap. In practice, the axial mode requires excitation via an endcap or correction electrode and the radial modes require a radially split electrode. Usually ω_{RF} matches the motional frequency ω_i and the frequency mismatch is smaller than the Fourier width, i.e. $\omega_{RF} - \omega_i \ll 1/T_{excit}$, where T_{excit} is the excitation time. Besides the electric field amplitude, the excitation dynamics is determined by the oscillation amplitude of the ion and the relative phase difference. This can be exploited to measure the temperature of an ion (section 6.6) or to imprint an initial starting phase on the ion's motion for phase-sensitive frequency measurements (section 6.7).

2.4.3   Quadrupolar excitation and sideband coupling for radial frequency measurements

The quadrupolar excitation is the lowest-order excitation that allows coupling between modes. Its electric field is of type

$$\vec{E} = \frac{E_0}{d} \cos(\omega_{RF} t + \phi_{RF}) \begin{pmatrix} z \\ 0 \\ x \end{pmatrix}.\tag{2.48}$$

This configuration allows to couple the normally independent modes of a particle in a Penning trap. Energy is exchanged periodically if $\omega_{RF} = \omega_+ - \omega_z$ for cyclotron-axial coupling or $\omega_{RF} = \omega_z + \omega_-$ for magnetron-axial coupling. The inverse sign stems from the fact that the energy of the magnetron motion is more negative for higher magnetron radii. If the axial motion is continuously thermalized to the axial resonator, this allows to cool the radial amplitudes of arbitrary species.

Shining in the drive at the 'blue' sideband frequency, i.e. $\omega_{RF} = \omega_+ + \omega_z$ or $\omega_{RF} = \omega_z - \omega_-$, leads to an exponential increase of both modes. Note that in principle also a coupling between ω_+ and ω_- is possible, but not used in the course of this thesis.

The equations of motions have the exact same structure as a driven two-level system. The following arguments are restricted to the cyclotron-axial coupling but they hold true for the magnetron-axial coupling as well. The solution of the driven system is

$$z(t) = z_0 \sin\left(\frac{\Omega_0}{2} t\right) \sin(\omega_z t + \phi_z)\tag{2.49}$$

$$\rho_+(t) = \rho_+ \cos\left(\frac{\Omega_0}{2} t\right) \sin(\omega_+ t + \phi_+).\tag{2.50}$$

Here Ω_0 is the Rabi frequency

$$\Omega_0 = \frac{qE_0}{2md\sqrt{\omega_z \omega_+}}\tag{2.51}$$

It is evident that both modes are now composed of Fourier components at $\omega_{z/+} \pm \Omega_0/2$. As a consequence, the former single axial dip in the noise spectrum splits into a double dip, of which an example is shown in figure 2.5(a). The frequencies are related by

$$\omega_l + \omega_r = \omega_+ + \omega_z - \omega_{RF},\tag{2.52}$$

(a)

(b)
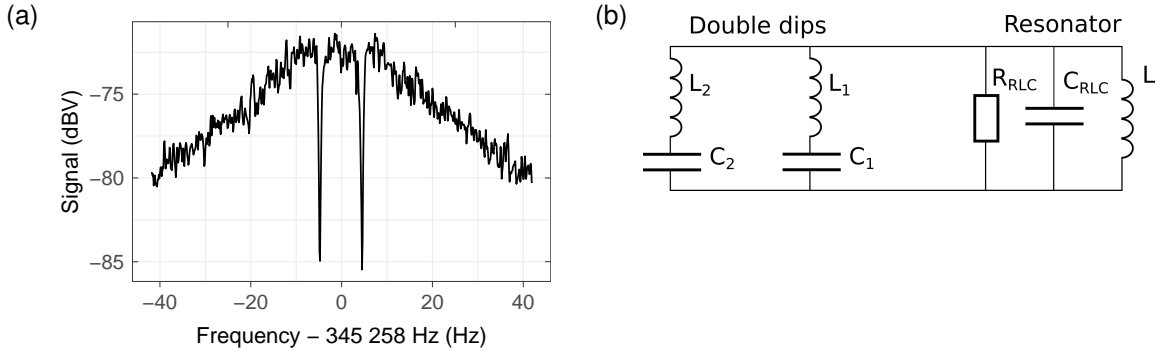
Figure 2.5: Example of a double dip spectrum (a) when shining in an electric rf-quadrupolar field at $\nu_{\mathrm{RF}} = \nu_+ - \nu_{\mathrm{z}}$ for the modified cyclotron motion or $\nu_{\mathrm{RF}} = \nu_- + \nu_{\mathrm{z}}$ for the magnetron motion. The equivalent circuit for modelling the lineshape is shown in (b).

where ω_{l} and ω_{r} are the left and right dip positions of the double dip. It follows that if no detuning is present, i.e. $\omega_{\mathrm{RF}} = \omega_+ - \omega_{\mathrm{z}}$, the double dip is generated symmetric about the former single dip. However, in the case of a detuning $\delta = \omega_{\mathrm{RF}} - (\omega_+ - \omega_{\mathrm{z}})$ the position of the dips is altered to

$$\omega_{\mathrm{l,r}} = \omega_{\mathrm{z}} - \frac{\delta}{2} \mp \frac{1}{2}\sqrt{\Omega_0^2 + \delta^2}. \tag{2.53}$$

Consequently, also the Rabi frequency is increased to

$$\Omega = \omega_{\mathrm{r}} - \omega_{\mathrm{l}} = \sqrt{\Omega_0^2 + \delta^2}. \tag{2.54}$$

Note that for non-zero detuning, Ω_0 in equations (2.49, 2.50) must be substituted by Ω. The frequency relation for a magnetron double dip is

$$\omega_{\mathrm{l}} + \omega_{\mathrm{r}} = \omega_{\mathrm{z}} - \omega_- + \omega_{\mathrm{RF}}. \tag{2.55}$$

For $\delta \neq 0$ equation (2.53) holds true as well.

The lineshape of such a double dip is modelled by adding another ion as series LC-circuit in the equivalent circuit picture, see figure 2.5(b). I refrain from deriving the rather cumbersome impedance of the full equivalent circuit at this point. Instead, in analogy to equation (2.43), I only state the practical version that is used to fit double dip spectra,

$$S(\nu) = n_0 + n_1 \frac{4\left(\frac{\nu-\nu_1}{\Delta\nu_1}\right)^2 \left(\frac{\nu-\nu_2}{\Delta\nu_2}\right)^2}{4\left(\frac{\nu-\nu_1}{\Delta\nu_1}\right)^2 \left(\frac{\nu-\nu_2}{\Delta\nu_2}\right)^2 + \left(4\frac{\nu-\nu_0}{\Delta\nu_0}\frac{\nu-\nu_1}{\Delta\nu_1}\frac{\nu-\nu_2}{\Delta\nu_2} - \frac{\nu-\nu_1}{\Delta\nu_1} - \frac{\nu-\nu_2}{\Delta\nu_2}\right)^2}. \tag{2.56}$$

Note that the equivalent circuit should only be considered a first-order model and in reality small deviations to the model are observed. For example, the double dips do not fully compensate the noise and have a reduced SNR.

Since the axial mode thermalizes to the effective resonator temperature, sideband coupling is commonly used to also thermalize the radial modes. In particular, the radial temperatures are [36]

$$T_+ = \frac{\omega_+}{\omega_{\mathrm{z}}} T_{\mathrm{z}} \tag{2.57}$$

$$T_- = -\frac{\omega_-}{\omega_{\mathrm{z}}} T_{\mathrm{z}} \tag{2.58}$$

Although the factors of $\omega_+/\omega_{\mathrm{z}}$ and $\omega_-/\omega_{\mathrm{z}}$ can be derived classically, a very intuitive explanation is that not energies, but rather quantum numbers are exchanged, compare equations (2.17) – (2.19).

2.5   Proton g-factor measurement and the need for advanced cooling

2.5.1   The continuous Stern-Gerlach effect

One of the most crucial requirements in a Penning-trap g-factor measurement is the non-destructive detection of the spin state, which is based on the continuous Stern-Gerlach effect. The basic idea to detect the spin state is that the axial frequency shifts as a function of the spin state if the proton is placed in a magnetic bottle, meaning a magnetic field with deliberately large B_2-coefficient. In particular, the cyclotron motion and the associated $\Delta\nu_{\mathrm{z}}(B_2, E_+)$-shift can also be expressed in terms of a magnetic moment $\mu_{\mathrm{z}}^{\mathrm{cyc}}$. However, the total magnetic moment $\mu_{\mathrm{z}}^{\mathrm{tot}}$ is the sum of the motional contribution and that of the spin $\mu_{\mathrm{z}}^{\mathrm{spin}}$,

$$\mu_{\mathrm{z}}^{\mathrm{tot}} = \mu_{\mathrm{z}}^{\mathrm{cyc}} + \mu_{\mathrm{z}}^{\mathrm{spin}} = \frac{qE_+}{m\omega_+} \pm \frac{ge}{2m}\,|\vec{s}|\,. \tag{2.59}$$

Here g is the g-factor of the proton, $|\vec{s}| = \hbar/2$ is the projection of the absolute value of the spin vector onto the z-axis and e the elementary charge. In a strong magnetic field, the spin aligns either parallel or antiparallel to the magnetic field ('spin up' or 'spin down'). The spin contribution to the magnetic moment can be derived by substituting $E_+ = -\mu_{\mathrm{z}}^{\mathrm{spin}}B_0$ in the formula for the $\nu_{\mathrm{z}}(B_2, E_+)$-shift (equation (2.28)). The axial frequency shift due to a spin-flip is then

$$\Delta\nu_{\mathrm{z}}^{\mathrm{spin}} = g\frac{B_2 e\hbar}{8\pi^2 m^2 \nu_{\mathrm{z}}}, \tag{2.60}$$

where a factor of 2 due to the magnetic moment change by $|2\mu_{\mathrm{z}}^{\mathrm{spin}}|$ (spin-*flip*) is accounted for. Note that only particles with $\omega_{\mathrm{c}} \approx \omega_+ \gg \omega_-$ are considered here, otherwise the magnetron motion would contribute significantly to the magnetic moment.

Inserting the parameters of our experiment of $\nu_{\mathrm{z}} \approx 500\,\mathrm{kHz}$ and $B_2 = 300\,000\,\mathrm{T/m^2}$ as well as the fundamental constants, equation (2.60) yields an axial frequency jump of $250\,\mathrm{mHz}$ for the spin-flip of a proton. Note that this value is comparably small, which makes a g-factor measurement of the proton particularly difficult. In comparison, although a free electron has a g-factor in the same order of magnitude, due to the $\Delta\nu_{\mathrm{z}}^{\mathrm{spin}} \propto 1/m^2$ scaling of equation (2.60) the axial frequency difference is larger by six orders of magnitude. Nevertheless, $250\,\mathrm{mHz}$ can be resolved, but only if the cyclotron energy is sufficiently small, as it will be outlined in the next subsections.

2.5.2   Double-trap g-factor measurement

In order to measure the g-factor, the spin precession frequency or Larmor frequency

$$\nu_{\mathrm{L}} = \frac{1}{2\pi}\frac{g}{2}\frac{q}{m}B_0 \tag{2.61}$$

is measured. To obtain the g-factor, the magnetic field must be determined very precisely. This is done by measuring the three individual motional frequencies of the trapped particle in the precision trap, which yield the free cyclotron frequency via $\nu_{\mathrm{c}} = \sqrt{\nu_+^2 + \nu_{\mathrm{z}}^2 + \nu_-^2} = \frac{1}{2\pi}\frac{q}{m}B_0$. Thus the g-factor is given by the ratio

$$g = 2\frac{\nu_{\mathrm{L}}}{\nu_{\mathrm{c}}}. \tag{2.62}$$

However, in practice the Larmor frequency cannot be measured directly. Instead, an external drive is applied to a small coil in vicinity of the trap that can cause a spin-flip if the drive frequency is close to the Larmor frequency. Note that in contrast to all other excitations, now the magnetic field and not the electric field of the drive is relevant. Therefore the coil is grounded on the other end so that the total resistance of the drive is small and a comparably large current can flow. Importantly, the detection of a spin-flip is not possible in the precision trap since the B_2-coefficient is tuned to (nearly) zero therein. For this reason, the particle is transported to the analysis trap (AT), which features an extremely large magnetic bottle of $B_2 = 300\,000\,\mathrm{T/m^2}$. Here, the spin-flip is detectable by the $\approx 250\,\mathrm{mHz}$ frequency jump. However, the cyclotron frequency of the particle can only be measured imprecisely in the AT due to the linewidth broadening from the B_2. Thus, both traps are operated in a symbiotic manner, where the motional frequency measurements and spin-flips are performed in the PT and the spin-state determination in the AT. To finally obtain the g-factor, the spin-flip probability is scanned as a function of the frequency of the Larmor drive. This results in a resonance from which, after small systematic corrections, the g-factor is obtained.

2.5.3   Cyclotron quantum number transition rates and the need for cooling

In order to resolve the $\approx 250\,\mathrm{mHz}$ axial frequency jump in the AT due to a spin-flip, other sources of axial frequency instability must be eliminated. The dominant contribution are quantum transitions of the modified cyclotron frequency. Due to the necessarily large B_2, the axial frequency inevitably depends strongly on $E_+ = (n_+ + 1/2)\hbar\omega_+$. In fact, a quantum number transition of $n_+ \rightarrow n_+ \pm 1$ results in an axial frequency shift of

$$\Delta\nu_{\mathrm{z}}(B_2, n_+ \rightarrow n_+ \pm 1) = \frac{B_2}{2B_0}\frac{\nu_{\mathrm{z}}}{\nu_-}\frac{\hbar}{2\pi m} \tag{2.63}$$
$$= 76\,\mathrm{mHz}.$$

A spin-flip thus corresponds to only a little more than 3 cyclotron quantum transitions. Consequently, minimizing the cyclotron quantum number transition rate[1] is of utmost importance for high-fidelity spin state readout. A detailed investigation of transition rates for a single antiproton in our sister experiment `BASE-CERN` can be found in ref. [56]. In summary, the transition rate $\xi_+ = \dot{n}_+$ is assumed to stem from a noise-driven quantum oscillator, yielding

$$\xi_+ = \frac{q^2 n_+}{2m\hbar\omega_+}S_{\mathrm{E}}(\omega_+). \tag{2.64}$$

Here $S_{\mathrm{E}}(\omega_+)$ is the spectral density of electric-field noise which the cyclotron motion is exposed to. By measuring the frequency stability as a function of averaging time, ref. [56] extracted $\xi_+ = 6(1)\,\mathrm{h^{-1}}$ and $S_{\mathrm{E}}(\omega_+) \leq 7.5 \times 10^{-20}\,\mathrm{V^2m^{-2}Hz^{-1}}$. Although it was never explicitly measured, a comparison of spin state fidelities as a function of n_+ hints that the last proton g-factor measurement had at least similar and possibly even lower transition rates. As a side note, this transition rate is orders of magnitude lower compared to cryogenic Paul traps or room-temperature Penning traps. As a result, it allowed to constrain the local density of millicharged particles [57], which would scatter off the ion and thus increase the transition rate. Millicharged particles are considered dark matter candidates within standard model extensions.

---

[1]Note that the transition rate is sometimes referred to as heating rate in other references. However, I prefer the term transition rate, since the cumulative change of n_+ over time can be modelled to a good degree as an *undirected* random walk.

An alternative way of expressing equation (2.64) is by introducing the creation and annihilation operators of a quantum mechanical harmonic oscillator ($\hat{a}^{\dagger}$ and $\hat{a}$, respectively) that act on the energy eigenstate $|n_+\rangle$ [58]:

$$\hat{a}^{\dagger} |n_+\rangle = \sqrt{n_+ + 1} |n_+ + 1\rangle \tag{2.65}$$

$$\hat{a} |n_+\rangle = \sqrt{n_+} |n_+ - 1\rangle \tag{2.66}$$

For both operators the actual transition probability is proportional to the absolute value squared of the wave function, thus yielding $\xi_+ \propto n_+$ again.

The relevant part of equation (2.64) for a g-factor measurement is the fact that $\xi_+ \propto n_+$. This means that the spin-state fidelity becomes worse the larger the cyclotron energy of the particle is, because the axial frequency jump due to a spin-flip is diffused by axial frequency fluctuations due to cyclotron energy transitions. This effect is illustrated in figure 2.6(a). Therefore, before attempting to observe a spin-flip, in practice the cyclotron motion of the proton is cooled below a certain threshold energy E_{thresh}. This can be done by means of a cyclotron resonator which is cooled with negative feedback (which will be introduced in section 3.5) to 3–13 K. However, the last proton g-factor measurement required $E_{\text{thresh}} = 600\,\text{mK} \cdot k_{\text{B}}$ [6] and the last antiproton g-factor measurement required an even lower $E_{\text{thresh}} = 200\,\text{mK} \cdot k_{\text{B}}$ [59]. Thus, the only way a cold particle can be prepared with this technique is by repeatedly sampling the Boltzmann distribution and selecting suitably low cyclotron energies. For example, assuming the parameters of the last proton g-factor measurement, $T_+ = 3.4\,\text{K}$ and $E_{\text{thresh}} = 600\,\text{mK} \cdot k_B$, the probability of finding a particle with sufficiently small energy is

$$p = \frac{1}{k_{\text{B}}T_+} \int_0^{E_{\text{thresh}}} \exp\left(-\frac{E_+}{k_{\text{B}}T_+}\right) dE_+ \tag{2.67}$$
$$= 16\%.$$

In addition, since a cyclotron-frequency measurement via the double-dip technique thermalizes the cyclotron energy to $T_+ = \frac{\omega_+}{\omega_z}T_z \approx 600\,\text{K}$ again, the selection process must be repeated after each cyclotron frequency measurement. Furthermore, the cooling time constant of a cyclotron resonator is typically on the order of $\tau \approx 30-90\,\text{s}$. Cooling the particle down from 600 K requires waiting a few cooling time constants, so that in total several minutes have to be invested for the cooling process alone. Another important ingredient is a sufficiently low cyclotron heating rate for the transport between the two different traps, which directly contributes to the final achievable cyclotron temperature.

Note that this discussion focused on the need for advanced cooling techniques and other specific details of the g-factor measurements such as the use of two particles in parallel have been omitted. Nevertheless, in summary the statistical uncertainty of the last proton g-factor measurement is larger by a factor of 2 compared to the systematic uncertainty, mainly due to the lack of advanced cooling techniques.

2.6   Advanced cooling techniques

At this point, it is clear that a more advanced cooling technique is required to improve the state-of-the-art magnetic moment measurements. The central question is therefore: *How can an (anti-)proton be cooled in less than one minute to a temperature below 1 K?*

A direct way would be to use a $^3\text{He}/^4\text{He}$ dilution refrigerator that reaches temperatures of a few mK and then resistively cool the cyclotron motion [60]. However, this concept imposes several new problems. First, the mechanical vibrations of the refrigerator are detrimental to any precision measurement and a sufficient decoupling is a complex engineering problem

(a)

(b)
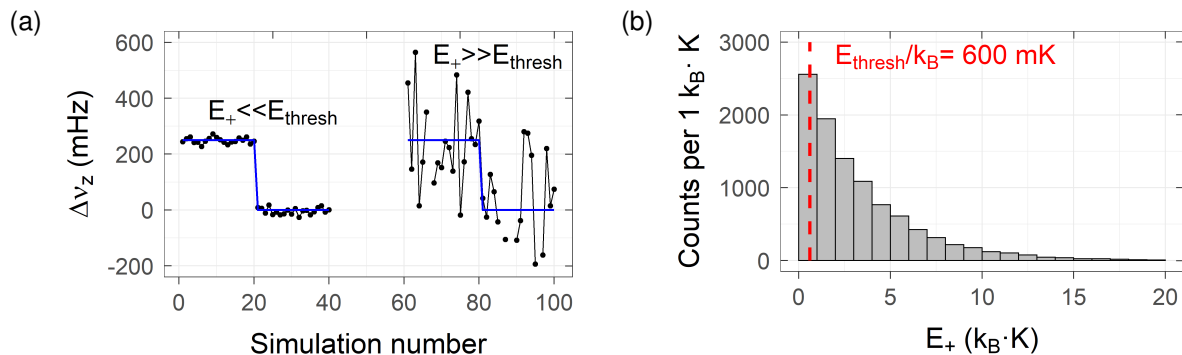
Figure 2.6: The difference in axial frequency stability between a cyclotron-cold and cyclotron-hot particle is shown in (a). The step is due to a spin-flip, which can be easily resolved if the particle is cold but not if it is hot. An exemplary Boltzmann distribution with $T_+ = 3.4\,\mathrm{K}$ is shown in (b). Only the particles with cyclotron energies left of the red line can be used to resolve spin-flips, thus a time-intensive preparation of a cold particle is required. Subfigure (a) is modified from ref. [28]

on its own. In fact, one of the first versions of the proton g-factor apparatus was operated with a $4\,\mathrm{K}$ closed-cycle cryocooler, however, this concept was abandoned due to afore-mentioned mechanical vibrations [54, 61]. It is not clear where the limitations of a more sophisticated engineering solution are. Second, the experimental heat load on the $4\,\mathrm{K}$ stage is about $0.3\,\mathrm{W}$, orders of magnitude higher than the cooling power of commerical dilution refrigerators. Another temperature stage with sufficient shielding would probably require a new magnet since already now the radial space between the cold experiment and the $300\,\mathrm{K}$ magnet bore is at maximum a few mm. Third and finally, the actual ion temperature is a sum of the physical temperature of the (cyclotron) resonator plus a contribution from the equivalent input noise of the attached amplifiers. For example, the effective detector temperature of the last antiproton g-factor measurement was $12.8(8)\,\mathrm{K}$ [59], a temperature at which NbTi is already not superconducting anymore. Thus reducing the physical temperature to mK is of no use if the equivalent input noise of the amplifiers is not reduced to a comparable level.

One cooling technique that has been incredibly successful over the last decades is laser-cooling [62]. Even the most basic version (Doppler cooling) achieves temperatures of typically several hundred µK. However, the particle of interest requires a suitable optical transition to cool it. Obviously, both the proton and antiproton lack these. Consequently, the only way an (anti)-proton can be cooled is by employing sympathetic cooling techniques. In the hitherto established version of sympathetic cooling, the particle of interest is cooled by Coulomb collisions with a co-trapped laser-coolable species [15]. While this might be suitable for the proton, it is not applicable to the antiproton. Besides concerns about annihilation, a negatively charged laser-coolable ion is an exotic species on its own [19, 20] and therefore not suitable for routine operation.

As a result, the ion of interest and the laser-coolable species must be placed in separate potential wells that can have different polarities. To this end, two methods are possible: The potential wells can be axially spaced apart by $< 5\,\mathrm{mm}$ such that the ion-ion Coulomb-interaction is still strong enough to mediate the coupling [17, 18]. This is the approach the `BASE-Hanover` subgroup pursues with the final goal of implementing quantum-logic tech-niques for (anti-)protons [63]. While this method allows for theoretical Rabi frequencies of several tens of Hz, the challenge is the manufacturing of sufficiently small electrodes that enable the short axial separation distances of the potential wells while ensuring a sufficiently small heating rate at the same time.

Another approach relies on placing the ions in completely distinct traps separated by

macroscopic distances of several cm or even more. In that case, the coupling is mediated by image currents both ions species induce in adjacent electrodes. Originally proposed in ref. [24], this is the approach pursued in our group `BASE-Mainz` and further investigated in the course of this thesis. In general, the challenge here is that the energy exchange rates are much lower and thus the ion frequencies must be well under control. On the other hand, although dedicated coupling traps were built, the specific demands on the trap electrodes are much more relaxed and the heating rates are significantly lower.

2.7 Doppler cooling of beryllium ions in a Penning trap

2.7.1 Basics of light-ion interaction

The physics of light-atom interaction is a field with active research on its own, so that I will limit myself to the basics that are relevant for our experiment. More comprehensive introductions can be found in e.g. refs. [64, 65, 66].
The description of a spectral line involves three processes referred to as spontaneous emission, stimulated emission, and absorption. The probability of the respective process to occur is proportional to the Einstein coefficients. Based on modelling the electronic transition between two levels of an atom or ion as a damped harmonic oscillator, it can be shown that the spectral intensity distribution of the emitted light follows a Lorentzian profile

$$I(\omega) = I_0 \frac{(\Gamma/2)^2}{(\omega - \omega_{L0})^2 + (\Gamma/2)^2}, \tag{2.68}$$

where ω is the angular frequency of the emitted light, ω_{L0} is the angular transition frequency, Γ is the natural linewidth and I_0 the maximum intensity for $\omega = \omega_{L0}$. The natural lifetime of the excited state is given by $\tau = 1/\Gamma$. The probability of a spontaneous decay $P_{\text{sp-em}}$ within a short time frame $\Delta t \ll \tau$ is given by

$$P_{\text{sp-em}} = \Gamma \Delta t. \tag{2.69}$$

Assuming a monochromatic light source with frequency ω and intensity I, the probability for absorption P_{abs} is given by [67, p. 140]

$$P_{\text{abs}}(\omega) = \frac{I}{I_{\text{sat}}} \frac{\Gamma^3 \Delta t/8}{(\omega - \omega_{L0})^2 + (\Gamma/2)^2}. \tag{2.70}$$

Here I_{sat} is the saturation intensity $I_{\text{sat}} = \frac{2\pi^2 h (\Gamma/2\pi) f_{L0}^3}{3c^2}$ with $f_{L0} = \omega_{L0}/(2\pi)$. Note that for practical use Δt must chosen sufficiently small such that $P_{\text{abs}}(\omega) \ll 1$. In addition, this probability should not be considered a normalized probability $0 \le p \; leq 1$ but rather the mean number of absorption or emission processes within the time frame Δt.

The probability of stimulated emission $P_{\text{st-em}}$ is given by

$$P_{\text{st-em}} = P_{\text{abs}}. \tag{2.71}$$

Note that this equality implies that the stimulated emission probability rises with larger laser power. This result can be understood by considering the stimulated emission as the time-reverse process of absorption. Alternatively, in a quantum mechanical picture, the external drive of the incoming photon disturbs the excited state and evolves it into a superposition of the excited state and ground state, which eventually collapses to the ground state. In yet another view, the stimulated emission is the result of the bosonic nature of light. Notably, the frequency and phase of a photon emitted by spontaneous

emission is the same as for the incoming photon, which is the fundamental principle a laser relies on. A practical consequence of the stimulated emission process is that it competes with the spontaneous emission process. Since the photons that are emitted by stimulated emission are indistinguishable from the laser photons, only spontaneously emitted photons are identified as 'scattered' photons. As a result, the number of experimentally observed scattered photons rises weaker than linearly with the light intensity and is given by [67, p. 143]

$$\gamma_{\mathrm{s}} = \frac{I}{I_{\mathrm{sat}}} \frac{\Gamma/2}{1 + \frac{I}{I_{\mathrm{sat}}} + 4\left(\frac{\omega - \omega_{\mathrm{L0}}}{\Gamma}\right)^2}. \tag{2.72}$$

2.7.2 Doppler cooling of $^9\mathrm{Be}^+$

Doppler cooling is the most basic version of laser cooling and allows cooling of atoms or ions to sub-mK temperatures. An instructive introduction can be found in [62] and comprehensive quantitative treatments in refs. [66, 68]. The idea is to tune the frequency of a laser beam slightly below a suitable electronic transition of the ion of interest (red detuned). If the particle moves towards the direction of the laser beam, it is subject to the Doppler shift and thus resonantly absorbs more photons. If $\delta_{\mathrm{L}} = f_{\mathrm{L}} - f_{\mathrm{L0}} < 0$ is the laser detuning and $\vec{k}_{\mathrm{L}}\vec{v}$ the Doppler shift due to the ion's velocity, equation (2.72) becomes

$$\gamma_{\mathrm{s}} = \frac{I}{I_{\mathrm{sat}}} \frac{\Gamma/2}{1 + \frac{I}{I_{\mathrm{sat}}} + 4\left(\frac{2\pi\delta_{\mathrm{L}} - \vec{k}_{\mathrm{L}}\vec{v}}{\Gamma}\right)^2}. \tag{2.73}$$

It is evident that the scattering rate has a maximum at $2\pi\delta_{\mathrm{L}} = \vec{k}_{\mathrm{L}}\vec{v}$, i.e. if photon wave vector and ion velocity are antiparallel, $\vec{k}_{\mathrm{L}}\vec{v} < 0$. Upon absorption of such a counter-propagating photon, the momentum of the photon is transferred to the ion, reducing its velocity by the recoil velocity and thus effectively cooling it. The cooling mechanism comes about through two important aspects: First, the re-emission of the photon is spontaneous and hence in a random direction, transferring on average zero momentum. Second, the emitted photon has, on average, a slightly higher energy than the absorbed laser photon as its frequency corresponds to the non-detuned electronic transition in the laboratory frame. From a thermodynamic perspective, low-entropy laser light enters the sample and high-entropy fluorescence light leaves it, thus cooling the sample. It can be shown that the lowest temperature, referred to as Doppler limit, is achieved at $\delta_{\mathrm{L}} \approx -\Gamma/2$ and is on the order of hundreds of microkelvin for most species.

In the following, the details of Doppler cooling of beryllium ions are discussed. Beryllium ions are the species of choice since they are the lightest singly-charged ion with a practicably accessible optical laser transition. As such they induce the largest image current and feature the strongest image-current coupling to the proton. This argument will be derived more formally in section 6. As an alkaline earth metal, a singly-charged beryllium ion has a lithium-like electron configuration $(1\mathrm{s}^2 2\mathrm{s}^1)$ and thus a comparably simple level scheme. Dipole-allowed transitions between the $2^2S_{1/2}$ ground state and the two fine structure states $^2\mathrm{P}_{1/2}$ and $^2\mathrm{P}_{3/2}$ correspond to photon wavelengths of about 313 nm and are accessible with a commercial laser system. This transition has a natural width of $\Gamma = 19.6\,\mathrm{MHz}$ and a lifetime of 8.1 ns [69]. Furthermore, the beryllium nucleus carries a spin of $I = 3/2$ which generates hyperfine structure. However, in the strong magnetic field of a Penning trap, the electronic and nuclear angular momenta $\vec{J}$ and $\vec{I}$ decouple (Paschen-Back-effect). As a result, m_{I} and m_{J} are the 'good' quantum numbers.

Since a photon carries a momentum of $L_{\mathrm{ph}} = 1$, for light that is circularly polarized and travels parallel to the magnetic field, m_{J} must change by $\Delta m_{\mathrm{J}} = \pm 1$ in a transition from
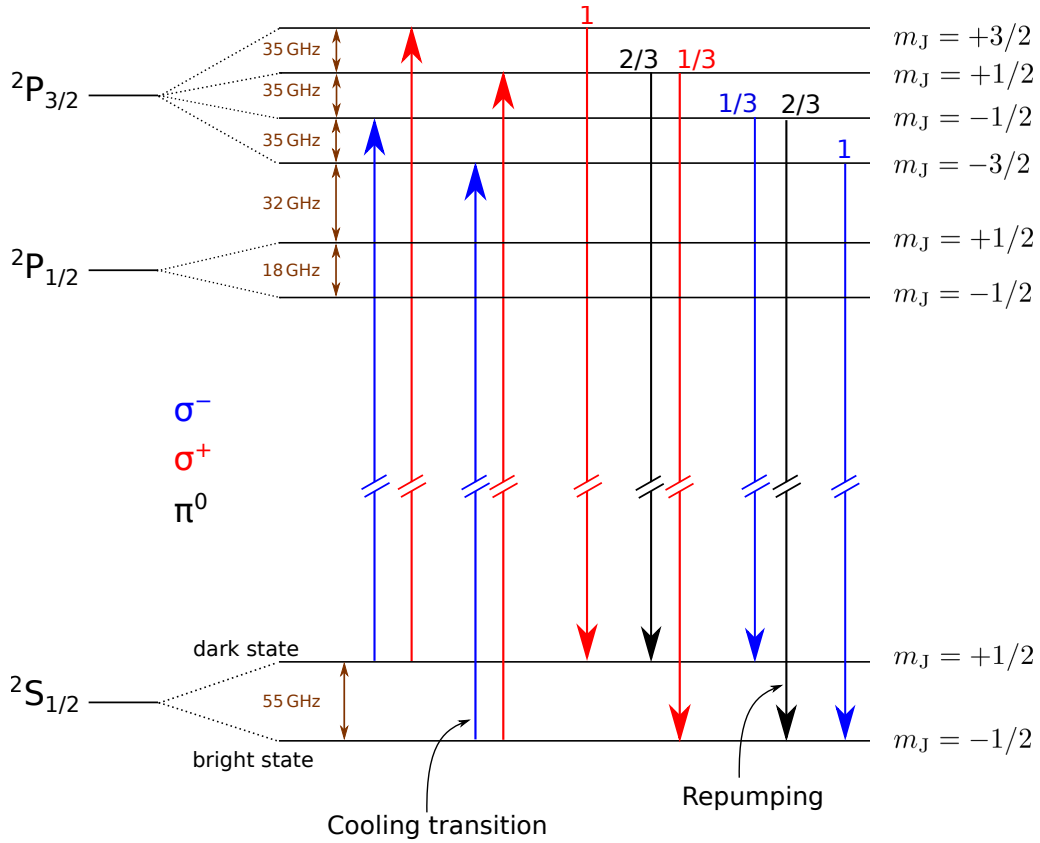
Figure 2.7: Relevant level scheme for laser-cooling of a single beryllium ion in a 1.9 T magnetic field. Transitions from the $^2\text{S}_{1/2}$ ground state to the $^2\text{P}_{3/2}$ excited state are shown. Note that the spacings of the levels are not to scale. σ^-, σ^+ and π^0 transitions are shown in blue, red and black, respectively. The annotated numbers for the decays are the squared Clebsch-Gordan-coefficients.

the ground state to the excited state ($\sigma^\pm$-light). A spontaneous decay however can emit light with $m_\text{L} = \pm 1$ but also with $m_\text{L} = 0$ (π-light).

In the course of this thesis, σ^--polarized light ($m_\text{L} = -1$, $\Delta m_\text{J} = -1$) is used to drive the laser cooling transition. Thus, the transition $|m_\text{I,g}, m_\text{J,g}\rangle \rightarrow |m_\text{I,ex}, m_\text{J,ex}\rangle = |-3/2, -1/2\rangle \rightarrow |-3/2, -3/2\rangle$ is employed for cooling, where the additional subscripts 'g' and 'ex' denote the ground and excited state, respectively. It would be possible to use σ^+-light and drive the $|+3/2, +1/2\rangle \rightarrow |+3/2, +3/2\rangle$ transition as well.

The hyperfine structure can be disregarded as with circularly polarized light the beryllium ion is pumped into the correct hyperfine state. In general, a closed cooling cycle is required for continuous cooling of the ion. If an ion leaves this cycle, it scatters significantly less photons and no further cooling can occur. For this reason, the corresponding electronic ground states are referred to as dark states. Usually, it is necessary to (re-)pump the ions out of these dark states with a dedicated laser. However, a feature of $^9\text{Be}^+$ is that its level structure provides an enhanced intrinsic repump mechanism. Assuming σ^--light, in our case the $^2\text{S}_{1/2}\, m_\text{J} = +1/2$ state is the dark state and the $m_\text{J} = -1/2$ state the bright one. If the ion happens to be in the dark state, off-resonant σ^--transitions of the cooling laser can pump the ion into the $^2\text{P}_{3/2}\, m_\text{J} = -1/2$ state. From there, the excited beryllium ion can spontaneously decay back on a σ^-- or a π-transition. The relative probabilities are given by the square of the Clebsch-Gordan-coefficients [70],

$$\langle L_\text{ph} = 1, m_\text{L,ph} = \quad 0; J_\text{g} = 1/2, m_\text{J,g} = -1/2 | J_\text{ex} = 3/2, m_\text{J,ex} = -1/2 \rangle^2 = 2/3 \quad (2.74)$$

$$\langle L_\text{ph} = 1, m_\text{L,ph} = -1; J_\text{g} = 1/2, m_\text{J,g} = +1/2 | J_\text{ex} = 3/2, m_\text{J,ex} = -1/2 \rangle^2 = 1/3 \quad (2.75)$$

The fact that the $m_J = -1/2$ ground state is preferentially populated is the aforementioned enhanced intrinsic repump rate. Note that this argument assumes that the decay of the $m_J = -1/2$ excited state is due to spontaneous emission and stimulated emission is highly suppressed. This is however generally true, as the photon frequency difference between the respective σ^- transitions of the dark and bright state is estimated to be on the order of $20\,\mathrm{GHz}$ in a $1.9\,\mathrm{T}$ magnetic field.

In addition, for the ion to be in the $^2\mathrm{S}_{1/2}\,m_J = +1/2$ state in the first place, an off-resonant and therefore suppressed transition must occur, e.g. $^2\mathrm{S}_{1/2}\,m_J = -1/2 \longrightarrow {}^2\mathrm{P}_{3/2}\,m_J = -1/2$.

Finally, the $^2\mathrm{P}_{1/2}$ state can be safely neglected as well since no σ^--transition of the bright ground state to any hyperfine level of the $^2\mathrm{P}_{1/2}$ state exists. Furthermore, a σ^--transition from the dark ground state into the $^2\mathrm{P}_{1/2}\,m_J = -1/2$ state is detuned by about $105\,\mathrm{GHz}$ compared to the cooling transition and thus highly suppressed. In references [26, 71, 72] dark state occupation times of $< 0.7\,\mathrm{s}$ are estimated. Considering the heating rate of a single beryllium ion is given by the dip width of $\leq 0.2\,\mathrm{Hz}$ for the traps used in this thesis, the dark state occupation does not pose an issue.

2.7.3   Laser-cooling of the radial modes

In our experiment the wave vector of the laser is nearly parallel to the magnetic field lines. In practice however, the angle will always be non-zero and accompanied by a radial offset between laser and equilibrium position of the ions. In this subsection I will outline how this seemingly small imperfection can have drastic experimental consequences on the cooling of the radial modes of the beryllium ion cloud.

Considering the absorption and subsequent spontaneous re-emission of a photon, let $\vec{k}$ be the wave vector of the incoming laser beam photon and $\vec{k}_{\mathrm{sp}}$ the wave vector of the spontaneously emitted photon. This process induces a change of the ion velocity by $\Delta\vec{v} = \hbar/m(\vec{k} - \vec{k}_{\mathrm{sp}})$. Accounting only for the radial modes, for brevity $\Delta\vec{v}$ will be abbreviated as $\Delta\vec{v} \equiv (\Delta\dot{x}, \Delta\dot{y})$. Invoking equations (2.12, 2.13), the change in squared cyclotron radius can be calculated to be

$$\Delta\hat{\rho}_+^2 = \hat{\rho}_+'^2 - \hat{\rho}_+^2 \tag{2.76}$$

$$= \frac{\Delta\dot{x}^2 + \Delta\dot{y}^2}{(\omega_+ - \omega_-)^2} + \frac{2}{\omega_+ - \omega_-}\left[\Delta\dot{x}\left(\frac{\dot{x}}{\omega_+ - \omega_-} + \underbrace{y - \frac{y}{\omega_+ - \omega_-}\omega_+}_{\approx 0}\right) + \right.$$

$$\left. \Delta\dot{y}\left(\frac{\dot{y}}{\omega_+ - \omega_-} \underbrace{- x + \frac{x}{\omega_+ - \omega_-}\omega_+}_{\approx 0}\right)\right],$$

where $\hat{\rho}_+^2 := \hat{\rho}_+^2(\dot{x}, \dot{y})$ and $\hat{\rho}_+'^2 := \hat{\rho}_+^2(\dot{x} + \Delta\dot{x}, \dot{y} + \Delta\dot{y})$. The first term is owed to the recoil of the spontaneously emitted photon (recoil heating). More importantly, the second term defines the necessary beam geometry for cooling. In order to reduce the cyclotron radius, i.e. $\Delta\hat{\rho}_+^2 < 0$, the product $\Delta\dot{x}\cdot\dot{x}$ and $\Delta\dot{y}\cdot\dot{y}$ must be negative. This implies that the velocity change must be antiparallel to the velocity itself, i.e. the laser and cyclotron motion must be in opposite direction. This is the same geometrical setting as for any harmonic oscillator, including the axial motion. In practice, the laser beam width is larger than the cyclotron radius of a cold particle, so that both cases of parallel and antiparallel absorption can occur. However, due to the red-detuning of the laser frequency, the antiparallel case occurs with higher probability compared to the parallel one, leading to overall cooling.
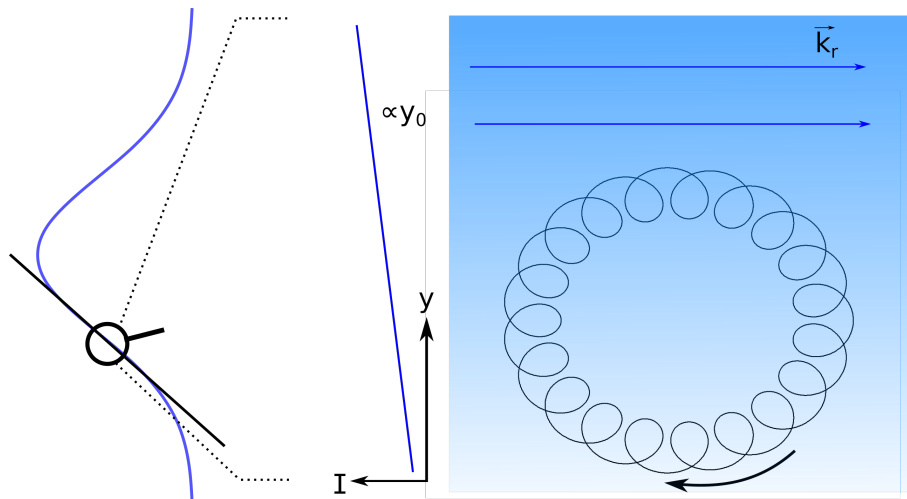
Figure 2.8: Radial laser beam configuration which allows simultaneous cooling of the magnetron and cyclotron mode. The left-hand side shows the full laser beam profile and the right-hand side a zoomed-in version. $\vec{k}_r$ is the wavevector of the laser projected on the radial plane. The laser beam width is larger than the cyclotron or magnetron amplitudes. The intensity maximum is offset relative to the ion position such that the ions are subject to an intensity gradient. The gradient can assumed to be linear on a scale of the radial amplitudes and the condition for simultaneous cooling, equation (2.78), can be derived.

Calculating the change of the magnetron radius[2] yields

$$\Delta\hat{\rho}_-^2 = \hat{\rho}_-'^2 - \hat{\rho}_-^2 \tag{2.77}$$

$$= \frac{\Delta\dot{x}^2 + \Delta\dot{y}^2}{(\omega_+ - \omega_-)^2} + \frac{2}{\omega_+ - \omega_-}\left(-\Delta\dot{x}\frac{\dot{x}}{\omega_-} - \Delta\dot{y}\frac{\dot{y}}{\omega_-}\right)$$

where in analogy $\hat{\rho}_-^2 := \hat{\rho}_-^2(\dot{x}, \dot{y})$ and $\hat{\rho}_-^{2\prime} := \hat{\rho}_-^2(\dot{x} + \Delta\dot{x}, \dot{y} + \Delta\dot{y})$. Now the situation is inverted and the products $\Delta\dot{x}\cdot\dot{x}$ and $\Delta\dot{y}\cdot\dot{y}$ have to be positive. This means that the laser propagation direction and magnetron motion must be parallel for cooling. This effect is a direct consequence of the negative magnetron energy where a removal of energy increases the radius. Again, the magnetron radius of a cold particle is smaller than the beam width.

Since the direction of rotation of the magnetron and cyclotron mode are identical, does this finding imply that simultaneous cooling of both radial modes is impossible? The answer is no [68, 73], but the ions must be illuminated in a certain configuration which will be outlined in the following. As a rule of thumb, the laser must be red-detuned in frequency and must have a certain radial offset that subjects the ions to an intensity gradient. The geometrical configuration along the y-direction is shown in figure 2.8. All arguments hold true for the x-direction or a combination of x and y as well. $\vec{k}_r$ is the radial projection of the total laser wave vector $\vec{k}_L$. In our experiment, $|\vec{k}_r|$ is small since the relative angle between $\vec{k}_L$ and the radial unity vector $\vec{e}_r$ is $\lesssim 1°$. The laser profile is assumed to be Gaussian or Lorentzian. Further, it is assumed that the cyclotron and magnetron amplitudes are small compared to the laser beam width. Then, the ions can be placed at the rising edge of the laser profile where the intensity is about half of the maximal intensity I_{max}, i.e. $I_{flank} \approx I_{max}/2$. For that position and on a scale of $|\hat{\rho}_- + \hat{\rho}_+|$, the beam profile can locally be approximated as a linear function, $I(y) = I_{flank}(1 + y/y_0)$ where y_0 defines the slope given by the beam width. In this configuration, it can be calculated [68] that the condition

---

[2]Throughout this thesis, magnetron cooling will refer to decreasing the magnetron radius, although technically energy is added.

for simultaneous cooling of the magnetron and cyclotron mode is

$$\nu_- < \underbrace{\frac{\lambda}{2\pi} \frac{\left(\frac{\Gamma}{2}\frac{1}{2\pi}\right)^2 + \delta_{\mathrm{L}}^2}{2y_0 \cdot (-\delta_{\mathrm{L}})}}_{=:\zeta} < \nu_+ \qquad (2.78)$$

where $\delta_{\mathrm{L}} < 0$ is the laser detuning.

In the following, this condition is not theoretically derived again, but its structure and individual components are discussed from an experimentalist's point of view. First of all, it is explicitly emphasized here that the required laser offset does *not* imply that the ions are exclusively illuminated by the laser if they move away from it. Instead, the purpose of the intensity gradient is that the ion scatters more photons if the magnetron velocity is parallel to the laser, i.e. ensuring magnetron cooling. However, the gradient must be small enough that this effect does not happen for the cyclotron motion, leading to the $\zeta \propto 1/y_0$ dependency.

The cyclotron cooling is provided by an effect called Doppler velocity selection [68]. Given a certain red-detuning, the scattering rate $I \propto 1/\left(2\pi\delta_{\mathrm{L}} - \vec{k}_{\mathrm{L}}\vec{v}\right)^2$ strongly depends on the relative angle of $\vec{k}_{\mathrm{L}}\vec{v}$. This implies that, even when the magnetron motion moves the ion away from the laser, within one cyclotron period the scattering rate is higher if the cyclotron velocity is antiparallel to the laser, thus leading to cooling of the cyclotron motion. As mentioned already, this holds true only if the intensity gradient over one cyclotron amplitude is sufficiently low. Furthermore, it requires a suitable red-detuning, giving rise to the $\zeta \propto (\approx \delta_{\mathrm{L}})$ dependency. In addition, this argument requires $\omega_- < \omega_+$, leading to the $\nu_- < \zeta < \nu_+$ hierarchy, which is anyhow the stability criterion of a Penning trap.

Note that although figure 2.8 suggests $\hat{\rho}_+ < \hat{\rho}_-$, these arguments hold true also for $\hat{\rho}_- < \hat{\rho}_+$. In section 7 detailed calculations for our specific experiment and some corresponding experimental demonstrations will be presented. In summary, although severely complicated by the negative-energy magnetron motion, laser-cooling of all three motional modes in a Penning trap is possible under certain conditions.

3 | Experimental apparatus and associated techniques

In this chapter the experimental setup will be introduced. After giving the reader an overview of the full apparatus, I will describe individual parts in more detail.

3.1 General setup

The first version of the experimental apparatus has been constructed in the course of ref. [54]. While conceptually unchanged, the most recent version features many additional modifications that enable laser-cooling of beryllium ions [26, 48, 74]. A rendered image of the apparatus is shown in figure 3.1. The superconducting magnet has a horizontal warm bore of 88 mm diameter. The traps are placed in the centre of the magnet bore where the magnetic field homogeneity is best. The trap chamber and the electronic section, consisting of the superconducting resonators and cryogenic amplifiers, are cooled to 4.2 K by means of a LHe bath cryostat. The connection between experiment and croystat is achieved via copper rods and flexible braids. The 4 K section is wrapped in multiple layers of superinsulating and reflective foil and is suspended by Kevlar strings within the 77 K shield, which consists of a rigid hollow-core aluminum cylinder.

Below the cryostat a 6-way DN200CF vacuum chamber cross is installed. In combination with the magnet bore, it encloses the cryogenic connection between the liquid helium bath and experiment. It thus constitutes the isolation vacuum stage at a pressure of below 1×10^{-6} mbar. Additionally, the 6-way cross serves as a mount for the electrical feedthroughs of the DC- and RF-lines of the experiment. The cryostat and vacuum chamber cross rest on a frame whose angles and offsets can be adjusted in all three dimensions with screws. This allows to position and orient the trap stack precisely within the magnet. For example, a measurement of the reduction in axial frequency due to the relative tilt between magnetic and electric field can be found in ref. [54]. Furthermore, the alignment frame rests on rails (not shown in figure 3.1) with which the trap chamber can be easily pushed in and out of the magnet during the (dis-)assembly of the experiment.

3.2 Traps

The trap stack consists of six independent Penning traps which all serve different purposes. In the following, I will briefly describe the properties of each trap individually. A photograph of the trap stack mounted on the cryomechanical support and the corresponding schematic is shown in figure 3.2. A larger version of the schematic with explicit electrode naming can be found in the appendix, figure 10.1. An overview of the properties of all traps including their resonators is given in the appendix in table 1. In general, all trap electrodes are biased with UM 1-14 power supplies from Stahl Electronics [75]. These voltage sources can be switched between a transport mode that allows continuous ramping of the output voltages or a high-precision mode with ultra-stable channels. If the traps are operated in high-precision mode, the endcap electrodes are hardwired to ground by relays.

Precision trap – PT

The precision trap (PT) is designed to measure the motional frequencies of the proton with highest precision [74]. It is a comparably large trap with an inner radius of $r =$
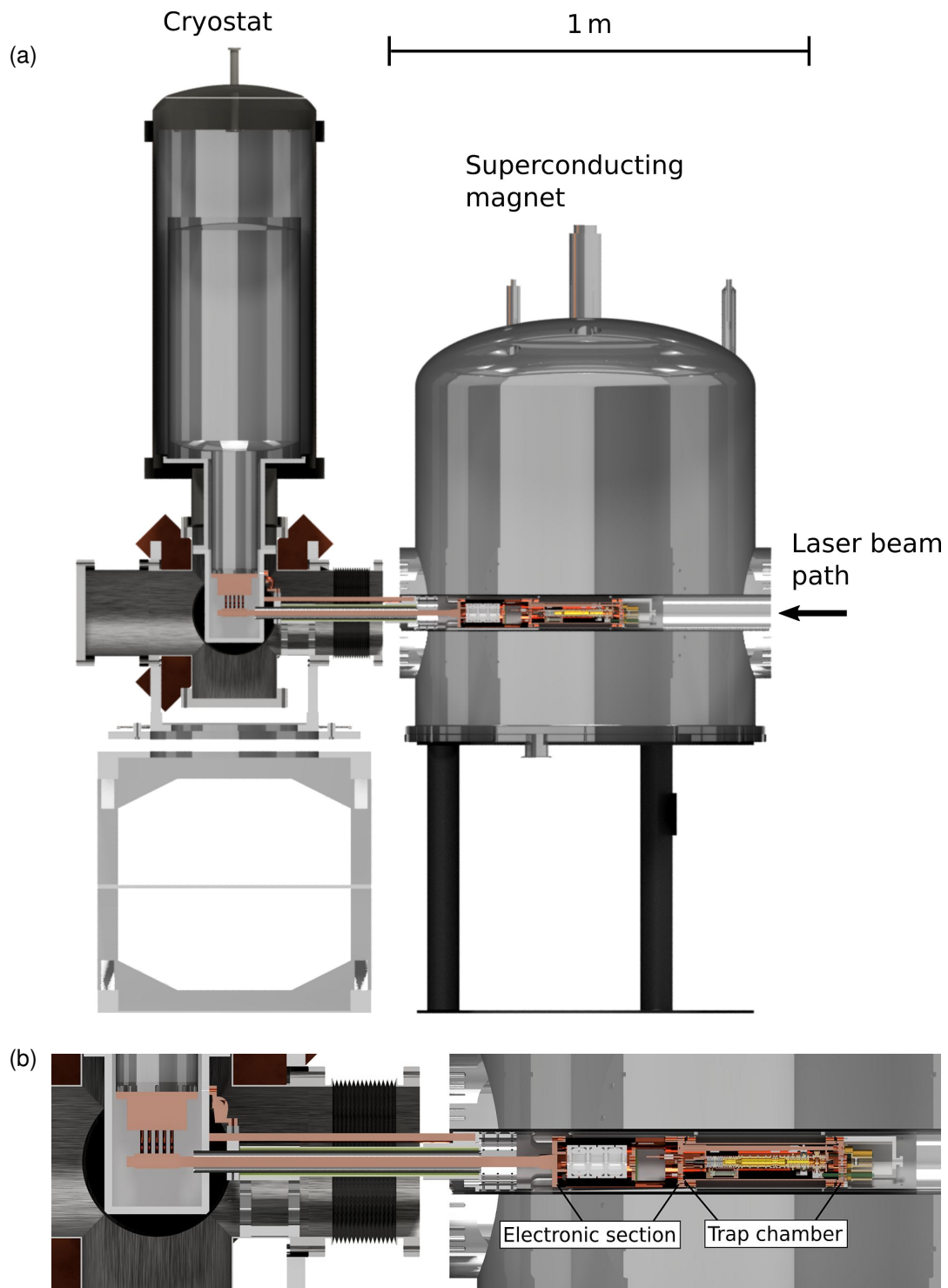
Figure 3.1: (a) Cut section view of the experimental apparatus. The trap stack with the attached cryogenic electronics is placed in the bore of the horizontal magnet and cooled to $4.2\,\mathrm{K}$ by a liquid helium bath cryostat. Not shown is the laser setup located at the right-hand side of the magnet. In (b) a zoomed-in image of the cryomechanical support structure and the $4\,\mathrm{K}$-section is shown.
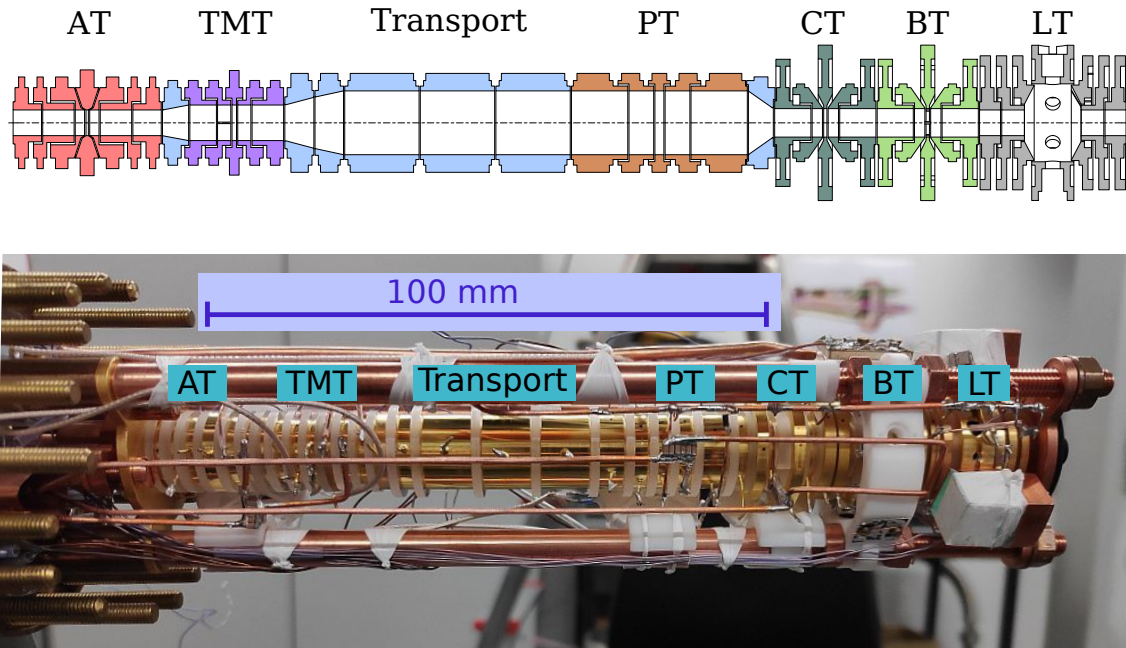
Figure 3.2: The trap stack consisting of six independent Penning traps and a transport section. The electrodes are gold-plated and separated by sapphire spacers. For details, see text.

4.5 mm. This allows an inherently small D_4 and, due to smaller relative manufacturing imperfections, a good degree of compensation and orthogonality. Furthermore, the image-charge shift [21] is reduced as well. During a g-factor measurement campaign, the spin-flips are driven in the PT. In the course of this thesis, the on-resonance cooling measurements presented in section 9 are performed with a proton in the PT.

Analysis trap – AT

The analysis trap (AT) is used to analyze the spin state of the proton. It features a magnetic bottle with $B_2 = 300\,000\,\text{T/m}^2$. It is the only trap that was, except for HV-cleaning of the proton (section 7), not employed in the course of this thesis. More information about its design and use can be found in refs. [8, 54, 61, 74, 76]. In order to preserve the homogeneous magnetic field at the position of the PT, a transport section separates the AT and TMT from the PT by about 60 mm.

Loading trap – LT

The loading trap (LT) is the most recent addition to the trap stack. A detailed description can be found in ref. [48]. The ring electrode of the LT hosts the proton target and beryllium target.

A dedicated loading trap is needed due to the observation that the laser ablation process produces many hot charge carriers of which only a tiny fraction is actually trapped. The majority leaves the trap by colliding with the surfaces of the electrodes. However, the collisions not necessarily neutralizes the ions, resulting in charges resting on the electrode surfaces. An additional mechanism is the adsorption of neutral particles on the electrode surfaces that change the relative permittivity. In either case, the effective potential created by the electrodes is different than the voltage applied to them ('patch potentials'), which

detrimentally alters the trapping potential. In practice, this means that the ring voltage and tuning ratio of all traps would need to be re-adjusted after every loading process. The LT prevents this by serving as a dedicated 'dirty' trap. It is designed such that no direct line of sights between the ablation targets and the next electrode of another trap (the BT endcap) exist. To achieve this, the correction electrodes have a conical shape. Although the effect of the laser-ablation induced patch potentials is significantly reduced, it is still observable, for which some reasons are discussed in section 7.

Coupling trap – CT

The coupling trap (CT) [74] is a dedicated trap for the sympathetic cooling of the proton. It is a comparably small trap with a radius of $r = 2.0\,\mathrm{mm}$ and $D_\mathrm{z} = 4.6\,\mathrm{mm}$, which enables high Rabi frequencies and therefore fast cooling. A cryogenic capacitance switch is connected to the CT and BT which allows to detune the resonator frequency by $18\,\mathrm{kHz}$ without changing the trapping potentials. More details about the switch can be found in section 3.6. Note that the CT and BT are designed for the off-resonant coupling with coherent energy exchange between proton and beryllium ions. As such, they feature two endcaps that are DC-isolated but are capacitively connected, which forms an effective common endcap electrode. The on-resonance scheme is incoherent and can also be done in the PT-LT combination. More detailed descriptions regarding the trap design can be found in [74].

Beryllium trap – BT

The beryllium trap (BT) [74] is a nearly identical copy of the CT and traps the beryllium cloud during the sympathetic cooling. The only difference is that the ring electrode is splitted, which allows to detect fluorescence light of the laser-cooled beryllium ions [48]. Furthermore, the splitting allows to apply a rotating wall potential to confine the ions radially, which was however not needed so far.

Temperature measurement trap – TMT

The temperature measurement trap (TMT) can measure the cyclotron energy of the proton with a resolution on the order of $\delta E_+ \lesssim 100\,\mathrm{mK}$. To achieve this, it relies on the same principle as the AT, namely on the axial frequency shift due to non-zero E_+ and large B_2. The ring electrode is made from a nickel alloy and more detailed design considerations can be found in [48]. Although the AT could be used as a temperature measurement trap [44, 74], the resulting axial frequency distribution is large for the temperatures we currently aim at, about $5\,\mathrm{kHz}$ per Kelvin axial temperature assuming sideband coupling. As a result, any temperature measurement with the AT is very time-consuming. In contrast, the B_2-coefficient of the TMT is a factor of 10 smaller and the axial frequency shift of $500\,\mathrm{Hz}$ per Kelvin of axial temperature constitutes an excellent compromise between measurement time and resolution. If the resolution is not sufficient at some point, one can simply employ the AT as the temperature measurement trap. Virtually all temperature measurements presented in this thesis are performed with the TMT. Note that the TMT is a refurbished trap which initially had no ferromagnetic ring electrode and was used as source trap (ST).
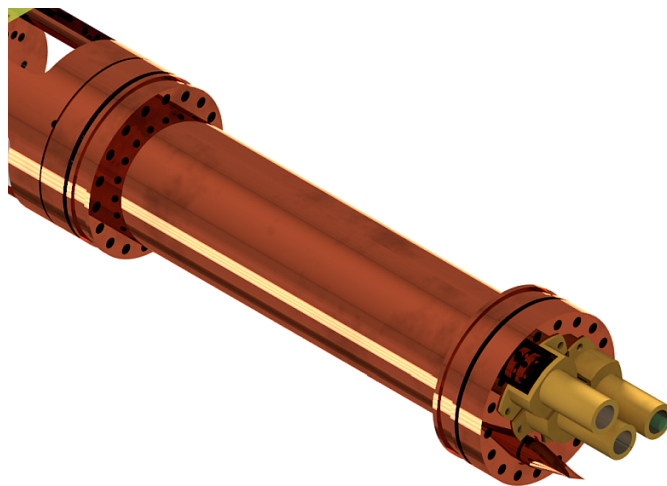
Figure 3.3: The trap chamber encloses the trap stack. The flange on the lower-right side provides laser access via three windows, two radially offset ones for the ablation laser and a central one for the cooling laser. The golden mounts are straylight shieldings with black aluminum foil inside.

Source trap – ST (discontinued)

The source trap (ST) is an older version of the TMT that featured no ferromagnetic ring electrode but is otherwise identical. It is not used for the measurements in section 7 and 9. However, the simulation framework developed in the course of this thesis was initially benchmarked with measurements performed with the ST. The name ST might be used in other references for its ferromagnetic version as well, but to avoid confusion I will refer to this trap as TMT.

3.3   4 K section

The trap stack is enclosed by a trap chamber and two flanges, shown as a rendered image in figure 3.3. Leak-tightness of the connection between chamber and flanges at cryogenic temperatures is ensured by an indium sealing. The flange towards the electronic section hosts the electrical feedthroughs. The opposite flange accommodates the three windows for the cooling and ablation laser paths. In addition, a copper tube with a diameter of about $10\,\text{mm}$ is embedded into this flange. Before cooling down the experiment, the trap chamber is pumped through this copper tube. After a pressure of better than $1 \times 10^{-7}\,\text{mbar}$ is reached in the trap chamber, the copper capillary is pinched off with a special tool. For reference, a pressure of about $1 \times 10^{-4}\,\text{mbar}$ corresponds to a 100% covering of the surfaces due to cryogenic adsorption. The pinched tube is indicated below the straylight shieldings in figure 3.3. This process hermetically seals the trap chamber and conserves the vacuum inside. After cooling down the experiment, the pressure can only rise through outgassing, which is highly suppressed at $4\,\text{K}$, or small leaks, which are negligible due to the surrounding first vacuum stage. After the full cooldown of the experiment, the remaining gas inside the trap chamber freezes out on the surfaces. The vacuum conditions can then only be gauged based on the particle lifetime. In the experimental runs of this thesis, the particle lifetimes are too long to be measured, i.e. at least months. Our sister experiment `BASE-CERN` employs the very same concept and has put a direct limit on the antiproton lifetime by simply trapping it for over one year [77], corresponding to pressures of $p \lesssim 1 \times 10^{-18}\,\text{mbar}$ in the trap chamber.
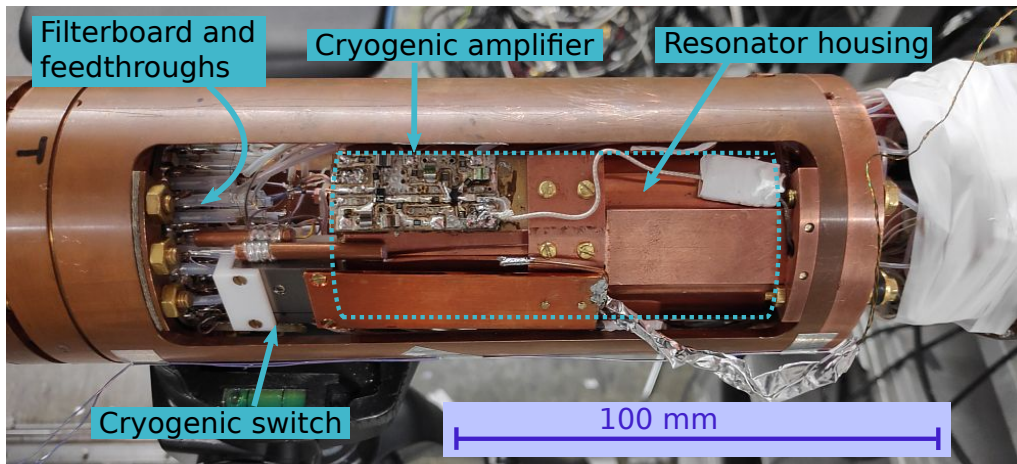
Figure 3.4: Cryogenic electronic section of the experiment. The electronic section is separated from the trap stack by a feedthrough flange. Directly above this flange a DC-filterboard is installed. One of the three cryogenic amplifier boards is mounted on one branch of the fork-like support structure. The cryogenic switch is mounted on the other branch. It is oriented inwards, since otherwise no radial space is available. The two other amplifier boards are mounted on the opposite side. The superconducting NbTi coils are located inside the resonator housing, whose outline is indicated by the dotted frame. Before cooling down the experiment, the whole section is wrapped in several layers of Teflon tape for electrical insulation.

The other part of the 4 K section accommodates the cryogenic electronics. A photograph of this section is shown in figure 3.4. Directly upstream of the feedthroughs, a 4 K-filterboard provides a final low-pass filtering of the DC bias lines. The three coils for the image-current detection are placed in a common copper housing whose outline is indicated as dotted line in figure 3.4. The fact that all three coils are placed in the same housing is necessary due to the extremely tight space constraints and the historical dimensioning of the electronic section. This design compromise has been source of considerable technical challenges when optimizing the Q-factor of the resonators, as discussed in more detail in ref. [48]. Besides, the electronic section hosts the three cryogenic amplifiers and a cryogenic switch, which are both described in the next two subsections.

3.4   Axial detection systems

One of the key components of the experiment is the axial detection system. A schematic of one resonator and two traps is shown in figure 3.5. In total, three resonators are employed where a pair of two traps is connected to one resonator each. Note that, since the resonator mediates the image-current coupling, this setup is a requirement for the traps intended to be used for sympathetic cooling. For the other traps, it is merely a necessity due to the extremely tight space constraints of the electronic section (compare figure 3.4).

The performance of the axial detection system can be characterized by three quantities: The Q-factor of the noise resonance, the signal-to-noise ratio (SNR), and the effective temperature of the noise resonance. The Q-factor and SNR optimization of the coils has been a major effort and is described in detail in ref. [48]. The effective temperature is defined by the actual physical temperature of the material plus the temperature-equivalent input noise of the amplifier. To minimize this noise, cryogenic ultra-low noise amplifiers are employed. These amplifiers are custom-built and manufactured by ourselves with a milling machine. Printed circuit boards (PCB) based on a ceramic material (e.g. ROGERS
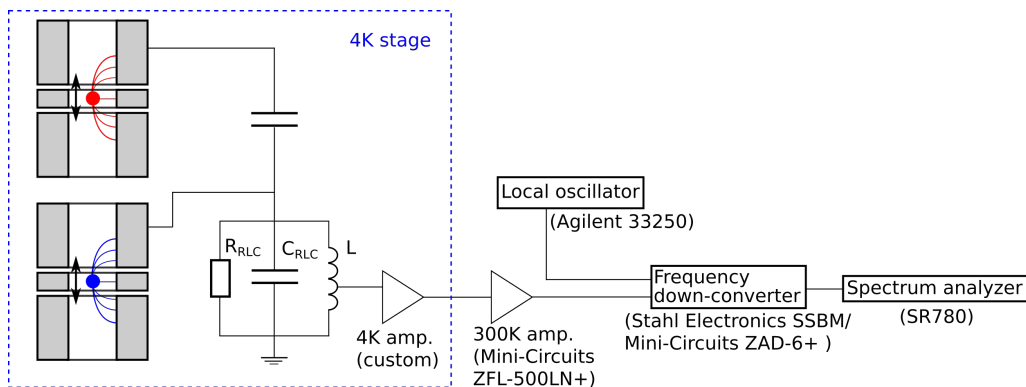
Figure 3.5: Schematic of the electronic detection system. The thermal noise resonance is amplified once at the cryogenic stage and once at room temperature. The signal is then mixed down and recorded with an FFT analyzer.

4003C) are used which offer a superior dielectric loss coefficient compared to the standard epoxy resin (FR4) material. Each amplifier board features two amplification stages with GaAs field effect transistors (FETs), in this case model 3SK164 from Sony and CF739 from Siemens. An amplification of about 12–18 dB and an input noise of $\lesssim 1\,\mathrm{nV}/\sqrt{\mathrm{Hz}}$ at 4 K is routinely achieved. Further design considerations can be found in [50, 54, 78].

After the first amplification at 4 K, the signal is further amplified at 300 K by one or two commercial Mini-Circuits ZFL-500LN+ amplifier. Then, it is mixed down by means of a single-sideband mixer (SSBM) from Stahl Electronics. Finally, the frequency spectrum is recorded with an FFT analyzer from Stanford Research Systems (SR780). Since the SSBM only has two inputs, the third resonator signal is mixed down with a Mini-Circuits ZAD-6+ balanced double-sideband mixer.

3.5   Feedback

A standard technique to manipulate the ion-resonator interaction is the application of electronic feedback [79]. Here, the resonator signal is phase-shifted and attenuated at 300 K and subsequently fed back to a signal line that is capacitively coupled to the trap electrode that is connected to the resonator, see figure 3.6. Depending on the phase shift $\Delta\varphi$ and the attenuation, the feedback gain G_{FB} can be adjusted to a positive or negative value. With feedback applied, the effective parallel resistance and temperature of the resonator scale according to

$$R_{\mathrm{RLC,FB}} = R_{\mathrm{RLC}}(1 + G_{\mathrm{FB}}) \tag{3.1}$$

$$T_{\mathrm{z,FB}} = T_{\mathrm{z}}(1 + G_{\mathrm{FB}}). \tag{3.2}$$

Since the dip width is proportional to the effective parallel resistance, the ion temperature can be manipulated based on G_{FB} and monitored via the dip width. In practice, G_{FB} is adjusted by changing the total attenuation either manually by adding or removing fixed attenuators (e.g. MiniCircuits HAT-10+) or with a voltage-controlled attenuator, albeit the latter can be a source of additional noise. In addition, the coupling capacitance is not a dedicated component but rather the stray capacitance between the detector line and the open end of the wire of the feedback line, which are tied together and separated only by the Teflon insulation. Furthermore, a certain noise floor introduced by feeding back broadband and incoherent noise prevents reaching arbitrary low temperatures, typically about $T_{\mathrm{z,FB}} = 1 - 2\,\mathrm{K}$. Note that although this description assumed an axial resonator, feedback can be applied in the very same manner to cyclotron resonators as well [78].
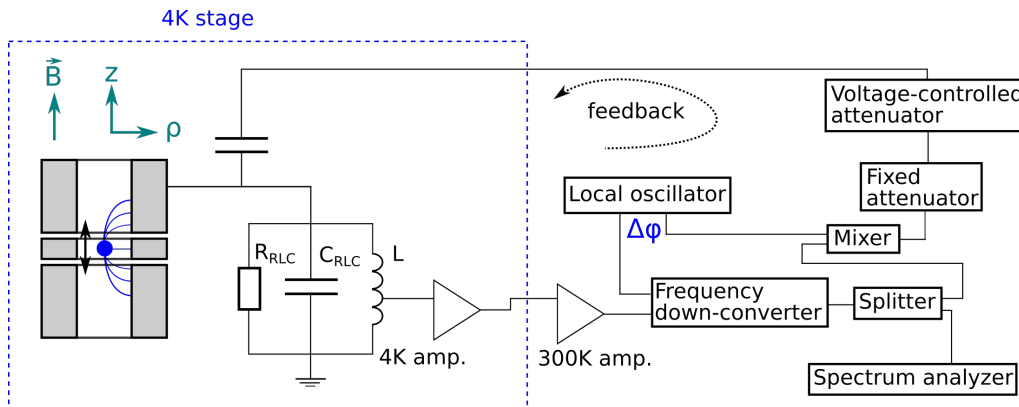
Figure 3.6: Schematic of the feedback setup. The signal after the frequency down-converter is mixed up again with the second, phase-locked output of the local oscillator. This signal is then attenuated and capacitively coupled to the end of the RLC circuit that is connected to the trap electrode. The relative phase of the two outputs of the local oscillator and the attenuation define the magnitude and sign of the feedback gain G_{FB}.

3.6 Cryogenic switch

In order to coherently exchange energy between the proton and beryllium cloud, the resonator as a heat source must be detuned sufficiently far in frequency. While it might be tempting to simply change the trapping potentials of both ions, the axial frequencies must be matched to better than a few hundred mHz, as will be demonstrated in section 6. This level of frequency matching can only be achieved with precise frequency measurements for which the resonator is needed. Consequently, the resonator frequency instead of the ion's frequency must be detuned while conserving the trapping potentials.

A component that is commonly used to vary the eigenfrequency of resonators is a varactor diode [78, 80]. Here, the p-n junction of a diode is reversely biased, resulting in a voltage-dependent capacitance, which thus constitutes a voltage-controlled capacitor. However, such a varactor is usually detrimental to the Q-factor of the resonator, which is one of the most important quantities for efficient sympathetic cooling. On the other hand, the sympathetic cooling procedure does not necessarily require continuous variation of the resonator frequency. We therefore employ a cryogenic piezo-motor (SmarAct SLC-1720, UHV, cryogenic and non-magnetic version) [25, 48] whose movement opens or closes an electrical connection. A photograph of the cryogenic switch is shown in figure 3.7(a). The movable pin is connected in parallel to the wire that connects the trap electrode with the superconducting coil. If the pin connection is closed, the total parallel capacitance of the RLC circuit becomes $C_{\mathrm{RLC}} \to C_{\mathrm{RLC}} + C_{\mathrm{switch}}$, where C_{switch} is the capacitance added by the switch (figure 3.7(b)). The change in resonator frequency is

$$\delta\nu_{\mathrm{RLC}} = \frac{1}{2\pi} \left(\sqrt{\frac{1}{LC_{\mathrm{RLC}}}} - \sqrt{\frac{1}{L(C_{\mathrm{RLC}} + C_{\mathrm{switch}})}} \right) \tag{3.3}$$

accordingly. C_{switch} can be fine-tuned offline with semi-rigid coaxial cable, which has a convenient capacitance of about $1\,\mathrm{pF/cm}$ without any detrimental effects on the Q-factor. The piezo-motor as mounted in the experiment is shown in figure 3.4. Due to the very limited space in the electronic section it must be placed between the $4\,\mathrm{K}$ filter board and the resonator housing, since elsewhere the required radial space is not available.

As final practical note, other experiments that employ a similar concept have observed ion loss when moving the piezo-motor. This was not the case for our setup, but it is certainly a
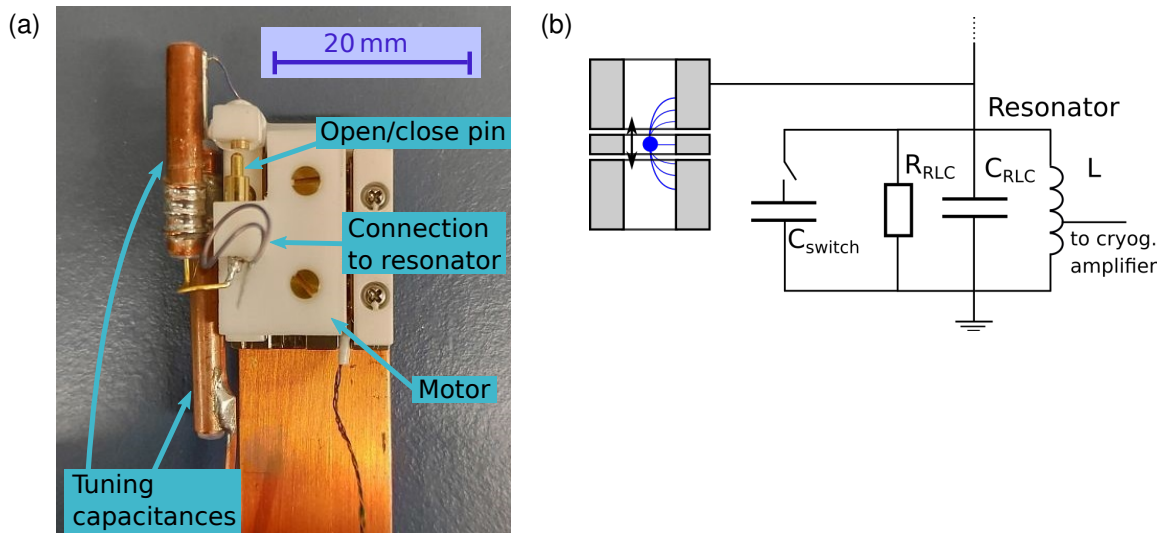
Figure 3.7: Photograph and schematic of the cryogenic capacitance switch. A piezo motor closes or opens the electrical connection to an additional capacitance. The value of the additional capacitance can be fine-tuned without Q-factor loss by using the stray capacitance of semi-rigid coaxial cable.

possibility since also we observe strong noise when moving the motor. The noise most likely stems from the AC drive voltage of the motor. Since the supply cables have a rather bulky connector, wrapping the supply cables in grounded aluminum foil was the only possibility for shielding without cutting the cables (compare figure 3.4). However, this might have been the decisive difference why we did not observe any ion loss.

3.7 Ablation laser and targets

The ablation laser is a commercial Nd:YAG solid-state laser (Continuum Minilite). We use a version with one frequency-doubling stage to generate green light at 532 nm. The laser beam is pulsed with a repetition rate of 1-15 Hz and the individual pulses have a temporal width of 5-7 ns. These laser pulses are directed via mirrors, a viewport on the magnet flange, and through one of the two window flanges of the trap chamber into the LT, see figure 3.8. Deflection and focusing onto the beryllium or proton target is provided by a right-angle prism and a lense. The prisms and lenses are mounted in the box-shaped radial extensions of the LT, visible in figure 3.2.

Once the focused ablation laser pulse impinges on the target, it heats the target locally and a cocktail of atoms and ions is released. The exact process is complex and a field of active research in the plasma physics community. However, we follow a result-oriented approach and simply increase the laser pulse energy until we can detect trapped ions of the species of interest.

The beryllium target consists of a beryllium foil. Laser pulse energies between 200–250 µJ have been used to produce clouds of up to several thousands of ions. This beryllium target has been in use for several years now and has proven to be very reliable. In contrast, the proton target required active debugging. In a first experimental run, a conductive plastic foil (Polyethylen, PE) was installed. Due to the higher ionization potential of hydrogen, larger laser pulse energies of 300–320 µJ are needed. On the other hand, the number of produced ions is a much stronger than linear function of the laser energy. These facts combined gave rise to the challenging situation that although protons were produced and observed, they were contaminated by large amounts of e.g. C^+, C^{2+}, C^{3+}, H_3^+, and
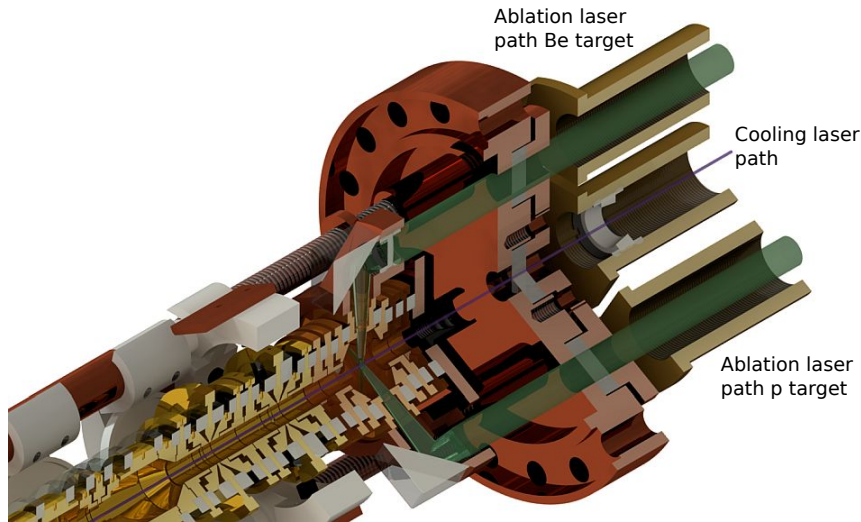
Figure 3.8: The two possible beam paths for the ablation laser including deflection and focusing at the LT are shown in green. One beam path ends on a tantalum disc employed as proton target and the other path ends on a beryllium foil to produce beryllium ions.

H_2^+. This is to some degree expected and established cleaning procedures were applied, see section 7. Yet, the ratio between contaminants and protons proved to be such unfavourable that it was not possible to remove the contaminants while retaining the proton cloud. Consequently, in a second experimental run the plastic foil was exchanged with a tantalum disc. According to ref. [81], commercial tantalum contains significant amounts of hydrogen as impurities in its crystal structure, which can be freed and ionized upon ablation. This observation was subsequently confirmed for our experiment as well and protons can now be reproducibly loaded with the new tantalum target. While the ablation process still produces immense amounts of undesired ions, the main contaminant is now tantalum with a much larger atomic mass of about 181 u. Due to the larger difference of the mass ratios, significantly less aggressive cleaning procedures can be employed. As a result, the proton loading process is now routine and a clean cloud of protons can usually be prepared in less than one hour. Exemplary mass spectra for both the old and new target are given in section 7.1.

3.8   Cooling laser setup

The UV laser is a commercial system from Toptica (TA-FHG) [82]. It is based on an external cavity diode laser at 1252 nm, whose beam is amplified by a tapered amplifier (TA) and subsequently frequency doubled in two cascaded second harmonic generation stages (SHG), see figure 3.9. The resulting 313 nm laser light is attenuated and polarization-adjusted before being fed into a UV fiber. The attenuation is achieved by means of a rotator plate and a variable neutral density filter and allows continuous adjustment of the laser power over about two orders of magnitude. The UV fiber is a single-mode photonic crystal fiber that was hydrogen-loaded in a pressure chamber and conditioned with 313 nm light to prevent transmission loss [26, 83]. The exact manufacturing process has been described step by step in [26]. The very first cooling laser setup fundamentally required the UV fiber as it went through a vacuum feedthrough and was attached directly to the trap can [26]. While this setup was abandoned for technical reasons, the UV fiber persisted for laser safety reasons, due to its mode cleaning properties, and since it allows adjusting the laser beam paths before and after the fiber independently.
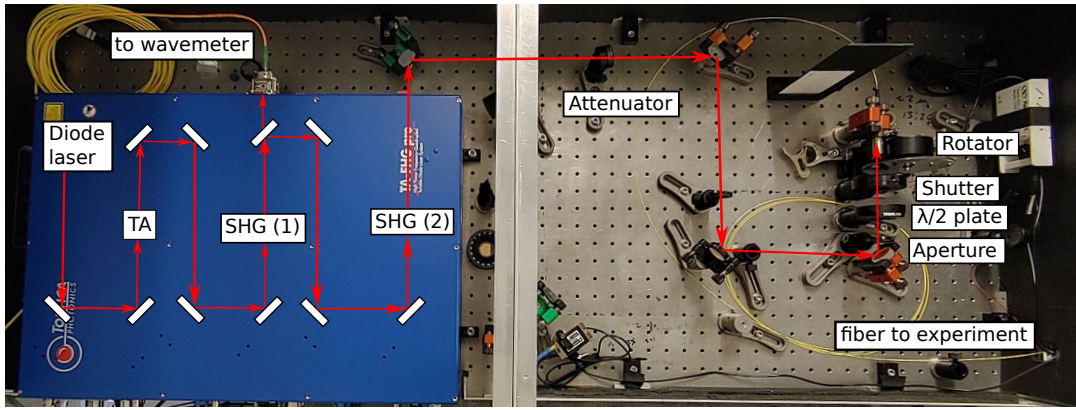
Figure 3.9: Setup of the 313 nm cooling laser. The initial laser beam is generated with a diode laser, amplified with a tapered amplifier (TA) and frequency-doubled twice by second harmonic generation stages (SHG). The 313 nm light is then attenuated, polarization-adjusted, and fed into a photonic crystal fiber.

The laser is tunable and can be PID locked to a wavemeter (HighFinesse WSU-30). To this end, the small fraction of transmitted light through a reflective mirror after the first SHG stage (626 nm light) is fed into a wavemeter via a fiber. The wavemeter cannot only lock the laser to a constant frequency, but also allows to modulate the laser frequency with e.g. a sawtooth or a rectangular function on a second-timescale. The datasheet of the laser states an instantaneous linewidth of < 0.5 MHz [82], so that in practice the laser frequency is limited by long-term drifts of the wavemeter of about 2–10 MHz for the present laboratory conditions.

The setup downstream of the UV fiber is shown in figure 3.10. The fiber collimator is installed on a piezo motor mirror mount. Subsequently, the laser light is polarization-filtered by an alpha-BBO Glan-Laser Polarizer from Thorlabs [84]. The reflected light of order 10% is diverted to a power meter to measure the beam power. The polarization state of the transmitted 90% is adjusted by means of $\lambda/2$ and $\lambda/4$ waveplates and then sent into the experiment via a mirror which is mounted on a second piezo-motor stage. These two mirror mounts, in the following referred to as M1 and M2, allow a precise adjustment of the offset and angle at which the beam is sent into the trap chamber. A photo diode mounted on top of the resonator housing facilitates finding an initial mirror setting for which the laser beam passes through the trap stack. The fine-tuning is then performed based on the fluorescence signal of the beryllium ions and is described in section 7.

3.9 Fluorescence detection

The ability to detect fluorescence light is extremely useful for the sympathetic cooling experiments presented in this thesis. However, the boundary conditions imposed by a cryogenic experiment in a strong magnetic field with very limited optical access significantly complicate the technical implementation. Our working solution is to radially split the ring electrode of the respective trap and detect the fluorescence photons with silicon photomultipliers (SiPMs), as shown for the BT in figure 3.11. A detailed description of the SiPM performance and the implementation in our experiment can be found in [48, 85]. Each SiPM (MicroFJ-30035-TSV from onsemi) is soldered on a custom PCB which hosts a two-stage low-pass filter for the biasing voltage and a $50\,\Omega$ readout resistance. The SiPM signal of an absorbed photon is an asymmetric pulse with about 2 ns width at 4 K, which allows to operate the SiPMs in single-photon mode. The number of detected photons is
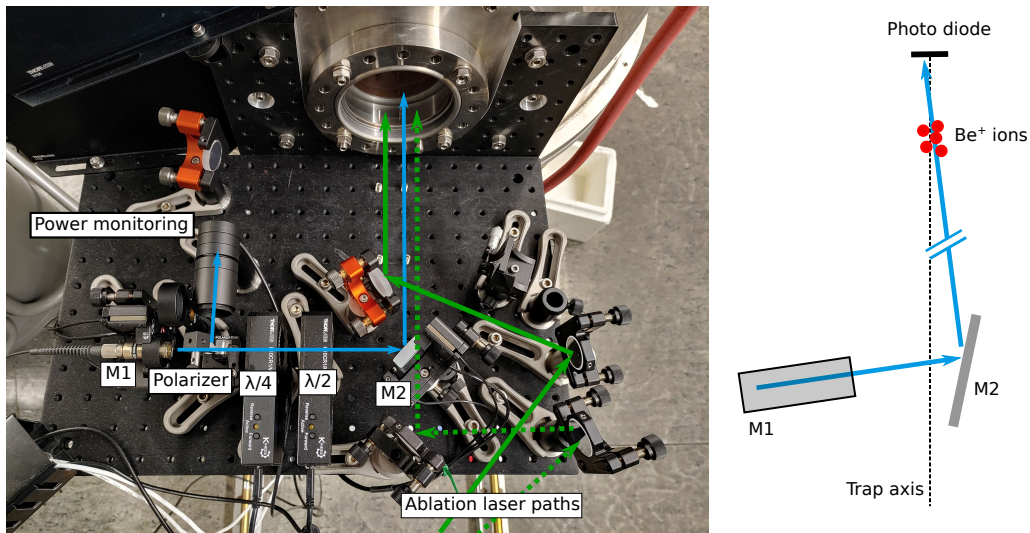
Figure 3.10: Optical breadboard mounted on the magnet flange. The laser beam is polarization-filtered and -adjusted and its path is determined by two motorized mirror mounts (M1 and M2). The schematic on the right depicts in an exaggerated way how the offset and angle of the laser beam relative to the trap axis can be adjusted with M1 and M2.

counted with a photon counter (Stanford Research Systems SR400).

Besides the BT, SiPMs can be installed in the LT as well. In the experimental setup used for this thesis, two SiPMs were installed for the BT and one SiPM for the LT.
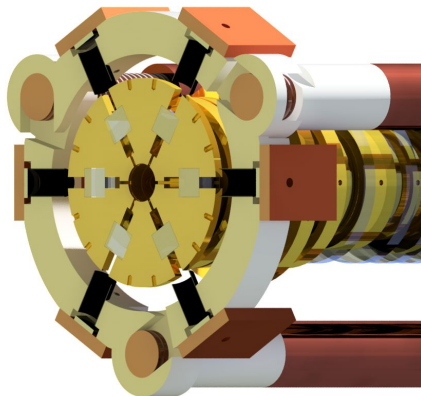
Figure 3.11: Rendered section view of the beryllium trap (BT). The six-fold radial splitting allows the detection of fluorescence light through the slits with silicon photomultipliers (SiPMs). The SiPMs are mounted on small electronic boards. In the real setup only two SiPMs are installed.

3.10   Overview of image-current based sympathetic cooling methods

I explicitly highlight that this section as well as section 6.4, 6.5 and parts of section 6.1 have been published in the open-access reference [28] with me as the first and leading author already. Although the coauthors have contributed significantly in the form of discussions and comments, the manuscript was written exclusively by me. Since there is no value in re-writing, most of the text passages and figures have been copied verbatim. Partially, content has been added which will be indicated at the beginning of the respective sections. In all aforementioned sections small modifications to the text and figures have been made to ensure consistency.

One technique which satisfies the challenging requirements on the cooling techniques described in section 2.5.3 and section 2.6 is image-current coupling, where the proton is sympathetically cooled by a cloud of laser-cooled $^9\mathrm{Be}^+$stored in a separate trap and the two species are coupled through image currents. Our experimental apparatus allows for two versions of image-current coupling, depicted in figure 3.12.
One version features a common endcap electrode with which the coupling scheme first described in refs. [24, 25] can be realized. Here, the proton and beryllium ions are stored in the CT and BT, respectively. These traps share an effective common endcap electrode, as described in section 3.2. The image current induced by the particles charges up the capacitance of the common-endcap electrode. The resulting voltage generates a force on the particles, so that a system of two coupled oscillators is created. By laser cooling the beryllium ions, they act as a heat sink and the proton will be cooled sympathetically as well. The resonator, which is still required for detecting the particles and matching their axial frequency, can be decoupled by adding or subtracting an additional parallel capacitance using the cryogenic switch [48] as described in section 3.6. This switch changes the resonator's eigenfrequency by a preset amount that can be adjusted to $> 100\,\mathrm{kHz}$. Using such a switch has the advantage that the particle frequencies can be matched on resonance and no adjustment of the trapping potentials is necessary when starting the coupling procedure. Furthermore, at $> 100\,\mathrm{kHz}$ resonator detuning no significant source of heating is present, which is the advantage of this specific approach.

Alternatively, the particle can be trapped in the PT-ST combination with the old experimental setup for with which the simulations were performed, or the PT-LT combination as the setup that was used for the experimental campaigns of this thesis. Since the resonator is an oscillator itself, this configuration represents a system of three coupled oscillators. The advantage of the RLC resonator is that it amplifies the image-current coupling strength by the Q-factor of the resonator, resulting in a fast energy exchange between the particles. In turn, however, the cooling effect competes with the stochastic heating by the noise, ultimately limiting the minimal proton temperature. This resonator-coupling scheme was employed in the first demonstration of sympathetic cooling through image currents recently conducted by our group [27] and was used for the improved sympathetic cooling measurements in section 9 as well. The particle-to-detector coupling rate, which governs both the heating and cooling rate, can be reduced by detuning the particles from the resonator eigenfrequency. The reduction in heating rate allows for colder particle temperatures and this specific scheme will be investigated in section 6.5.3 with simulations.
It should be mentioned that the ST has been modified to the temperature measurement trap (TMT) in a new version of the experimental apparatus, but the simulations presented in the section 6 have been performed for the old setup. In general, the on-resonance coupling can be performed with any pair of traps that are connected to the same resonator. For the sympathetic cooling measurements presented in this thesis, the PT-LT combination was used.
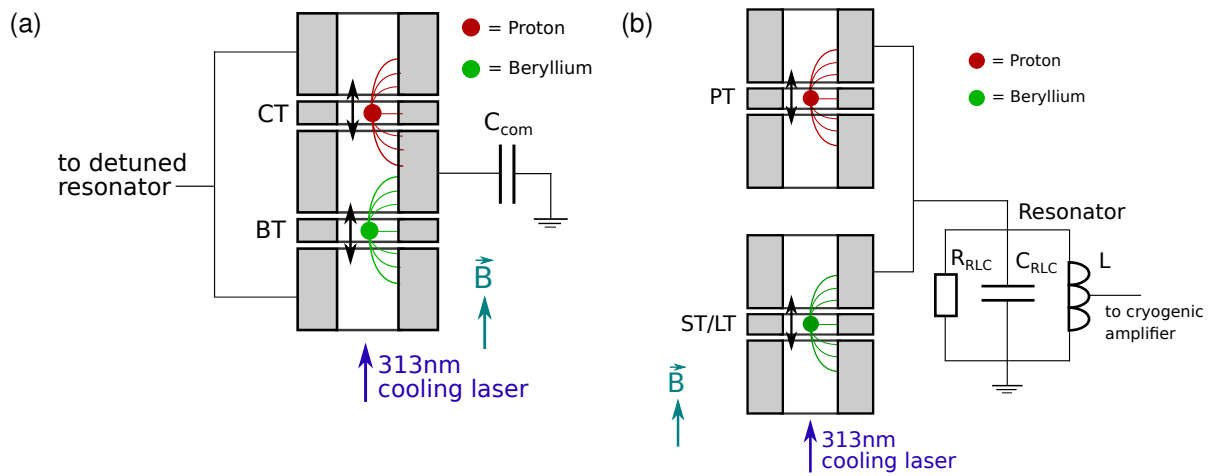
Figure 3.12: (a) Sketch of the experimental setup for the common-endcap coupling. The common endcap electrode can be modelled as a ideal capacitor. A resonator is required for particle detection, however, when performing the common-endcap coupling, it is decoupled by detuning its eigenfrequency with a cryogenic switch [48]. In this case, the common endcap electrode mediates the energy exchange between the particles. (b) Sketch of the experimental setup for the common-resonator coupling. The proton and $^9\mathrm{Be}^+$ ions are stored in two independent traps, which share a common resonator that mediates energy exchange between the particles.

4 | Design and first tests of a superconducting shim coil system

In this chapter I will present the design and first tests of a superconducting shim-coil system that is able to compensate the first- and second-order magnetic field inhomogeneities while leaving the absolute magnetic field unchanged. Following the introduction about magnetic field inhomogeneities in section 2.2.2, I will now refer to the magnetic field produced by the superconducting 1.9 T-magnet as

$$B_z^{\text{trap}}(z) = B_0^{\text{trap}} + B_1^{\text{trap}} z + B_2^{\text{trap}} z^2 + B_3^{\text{trap}} z^3 + ... \tag{4.1}$$

The additional superscript avoids confusion with the magnetic field produced by the shim coil system, which can analogously be expanded about the position of the ion ($z = 0$):

$$B_z^{\text{coil}}(z) = B_0^{\text{coil}} + B_1^{\text{coil}} z + B_2^{\text{coil}} z^2 + B_3^{\text{coil}} z^3 + ... \tag{4.2}$$

An ideal shim coil has the coefficients $B_0^{\text{coil}} = 0$, $B_1^{\text{coil}} + B_1^{\text{trap}} = 0$ and $B_2^{\text{coil}} + B_2^{\text{trap}} = 0$. To achieve this, several design challenges must be accounted for, which I will discuss in the following. Shim-coil systems have been implemented in other experiments already [86, 87], however, the boundary conditions of each experiment are too specific to formulate a general recipe.

The primary goal is to compensate B_2^{trap} since the associated frequency shifts enter as contribution to the systematic uncertainty in a g-factor measurement. Since our superconducting magnet is already shimmed to $< 1\,\text{T/m}^2$, the coil system only needs to shim the residual inhomogeneity at the position of the ion in the precision trap. This allows us to employ a persistent superconducting coil system. A non-persistent setup would, due to the finite stability of the power supply, be a major noise source in direct vicinity of our trap. Also, due to the non-zero resistance of the wire, it would significantly increase the liquid helium consumption of the experiment, which is also detrimental to the overall stability.

The basic design idea is to employ two independent cylindrical coil systems, where one compensates B_2^{trap} and the other B_1^{trap} and both individually do not change the absolute magnetic field. I will refer to them as B_1- and B_2-coil in the following and in order to avoid confusion, explicitly label the associated coil in the superscript of the respective symbol. Due to the extremely tight space constraints at the 4K-stage of the experimental setup, the coils can only be placed on the outer side of the trap can. This already fixes one free parameter, namely the radius of the coils to about 25 mm.

4.1 B_2-coil design

The B_2-coil consists of three subcoils schematically shown in figure 4.1(a), a central coil placed around the position of the ion and two coils in Helmholtz-configuration placed axially symmetric with respect to the central coil. The combined three subcoils are intended to be wound from the same wire to ensure that all subcoils are loaded with the same current and to reduce the number of required electrical feedthroughs. This configuration produces a quadratic magnetic field gradient $B_2^{\text{B2-coil}}$ that can be controlled with the loading current such that $B_2^{\text{B2-coil}} + B_2^{\text{trap}} = 0$. If the central coil is wound in opposite direction to the Helmholtz pair, the ratio between the number of windings of the central coil and Helmholtz coils can be used to ensure that the absolute magnetic fields cancel each other, i.e. $B_0^{\text{B2-coil}} = 0$. To quantify these considerations, consider the magnetic field
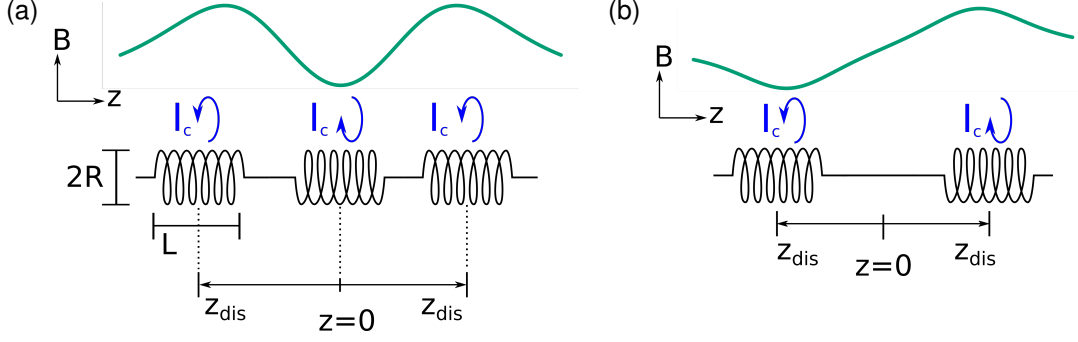
Figure 4.1: Schematic of a coil system that is able to compensate the quadratic coefficient B_2^{trap} (a) and the linear coefficient B_1^{trap} (b) at the position of the ion $z = 0$. The B_2-coil is made of three subcoils, where the winding direction of the inner coil is swapped. The B_1-coil is made of one coil pair in Anti-Helmholtz design. The magnetic field is shown schematically in green. Both coil system can be designed to not alter B_0.

of a cylindrical coil in axial direction,

$$B_z(z, L, N) = \mu_0 \frac{N I_{\text{c}}}{2L} \left(\frac{z + L/2}{\sqrt{R^2 + (z + L/2)^2}} - \frac{z - L/2}{\sqrt{R^2 + (z - L/2)^2}} \right). \qquad (4.3)$$

Here N is the number of windings, L the axial length of the coil, R the radius, I_{c} the current and μ_0 the vacuum permeability. Note that this formula does not require the often-cited condition of $L \gg R$ for cylindrical coils. The radius is fixed at $R = 25.5\,\text{mm}$, where $25\,\text{mm}$ is the outer radius of the trap can and the remaining $0.5\,\text{mm}$ is the thickness of the coil support structure. In order to conserve the axial symmetry, both outer coils are identical. As a result, B_1^{coil} and B_3^{coil} automatically vanish for the ideal design without the need to tune any parameters. The total magnetic field is then given by

$$B_z^{\text{B2-coil}}(z) = B_z(z - z_{\text{dis}}, L_{\text{out}}, N_{\text{out}}, I) + B_z(z, L_{\text{in}}, N_{\text{in}}, -I) + B_z(z + z_{\text{dis}}, L_{\text{out}}, N_{\text{out}}, I) \qquad (4.4)$$

where the indices 'in' and 'out' denote the inner and outer coils, respectively. z_{dis} is the displacement of the center of the outer coils relative to the center of the inner coil.

For simplicity, I will assume $L_{\text{out}} = L_{\text{in}} = 11\,\text{mm}$ and $N_{\text{in}} = 100$ in the following, which allows winding a monolayer of superconducting wire with the common width of $100\,\mu\text{m}$ while leaving 10% tolerance for a non-ideal winding density. As a result, z_{dis} and the winding ratio $N_{\text{out}}/N_{\text{in}}$ remain as free parameters. Figure 4.2 shows $B_0^{\text{B2-coil}}$ and $B_2^{\text{B2-coil}}$ at the position of the ion ($z = 0$) as a function of these two parameters assuming a current of $I = 100\,\text{mA}$. $B_2^{\text{B2-coil}}$ is determined by calculating the second derivative of B_z^{trap}, including a factor of 2 for consistency with equation (4.2).

In general, one would like to maximize the winding ratio to achieve the highest $B_2^{\text{B2-coil}}$ for a given current. However, eventually the thermalization between different wire layers might limit the current the coils can be loaded with such that the winding ratio will be limited to ≤ 2.0 here. Furthermore, the maximum of $B_2^{\text{B2-coil}}$ does not coincide with $B_0^{\text{B2-coil}} = 0$. Although one might be tempted to neglect the requirement of $B_0^{\text{B2-coil}} = 0$, a quick estimate demonstrates its importance: Assuming a $200\,\mu\text{T}$ magnetic field change, the cyclotron frequency of the proton changes by about $\frac{200\,\mu\text{T}}{2\,\text{T}} \times 29\,\text{MHz} = 2.9\,\text{kHz}$. While the change in B_0 can be calculated and thus roughly compensated, the associated uncertainties would make optimizing $B_2^{\text{B2-coil}}$ extremely laborious as one would need to search the cyclotron frequency for each loading current again. A numerical evaluation of the condition that $B_2^{\text{B2-coil}}$ is at its local maximum while $B_0^{\text{B2-coil}} = 0$ yields the parameters $z_{\text{dis}} = 23.26\,\text{mm}$ and $N_{\text{out}}/N_{\text{in}} = 1.19$.
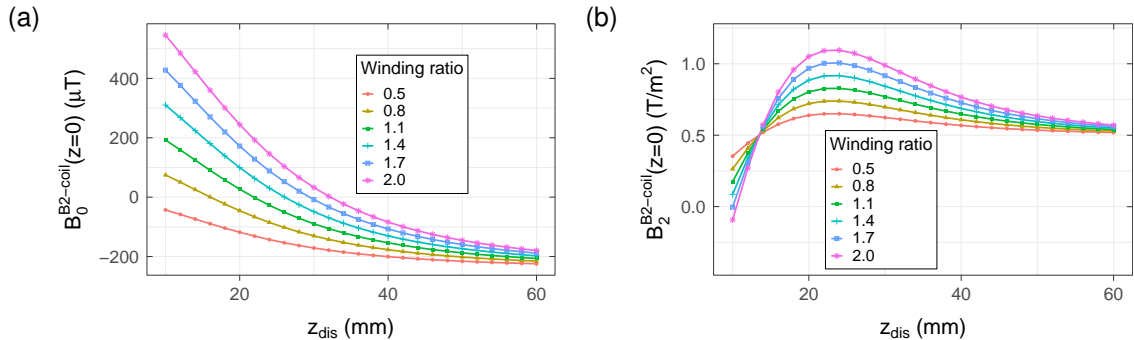
Figure 4.2:   Absolute magnetic field (a) and quadratic field coefficient (b) of the B_2-coil at $z = 0$ as a function of the distance z_{dis} between the position of the ion ($z = 0$) and the center of the outer two subcoils. By choosing the proper ratio between the number of windings of the outer and inner coils, the absolute magnetic field change can be nulled. The coil current is assumed to be $100\,mA$ and the number of windings $N_{in} = 100$. The achievable B_2^{coil} of $0.5 - 1.0\,T/m^2$ should be sufficient to compensate the residual magnetic field inhomogeneity of the precision trap.

The trap inhomogeneity B_2^{trap} has been measured in the course of the last g-factor measurement campaign to be $B_2^{trap} = 0.1(1)\,T/m^2$ [6, 74]. More recently, with the experiment modified for laser-cooling of beryllium ions, the value changed to $B_2^{trap} = -0.39(11)\,T/m^2$ [26]. Since then, additional significant changes to the trap stack have been made that will have very likely altered B_2^{trap}. Nevertheless, the B_2-coil design described in this section is able to produce $B_2^{B2\text{-}coil} \approx \pm 0.8\,T/m^2$ per $\pm 100\,mA$ of loading current. Although the value of B_2^{trap} that can be ultimately compensated depends on the maximal current the coil can be loaded with, a realistic loading current of $100\,mA$ still leaves a factor of 2 as buffer.

4.2 B_1-coil design

The B_1-coil is designed to be an anti-Helmholtz coil (also called Maxwell coil), i.e. two coils placed symmetrically along the z-axis around the position of the ion and wound from the same wire in opposite direction as shown in figure 4.1(b). The symmetry causes the magnetic field in the center to vanish exactly and a linear magnetic field gradient $B_1^{B1\text{-}coil}$ remains. The magnetic field is calculated by

$$B_z^{B1\text{-}coil}(z) = B_z(z - z_{dis}, L, N, I) + B_z(z + z_{dis}, L, N, -I). \tag{4.5}$$

$B_1^{B1\text{-}coil}$ can then be controlled with the loading current and will be tuned such that $B_1^{coil} + B_1^{trap} = 0$. The magnetic field as a function of distance from the center is shown in figure 4.3(a) assuming $I = 100\,mA$, $N = 100$, $L = 11\,mm$ and $z_{dis} = 30\,mm$. The linearity of the gradient is not ideal, but the displacement z_{dis} can be chosen such that the $B_1^{B1\text{-}coil}$-scaling with z is very weak, as demonstrated in figure 4.3(b). The individual curves are offset by the annotated amount for better visibility. Note that the axial extent of the B_2-coil as designed in the previous subsection only allows $z_{dis} > 27.7\,mm$ for the B_1-coil, assuming there is no radial offset between both. Nevertheless, even for $z_{dis} = 30\,mm$ the $B_1^{B1\text{-}coil}$-scaling with z is still sufficiently weak that the resulting $B_2^{B1\text{-}coil}$ is negligible.

4.3   Effect of imperfections

The previous considerations have assumed an ideal system, however, in reality several imperfections can occur. The dominant imperfection will most likely be a small axial
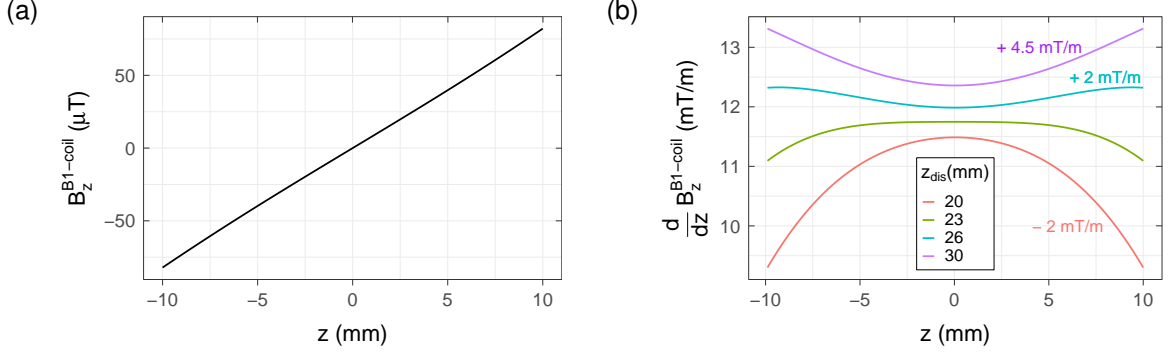
Figure 4.3: Magnetic field of the B_1-coil in Anti-Helmholtz design for a current of $I = 100\,\text{mA}$, $N = 100$ windings and an axial coil length of $L = 11\,\text{mm}$. (a) $B_z^{\text{B1-coil}}$ as a function of axial distance. The subcoils are distanced by $2z_{\text{dis}} = 2 \cdot 30\,\text{mm}$ apart. The magnetic field at the position of the ion ($z = 0$) vanishes and to first order the desired linear gradient remains. (b) The linearity of the gradient can be tuned by choosing the proper distance z_{dis} between the center of the two subcoils and $z = 0$. However, even for non-ideal z_{dis} the scaling of B_1 as a function of z is weak and should not pose an issue. Note that the individual curves are shifted by the annotated absolute amount for better visiblity.
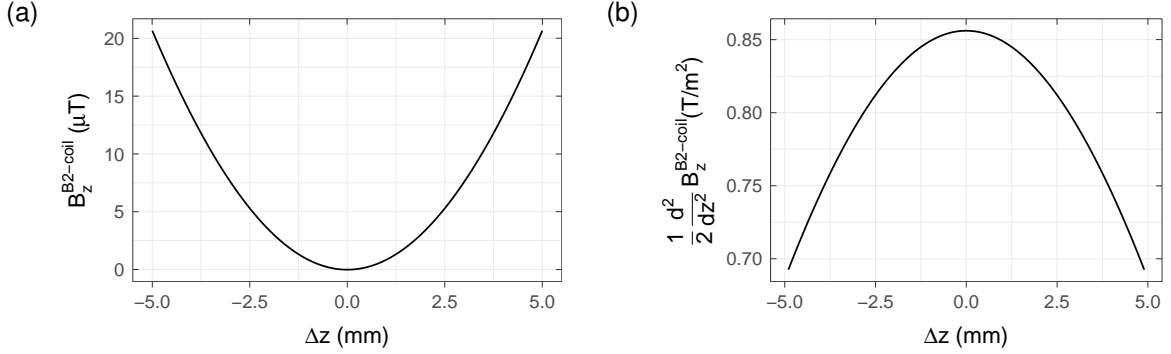
Figure 4.4: Effect of an axial offset Δz between ion position and center of the coil system for the B_2-coil. Subfigure (a) shows the absolute magnetic field change $B_z^{\text{B2-coil}}$ and subfigure (b) the change in $B_2^{\text{B2-coil}}$.

offset Δz between the center of the coil system z_{CC} and the position of the ion z_{ion}, i.e. $\Delta z = z_{\text{ion}} - z_{\text{CC}}$. In the following, a maximal deviation of a few mm is assumed. Figure 4.4 shows $B_z^{\text{B2-coil}}$ and $\frac{1}{2}\frac{d^2}{dz^2}B_z^{\text{B2-coil}}$ as a function of axial offset, assuming the ideal parameters described in section 4.1 of $L = 11\,\text{mm}$, $z_{\text{dis}} = 23.26\,\text{mm}$, $N_{\text{out}}/N_{\text{in}} = 1.19$, $R = 25.5\,\text{mm}$ and $I = 100\,\text{mA}$. Note the factor of $1/2$ for the second derivative is needed for consistency with equation (4.2). The absolute magnetic field change of order $10\,\mu\text{T}$ translates into a proton cyclotron frequency change of order $150\,\text{Hz}$. In practice, one will successively increase the loading current, so that the cyclotron frequency change should be easily trackable and not pose an issue. In fact, cyclotron frequency changes on this scale might actually be convenient as they give direct feedback within one minute whether the loading process has succeeded. The scaling of $B_2^{\text{B2-coil}}$ as a function of z is intrinsically defined by the $B_2^{\text{B2-coil}}$-coefficient of about $0.8\,\text{T/m}^2$. Analogously, the scaling of $B_2^{\text{B2-coil}}$ as a function of z, plotted in figure 4.4(b), can be examined. A few mm displacement induce a reduction in $B_2^{\text{B2-coil}}$ on the order of $10\text{--}20\%$, which is comparable to the uncertainty B_2^{trap} can be measured with. More precisely, the scaling of $B_2^{\text{B2-coil}}(z)$ is defined by $B_4^{\text{B2-coil}} = 1.1\,\text{kT/m}^4$. In essence, it is important to emphasize that B_2^{trap} can still be compensated even in the presence of rather large axial displacements by simply loading the coil with more current.
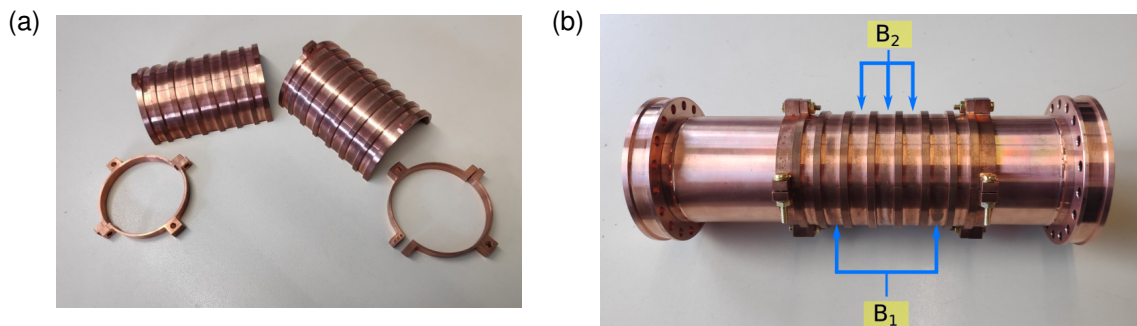
Figure 4.5:   Support structure for the shim coil. In subfigure (a) the individual parts are shown and in subfigure (b) the assembled parts mounted on the trap can. The inner three groves will be used to compensate B_2^{trap} and the next outer pair to compensate B_1^{trap}. The two outermost grooves only provide space for the nut.

In case of the B_1-coil the effect of imperfections is already indirectly shown in figure 4.3. Assuming $z_{\text{dis}} = 30\,\text{mm}$, the parameter that defines $B_2^{\text{B1-coil}}$ for a certain axial offset is $B_3^{\text{B1-coil}} \approx 4\,\text{T/m}^3$. This implies that $B_2^{\text{B1-coil}} < 0.05\,\text{T/m}^2$ for a few mm of axial offset, which is currently negligible. Even if it becomes relevant in the future, it can of course be compensated by the B_2-coil.

In summary, although only axial displacements were looked into here, the general behavior is the same for other uncertainties as well: The B_2-coil introduces an undesired B_1 and vice versa, however, they are small and can easily be corrected with the respective other coil. Consequently, the final optimization will be an iterative process that should converge quickly.

4.4   Implementation in the existing experiment

The idea to mount the coil system on the trap can is by means of two copper half-shells that have radial grooves in which the NbTi wire is wound, see figure 4.5. Compared to winding the coils directly on the trap can this has the advantage that the axial lengths of the grooves, which mainly define the properties of the B_2- and B_1-coil, can be manufactured precisely 'offline' and no simultaneous measuring of the lengths of the axial coil segments while winding the coil is necessary. Furthermore, the inner diameter of the half-shells is chosen to be identical to the outer diameter of the trap can. This ensures good surface contact with the trap can. The material removed from the process of cutting the shells in half is sufficient that they are still axially movable on the trap can even after winding the coils. Not only allows this a precise alignment between precision trap and coil center, it also allows to change the position of the coils in case the position of the precision trap changes in the future. Once aligned, the half-shells can be screwed to two clamps, which have a slightly smaller inner diameter than the trap can. Screwing the clamps together then tightly presses them on the trap can and fixes the whole support structure in place. Moreover, this design also allows to add a self-shielding coil system such as in ref. [88] as an additional outer layer.

4.5   Loading procedure and joint manufacturing

Besides the coil parameters, the concept and procedure to load a current into the coil system is equally important. A schematic of the concept is shown in figure 4.6(a). To

load a current into the superconducting coil, at first a quench heater is turned on, which is located in the short wire branch that does not contain the coil. The quench heater is a standard thick-film resistor of a few kΩ around which a few windings of the superconducting wire are wound. If a current is sent through this resistor, the dissipated heat quenches this superconductor branch locally and any loading current will only flow through the superconducting coil. Once the quench heater is turned off, the short branch becomes superconducting again and the loading current flowing through the coil now has a fully superconducting path along which it will be stored, i.e. the coil is put in persistent mode.

One of the major technological challenge is the manufacturing of the joint which provides a superconducting connection between the two coil wire endings. Several approaches are conceivable [89], for example the `BASE-CERN` group has successfully spot-welded the two wires on several points together [90]. However, in this thesis work an approach is pursued that has been done successfully in Mainz at the former highly-charged ion experiment [91] that relies on a bulk NbTi connector. A photograph of a recently manufactured joint is shown in figure 4.6(b). The manufacturing procedure is as follows: First, a narrow groove about one radius deep in radial direction is wire-cut along the full axial length of a small but solid cylinder of NbTi. The two wire endings of the superconducting coil are then stripped, twisted together and laid in the full axial length of this groove. Then the groove is cautiously crimped such that the wire endings are held in place. Finally, the end of the cylinder opposite to the wires is spot-welded. The actual manufacturing has been carried out by the mechanical workshop of the Institute of Physics at the University of Mainz.

At this point it should be mentioned that the `BASE-CERN` group has observed that placing the superconducting joint in a strong magnetic field ($B \approx 2\,\mathrm{T}$) severely limits the loading current. Since this process is not fully understood, it will be interesting to see whether it occurs for our superconducting joint design as well.

Another potential point of failure is the loading joint, i.e. the transition from copper to NbTi. In fact, this has been the limitation in the past for other experiments [91]. This transition must have a very small contact resistance and a good thermal connection to the 4 K bath, otherwise the loading current will heat up the surrounding NbTi-wire and the coil will immediately quench after turning off the loading current. The practical problem when working with NbTi wire of 100 μm diameter is that while it is nicely bendable, it does not stay in position but rather acts as a spring and returns to its previous position. This makes it difficult to establish a good contact between NbTi and copper over a large surface area. Our procedure is the following: First, we strip the NbTi over a few cm and then tightly wind the stripped part around a thick ($\gtrsim 1\,\mathrm{mm}$), ideally oxygen-free copper wire whose surface has been priorly cleaned with abrasive paper to remove the oxide layer. After at least 10 windings, we secure the NbTi wire in place by tightly winding an additional smaller copper wire around the NbTi-windings, thus 'sandwiching' the NbTi between two layers of copper. Finally, we cover the whole area with solder. Not only improves this the electrical contact further, it also prevents the copper wires from moving relative to each other which could create stress on the fragile NbTi wire.

4.6   First tests of persistent current loading

In order to test the superconducting joint concept, an initial trial was performed by winding a test coil with $N \approx 100$ around a spare trap can. In a first step, the trap can was mounted to a coldhead and cooled to 4 K. A 4-wire measurement of the resistance of the coil was conducted, which yielded a resistance compatible with 0. Next, a test with a magnetic field sensor was planned. However, meanwhile it became apparent that on the
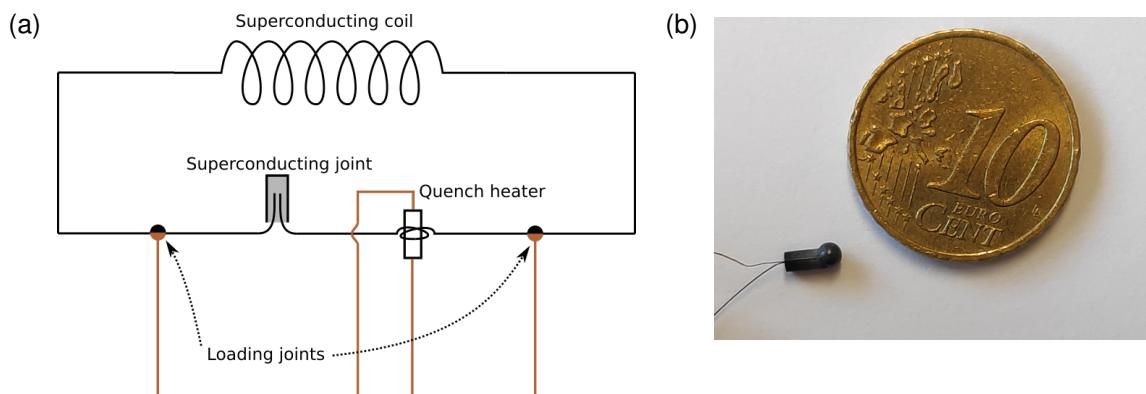
Figure 4.6:   (a) Schematic of the concept to load a persistent current into the superconducting coil. The superconducting joint creates a superconducting connection between the two wire endings and the quench heater allows to load a persistent current. Superconducting wires are colored in black and copper wires are copper-coloured. (b) Photograph of a superconducting joint as it has been manufactured in the course of this thesis. The two NbTi wire endings are arc-welded to a bulk NbTi cylinder. For details, see text.

road towards the next *g*-factor measurement the sympathetic cooling techniques will be the major bottleneck. Consequently, I focused on the development of the simulations and performing subsequent cooling measurements, see section 6 and 9.

Nevertheless, due to the ongoing success of the sympathetic cooling methods, the shim coil project became relevant again and the testing has continued together with my colleagues Hüseyin Yildiz and Peter Micke. A full cycle of loading and quenching a persistent current in the test coil is demonstrated in figure 4.7. The magnetic field is detected by means of a giant magnetoresistive (GMR) sensor[3] that is operable at 4 K. The measurement starts with the quench heater (QH) turned on, followed by turning on the loading current of $I_c = 500 \, \text{mA}$ after about 10 s, which creates the step upwards in the sensor signal. Next, the QH is turned off, which restores the superconductivity of the branch that contains the joint. Then, at around 40 s, the decisive action is performed where the loading current is turned off. The fact that no change in sensor signal is observed proves that the coil has, in fact, been loaded with a persistent current. Finally, the QH is turned on again and the coil is quenched. The ability to load 500 mA of current is a factor of 5 above the design value and implies that the contact resistance of the NbTi-copper transition is negligible in this test setup.

With this very promising outlook I close this section. These first tests pave the way for an improved experimental setup with which a $< 1 \times 10^{-10}$ measurement of the *g*-factor of the proton will be possible. The only question that remains is how our version of the superconducting joint performs in a strong magnetic field. However, even if it does not perform well, it should be possible to place the joint further away from the trap center in a low-field region. However, since the superconductivity of NbTi at 4K implies an extremely bad thermal conductivity (at least 6 orders of magnitude worse than copper at 4 K), the proper thermalization of the wire that bridges the distance has to be guaranteed. This issue could be resolved by employing NbTi wire that is embedded in a copper matrix. In addition, this would also allow to wind the coils with more than 2 layers of NbTi wire, thus strongly relaxing the amount of loading current required to compensate B_2^{trap}. Consequently, this is certainly a worthwhile project for future work.

---

[3]Model NVE AAH002-02E
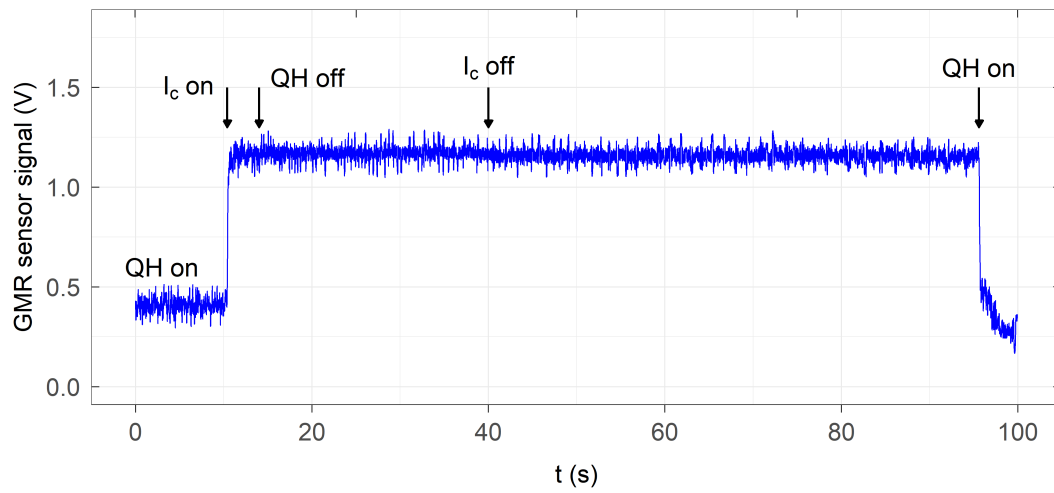
Figure 4.7: Demonstration of loading a test coil with a persistent current $I_c = 500\,\text{mA}$. The GMR sensor signal is approximately linear with the magnetic field. After loading the coil and turning the quench heater (QH) off, the loading current can be switched off and the magnetic field remains, which is a distinct sign of superconductivity.

5 | Pressure stabilization

The stability of the pressure of the gas phase of the liquid helium (LHe) cryostat affects the traps in two ways: First, on a short-term time scale, an uncontrolled boil-off produces vibrations of the trap stack. These vibrations induce eddy currents in any electrical conductor that is not in a perfectly homogeneous magnetic field. The eddy currents in turn generate a magnetic field that is detrimental to the frequency stability, especially to that of the cyclotron motion. An example of such short-term noise is shown in figure 5.1, where the pressure in the helium recovery line is measured. The periodic fluctuations are most likely caused by the regulation loop of the pumps and compressors of the helium liquifier. Coincidentally, the time period is approximately the same as the one for a motional frequency measurement of an ion (60 s). Exposing either the helium reservoir of the experiment or magnet to these fluctuations thus certainly affects the frequency stability adversely.

Second, on a long-term time scale (several hours to days), the helium gas pressure in the recovery line drifts by up to $\approx 50\,\mathrm{mbar}$. Since the pressure defines the boiling point of the LHe with about $1\,\mathrm{mK/mbar}$, these long-term drifts result in significant cyclotron frequency changes. Although it is tempting to explain this behavior with the thermal expansion of the components thermalized to LHe temperature and the resulting movement within the magnet, a quick estimate shows that this cannot be true: Assuming an upper limit of $\Delta P = 50\,\mathrm{mbar}$, this results in a maximum of $\Delta T = 50\,\mathrm{mK}$. The thermal expansion coefficient of copper at $4\,\mathrm{K}$ is $\alpha \simeq 3 \times 10^{-9}\,\mathrm{K}^{-1}$ [92]. Consequently, for $\Delta T = 50\,\mathrm{mK}$ one meter would change by $0.15\,\mathrm{nm}$, which is even in the extremely large magnetic inhomogeneity of the analysis trap ($B_2 = 300 \times 10^3\,\mathrm{T/m}^2$) negligible. In contrast, small changes in magnetic field susceptibility $\Delta\chi$ can result in a significant magnetic field change $\Delta B/B \approx \Delta\chi$. Ref. [92] finds a temperature dependence of about $\Delta\chi/\Delta T = -3.6 \times 10^{-6}\,\mathrm{K}^{-1}$ for high-purity copper. Thus $\Delta T = 50\,\mathrm{mK}$ would result in $\Delta B/B = -0.17 \times 10^{-7}$ or $\approx 5\,\mathrm{Hz}$ for the cyclotron frequency of the proton at $29\,\mathrm{MHz}$. While $\Delta P = 50\,\mathrm{mbar}$ is certainly an upper limit, the effect is amplified by any ferromagnetic impurities in the copper or material in vicinity of the traps.
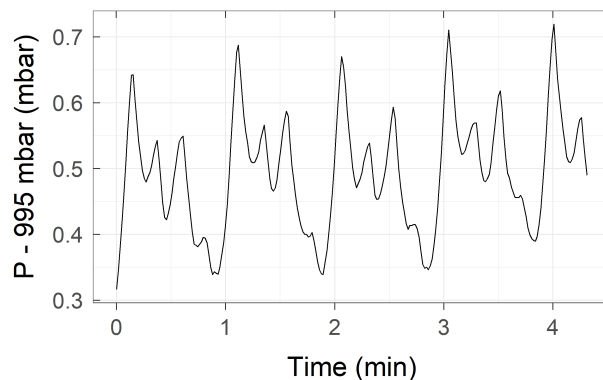
Figure 5.1: Measurement of the helium gas pressure in the recovery line without any stabilization active. The periodic fluctuations most likely stem from the regulation of the pumps and compressors of the helium liquifier and are detrimentral to the frequency stability of a trapped ion.
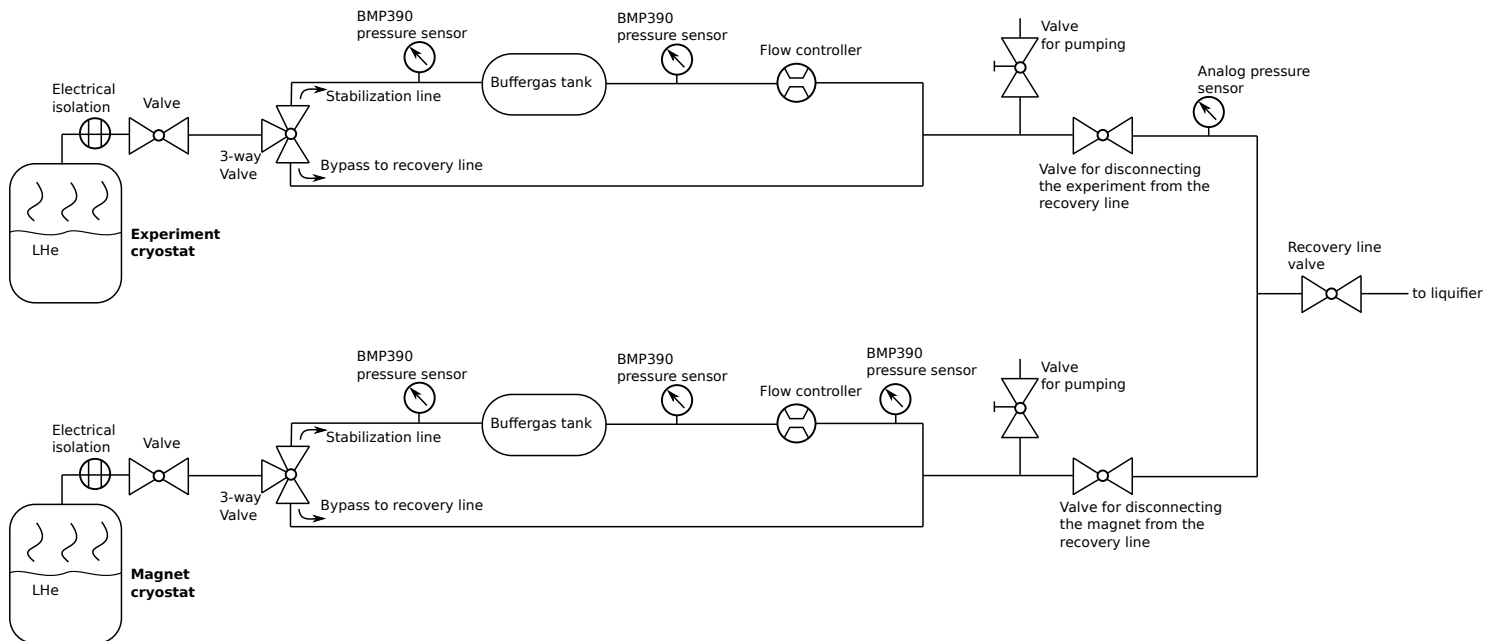
Figure 5.2: (Larger version of this figure is available in the appendix, figure 10.2). Overview of the pressure stabilization system. The helium reservoirs of the experiment and magnet are independently stabilized and the systems are nearly identical copies of each other. A 3-way valve allows switching between the stabilization line and a bypass line, which is required for high volume flows when e.g. refilling LHe. The pressure is stabilized by means of an adjustable valve (flow controller) that is opened based on the pressure sensor signal. A buffergas tank increases the available regulation volume and improves the stability. KF25 hoses are used for connecting the individual components.

5.1 Basic setup

A pressure stabilization system can compensate both the short- and long-term drifts of the pressure and is a crucial part of any cryogenic high-precision Penning-trap experiment. The basic idea for the implementation is the following: A fixed setpoint pressure $\Delta P = 50 - 100\,\mathrm{mbar}$ above the recovery line pressure is defined. The actual pressure inside the cryostat is measured by a sensor and is fed to an adjustable valve (flow controller[4]). If the measured pressure is below the setpoint value, the flow controller closes its valve further and the pressure rises. Analogously, if the pressure is too high, the valve opens and more gas is released towards the recovery line, reducing the pressure.

The real setup, depicted schematically in figure 5.2, requires additional components. The stabilization lines for the experiment and magnet cryostats are decoupled but nearly identical copies of each other. This allows for independent operation and optimization. For example, the magnet evaporates only $\approx 0.6\,\mathrm{mbar} \cdot \ell/\mathrm{s}$ of gaseous helium, while the consumption of the experiment is about 15 times larger. It will be shown later that this results in different control parameters and a different level of stability.
Starting from the liquid helium reservoirs, the first element is an electrical isolation that decouples the pressure stabilization setup from the experiment, preventing electrical noise signals from coupling in. These can either stem directly from other experiments or, since the pressure stabilization and recovery line can be considered a large antenna, from picked-up electromagnetic waves. Next, a 3-way ball valve is installed to allow switching between

---

[4]It is actually misleading to call this adjustable valve flow controller as we do not regulate the flow but rather the pressure, however, due to the naming by the company and other experiments I will follow this convention.

the stabilization line and a bypass line with larger cross section. This is needed because when refilling LHe, the gas flow is orders of magnitude higher compared to the usual operation and too large for the small cross section of the flow controller valve.

The pressure is stabilized by means of a BMP390 pressure sensor [93] and a Bronkhorst EL-FLOW Select F-201CV-500-BGD-22-V mass flow controller [94]. The BMP390 employs a piezo-resistive sensor that uses pressure-induced mechanical strain for pressure determination. Therefore it provides an absolute pressure measurement and is gas-independent, two important features in our application. Furthermore it comes at a comparably cheap price of about 10€, which allows to install several redundant sensors. The sensor has 24-bit resolution and a maximum sampling rate of 200 Hz, albeit the latter is not needed in our case. The datasheet states a typical RMS noise of 0.02 Pa or in relative terms 2×10^{-7} assuming ambient pressure [93]. Although a slighlty higher relative RMS noise of 5×10^{-7} is measured in the course of subsection 5.2, this is nevertheless sufficient for our application. KF25 hoses are used throughout the full setup which provide a sufficiently large cross section so that no pressure differentials between the sensors and cryostats can occur.

The flow controllers consists of small proportional valves whose cross sections were specified based on the desired pressure difference ΔP and the given evaporation rates. Additionally, they are capable of measuring and controlling mass flow, which is however not relevant for us. Instead, the valve position is directly adjusted based on the pressure signal of the BMP390.

5.2   Achieved pressure stability

A first trial run was performed using the pressure sensor and the flow controller of the experiment line. The pressure sensor was configured to operate in the highest resolution mode at which it has a 100 Hz sampling rate. The pressure readings were read out via an Arduino Nano [95], which was programmed to average 100 measurements, yielding an effective 1 Hz sampling rate. These pressure measurements were then fed into a Lab-View™ program and the valve of the flow controller was actuated based on an optimized proportional-integral-derivative (PID) controller. The setpoint pressure was 1080 mbar. Figure 5.3 shows the standard deviation of 1 h time intervals of the measured pressure as a function of time after refilling LHe, in this case starting on a Friday around noon until the next Monday morning. The PID coefficients were not changed and the gas flow is approximately constant. Since the only parameter that naturally changes is the remaining amount of liquid helium in the cryostat, the improving stability can be attributed to the increased volume the flow controller can regulate on. The maximum available volume is calculated based on the cryostat capacity of 35 ℓ, an estimated 5 ℓ of overhead and our LHe standing time of about 80 h. An exponential fit yields about a factor of 2 improvement for every additional 6 ℓ of available gas volume.

Thus, a dedicated buffer gas volume of 80 ℓ was added between each flow controller and cryostat for the next experimental run. In regard to the available volume, these additional 80 ℓ would theoretically allow for better than 0.05 μbar of stability per 1 h time block. The buffer gas tanks are aluminum pressure vessels (Model 902 528 from Frauenthal Airtank) that are normally used as pressure reservoirs for pneumatic truck brakes. However, they have proven to be sufficiently leak-tight for our helium application as well and are thus a good alternative compared to expensive and heavy vacuum vessels.
Having these buffer gas tanks added, the optimization of the PID parameters was repeated to reach the best stability. Note that one should do this only > 1 h after introducing the 50–
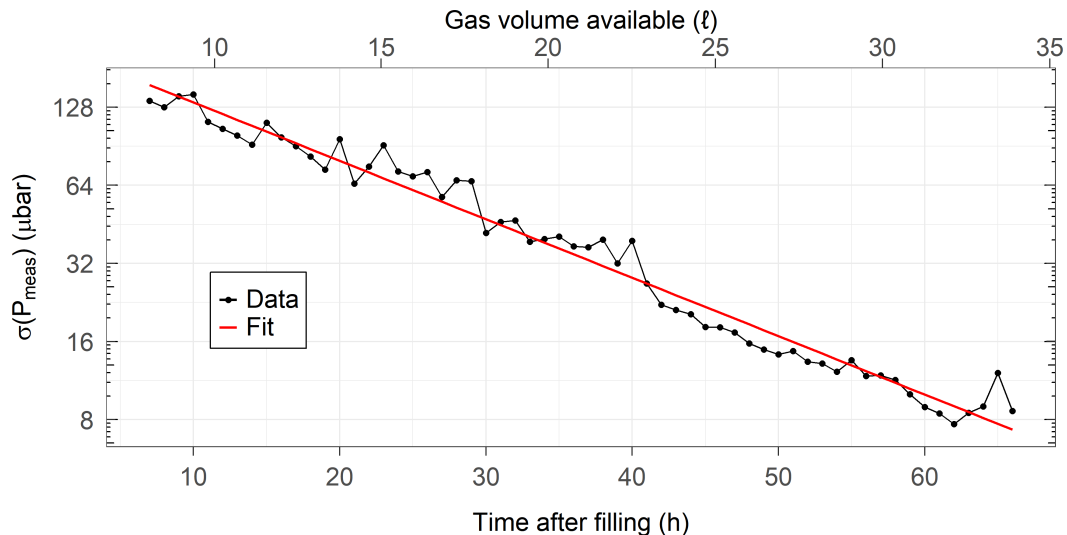
Figure 5.3: Demonstration of the need for an additional buffer gas tank: The pressure is stabilized over the course of nearly three days without a buffergas tank and the standard deviation of 1 h-long time blocks is shown. Since all other parameters such as the helium evaporation rate stay constant, the improving stability can be attributed to the additional gas volume that becomes available due to the evaporation of the liquid helium. A fit yields a factor of 2 improvement for every additional $6\,\ell$ available.

100 mbar overpressure. This is because the increase in pressure also causes an increase in the boiling point of the LHe, which defines the temperature of the whole bulk material that is thermalized to 4 K. As a result, directly after increasing the pressure the bulk material is still colder than the LHe reservoir and the helium evaporation rate is smaller by up to a factor of 2. The final stability with optimized PID coefficients is shown in figure 5.4. The experiment reservoir (subfigure (a)) can be stabilized to a standard deviation of 3.0 µbar for the 1 Hz sampling- and regulation rate. The magnet reservoir can be independently optimized to reach 0.5 µbar for the same sampling- and regulation rate. In both cases the standard deviation is, within the expected statistical scatter, constant over time so that both values refer to the full dataset. The difference between experiment and magnet most likely stems from the different evaporation rates; the experiment consumes about $10\,\ell$ of LHe per day while the magnet only consumes about $0.6\,\ell$. This behavior is also observed by other experiments that employ a pressure stabilization. For example, the PENTATRAP experiment [30] reaches with a similar helium consumption practically the same stability [96, 97]. It would probably be possible to improve the magnet stability even further since the resolution of the pressure sensor becomes the limiting factor, as it is visible by the discrete steps in figure 5.4(b). Interestingly, apart from constant offsets, no effect on the stability was observed depending on whether a BMP390 sensor before or after the buffergas tank was used (compare figure 5.2). Thus, if a further improved stability is needed, the valve could be regulated on the mean of several independent sensor signals or simply a sensor with superior resolution could be installed. Finally, at this level of stability long-term drifts of the sensor signal itself must be taken into account. The datasheet of the BMP390 states a 12-month stability of ± 0.16 mbar and an absolute pressure reference (APR) would be required to compensate the internal drifts of the sensor [96, 98]. However, at our current level of stability these drifts are negligible and other effects such as the filling cycle dominate, see for example figure 7.8 in section 7.3.

(a)

(b)
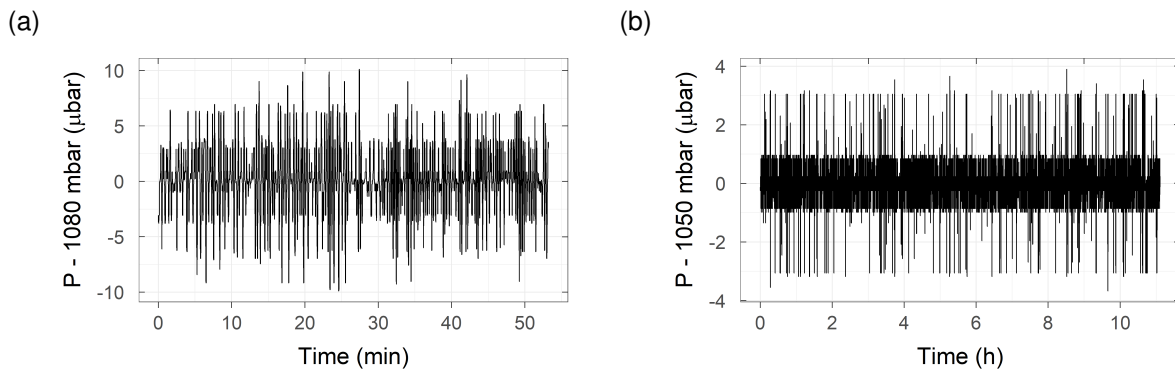
Figure 5.4: Final pressure stability reached for the experiment (a) and magnet (b) liquid helium reservoirs. A standard deviation of 3.0 µbar and 0.5 µbar for a sampling- and regulation rate of 1 Hz is obtained for the experiment and magnet, respectively. The difference most likely stems from the different helium evaporation rates. The pressure stability of the magnet is limited by the sensor resolution, visible as discrete step sizes.

5.3   Impact of pressure fluctuations on the particle frequency stability

After building and implementing a stabilization system, of course one would like to evaluate whether the quantity of interest is sufficiently stabilized. However, in the case of the pressure stabilization this is actually rather difficult to assess as the scatter and drift of the cyclotron frequency can originate from many different sources. At the time the measurements presented here took place, we were in the process of developing sympathetic cooling techniques and thus the experiment was not optimized for highest stability and precision. In particular, our laboratory had many different users so that the door was regularly opened causing temperature fluctuations, coldheads were switched on and off, or people worked with magnetic material near the superconducting magnet. For example, the peak at around 65 h in figure 5.3 stems from people starting their work in the laboratory on Monday morning. Consequently, comparing two measurements of the cyclotron frequency stability, one with stabilized pressure and another one without, will not yield definitive results.

Nevertheless, manually inducing pressure changes while observing the cyclotron frequency allows to estimate the sensitivity. The cyclotron frequency of the proton is measured in the precision trap by radiating a sideband drive at frequency $\nu_{\mathrm{RF}} = \nu_+ - \nu_{\mathrm{z}}$ and observing the position of the double dip. Simultaneously, the pressure in the experiment recovery line is logged. Both time traces are shown in figure 5.5(a). At around $t = 30\,\mathrm{min}$, the valve that (dis-)connects the experiment from the recovery line is closed slightly. The reduced cross section causes the pressure to rise (upper plot). The cyclotron frequency (lower plot) follows the same trend. Linking the signals to each other via the time stamp leads to figure 5.5(b), where the cyclotron frequency change as a function of pressure is shown. A linear fit yields a pressure sensitivity of the cyclotron frequency of 0.4 Hz/mbar.

It should be emphasized that several of such measurements were performed and for some no cyclotron frequency change at all was observed, even for several mbar of pressure increase. It follows that the measurement shown here is almost certainly the result of the positive interference of several other, unrecorded sources of frequency drifts. However, this measurement is deliberately presented as even for 0.4 Hz/mbar the achieved stability of 3 µbar allows to constrain the frequency fluctuations due to pressure fluctuations to $< 1.2\,\mathrm{mHz}$. With regard to the pressure, this stability consequently allows a relative cyclotron frequency stability of better than 4×10^{-11} per shot. This is a factor of 30 smaller than the linewidth of the last *g*-factor measurement of the proton [6] and should thus not
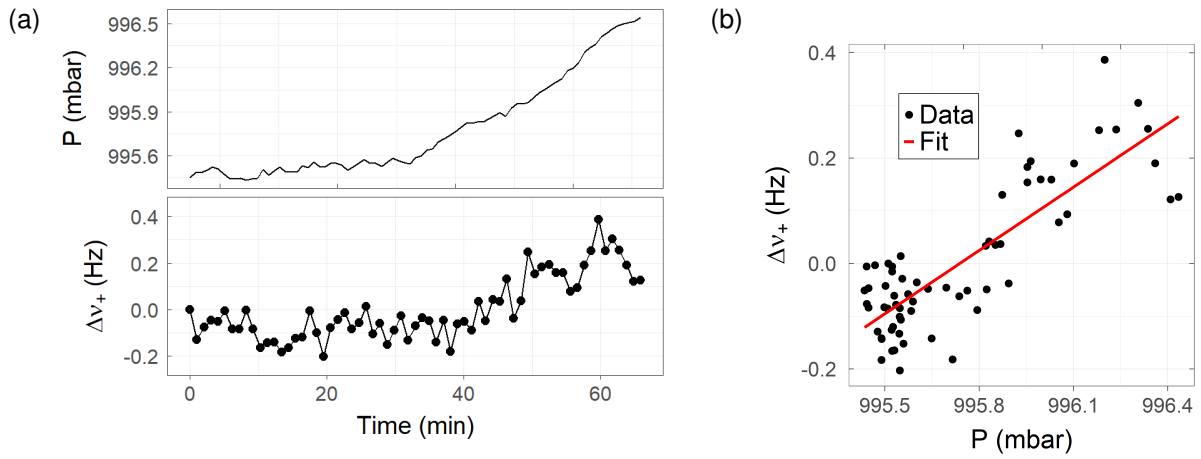
Figure 5.5: Influence of the pressure in the gaseous phase of the liquid helium reservoir of the experiment on the modified cyclotron frequency of a proton in the precision trap. The time-resolved correlation between pressure (upper plot) and cyclotron frequency (lower plot) is shown in (a). Linking the data via the timestamp (b) allows estimating the sensitivity. A linear fit yields $0.4\,\mathrm{Hz/mbar}$.

limit the precision of the next-generation measurement.

6 | Simulations

What initially started out as my home office project during the first Covid-19 shutdown in March 2020 has now evolved into the major methodical-technological advancement developed in the course of this thesis: The development of numerical simulations of the coupled proton-beryllium-resonator system with immediate applicability for studying different sympathetic cooling schemes. Around this time, we recorded the first cooling signals with a single proton in one trap and a cloud of laser-cooled beryllium ions in another trap [26, 27]. Although initially common-endcap coupling had been proposed [24, 25], the experimental method of choice was on-resonance coupling with a common resonator, since we expected the coupling signals to be more easily observable. However, the addition of the resonator severely complicates the situation, which is summarized in figure 6.1. We desire to cool one oscillator (the proton) in a coupled system of three harmonic oscillators. Another oscillator (the beryllium ion cloud) can be variably coupled to a very cold thermal bath. However, the coupling between these two can only be performed via a third oscillator (the resonator), which is coupled to a hot noise thermal bath. A central question was, for example, to which intensity the cooling laser should be adjusted. Since the ion-resonator coupling relies on image currents, a strong damping decouples the beryllium ions from the interaction with the resonator and the proton. On the other hand, in the limit of vanishing damping, the beryllium ions and therefore the proton are not cooled at all. This question among many others will be answered in this section. It turns out that the ideal laser settings are, depending on which cooling scheme is employed, completely different.

Section 6.1 will give an overview of the numerical implementation. Afterwards, the numerical precision in terms of frequency and energy is briefly investigated. The five applications in section 6.4 - 6.8 constitute the main part of this chapter.
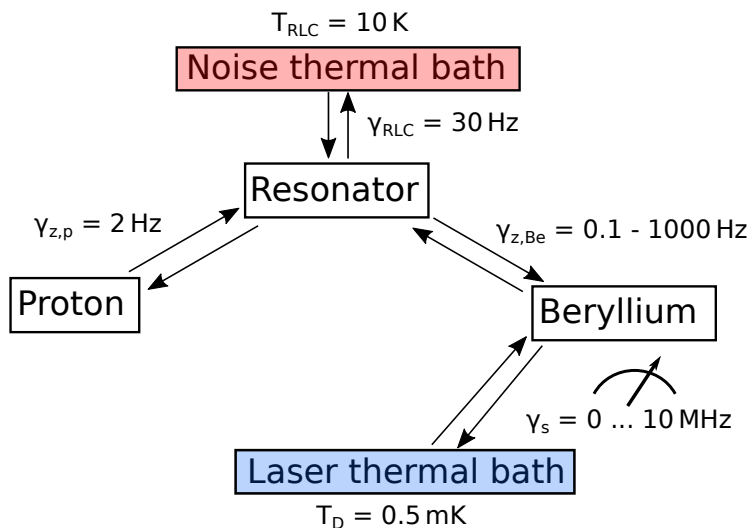
Figure 6.1: Overview of the three involved oscillators with their mutual coupling. The goal is to transfer the mK-temperatures of the laser thermal bath to the single proton. Note that the coupling rates are given for the case of on-resonant coupling and can be different for off-resonant schemes.

6.1 Numerical implementation

I explicitly emphasize again (see section 3.10 for the initial statement) that about half of this section has been published in reference [28] already with me as first and leading author. The numerical implementation of the integration of the radial modes has been added for this thesis. Small modifications to the text and figures have been made to ensure consistency. All other content has been copied mostly verbatim.

In general, the physics is implemented from first principles in the simulations. Only experimentally established model assumptions are made and no heuristic scaling factors are used. Although this concept comes at a higher computational cost, it does not pose an issue, as will be outlined in section 6.2.

6.1.1 Numerical integration of the resonator and particle's axial motion

At first, the equations governing the simulations will be summarized again. The following description covers both cases of resonator-mediated and common-endcap mediated coupling simultaneously. If only one case shall be simulated, the other one can be turned off by setting $T_{\mathrm{RLC}} = 0, R_{\mathrm{RLC}} \to \infty$ or $C_{\mathrm{com}} \to \infty$ to disregard the resonator or common-endcap simulation, respectively. The proton and $^9\mathrm{Be}^+$ ions induce image currents [33]

$$I_{\mathrm{RLC/com,p}} = \frac{q}{D_{\mathrm{RLC/com,p}}} \dot{z}_{\mathrm{p}} \qquad \text{and} \qquad I_{\mathrm{RLC/com,Be}} = \frac{q}{D_{\mathrm{RLC/com,Be}}} \dot{z}_{\mathrm{Be}} \qquad (6.1)$$

in the resonator or the common endcap electrode, denoted with subscript 'RLC' and 'com', respectively. In all cases $D_{\mathrm{res/com,p/Be}}$ is a geometrical parameter defined by the trap geometry and can be considered an 'effective electrode distance'. The common endcap is modelled as an ideal capacitor C_{com} charged by the image currents. The potential U_{com} due to the accumulated charge leads to a force on the particles, $F_{\mathrm{com,p/Be}} = \frac{q}{D_{\mathrm{com,\ p/Be}}} U_{\mathrm{com}}$. Similarly, the particles are driven and damped by the oscillating voltage of the resonator U_{RLC} at a corresponding force $F_{\mathrm{RLC}} = \frac{q}{D_{\mathrm{RLC,p/Be}}} U_{\mathrm{RLC}} = \frac{q}{D_{\mathrm{RLC,p/Be}}} L \dot{I}_{\mathrm{L}}$. The resonator itself is described by a second-order differential equation. In addition to the ion-induced currents, the resonator is charged by the effective thermal Johnson-Nyquist noise current I_{noise}. In the following, the differential equations of the resonator will be described in terms of the current through the coil I_{L}. Other choices for the quantity describing the resonator are possible, for example the voltage U_{RLC}. However, since the ions are current sources, the implementation via I_{L} is the most convenient one. The full set of coupled differential equations, expressed in terms of input parameters of the simulation, is then:

$$m_{\mathrm{p}}\, \ddot{z}_{\mathrm{p}} + 2\, q_{\mathrm{p}}\, C_{2,\mathrm{p}}\, U_{0,p}\, z_{\mathrm{p}} - \frac{q_{\mathrm{p}}}{D_{\mathrm{RLC,p}}} L\, \dot{I}_L - \frac{q_{\mathrm{p}}}{D_{\mathrm{com,p}}} U_{\mathrm{com}} = 0 \qquad (6.2)$$

$$m_{\mathrm{Be}}\, \ddot{z}_{\mathrm{Be}} + 2\, q_{\mathrm{Be}}\, C_{2,\mathrm{Be}}\, U_{0,\mathrm{Be}}\, z_{\mathrm{Be}} - \frac{q_{\mathrm{Be}}}{D_{\mathrm{RLC,\ Be}}} L\, \dot{I}_L + \frac{q_{\mathrm{Be}}}{D_{\mathrm{com,Be}}} U_{\mathrm{com}} = 0 \qquad (6.3)$$

$$L\, C_{\mathrm{RLC}}\, \ddot{I}_L + \frac{L}{R} \dot{I}_L + I_L + I_{\mathrm{noise}} + \frac{q_{\mathrm{p}}}{D_{\mathrm{RLC,p}}} \dot{z}_{\mathrm{p}} + \frac{q_{\mathrm{Be}}}{D_{\mathrm{RLC,Be}}} \dot{z}_{\mathrm{Be}} = 0 \qquad (6.4)$$

$$U_{\mathrm{com}} = \frac{1}{C_{\mathrm{com}}} \int \left(\frac{q_{\mathrm{p}}}{D_{\mathrm{com,p}}} \dot{z}_{\mathrm{p}} - \frac{q_{\mathrm{Be}}}{D_{\mathrm{com,\ Be}}} \dot{z}_{\mathrm{Be}} \right) \mathrm{dt}. \qquad (6.5)$$

Here, the first two equations describe the axial motion of the particles with external forces F_{RLC} and F_{com} and the latter two the resonator and common endcap capacitance.

The Coulomb interaction between the beryllium ions is neglected since only the common mode of the beryllium cloud interacts with the resonator, as will be outlined in section

6.5.2. If the motion of more than one beryllium ion is simulated, either an effective cloud or an array of individual beryllium ions is calculated, depending on whether the single particle behaviour is of interest.

A key ingredient of the simulation code is the proper implementation of I_{noise}. Equation (6.4) is a type of Langevin equation where the resistance R_{RLC} determines, according to the fluctuation-dissipation-theorem, both the dissipation and noise terms. In this case I_{noise} obeys a delta-correlated Gaussian probability distribution with zero mean. The mean squared value of the single-sided power spectral density is given by $\langle I_{\text{noise}}^2 \rangle = 4k_B T_{\text{RLC}} \Delta f / R_{\text{RLC}}$. In the time domain representation, the bandwidth Δf must be substituted by the Nyquist frequency, which is equal to half of the sampling frequency $f_s = 1/\Delta t$ according to the Nyquist–Shannon sampling theorem, yielding $\Delta f = 1/(2\Delta t)$. Furthermore, in order to achieve a delta-correlation of two subsequent noise samples, each noise value is multiplied with a random value drawn from a Gaussian distribution with a mean of 0 and a standard deviation of 1, abbreviated as $\mathcal{N}_{\text{n}}(0,1)$. In total, in each step n the equation for the noise sample then reads

$$I_{\text{noise,n}} = \sqrt{2k_B T_{\text{RLC}}/(R\Delta t)} \cdot \mathcal{N}_{\text{n}}(0,1). \tag{6.6}$$

The differential equations (6.2)-(6.5) are solved individually by employing a fourth-order symplectic integrator [99]. A symplectic integrator evolves the system in time by performing canonical transformations and thus conserves the system's Hamiltonian. It can be applied directly to the equations of motion of the particles. Consequently, in the absence of additional forces the integrator conserves the energy of the particles, which is an essential feature in sympathetic cooling studies with long integration times. The intermediate steps to evolve the particle coordinates from time t to time $t + \Delta t$ are

$$z_n^{(1)} = z_n + c_1 \dot{z}_n \Delta t \tag{6.7}$$

$$\dot{z}_n^{(1)} = \dot{z}_n + d_1 \ddot{z}\left(z_n^{(1)}\right) \Delta t \tag{6.8}$$

$$z_n^{(2)} = z_n^{(1)} + c_2 \dot{z}_n^{(1)} \Delta t \tag{6.9}$$

$$\dot{z}_n^{(2)} = \dot{z}_n^{(1)} + d_2 \ddot{z}\left(z_n^{(2)}\right) \Delta t \tag{6.10}$$

$$z_n^{(3)} = z_n^{(2)} + c_3 \dot{z}_n^{(2)} \Delta t \tag{6.11}$$

$$\dot{z}_n^{(3)} = \dot{z}_n^{(2)} + d_3 \ddot{z}\left(z_n^{(3)}\right) \Delta t \tag{6.12}$$

$$z_{n+1} \equiv z_n^{(4)} = z_n^{(3)} + c_4 \dot{z}_n^{(3)} \Delta t \tag{6.13}$$

$$\dot{z}_{n+1} \equiv \dot{z}_n^{(4)} = \dot{z}_n^{(3)} \tag{6.14}$$

where $\ddot{z}\left(z_n^{(i)}\right)$ is the acceleration due to the forces acting on the particle,

$$\ddot{z}\left(z_n^{(i)}\right) = \left(-2qC_2U_0 z_n^{(i)} + F_{\text{com}} + F_{\text{RLC}} + F_{\text{z,ext}}\right)/m. \tag{6.15}$$

Here $F_{\text{z,ext}}$ summarizes additional external forces in z-direction, for example due to rf excitations. The symplectic properties of the algorithm arise from the correct choice of the dimensionless coefficients c_i and d_i. They are given by [99]

$$c_1 = c_4 = \frac{1}{2(2 - 2^{1/3})}, \qquad c_2 = c_3 = \frac{1 - 2^{1/3}}{2(2 - 2^{1/3})} \tag{6.16}$$

$$d_1 = d_3 = \frac{1}{2 - 2^{1/3}}, \qquad d_2 = -\frac{2^{1/3}}{2 - 2^{1/3}}, \qquad d_4 = 0. \tag{6.17}$$

Although two out of four coefficients are negative, i.e. correspond to an intermediate step backwards in time, their sum obeys $\sum c_i = \sum d_i = 1$. Notably, the integration scheme is also time-reversal invariant. The integrator is applied to each particle individually. Although the resonator noise damps and excites the particles, this method avoids long-term drifts and reproduces energy conservation in the limit $R \to \infty$.

While the integrator can be applied directly to the equations of motion of the particles, the integrator for the resonator equation requires a modification due to the dissipative term. In particular, the second derivative of the coil current is also a function of the first derivative, i.e. $\ddot{I} \equiv \ddot{I}(I, \dot{I})$, where here and in the following the index L will be omitted for brevity. Substituting $\ddot{I}$ from the differential equation in $\dot{I}^{(i)} = \dot{I}^{(i-1)} + d_i \ddot{I}\left(I^{(i-1)}, \dot{I}^{(i-1)}\right)\Delta t$ and solving for $\dot{I}^{(i)}$ yields the modified discretized integrator of the RLC circuit equation,

$$
\begin{aligned}
I_{\mathrm{n}}^{(i)} &= I_{\mathrm{n}}^{(i-1)} + c_i \dot{I}_{\mathrm{n}}^{(i-1)} \Delta t \\
\dot{I}_{\mathrm{n}}^{(i)} &= \frac{1}{1 + \frac{d_i \Delta t}{RC}} \dot{I}_{\mathrm{n}}^{(i-1)} - \frac{1}{1 + \frac{d_i \Delta t}{RC}} \frac{d_i \Delta t}{LC} \left(I_{\mathrm{n}}^{(i-1)} + I_{\mathrm{ext}}\right).
\end{aligned}
\tag{6.18}
$$

Here $i \in \{1, 2, 3, 4\}$ denotes the same sub-steps as in equations (6.7) - (6.14), that is $I_{\mathrm{n}}^{(0)} \equiv I_{\mathrm{n}}$, $\dot{I}_{\mathrm{n}}^{(0)} \equiv \dot{I}_{\mathrm{n}}$, $I_{\mathrm{n}}^{(4)} \equiv I_{n+1}$ and $\dot{I}_{\mathrm{n}}^{(4)} \equiv \dot{I}_{\mathrm{n}}^{(3)} \equiv \dot{I}_{n+1}$. Besides, $I_{\mathrm{ext}} = I_{\mathrm{noise}} + I_{\mathrm{RLC,p}} + I_{\mathrm{RLC,Be}}$ is the external current. In the case of $R \to \infty$ the factor $1 \big/ \left(1 + \frac{d_i \Delta t}{RC}\right)$ is 1 and the energy-conserving case is restored.

6.1.2 Numerical integration of the radial motions

At first glance one would expect the numerical integration of the radial motions to be more complicated since it is the nature of the Lorentz force that the force in x-direction is a function of the velocity in y-direction and vice versa. However, it can be shown [100] that a successive and not an interleaved integration of x and y reproduces the analytical solution to a good degree. The particular integration steps are the exact same as equations (6.7) - (6.14) where z is exchanged with x, y. Only the accelerations are different, namely

$$
\ddot{x}\left(x_n^{(i)}, \dot{y}_n\right) = \left(qC_2 U_0 x_n^{(i)} + qB_0 \dot{y}_n + F_{\mathrm{ext,x}}\right)/m
\tag{6.19}
$$

$$
\ddot{y}\left(y_n^{(i)}, \dot{x}_{n+1},\right) = \left(qC_2 U_0 y_n^{(i)} - qB_0 \dot{x}_{n+1} + F_{\mathrm{ext,y}}\right)/m
\tag{6.20}
$$

where it was implicitly assumed that the x-integration was performed before the y-integration and $i \in \{1, 2, 3, 4\}$ again.

A frequency correction factor is necessary for reproducing the analytical value of the modified cyclotron frequency to a good precision. The derivation can be found in [100] and the ratio α between simulated free cyclotron frequency $\omega_{\mathrm{c,sim}}$ and analytical cyclotron frequency $\omega_{\mathrm{c,ana}}$ is given by

$$
\alpha := \frac{\omega_{\mathrm{c,ana}}}{\omega_{\mathrm{c,sim}}} = \frac{\sin\left(\omega_{\mathrm{c}} \Delta t / 2\right)}{\omega_{\mathrm{c}} \Delta t / 2}
\tag{6.21}
$$

Hence, a convenient way to incorporate this correction factor is by replacing $B_0 \to \alpha B_0$. Note that this is the first and only numerical correction factor employed in the whole simulation code.

6.1.3   Numerical implementation of laser cooling

Laser cooling of the $^9\text{Be}^+$ ions is modelled by assuming that a narrow linewidth laser with frequency f_L, detuned by δ_L relative to the transition frequency $f_0 = f_\text{L} - \delta_\text{L}$, interacts with the $^9\text{Be}^+$ ions. Based on the theory of light-ion interaction briefly introduced in section 2.7.1, in each simulation step in which a $^9\text{Be}^+$ ion is in the ground state it can absorb a photon with probability

$$P_\text{abs} = \frac{I_\text{laser}}{I_\text{sat}} \frac{\Gamma \Delta t / 2}{1 + 4 \left(\frac{2\pi \delta_\text{L} + k_\text{L} \dot{z}_\text{Be}}{\Gamma} \right)^2}. \tag{6.22}$$

The fraction $\frac{I_\text{laser}}{I_\text{sat}}$ is a free parameter and is the simulation equivalent to the laser intensity in the experiment. If an absorption occurs, the ion's velocity is reduced by $\hbar k_\text{L} / m_\text{Be}$ and it enters the excited internal electronic state. In the excited state the ion cannot absorb photons but can spontaneously decay to the electronic ground state with probability $P_\text{sp-em} = \Gamma \Delta t$. Upon spontaneous decay, the ion receives an axial velocity kick, $\hbar k / m_\text{Be} \cos(\varphi)$, where φ is randomly distributed from 0 to 2π to account for the randomness in the direction of the spontaneous emission. Additionally, the ion can emit photons by stimulated emission with probability $P_\text{st-em} = P_\text{abs}$ where the ion's velocity is increased by $+\hbar k_\text{L} / m_\text{Be}$. This implementation of laser cooling is a simplified model, which is however sufficient for the studies in this thesis. For example, the model does not account for the anisotropy of spontaneous emission in a magnetic field [68] or the different m_I and m_J sublevels of the electronic transition.

6.1.4   Implementation of experimental imperfections

The above considerations enable accurate simulations of the dynamics of the trapped particles and resonator including laser cooling of the beryllium ions under ideal conditions. However, in practice, several experimental uncertainties can occur. While long-term axial frequency drifts can easily be compensated, drifts on the order of the duration of one axial frequency measurement, typically about 60 s, lead to frequency fluctuations that affect the energy exchange between the particles. The sources of these fluctuations are various, for example voltage instabilities and drifts of the power supplies, finite pressure and temperature stabilities of the liquid helium bath, drifts due to the Coulomb-interaction between the $^9\text{Be}^+$ ions, or residual inhomogeneities of the electric potential or magnetic field. A realistic estimate for the axial frequency fluctuation of the proton is $\sigma(\nu_z) \approx 50 - 100\,\text{mHz}$ or $\sigma(\nu_z)/\nu_z \approx 1 \times 10^{-7}$ at 60 s for our experiment [74]. In the following, the individual contributions are summarized by introducing an effective dynamical axial frequency variation by adding a modification ΔU to the trapping potential, where ΔU performs a random walk:

$$\Delta U_{n+1} = \Delta U_\text{n} + \delta U \cdot \tilde{\mathcal{N}}_\text{n}(0, 1). \tag{6.23}$$

The index n indicates the step number again and $\tilde{\mathcal{N}}_\text{n}(0, 1)$ is a number drawn from a Gaussian distribution with mean 0 and a standard deviation of 1. δU is a scaling factor determining the expectation value of the standard deviation of the random walk $\sigma(U_0)$ and is related to the frequency stability by $\sigma(U_0)/U_0 = 2\sigma(\nu_z)/\nu_z$. In order to express δU in terms of practical experimental quantities, ξ_stab is defined as the relative voltage stability for frequency measurements of length 60 s and obtain

$$\delta U_0 = \xi_\text{stab} \cdot U_0 \cdot \sqrt{\frac{1}{n(t = 60\,\text{s})}}. \tag{6.24}$$

Here $n(t = 60\,\mathrm{s})$ indicates the number of steps required for $60\,\mathrm{s}$ of simulated time. It should be noted that ΔU_n does not necessarily correspond to the actual behavior of the power supplies used in the experiment but is rather only a convenient tool to implement dynamical frequency fluctuations within one simulation run.

6.2   Practical aspects and computation time

The simulations are performed by employing a combination of the programming languages `R` and `C++`. A main `R`-script is employed for the initial preparation such as setting the simulation parameters. Since typical time spans of sympathetic cooling simulations are 30–$60\,\mathrm{s}$ and the time steps are $\Delta t = 1$–$5\,\mathrm{ns}$, these settings imply about 10^{10} simulation steps, each with several dozens of operations. In light of these large number of steps, even with modern computational power it is crucial to optimize the computing time. Concerning the overall concept, the most important aspect in this regard is that the calculation-intensive part is outsourced to a compiled `C++` program via the `Rcpp`-package [101]. The run time of the `C++`-code is optimized in several ways. For example, it is compiled with the `gcc -O3` compiler flag that turns on all possible optimization flags [102]. Furthermore, the contribution of each code part to the overall run time is measured via `clock_t`-statements. This has lead to some unexpected and unconventional code modifications. To give one example, the possibility of subjecting the particles to radiofrequency excitations has been implemented. In case they are not used, the rf amplitude is simply set to zero. However, the $\sin(\omega_\mathrm{RF}t)$-statement remains and is nevertheless executed despite the amplitude being zero. Since the sinus as a high-order polynomial is a computationally expensive function to calculate, each code line containing an unused $\sin(\omega_\mathrm{RF}t)$ increases the overall computation time by about $1/3$ compared to the bare particle-resonator simulation. This issue is easily resolved by simply encapsulating each $\sin(\omega_\mathrm{RF}t)$-line with a conditional statement that the amplitude is greater than zero, i.e. `if(A_RF > 0){...}`. The compiler then recognizes that the amplitude is 0 over the whole execution time and disregards the sin()-calculation.

In addition, the simulations are fully parallelized. The main R script can call several instances of the `C++` program with different parameters via the `doParallel`- and `foreach`-package [103, 104]. This allows threads up to the number of virtual cores to run in parallel, greatly reducing the overall computation time when scanning one or several different parameters. While in principle available, these optimizations make the use of a high-performance computer obsolete. All simulations presented in this thesis are performed on a slightly upgraded office PC with $64\,\mathrm{GB}$ RAM and an AMD Ryzen 7 3700X processor with 8 real and 16 virtual cores. With these optimizations incorporated, a simulation with 1×10^{10} steps takes about $15\,\mathrm{min}$ per oscillator mode. For example, a $60\,\mathrm{s}$ simulation of the axial mode of the proton, the axial mode of one beryllium ion, and the resonator with a commonly used time step of $4\,\mathrm{ns}$ requires only a bit more than one hour of computation time. Due to the parallelization, within this one hour 15 different parameter sets can be simulated[5].

After the `C++`-program has finished the numerical integration, the previously specified time evolution data of for example the proton, the beryllium ion(s) and the resonator is returned to the main `R`-program. Finally, the energies and discrete Fast Fourier transforms (FFTs) of the oscillators are calculated and saved. Notably, the sample rate of the time evolution data must be reduced compared to the one given by the time step Δt, because otherwise the available memory is not sufficient. For example, assuming a scan with 15 parallel instances, seven columns of the time evolution data (time and the two coordinates for each of the three oscillators), 1×10^{10} steps and 8 byte per cell (`double` precision), a RAM of $560\,\mathrm{GB}$

---

[5]One of the 16 virtual cores is not used for the simulations so that the computer is still usable.
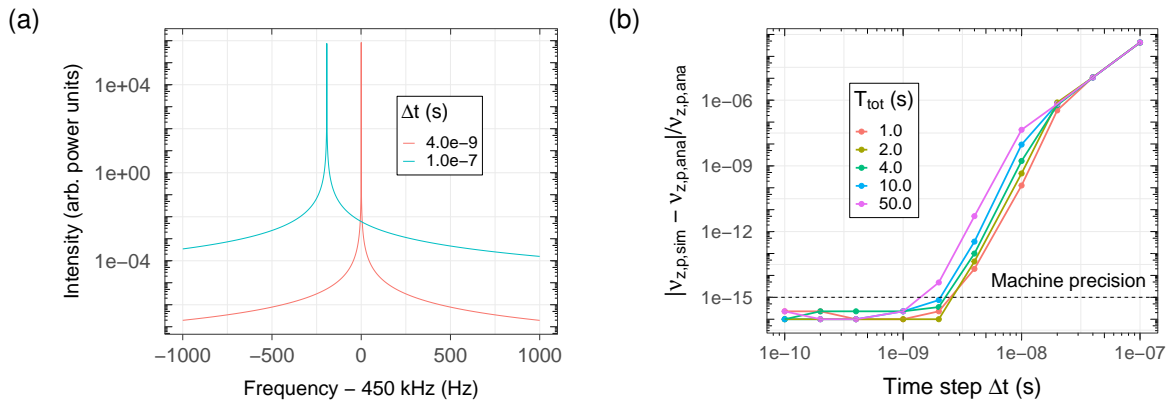
Figure 6.2:   (a) Exemplary axial frequency shift of a simulated single proton due to the time step. For $\Delta t = 1.0 \times 10^{-7}$ s a significant deviation to the analytical value of $450\,\text{kHz}$ is observed. However, this frequency shift decreases very strongly with smaller time steps, as shown in terms of a relative axial frequency shift between simulation and analytical calculation in (b). A slight non-linear phase accumulation error is observed, however, it can be easily compensated with a sufficiently small time step. At 1×10^{-15} the 15-digit `double` precision is reached so that the difference cannot be resolved anymore.

would be required. However, saving only e.g. every 200th data point relaxes this condition significantly. If the resulting effective sampling rate is at least twice above the largest oscillator frequency, all oscillator frequencies can be calculated nonetheless. Of course other solutions such as the calculation of intermediate FFTs and a subsequent averaging are conceivable. However, this was not necessary for the simulation studies presented in this thesis.

6.3   Numerical precision

Before employing the simulations for practical studies, it must be ensured that the finite numerical precision does not negatively affect the results. Thus, in this subchapter the performance of the simulations with respect to particle frequencies and energies is investigated.

In general, the time step Δt must be large enough such that the mode with the highest frequency is sampled at least twice per oscillation period. Otherwise, the Nyquist-Shannon sampling theorem would not be fulfilled and the mode frequency becomes a complex number, leading to an exponentially growing amplitude. The numerical error of the integrator can in principle be calculated, however, due to the 8 coefficients the derivation is long and cumbersome. Instead, the performance is assessed based on a result-oriented approach, i.e. to simulate the ideal Penning trap and compare simulation results with analytical solutions.
The following data assumes a proton with axial frequency $\nu_z = 450\,\text{kHz}$ and cyclotron frequency $\nu_+ = 27.4\,\text{MHz}$. Note that omitted significant digits are exactly zero. The simulation of the resonator and common endcap capacitance is turned off, so that the particle is a perfect harmonic oscillator in axial direction. Since in the simulations direct access to the proton's phase space is available, the FFT can be directly calculated based on the time evolution of the position or velocity. The simulated frequency $\nu_{z/+,\text{p,sim}}$ is determined by calculating the weighted mean of the resulting FFT spectrum. An example for the largest time step $\Delta t = 1 \times 10^{-7}$ s and the time step $\Delta t = 4 \times 10^{-9}$ s that is commonly used in later studies is shown in figure 6.2(a). It is apparent that the simulation close to

70

Figure 6.3: Relative cyclotron frequency deviation of a simulated single proton. The analytical value for the cyclotron frequency is $\nu_{+,\mathrm{p,ana}} =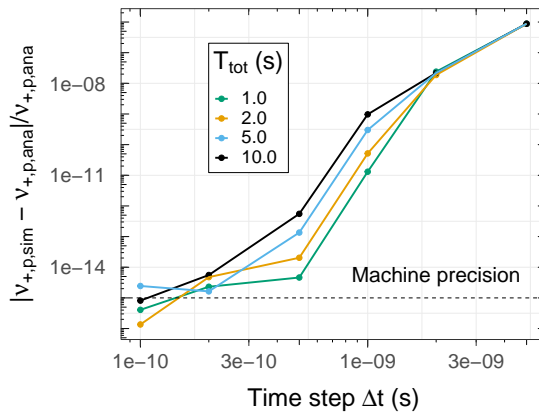 27.4\,\mathrm{MHz}$. At 1×10^{-15} the 15-digit `double` precision is reached so that the difference cannot be resolved anymore.

the largest possible time step yields a frequency that is about $200\,\mathrm{Hz}$ smaller than the analytical one. This effect is investigated for different time steps and longer total integration times $T_{\mathrm{tot}} = N\Delta t$, where N is the number of steps, with results plotted in figure 6.2(b). The strong scaling where one order of magnitude smaller time step yields about six orders of magnitude more accurate frequencies is owed to the high order of the integrator. The sampling rate and total integration time were chosen such that the discrete frequencies in the FFT include the analytical oscillator frequency exactly and the other frequency points are symmetric around it. Otherwise, the determination of the simulated axial frequencies would be limited by the Fourier width given by $1/T_{\mathrm{tot}}$. For time steps below $\Delta t \leq 2 \times 10^{-9}\,\mathrm{s}$ the relative frequency deviation is below the standard resolution of the `double` datatype with 15 significant digits and hence cannot be resolved. The observation that the relative frequency deviation rises with total integration time can be attributed to a small nonlinear phase error accumulation. However, even for the longest integration time of $50\,\mathrm{s}$, the relative deviation is smaller than 1×10^{-11} for the time step of $4 \times 10^{-9}\,\mathrm{s}$, which is used for the image-current coupling studies.

The same procedure can be carried out for the cyclotron motion of the proton with results shown in figure 6.3. Due to the higher frequency of $27.4\,\mathrm{MHz}$, the relative deviations are larger for a given time step. Nevertheless, for time steps of $\Delta t = 1 \times 10^{-10}\,\mathrm{s}$ the `double` machine precision limit can be reached as well. Again, a nonlinear phase error accumulation occurs. Note that $T_{\mathrm{tot}} \leq 10\,\mathrm{s}$ is the limit imposed by the available RAM of the computer if the frequency is determined via the entire phase space evolution. However, in section 6.7 total integration times of up to $60\,\mathrm{s}$ will be used in the context of phase sensitive simulations, where the storage of only one axial period is necessary and the cyclotron frequency is nevertheless determined to $\approx 1 \times 10^{-12}$ relative precision.

Besides frequencies, the second quantity of interest is the energy of the involved oscillators. In fact, the symplectic integrator was specifically chosen due to its energy-conserving properties. Although other algorithms such as the fourth-order Runge-Kutta (RK4) method might have a significantly better time-step error, the particle amplitudes are not bounded and grow exponentially very quickly with these schemes. Energy conservation over long integration times is absolutely essential for sympathetic cooling studies.
The energy conservation is studied by simulating all three modes of a single proton again, but this time also coupled resonantly to an axial detector. The respective mode energies are calculated with equations (2.14) - (2.16). The energy evolution over one second is shown in figure 6.4(a). A time step of $\Delta t = 1 \times 10^{-10}\,\mathrm{s}$ was used. The parallel resistance
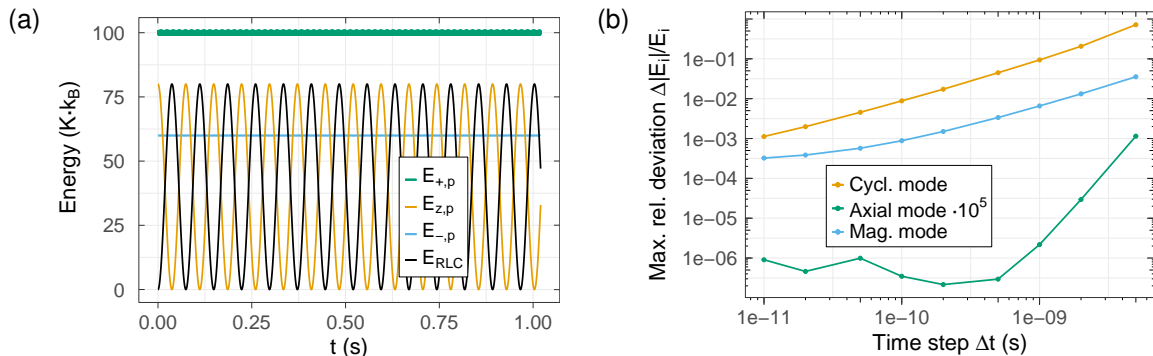
Figure 6.4: Demonstration of energy conservation based on all three modes of a single proton. An example where the proton is additionally coupled to a noiseless resonator is given in (a). The maximum relative energy deviations are shown as a function of time step in (b). The cyclotron energy exhibits the largest deviation since it is the mode with highest frequency. However, an essential property of the symplectic integrator is that energy deviation only scales with the time step Δt and not with the number of steps.

R_{RLC} of the resonator was set to infinity and its noise temperature to 0 in order to not disturb the energy conservation. The proton periodically exchanges axial energy with the resonator, where the rate is determined by its dip width. In contrast, the magnetron and cyclotron energy are constant over time. All mode energies are slightly modulated due to the step error, with the cyclotron energy exhibiting the strongest modulation since it has the largest frequency. However, the important feature is that the modulation scales only with Δt and not with $N \cdot \Delta t$, i.e. it the energy is bounded by the time step and constant over arbitrary integration times. Note that integration times of up to $150\,\mathrm{s}$ are employed in the context of figure 6.10 in section 6.5.1, demonstrating energy conservation over an additional two orders of magnitude.

The maximal relative energy deviation is plotted as a function of time step size in figure 6.4(b). For visibility purposes the energy deviations of the axial mode are scaled up by a factor of 1×10^5. Since the radial energies are calculated via the radial coordinates $x, y, \dot{x}, \dot{y}$ and the two radial modes are coupled in this regard, the energy deviation of the magnetron mode stems from that of the cyclotron mode. Nevertheless, about one percent maximal energy deviation for a time step of $1 \times 10^{-10}\,\mathrm{s}$ is definitely acceptable for the studies in this thesis and does not pose any issue.

In summary, in this section it was demonstrated that the simulations can reproduce the mode frequencies and conserve the mode energies. With this crucial prerequisite fulfilled, the next five subsections will deal with various applications of the simulations.

6.4   Application I: Verification of previous experimental data of image-current coupling

I explicitly highlight again (see section 3.10 for the initial statement) that about 80% of this section has been published in ref. [28] already with me as the lead and first author. Small modifications to the text and figures have been made to ensure consistency. Figure 6.6 and the corresponding text passages have been added, all other content has been copied mostly verbatim.

In this subchapter it will be demonstrated that the simulation results agree well with theory and experimental data, in particular those published in ref. [27]. Note that the experimental data referred to herein was recorded with a former version of the trap stack,
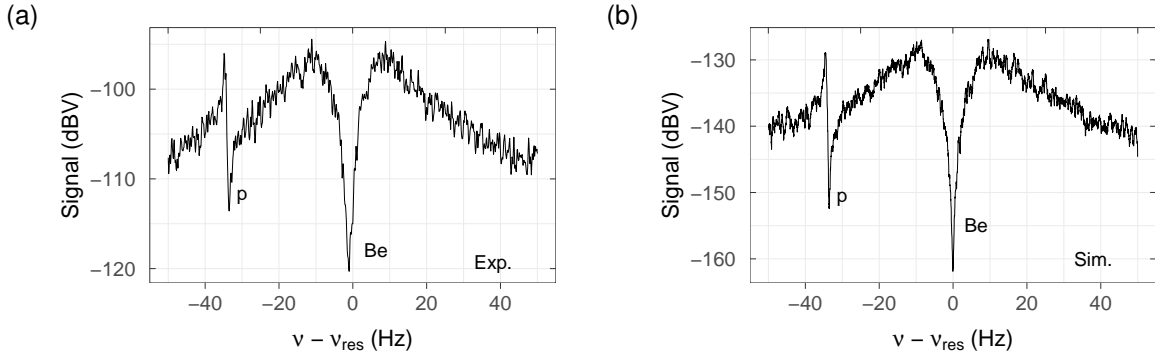
Figure 6.5:   Example FFT spectra of the voltage drop across the RLC circuit. An experimental spectrum is shown in (a) and a simulated one with approximately matched parameters in (b). The broad peak is the resonance of the RLC circuit and the two dips stem from a proton and several ^{9}Be$^+$ ions stored in independent traps, but coupled to the same resonator. The proton is detuned from the detector by about -35 Hz, leading to a dispersive dip. The dip widths are defined by the trap size, the number of ions in the trap and the ion masses [33].

where the PT and ST shared a common resonator, see section 3.2.

The ^{9}Be$^+$ ions are simulated individually and no additional heating effects besides the one stemming from the resonator are considered [56]. Figure 6.5 shows an FFT spectrum recorded with a common resonator involving the detector resonance, a proton in the PT detuned by -35 Hz from the detector's resonance frequency ν_{RLC} and several ^{9}Be$^+$ ions with $\nu_{z,\mathrm{Be}} = \nu_{\mathrm{RLC}}$ in the ST. Compared to the simulated spectrum in figure 6.5(b), the absolute signal level of the experimental spectrum in figure 6.5(a) is boosted by several amplifier stages. The dip widths of the simulated dip spectra match with equation (2.42). Similarly, the simulated noise resonance has the same FWHM as expected from theory. Next, since the resonator is a noisy thermal bath, the particle energies follow a Boltzmann distribution with the mean temperature defined by the resonator. An excerpt of the energy evolution of a single proton and a single beryllium ion confined in different traps but coupled resonantly to a resonator with 10 K temperature is shown in figure 6.6(a). Since the particle dip widths are about 2 Hz and the width of the noise resonance about 30 Hz, the resonator samples its Boltzmann distribution significantly faster. It is confirmed that the resonator energy fluctuations correctly reproduce a Boltzmann distribution with the temperature T_{RLC}, which is a free input parameter in the simulations. The same holds true for a single particle coupled to the resonator. Regarding laser cooling, the theoretical Doppler limit of $T_D \approx \frac{\hbar\Gamma}{2k_B} = 0.47$ mK as minimal temperature of the ^{9}Be$^+$ ions is reproduced, as shown in figure 6.6(b). The data was generated with a laser intensity of 10 % of the saturation intensity. If only one laser beam is used, as it is done in our experiment, the corresponding heating rate is reduced and slightly lower temperatures can be achieved. Furthermore, the scattering rate of photons γ_s for a single ^{9}Be$^+$ ion artificially held at a constant velocity matches the theoretical one [66]:

$$\gamma_s = \frac{I_{\mathrm{laser}}}{I_{\mathrm{sat}}} \frac{\Gamma/2}{1 + \frac{I_{\mathrm{laser}}}{I_{\mathrm{sat}}} + 4\left(\frac{2\pi\delta_{\mathrm{L}} + k_{\mathrm{L}}\dot{z}_{\mathrm{Be}}}{\Gamma}\right)^2}. \tag{6.25}$$

While the previously mentioned properties must be met for each oscillator individually and are straightforward to check, the coupling between them, especially between the proton and the ^{9}Be$^+$ ions, is more subtle. In order to reach our goal of ≈ 10 mK axial proton temperature, it is crucial to understand the coupling mechanism in detail. In the following, the experimental data of ref. [27] will be compared with FFT spectra of simulation data for three different temperature regions. Additionally, since the simulations provide access
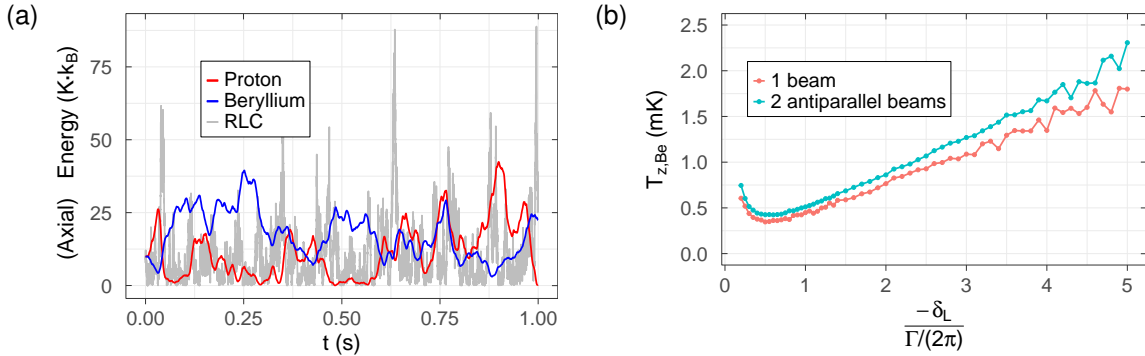
Figure 6.6: In (a) the simulated energy evolution of a single proton, a single beryllium ion, and the RLC circuit (resonator) is shown. All oscillators sample a Boltzmann distribution with the same temperature, but since the resonator has a larger width, it samples the Boltzmann distribution faster. The simulated axial temperature of a single beryllium subjected to a laser is shown in (b). The Doppler limit of about $0.47\,\mathrm{mK}$, which assumes two antiparallel beams, is reproduced by the simulations. A slightly lower temperature is achieved for only one beam, which is the setup corresponding to our experiment.

to the time domain data, it will be demonstrated that our experimental signature is truly caused by a temperature manipulation.

Ref. [27] employed the coupling scheme with a common RLC resonator. First, the coupling between the proton and $^9\mathrm{Be}^+$ ions was demonstrated above the resonator temperature by bringing the proton into resonance with excited beryllium ions. Therefore, the first temperature scale at which the simulations are compared to the experiment is at particle temperatures above the resonator temperature, depicted in figure 6.7. Here, a single proton and a cloud of 10 $^9\mathrm{Be}^+$ ions is simulated. The beryllium ions are excited by a parametric drive with frequency $2\nu_{\mathrm{z,Be}}$, which is implemented as an additional monopolar force $F_{\mathrm{z,ext}}(t) = F_{0,\mathrm{ext}} \cos(4\pi\nu_{\mathrm{z,Be}}t)$ in equation (6.15). In the experiment, special care was taken to ensure that the proton was not directly affected by the heating drive but only via the coupling to the $^9\mathrm{Be}^+$ ions. Since the axial frequencies of both particles are matched, not only the $^9\mathrm{Be}^+$ ions but also the proton significantly gains energy, demonstrating resonator-mediated energy exchange between the particles. Since the dip widths follow the hierarchy $\Delta\nu_{\mathrm{1,p}} < \Delta\nu_{\mathrm{1,Be}} < \Delta\nu_0$, the proton reaches a temperature higher than the one of the resonator. This results in a sharp peak above the resonator signal in the FFT spectrum in both the experimental and simulation FFTs, see figure 6.7(a) and (b), respectively. The slight asymmetry in the experimental FFT spectrum stems from a small anharmonic component of the axial potential in the proton trap. Since this is a well-understood effect [27, 41], such an anharmonicity was included in the simulations as well to reproduce the experimental signal. The time domain data of the simulations are depicted in figure 6.7(c). Here, the heating drive is switched on at $t = 10\,\mathrm{s}$. Before that, the energies of all three oscillators perform random walks through a Boltzmann distribution with the same temperature. With the parametric drive switched on, both the proton and $^9\mathrm{Be}^+$ ions gain energy equivalent to several hundred Kelvin. The average energy per ion is plotted for the beryllium cloud.

Second, the coupling at the equilibrium temperature of the resonator was demonstrated. To this end, the characteristic response of the coupled three-oscillator system is recorded, shown in figure 6.8. A single proton and a single $^9\mathrm{Be}^+$ ion is employed in both experiment and simulation. The axial frequencies of both particles are detuned $130\,\mathrm{Hz}$ from the resonator eigenfrequency. The beryllium frequency is then swept over the proton frequency and the signal power of the corresponding frequency spectra is displayed as colour-coded

74

columns in a heat map. Both the experimental and simulated data in figure 6.8(a) and (b) exhibit the characteristic response of a coupled three-oscillator system. In addition, the energy exchange between the proton, the $^9\text{Be}^+$ ion and the resonator at 130 Hz detuning is plotted in the time domain for the simulated data in figure 6.8(c). To emphasize the coupling between the proton and $^9\text{Be}^+$ ions, noise and dissipation were turned off by setting $R = \infty$ and $T_{\text{RLC}} = 0$ for this plot. Since the resonator FWHM $\Delta\nu_0$ is $\approx 30\,\text{Hz}$, the resonator is only weakly excited by the particles. The exact behavior of the energy exchange in figure 6.8(c) strongly depends on the initial relative particle phase.

Last, on-resonance common-resonator cooling between a single proton and 50 laser-cooled $^9\text{Be}^+$ ions is established. The frequency domain data in both experiment and simulation, figure 6.9(a) and figure 6.9(b) respectively, show a broad dip with reduced signal-to-noise and a superimposed narrow dip below. The broad dip corresponds to the beryllium cloud which, due to the laser cooling, cannot fully compensate the resonator noise current and hence exhibits a reduced SNR. The narrow dip corresponds to the proton, which is coupled to both the resonator and the $^9\text{Be}^+$ cloud. In the time-domain plot, figure 6.9(c), both particles have an initial energy of $10\,\text{K} \cdot k_B$. After turning on the laser at $t = 7.5\,\text{s}$, not only the beryllium ions but also the proton is significantly cooled within a few seconds. This is exactly the desired effect and this specific cooling scheme will be more thoroughly investigated by simulations in section 6.5.2 and by experiment in section 9.

In this section, it was demonstrated that the simulations are able to unambiguously reproduce the observed experimental signatures and match theory. By giving access to the time domain data, the results provide another layer of understanding. The simulated laser cooling of beryllium ions matches the theoretical expectations down to the Doppler limit. This proves that the simulations are a practical and credible tool to investigate cooling schemes that achieve proton temperatures in the mK-regime.
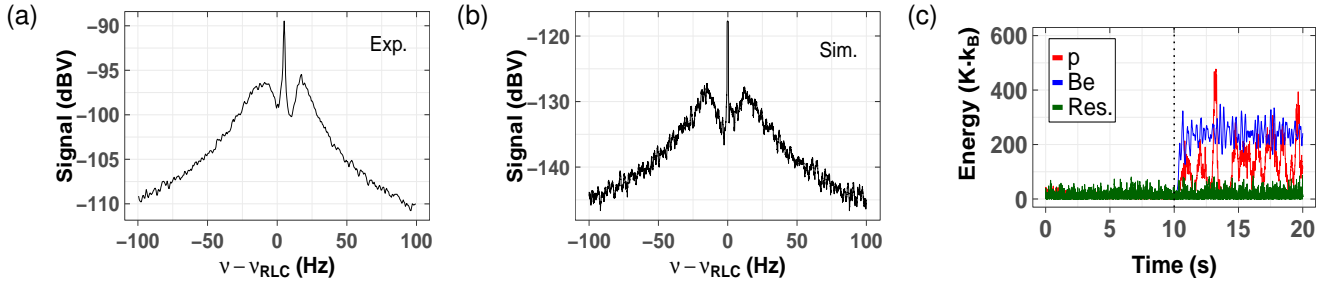
Figure 6.7: Comparison between experiment and simulation for $T_{z,p} \gg T_{RLC}$. The $^9Be^+$ cloud is heated by a parametric $2\nu_z$-drive. The proton is located in a different trap and is heated only due to the coupling to the $^9Be^+$ ions, creating the narrow peak signal in the FFT spectrum. (a) and (b) show the FFT spectrum of the experiment and simulation, respectively. The simulated effect of switching on the heating drive at $t = 10\,s$ (dashed line) is demonstrated in (c). The energy per ion is depicted for the beryllium cloud. Figures from [28].
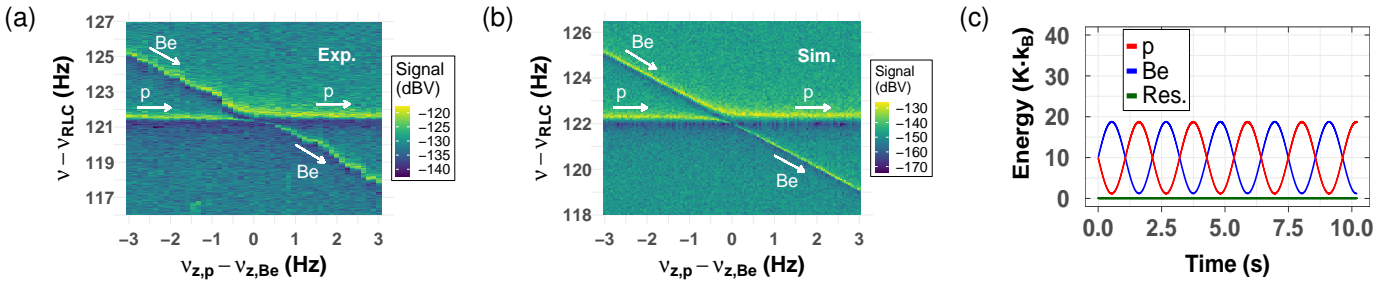
Figure 6.8: The coupling between the proton and $^9Be^+$ is demonstrated at $T_{z,p} = T_{RLC}$ by sweeping $\nu_{z,Be}$ over $\nu_{z,p}$. The experiment data in (a) and simulation data in (b) show the characteristic response of a coupled three-oscillator system. In (c) simulated time domain data for the simplified case with no resonator noise are shown. Figures from [28].
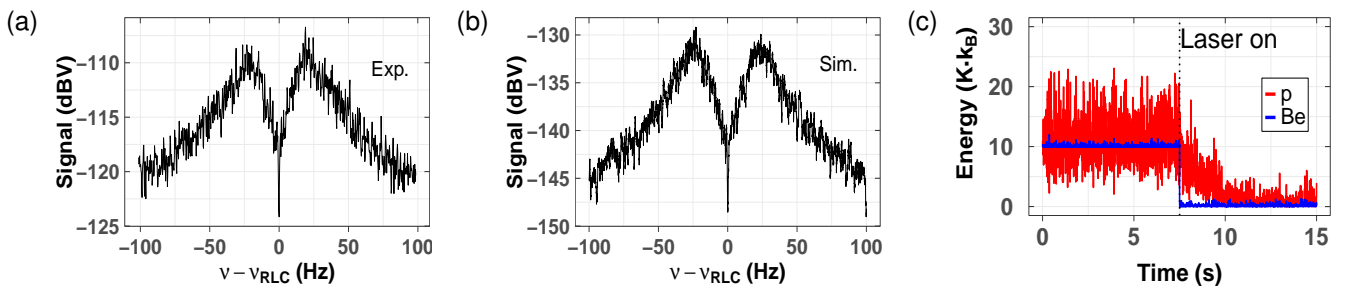
Figure 6.9: Comparison between experiment and simulation for $T_{z,p} < T_{RLC}$. Both the experiment data in (a) and the simulation data in (b) show a common-resonator FFT with a laser-cooled beryllium cloud (broad dip with reduced signal strength) superimposed by a single proton (narrow dip). In (c) the cooling laser is switched on at $t = 7.5\,s$, making the cooling effect on the proton visible. The energy per ion is depicted for the beryllium cloud. Figures from [28].

6.5   Application II: Investigation of the performance of different sympathetic cooling schemes

I explicitly highlight again (see section 3.10 for the initial statement) that this section has been published in ref. [28] already with me as the first and lead author. Figures 6.14 and 6.15 have been added for this thesis with the corresponding text passages. The first paragraph in this chapter was expanded to provide more context on the impact of the simulations. Apart from small modifications to the text and figures, all other content has been copied verbatim.

In this subchapter the three coupling scenarios whose experimental setups were described in section 3.10, will be investigated, namely common-endcap coupling, resonant coupling via a common RLC circuit, and off-resonant coupling via a common RLC circuit. As mentioned previously already, the experimental setup is assumed to be the old one with which the proof-of-principle measurements in refs. [26, 27] were conducted, including the ST as discontinued trap. Notably, as one the main methodical subchapters of this thesis, the simulation work presented herein will be accompanied by some purely theoretical work as well. These combined studies provide crucial insight in the fundamental experimental feasibility of the different schemes. Furthermore, they postulate how the considerable amount of various experimental parameters should be adjusted to achieve optimal cooling. In fact, the previous best-ever temperature measurement of a sympathetically cooled proton of $2.6(2.5)\,\mathrm{K}$ [27] was beaten on the very first try and was subsequently improved by a factor of 16–18 within a time span of only a few weeks, see section 9. This accomplishment was only achievable due to the strong foundation the preceding simulation work has laid. As a result, the simulations have already saved valuable experimental time and will continue to govern and support the experimental effort in the future.

The beryllium ions are simulated individually in section 6.5.2 and effective clouds otherwise since only in section 6.5.2 absolute laser intensities are of interest. The phase initialization of the particle modes is randomized and has no influence on the coupling schemes. If not explicitly stated otherwise, the following simulation parameters for the resonator are used: $R = 236 \times 10^6\,\Omega$, $L = 3\,\mathrm{mH}$, $C_{\mathrm{RLC}} = 21.4\,\mathrm{pF}$, yielding a resonator Q-factor of $20\,000$ and a resonance frequency of $626.9\,\mathrm{kHz}$. Regarding the trap parameters, the product $C_2 U_0$ is adjusted such that the particle oscillates at the desired frequency. The effective electrode distances are $D_{\mathrm{RLC,p}} = 10.0\,\mathrm{mm}$ for the PT, $D_{\mathrm{RLC,Be}} = 5.7\,\mathrm{mm}$ for the ST and $D_{\mathrm{com,p}} = D_{\mathrm{com,Be}} = 3.2\,\mathrm{mm}$ for the CT and BT (compare table 1) [74]. The common endcap capacitance is $C_{\mathrm{com}} = 5.5\,\mathrm{pF}$ for the common-endcap coupling in section 6.5.1 and $C_{\mathrm{com}} \to \infty$ for the resonator coupling in section 6.5.2 and 6.5.3. Additionally, it is assumed that the resonator has an effective noise temperature of $10\,\mathrm{K}$, accounting for the fundamental Johnson-Nyquist noise at $4.2\,\mathrm{K}$ (the physical temperature of the experiment) and the input noise of our cryogenic amplifiers [50, 105]. 80 $^9\mathrm{Be}^+$ ions are used as this is approximately the largest number of $^9\mathrm{Be}^+$ ions that were used in ref. [27]. Finally, only the axial modes of the particles were simulated with a time step of $\Delta t = 4\,\mathrm{ns}$ for all simulations in this subsection.

6.5.1   Common-endcap coupling

In order to simulate the common-endcap coupling in our trap system, the resonator eigenfrequency is detuned by $200\,\mathrm{kHz}$ so that the energy exchange is dominated by the common-endcap coupling. Since the resonator terms in equation (6.2) - (6.5) are then negligible for the ion-ion-coupling with no laser applied, the system of coupled differential equations can be solved analytically. In order to derive a general solution, more than one parti-
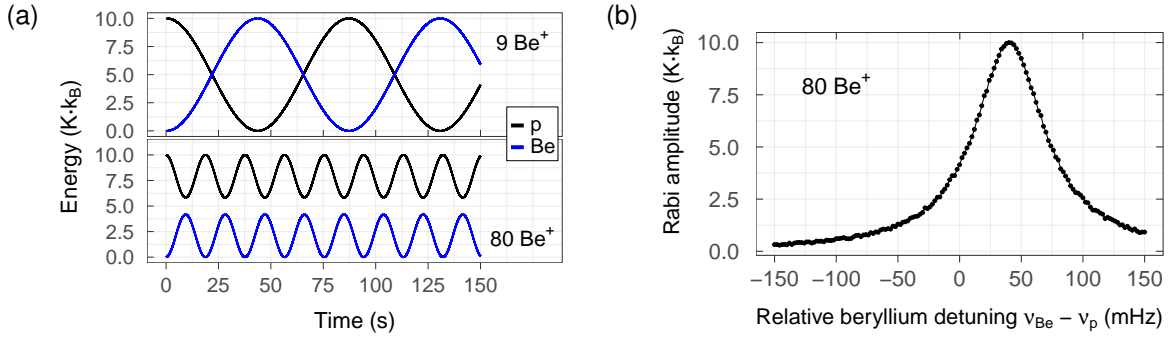
Figure 6.10: (a) Simulated energy of a single proton capacitively coupled to a cloud of $^9\text{Be}^+$ ions. In the case of $D_{\text{com,p}} = D_{\text{com,Be}}$ the energy is exchanged completely only for 9 beryllium ions (upper plot). In contrast, for 80 beryllium ions the energy exchange is incomplete. (b) Energy exchange amplitude as a function of relative particle detuning for 80 $^9\text{Be}^+$ ions. The maximum Rabi oscillation amplitude is restored by detuning the beryllium ions relative to the proton by $+40\,\text{mHz}$.

cle in each cloud is allowed by setting $q_{\text{p}} \to N_{\text{p}}\, q_{\text{p}}$, $m_{\text{p}} \to N_{\text{p}}\, m_{\text{p}}$, $q_{\text{Be}} \to N_{\text{Be}}\, q_{\text{Be}}$ and $m_{\text{Be}} \to N_{\text{Be}}\, m_{\text{Be}}$ in equation (6.4, 6.5), where $N_{\text{p,Be}}$ is the number of protons and beryllium ions, respectively. For the sake of a compact notation, the abbreviations $D_{\text{com,p}} \equiv D_{\text{p}}$ and $D_{\text{com,Be}} \equiv D_{\text{Be}}$ are used in the following calculations. Furthermore, it is assumed that the particle eigenfrequencies are exactly matched, i.e. $\frac{2q_{\text{p}}C_{2,\text{p}}U_{0,\text{p}}}{m_{\text{p}}} = \frac{2q_{\text{Be}}C_{2,\text{Be}}U_{0,\text{Be}}}{m_{\text{Be}}} = \omega_1^2$. Solving the coupled differential equation for the proton motion yields

$$z_{\text{p}}(t) = c_1 e^{i\lambda_1 t} + c_2 e^{i\lambda_2 t} + c_3 e^{i\lambda_3 t} + c_4 e^{i\lambda_4 t} \tag{6.26}$$

where $c_{1,2,3,4}$ are free coefficients determined by the initial conditions and $\lambda_{1,2,3,4}$ are the corresponding eigenfrequencies:

$$\lambda_{1,2} = \pm\,\omega_1 \tag{6.27}$$

$$\lambda_{3,4} = \pm\sqrt{\omega_1^2 - \frac{m_{\text{p}}D_{\text{p}}^2 N_{\text{Be}}q_{\text{Be}}^2 + m_{\text{Be}}D_{\text{Be}}^2 N_{\text{p}}q_{\text{p}}^2}{C_{\text{com}}D_{\text{p}}^2 D_{\text{Be}}^2 m_{\text{p}}m_{\text{Be}}}} \tag{6.28}$$

$$\approx \pm(\omega_1 - \Omega). \tag{6.29}$$

Here the abbreviation

$$\Omega = \frac{1}{2}\frac{m_{\text{p}}D_{\text{p}}^2 N_{\text{Be}}q_{\text{Be}}^2 + m_{\text{Be}}D_{\text{Be}}^2 N_{\text{p}}q_{\text{p}}^2}{\omega_1 C_{\text{com}}D_{\text{p}}^2 D_{\text{Be}}^2 m_{\text{p}}m_{\text{Be}}} \tag{6.30}$$

was introduced.

Assuming the initial conditions $z_{\text{p}} = z_0$, $\dot{z}_{\text{p}} = 0$, $z_{\text{Be}} = 0$ and $\dot{z}_{\text{Be}} = 0$, the temporal evolution of the energy of the proton is

$$E_{\text{p}}(t) = \frac{1}{2}\frac{m_{\text{p}}z_0^2}{(m_{\text{p}}D_{\text{p}}^2 N_{\text{Be}}q_{\text{Be}}^2 + m_{\text{Be}}D_{\text{Be}}^2 N_{\text{p}}q_{\text{p}}^2)^2}\Bigg(\,\omega_1^2\,\big[(m_{\text{p}}D_{\text{p}}^2 N_{\text{Be}}q_{\text{Be}}^2)^2 + \tag{6.31}$$

$$(m_{\text{Be}}D_{\text{Be}}^2 N_{\text{p}}q_{\text{p}}^2)^2 + 2m_{\text{p}}m_{\text{Be}}N_{\text{p}}N_{\text{Be}}q_{\text{p}}^2 q_{\text{Be}}^2 D_{\text{p}}^2 D_{\text{Be}}^2 \cos(\Omega t)\big] + \mathcal{O}(\Omega\omega)\Bigg).$$

Since $\Omega \ll \omega_1$, the terms with $\mathcal{O}(\Omega\omega)$ can be neglegted. From equation (6.31) $\frac{\Omega}{2\pi}$ can be identified as the Rabi frequency of the coupled proton-beryllium system. The difference between equation (6.30) and previously reported versions [25, 29] arises from the fact that
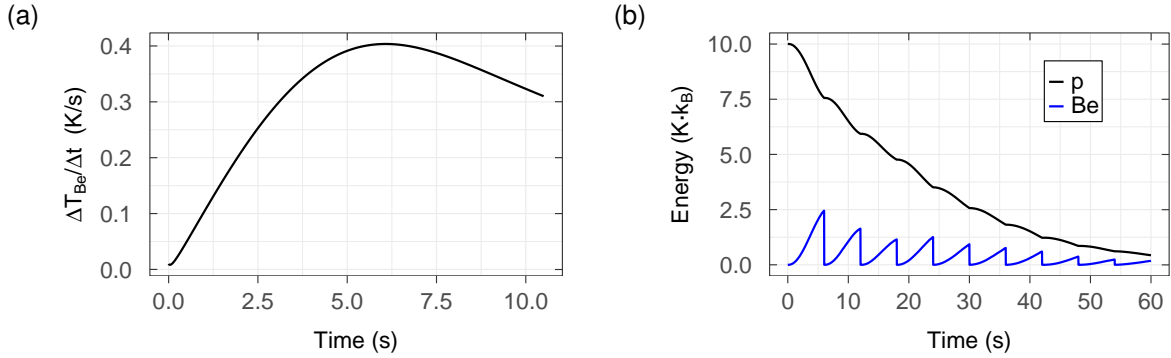
(a)

(b)

Figure 6.11: (a) Evolution of the simulated energy gain of the $^9\text{Be}^+$ cloud divided by the time after turning off the laser for the common-endcap coupling. The depicted data is an average temperature for initial axial frequency mismatches of $\Delta_{\text{unc}} = 100\,\text{mHz}$ and a dynamical stability of $\xi_{\text{stab}} = 1 \times 10^{-7}$ as defined in section 6.1.4. The maximum energy exchange rate is reached at $6.0\,\text{s}$ for $80\,\text{Be}^+$ ions, defining the optimal cycle time for the first laser pulse. (b) Representative example of the cooling process with a laser pulse applied every $6.0\,\text{s}$.

in this work, up to equation (6.29) no approximations were used. In order for the energy to be exchanged completely, i.e. $E_{\text{p}}(t = \pi/\Omega) = 0$, the condition

$$\frac{N_{\text{p}} q_{\text{p}}^2}{m_{\text{p}} D_{\text{p}}^2} \overset{!}{=} \frac{N_{\text{Be}} q_{\text{Be}}^2}{m_{\text{Be}} D_{\text{Be}}^2} \qquad (6.32)$$

must be satisfied. Inserting this condition into equation (6.30) reproduces the previously reported formula [25, 29] for the Rabi oscillation frequency. Equation (6.32) reflects the simultaneous conservation of energy and conservation of charge on the common-endcap capacitance within one Rabi cycle. Note that the studied system of coupled oscillators is symmetric in many other experiments and equation (6.32) is automatically fulfilled. However, it is important to emphasize that if the condition in equation (6.32) is not met, the energy is exchanged only partially and with a faster frequency. As demonstrated in the following, this has considerable implications for the realization of the cooling schemes in the experiment. Figure 6.10(a) shows an exemplary energy exchange between a single proton and 9 or 80 $^9\text{Be}^+$ ions, top and bottom plot, respectively. Since $D_{\text{p}} = D_{\text{Be}}$ and $m_{\text{Be}} \approx 9\,m_{\text{p}}$ in our case, the energy exchange is complete for 9 beryllium ions. While the Rabi frequency for 80 beryllium ions is higher, only a fraction of the proton's energy is exchanged. This would be a severe limitation of the common-endcap coupling technique as one would need to choose between a complete energy exchange ($N_{\text{Be}} = 9$) or a fast coupling time ($N_{\text{Be}} \gg 9$). However, the behavior of the Rabi oscillations when varying the number of beryllium ions is equivalent to introducing a small relative frequency detuning between the two species. Consequently, one can reverse the effect of using $N_{\text{Be}} \gg 9$ by introducing a small relative detuning. The analytical calculations are laborious, thus the numerical simulations are employed here. Figure 6.10(b) shows the Rabi oscillation amplitude (peak-to-peak) for 80 $^9\text{Be}^+$ ions as a function of relative particle detuning. While for an exact frequency matching only $\approx 4\,\text{K} \cdot k_B$ are exchanged per Rabi cycle, at $+40\,\text{mHz}$ relative detuning the full Rabi amplitude is recovered. In the case of nonzero detunings equation (6.30) does not hold true anymore. However, if the detuning is chosen such that the energy is exchanged completely, the previously reported $\Omega \propto \sqrt{N_{\text{Be}}}$ is preserved, i.e. $\Omega(40\,\text{mHz}, 80\,\text{Be}) = \sqrt{\frac{80}{9}}\Omega(0\,\text{mHz}, 9\,\text{Be})$. The parameters presented here yield $\Omega(0\,\text{mHz}, 80\,\text{Be})/(2\pi) = 53\,\text{mHz}$ and $\Omega(40\,\text{mHz}, 80\,\text{Be})/(2\pi) = 34\,\text{mHz}$. Although matching two species to a few ten mHz is experimentally challenging, it is crucial to account for this in the experimental realization of the coupling scheme as it impacts the cooling times and the achieved temperature limits.
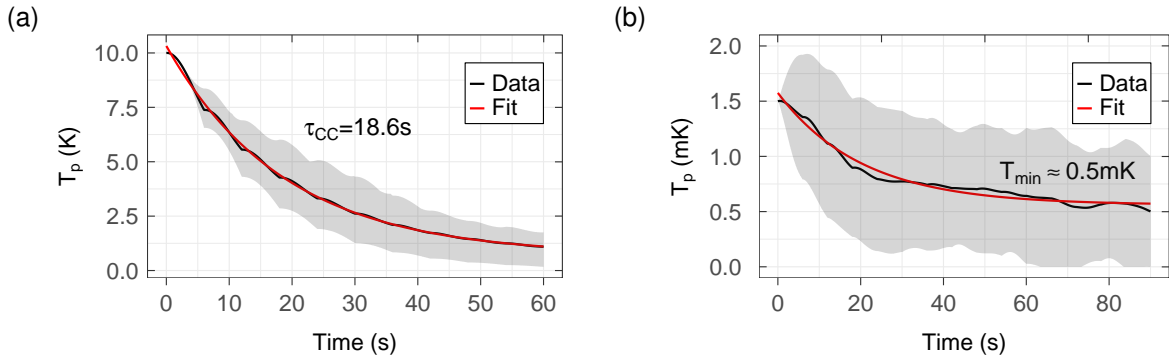
(a)

(b)

Figure 6.12: (a) Simulated proton energy over time when applying the chopped laser scheme for 80 $^9\mathrm{Be}^+$ ions, yielding a cooling time constant of $\tau_\mathrm{CC} = 18.6\,\mathrm{s}$. The depicted data is an average temperature for initial axial frequency mismatches of $\Delta_\mathrm{unc} = 100\,\mathrm{mHz}$ and a dynamical stability of $\xi_\mathrm{stab} = 1 \times 10^{-7}$ as defined in section 6.1.4. The gray band indicates one standard deviation. (b) Same as in (a), but with the proton initialized at 1.5 mK. Due to the 200 kHz-detuning from the resonator effectively no heating sources are present, such that the ultimate temperature limit is the Doppler temperature of the beryllium ions of $T_D \approx 0.5\,\mathrm{mK}$.

The initial proposals [24, 25] envisaged cooling close to the Doppler limit by coupling the target ion for exactly half a Rabi cycle (one π-pulse) to the subsequently laser-cooled $^9\mathrm{Be}^+$-cloud. However, figure 6.10(b) shows that a frequency mismatch of only $\approx 10\,\mathrm{mHz}$ limits the residual proton energy after one π-evolution to $\gtrsim 1\,\mathrm{K} \cdot k_B$, far higher than the 10 mK required for our experiment. As a result, in the following a cooling scheme is investigated that is based on repetitively turning on the cooling laser and performing several imperfect energy exchanges. Compared to continuous laser operation, chopping the laser achieves orders of magnitude faster cooling. The reason for this can be understood in the Rabi oscillation picture: In the continuous case the $^9\mathrm{Be}^+$ cloud is artificially held at its minimal temperature. The cooling rate for the proton is given by the local slope of the energy exchange curve, i.e. it vanishes to first order for continuously cooled $^9\mathrm{Be}^+$ ions [29].

To determine a realistic cooling time constant, the experimental frequency uncertainties are incorporated in this subsection twofold: First, an additional detuning $\delta\nu$ is added to the proton frequency due to non-ideal matching to the $^9\mathrm{Be}^+$ frequency. $\delta\nu$ is drawn uniformly from the interval $\delta\nu \in [-\Delta_\mathrm{unc}, +\Delta_\mathrm{unc}]$ with $\Delta_\mathrm{unc} = 100\,\mathrm{mHz}$ and randomly for every simulation. Second, a relative voltage stability as defined in section 6.1 of $\xi_\mathrm{stab} = 1 \times 10^{-7}$ is assumed for both the proton and beryllium trapping voltages independently. In a first step the ideal laser cycle time for the chopped laser scheme is determined. The $^9\mathrm{Be}^+$ ions are initialized at an energy of $1\,\mathrm{mK} \cdot k_B$ and the proton at an energy of $10\,\mathrm{K} \cdot k_B$. The average temperature gain of the beryllium cloud over time, $\Delta T_\mathrm{Be}/\Delta t$, is used as figure of merit, displayed in figure 6.11(a). By switching on the cooling laser at the time of maximum $\Delta T_\mathrm{Be}/\Delta t$, in this simulated case at 6.0 s, to first order the fastest cooling time constant is achieved. Note that more complex laser schemes with varying cycle times could potentially lead to an even better cooling performance, however, in this work the discussion will be limited to schemes with constant laser cycle times. The on-time of the laser is set to 2% of the laser cycle time. Figure 6.11(b) shows a representative cooling run with the cooling laser turned on every 6.0 s. Averaging several of such runs with the uncertainties described above allows to perform a least-square fit with an exponential function

$$T_\mathrm{p} = T_{p,0}\, e^{-t/\tau_\mathrm{CC}} + T_\mathrm{p,min} \tag{6.33}$$

and to extract a cooling time constant τ_CC as it is done in figure 6.12(a). A cooling time constant of $\tau_\mathrm{CC} = 18.6(1.4)\,\mathrm{s}$ is obtained for the simulated case with 80 $^9\mathrm{Be}^+$ ions. The
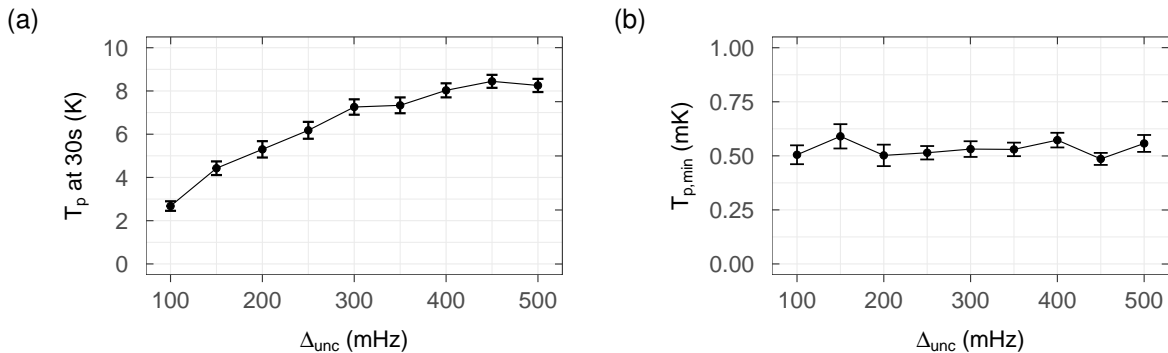
(a)

(b)

Figure 6.13: Simulation of the sensitivity of the common-endcap coupling approach to relative frequency matching uncertainties between the proton and 80 $^9\text{Be}^+$ ions. In (a) the proton temperature at 30 s after initialization as a measure of the cooling time is shown. In (b) the lower temperature limit as a function of Δ_{unc} is displayed for a proton initialized at $0.5\,\text{mK} \cdot k_B$. Due to the absence of heating effects in the common-endcap coupling scheme the lower temperature limit for the proton is not affected by a detuning and remains at the Doppler limit of $T_\text{D} \approx 0.5\,\text{mK}$.

uncertainty is estimated by fitting the single runs and calculating the standard deviation of the mean τ_{CC}.

In addition to the cooling time constant, the other parameter of interest is the lower temperature limit, determined by the equilibrium of the competing cooling and heating rate. In case of the common-endcap coupling, the heating by the resonator noise is strongly suppressed due to the resonator detuning of several hundred kHz. Additionally, other sources of heating are negligibly small [56]. The achievable lower limit is investigated by repeating the procedure for the cooling time constant, but initializing the proton at $1.5\,\text{mK}$, shown in figure 6.12(b). The cooling time constant is within uncertainty indistinguishable from the one with $10\,\text{K}$ initial proton temperature. More importantly, the lower temperature limit is dictated by the temperature of the $^9\text{Be}^+$ cloud, which itself is cooled to the Doppler limit of $T_\text{D} \approx 0.5\,\text{mK}$.

The last quantity of practical interest is the sensitivity of the cooling performance to relative axial frequency detunings between the proton and the $^9\text{Be}^+$ cloud. The cooling efficiency for a fixed relative detuning depends on the laser cycle time. In the worst case, even for a rather small relative detuning of $\approx 10\,\text{mHz}$ no cooling can occur if the laser cycle time is an integer multiple of the Rabi cycle. The relevant quantity in the experiment is the precision with which the particle frequencies can be matched. Hence the frequency matching precision Δ_{unc} as defined above is varied instead of introducing a fixed detuning. Furthermore, since for large detuning intervals fitting the temperature evolution with equation (6.33) becomes an erroneous measure of cooling effectiveness, the mean proton temperature at 30 s after initialization will be used instead. Figure 6.13(a) depicts the sensitivity of the proton temperature at 30 s as a function of the detuning uncertainty. The initial proton energy was $10\,\text{K} \cdot k_B$. The proton temperature at 30 s nearly doubles when increasing Δ_{unc} from $100\,\text{mHz}$ to $200\,\text{mHz}$, indicating that absolute detunings of $> 100\,\text{mHz}$ contribute little to the cooling process, which is a result of the comparably low Rabi frequency of $34\,\text{mHz}$. Figure 6.13(b) shows the simulated proton temperature after initializing the proton at $0.5\,\text{mK} \cdot k_B$ and letting it evolve for 30 s while applying the chopped laser to the $^9\text{Be}^+$ ions. Since for the common-endcap coupling the resonator is detuned, no heating process competes with the cooling process. As a result, the lower temperature limit is not affected and the proton temperature can still reach the Doppler limit of $T_\text{D} \approx 0.5\,\text{mK}$.

$$I_{\text{ind}} = 2\frac{q}{D}v_{\text{z}}$$

to resonator

(a)   (b)

$$E_{\text{sym}} = E_{\text{z}}^{(a)} + E_{\text{z}}^{(b)}$$
$$= 2E_{\text{z}}$$

$$E_{\text{asym}} = 0$$

to resonator $I_{\text{ind}} = 0$

(a)   (b)

$$E_{\text{sym}} = 0$$
$$E_{\text{asym}} = E_{\text{z}}^{(a)} + E_{\text{z}}^{(b)}$$
$$= 2E_{\text{z}}$$

Thermal equilibrium: $\langle E_{\text{sym}} \rangle = \langle E_{\text{asym}} \rangle$
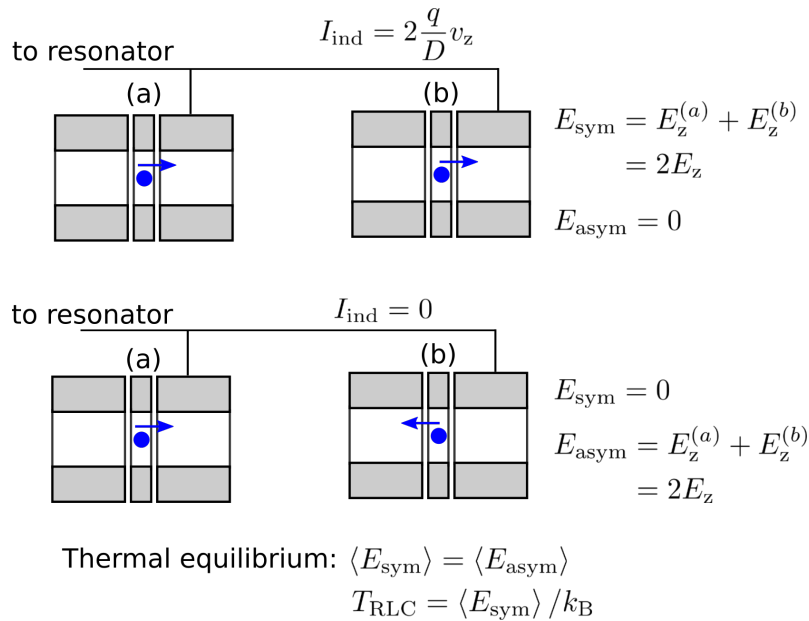$$T_{\text{RLC}} = \langle E_{\text{sym}} \rangle / k_{\text{B}}$$

Figure 6.14: Instructive example for the derivation of the temperature limit of the on-resonance sympathetic cooling scheme. Two identical ions with the same energies $E_{\text{z}}^{(a)} = E_{\text{z}}^{(b)} \equiv E_{\text{z}}$ are located in two identical traps (a) and (b) that are connected to the same resonator. In terms of coupling to the resonator, the motion of the ions can be described by a symmetric mode where both ions oscillate in phase or an antisymmetric mode where the phase of the ion's is shifted by π. The respective energies are E_{sym} and E_{asym}. Without external intervention the symmetric and antisymmetric mode have, on average, the same energy. However, only the symmetric mode thermalizes to the resonator temperature as for the antisymmetric mode the image currents of each ion have opposite sign and cancel each other.

6.5.2   Resonant coupling mediated by an RLC resonator

A sketch of the experimental setup for the resonant coupling scheme is shown in figure 3.12(b) and the experimental proof of principle was recently demonstrated in ref. [27]. This approach is the easiest to observe experimentally as the proton and the $^9\text{Be}^+$ ions are continuously being detected in resonance with the RLC resonator, which is the standard operation mode of our Penning-trap experiment.

In the case of resonant coupling with an RLC circuit, the resonator noise causes the energy exchange between the proton and $^9\text{Be}^+$ ions to be highly incoherent on a ms-timescale. As a result, a cooling scheme that relies on single π-pulses will not be able to consistently achieve the desired 10 mK.

As an introductory theoretical analysis, at first two ions are considered, depicted schematically in figure 6.14. The ions are of the same species and have the same energy. The traps are identical and connected to a common resonator. The motion of these two ions can be described by a symmetric and antisymmetric mode, where the individual oscillations are in phase or shifted by a phase of π, respectively. The individual image currents induced into the resonator interfere destructively for the antisymmetric mode. As a result, the resonator only couples to the symmetric mode and only this mode is thermalized to the detector temperature. However, in reality any non-zero frequency difference $\Delta\nu_{\text{z}}$ between the ions will transfer energy from the symmetric mode into the asymmetric mode.
From the perspective of the resonator, it is impossible to distinguish whether the two ions are in the same trap or in different but identical traps connected to the same resonator.

$$E_{\mathrm{sym}} = E_{\mathrm{z}}^{(a)} + E_{\mathrm{sym}}^{(b)}$$
$$= E_{\mathrm{z}}^{(a)} + E_{\mathrm{z}}^{(b1)} + E_{\mathrm{z}}^{(b2)}$$
$$= 3E_{\mathrm{z}}$$

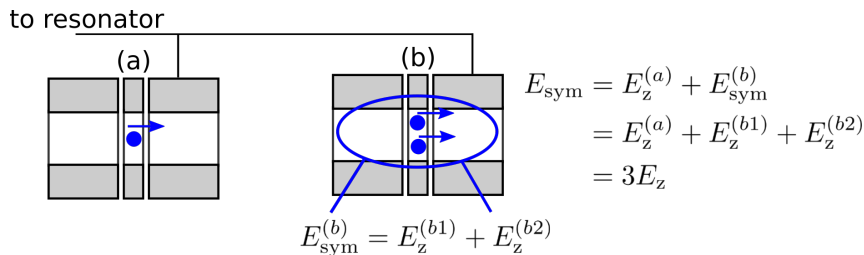$$E_{\mathrm{sym}}^{(b)} = E_{\mathrm{z}}^{(b1)} + E_{\mathrm{z}}^{(b2)}$$

Figure 6.15: Generalization of the two-ion case of figure 6.14 to arbitrary number of ions by induction: Assuming a second ion is added in trap (b) in phase and with the same energy $E_{\mathrm{z}}^{(b2)} = E_{\mathrm{z}}$, the two ions in trap (b) can be treated exactly as the two-ion case. The fact that both ions are in the same trap does not change the coupling to the resonator. Hence, both ions can be treated as one effective ion with energy symmetric mode energy $E_{\mathrm{sym}}^{(b)}$. The argumentation via induction also applies to the case of different ion species.

Consequently, the same concept can be applied in the very same manner to two identical ions in the same trap. Note this argument assumes vanishing Coulomb-interaction between the ions, which is, however, still valid due to the experimentally observed linear scaling of the dip width with the number of ions. This allows to generalize the argumentation to arbitrary number of ions via induction, as it is depicted in figure 6.15. The combined motion of the two ions in the same trap can be described in a basis symmetric and anti-symmetric relative to the single particle, thus reducing the setup to the two-particle case again. Different ion species or different trap parameters can be incorporated by assuming an elementary ion and constructing the desired ion (cloud) in terms of multiples of this elementary ion. Thus, the scaling of the relative energies is given by their dip width.
The experimental evidence of the aforementioned arguments is provided by the linear scaling of the dip width with the number of ions in the trap. This arises from substituting $q \to N \cdot q$ and $m \to N \cdot m$ in equation (2.42). However, this substitution is only valid for the symmetric mode of the ions.

The sympathetic cooling is achieved by a combination of three effects: First, the energy of the single ion in the upper case in figure 6.14 is given by $E_{\mathrm{z}} = E_{\mathrm{sym}}/2$. Second, the symmetric mode thermalizes to the resonator temperature, $T_{\mathrm{RLC}} = \langle E_{\mathrm{sym}} \rangle / k_{\mathrm{B}}$. Third, the energy in the antisymmetric mode can be transferred to the symmetric mode by subjecting one of the ions to an additional damping. In our experiment, the cooling laser constitutes this additional damping for the beryllium ions. The fact that only the symmetric mode is heated by the resonator and the damping of the $^9\mathrm{Be}^+$ ions by the laser continuously transfers energy between all modes implies that even a weak damping by the laser is sufficient to eventually cool all modes except the symmetric one down to the Doppler limit. In the case of negligible energy of the non-symmetric modes, the final proton temperature is determined by the proton's relative component of the symmetric mode temperature. The relative components are given by the relative dip widths, $\Delta\nu_{1,\mathrm{p}}$ and $\Delta\nu_{1,\mathrm{Be}}$, respectively:

$$T_{\mathrm{RLC}} = T_{\mathrm{p}} + T_{\mathrm{Be}} \tag{6.34}$$

$$T_{\mathrm{p}} = \frac{\Delta\nu_{1,\mathrm{p}}}{\Delta\nu_{1,\mathrm{Be}}} T_{\mathrm{Be}}. \tag{6.35}$$

These equations result in the $T_p \propto 1/N_{\mathrm{Be}}$-scaling initially proposed in ref. [24] and measured for the first time in ref. [27]:

$$T_{\mathrm{p}} = \frac{1}{1 + \frac{\Delta\nu_{1,\mathrm{Be}}}{\Delta\nu_{1,\mathrm{p}}}} T_{\mathrm{RLC}} \propto \frac{1}{N_{\mathrm{Be}}}. \tag{6.36}$$

In this form equation (6.36) is only true for weak laser intensities, i.e. if the damping rate of the $^9\mathrm{Be}^+$ ions due to the laser, γ_{L}, is much smaller than $\Delta\nu_{1,\mathrm{Be}}$. At higher laser intensities,

the beryllium cloud is decoupled from the resonator. This effect can be accounted for by a reduction of the effective dip width, expressed by the substitution $\Delta\nu_{1,\mathrm{Be}} \to \Delta\tilde{\nu}_{1,\mathrm{Be}} = k\,\Delta\nu_{1,\mathrm{Be}}$ with dimensionless scaling parameter $0 \le k \le 1$ in ref. [27]. As a final note of the initial theoretical analysis, although equation (6.36) had so far been predicted only by theory and simulations [28], it has been confirmed experimentally in the course of this thesis, including the prediction that only a weak damping by the laser is required. The corresponding measurements will be presented in section 9.

The simulation results show that, in contrast to the lower limit of the proton temperature, a higher laser intensity is beneficial for the cooling time constant as it increases the rate of energy dissipation. In order to study these relations quantitatively in terms of experimental parameters, the proton and a cloud of 80 continuously laser-cooled $^9\mathrm{Be}^+$ ions tuned on resonance with the detector are simulated. Figure 6.16 shows the cooling time constant τ_{RC} and the lower temperature limit $T_{\mathrm{p,min}}$ as a function of laser intensity for two exemplary laser detunings of $-20\,\mathrm{MHz}$ and $-200\,\mathrm{MHz}$, depicted in subfigures (a) and (b), respectively. The cooling time constant is determined by least-squares fits with equation (6.33) for an initial proton energy of $10\,\mathrm{K}\cdot k_B$. The lower temperature limit is determined by initializing the proton at $0\,\mathrm{K}\cdot k_B$ and averaging the proton energy after it has reached equilibrium.

While a much stronger laser intensity is required for $-200\,\mathrm{MHz}$ laser detuning, the general behavior of τ and $T_{\mathrm{p,min}}$ are the same: The cooling time constant drops with larger laser intensity as the $^9\mathrm{Be}^+$ ions are damped more strongly and reaches values down to a few hundred ms. However, at such high laser intensities the beryllium ions are decoupled too strongly from the resonator, leading to a suboptimal proton temperature limit. Instead, the proton temperature saturates in the region where $\gamma_{\mathrm{L}} \ll \Delta\nu_{1,\mathrm{Be}}$. The simulated values in the weak intensity limit agree well with the theoretical prediction of $T_{\mathrm{p,min}} = 350\,\mathrm{mK}$ by equation (6.36), indicated by the blue dashed line.

According to equation (2.42), the beryllium dip width can be increased not only by loading more beryllium ions, but also by reducing the effective electrode distance D_{RLC}. Since the cooling time constants are a function of both the laser intensity and $D_{\mathrm{RLC,Be}}$, the parameter $T_{\mathrm{p,min}}$ in the weak intensity limit is used as a measure of improved cooling performance. In figure 6.17(a), $D_{\mathrm{RLC,Be}}$ is decreased starting from the currently manufactured trap with $D_{\mathrm{RLC,Be}} = 5.7\,\mathrm{mm}$. The red line is the prediction of equation (6.36) and excellent agreement between simulation and theory is observed. However, even for a trap with $D_{\mathrm{RLC,Be}} = 2.0\,\mathrm{mm}$, which is challenging to manufacture and difficult to operate with 80 $^9\mathrm{Be}^+$ ions, the lower temperature limit is only about $50\,\mathrm{mK}$, a factor of 5 higher than our desired temperature.

While the resonant coupling scheme with continuous laser operation has a comparably high temperature limit, it is the most robust technique against experimental uncertainties. Figure 6.17(b) shows the final proton temperature as a function of the detuning of the $^9\mathrm{Be}^+$ cloud. The fact that the minimal $T_{\mathrm{p,min}}$ is shifted from $0\,\mathrm{Hz}$ detuning is caused by the effect of maximizing the coupling strength between the two particle species by introducing a relative detuning as described in section 6.5.1. However, since the laser is not chopped here, the effect on the cooling performance is negligible. Since the particles are continuously detected on resonance, matching and stabilizing them to $\approx 100\,\mathrm{mHz}$ is comparably straightforward and routinely done in our experiment. As figure 6.17(b) shows, the increase in $T_{\mathrm{p,min}}$ is negligible for $\approx 100\,\mathrm{mHz}$ detuning.

(a)

(b)
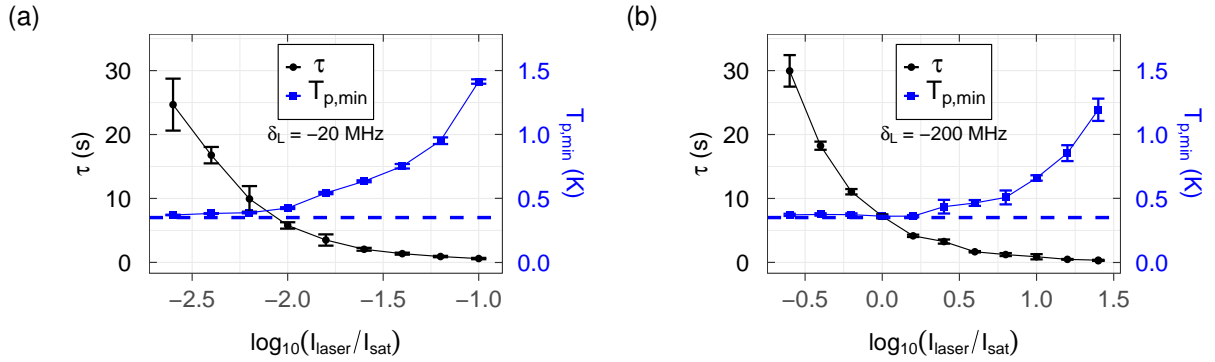
Figure 6.16: Simulated cooling time constant and lower proton temperature limit as a function of laser intensity for laser detunings $\delta_L = -20\,\text{MHz}$ (a) and $\delta_L = -200\,\text{MHz}$ (b). Although the absolute values of the laser intensity strongly differ, the scaling of τ and $T_{p,\text{min}}$ is very similar, indicating that no global favourable laser detuning exists and rather the combination of laser intensity and detuning defines the cooling performance. The blue dashed lines indicate the minimal proton temperature of $350\,\text{mK}$ predicted by equation (6.36).

(a)

(b)
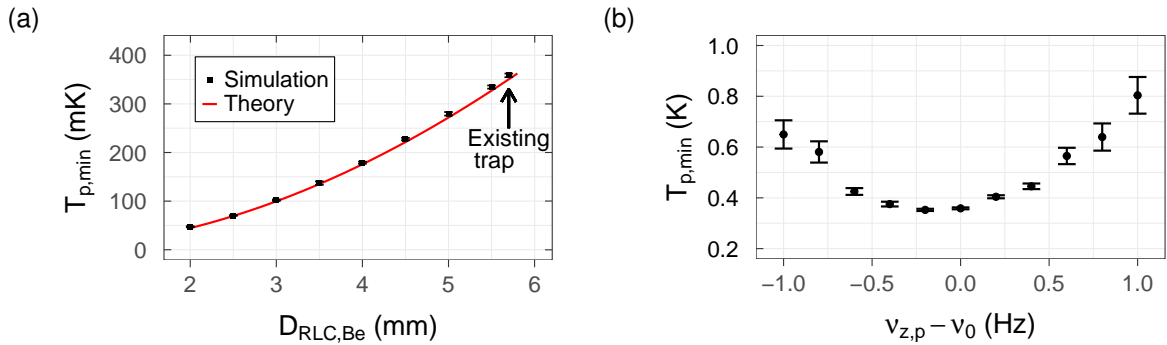
Figure 6.17: (a) The minimal proton temperature as a function of the effective beryllium trap size for 80 $^9\text{Be}^+$ ions. A smaller effective electrode distance increases the width of the beryllium dip, leading to a lower minimal proton temperature according to equation (6.36). The simulation data is generated with sufficiently low laser power. (b) The simulated final proton temperature as a function of the detuning of the proton from the resonator. The asymmetry arises from the effect described in section 6.5.1.

6.5.3   Off-resonant coupling mediated by an RLC resonator

The off-resonant resonator coupling approach combines the ideas of the previous two cool-ing schemes by detuning the particle frequencies by $\delta\nu_{\mathrm{RLC}}$ from the resonator eigenfre-quency, typically several kHz [29]. Similar to the common-endcap coupling, the particles then perform Rabi oscillations mediated by a common effective capacitance

$$C_{\mathrm{eff}} = \frac{\Im(Z_{\mathrm{RLC}}^{-1})}{\omega} \propto \delta\nu_{\mathrm{RLC}} \qquad (6.37)$$

where Z_{RLC} is the impedance of the RLC detection circuit. Combined with equation (6.30) this implies that the Rabi frequency decreases approximately linear with the resonator detuning. With this scheme, the application of π-pulses is not only inhibited by the required frequency matching precision, but also by the residual heating due to the resonator noise. As a result, a chopped laser scheme must be employed again.

In order to pinpoint the optimal laser cycle time and cooling time constant, the same pro-cedure as for the common-endcap coupling is performed for different resonator detunings. However, due to the residual particle heating by the resonator noise, the lower temperature limit is higher than the Doppler limit and is a function of $\delta\nu_{\mathrm{RLC}}$. Moreover, the incoherence introduced by the noise causes the ideal laser cycle time for the cooling time constant to become suboptimal for reaching the lowest final temperatures. Figure 6.18(a) shows the simulated proton temperature as a function of laser cycle time at 8 kHz resonator detun-ing. The proton was initialized at 50 mK and the system was evolved for 30 s to allow it to come into equilibrium. The displayed temperature is calculated from the mean energy of an additional 30 s-interval afterwards. While the laser cycle time for the cooling time constant is optimal at 3.5 s, about a factor of 2 in the lower temperature limit is gained by reducing it to 1.0 s. Equivalent scans were repeated for each resonator detuning in the following data.

The simulated performance of the off-resonant coupling scheme in terms of cooling time constants and lower temperature limits is summarized in figure 6.18(b). The cooling time constants rise roughly linearly with the detuning, as expected from equation (6.30) and equation (6.37). The lower temperature limits saturate at slightly below 10 mK, which results from the two opposing effects of the decline of resonator noise and the reduction of the Rabi frequency.

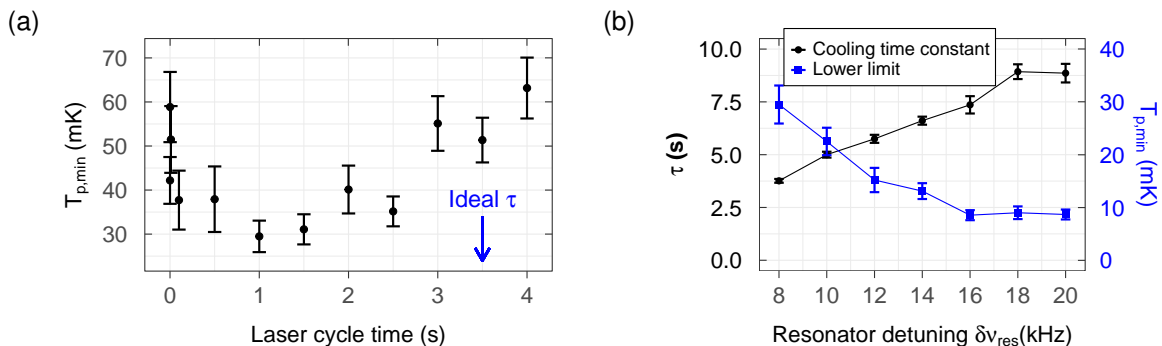Figure 6.18: (a) The simulated proton temperature limit as a function of laser cycle time for 8 kHz resonator detuning. Due to the resonator noise the ideal laser cycle time shifts from 3.5 s for the cooling time constant to 1.0 s for the minimal temperature. The behavior is similar for all resonator detunings. (b) Simulated cooling time constant and temperature limit as derived from (a) as a function of resonator detuning.
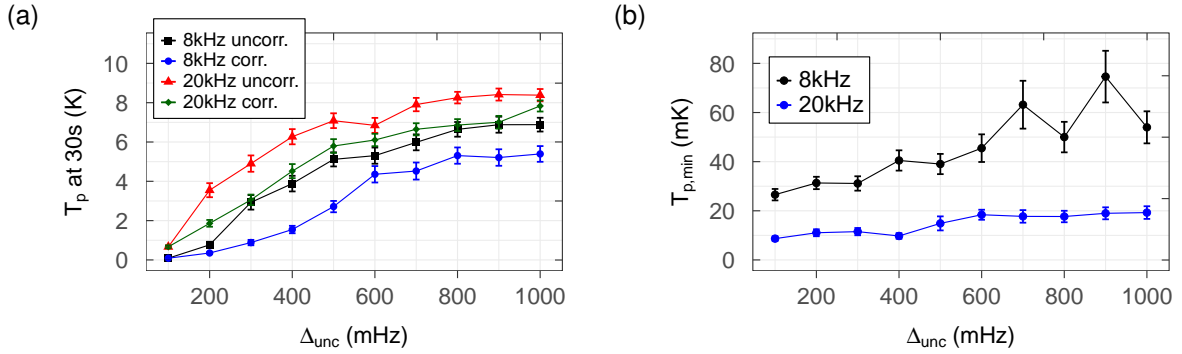
Figure 6.19: The simulated effect of the frequency matching uncertainty Δ_{unc} for the off-resonant coupling scheme for resonator detunings of 8 kHz and 20 kHz. The data points labelled 'uncorr.' (uncorrected) were generated with the ideal laser cycle time for $\Delta_{\text{unc}} = 100$ mHz. The data points labelled 'corr.' (corrected) were generated with the ideal laser cycle time for each value of Δ_{unc}. (a) The proton temperature at 30 s as a measure of cooling effectiveness. The initial energy was $10 \text{ K} \cdot k_B$. (b) The lower limit of the proton temperature with the same uncertainties as in (a).

The effect of the frequency matching uncertainty is investigated for 8 kHz and 20 kHz resonator detuning in the same manner as for the common-endcap coupling. Figure 6.19(a) shows the temperature at 30 s after initializing the proton at an energy of $10 \text{ K} \cdot k_B$. If the particle frequency matching precision Δ_{unc} is known experimentally, one can optimize the cooling time by adjusting the laser cycle time accordingly. For example, if the frequency matching precision is worse than the 100 mHz assumed in this work, one can decrease the laser cycle time to account for the faster (but incomplete) Rabi oscillations. However, this requires Δ_{unc} to be smaller than or at least comparable to the Rabi frequency. This condition is, in contrast to the common-endcap coupling, fulfilled for the coupling scheme investigated in this section. The procedure in context of figure 6.11(a) was repeated for every frequency matching precision for the blue and green data points labelled 'corr.' in figure 6.19(a), leading to a significantly better cooling performance compared to the uncorrected ones. Especially in the case of 8 kHz the sensitivity of the proton temperature to Δ_{unc} is significantly smaller compared to the common-endcap coupling. Additionally, figure 6.19(b) shows the equilibrium proton temperature as a function of the frequency matching uncertainty. An uncertainty of 1 Hz causes the temperature to be roughly a factor of 2 higher than for 100 mHz for both 8 kHz and 20 kHz resonator detuning.

6.6   Application III: Verification of a temperature measurement method used in the antiproton q/m measurement

The currently most precise measurement of the charge-to-mass ratio of the proton and antiproton at 16 ppt was performed by our sister experiment BASE-CERN [106]. In order to avoid systematic errors induced by different power supply polarities, the reference for the antiproton mass is not the proton but the H^- ion. The dominant systematic frequency shift of this measurement stems from the relative cyclotron frequency shift due to non-zero B_2 and non-zero axial temperature $T_z = T_{\text{RLC}}$. In particular, the relativistic shift of the cyclotron frequency ratio R scales for the parameters of this experiment with $\Delta R = 4.25 \Delta T_z$ ppt/K [106]. Consequently, the presence of an axial temperature difference ΔT_z between the proton and H^- ion would severely limit the measurement precision. Since the temperature determination is of utmost importance for the charge-to-mass ratio measurement and a factor of 2 discrepancy had been discovered in a temperature measurement that was
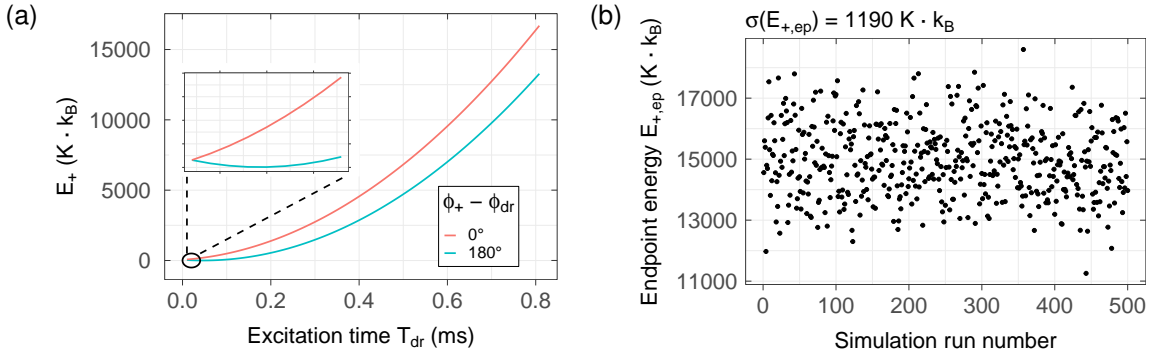
Figure 6.20: Simulation of a direct cyclotron excitation of a particle. In (a) the two extreme cases of the relative phase difference between the cyclotron motion and the excitation drive $\phi_+ - \phi_{\mathrm{dr}}$ are shown. If the cyclotron motion is excited out-of-phase, it is first damped to $0\,\mathrm{K} \cdot k_B$ and then increases exponentially. In contrast, for in-phase excitation the energy rises directly exponentially. In the experiment, the cyclotron phase is unknown so that the difference is uniformly distributed. From the resulting cyclotron energy scatter the initial temperature can be derived. A simulated example of the scatter for uniform phase differences and thermal cyclotron energies is shown in (b).

previously considered established (see section 8), the simulations were employed to provide an independent verification to the theory developed in [107].

The temperature measurement method of choice for this experiment was based on the axial frequency scatter after exciting the cyclotron mode directly [106, 107]. The idea is the following: When thermalizing the cyclotron energy of the particle via sideband coupling (section 2.4), the cyclotron energy continuously samples a Boltzmann distribution. Once the sideband drive is turned off, the energy remains constant at a random value drawn from the Boltzmann distribution. If the cyclotron energy is excited with a dipolar drive at $\nu_{\mathrm{dr}} = \nu_+$ for a fixed time T_{dr}, the resulting rise in cyclotron energy is a function of the relative phase $\phi_+ - \phi_{\mathrm{dr}}$ between the cyclotron mode and the excitation drive. A simulated example of the two extreme cases is shown in figure 6.20(a). Assuming the same initial cyclotron energy E_+, in the case of in-phase excitation (red curve) the endpoint cyclotron energy is significantly higher than in the case of out-of-phase excitation (blue curve). This is because for out-of-phase excitation the cyclotron energy first decreases and reaches $E_+ = 0$ K $\cdot k_B$ before exponentially increasing. Note that T_{dr} is sufficiently short so that any possible difference between ν_+ of the particle and the drive frequency ν_{dr} is negligible. The cyclotron energy can be measured via the residual B_2 as an axial frequency shift.

When repeating many of such measurements, the relative phase is equally distributed and gives a constant contribution to the cyclotron energy scatter. The only parameter that defines a further scatter is the initial cyclotron energy. By convoluting the Boltzmann distribution of the initial cyclotron energies $E_{+,\mathrm{th}}$ with the transfer function of the excitation drive and the random phases, the cyclotron energy scatter as a function of initial temperature is obtained [106, 107],

$$\sigma(E_{exc}) = \sqrt{2k_{\mathrm{B}}T_{+,\mathrm{th}} \langle E_{\mathrm{exc}} \rangle}\sqrt{1 + \frac{1}{2}\frac{k_{\mathrm{B}}T_{+,\mathrm{th}}}{\langle E_{\mathrm{exc}} \rangle}}. \tag{6.38}$$

In the simulations, the initial thermal distribution of cyclotron energies is defined by drawing a random value from a Boltzmann distribution with fixed temperature. The initial phase of the cyclotron mode is randomized. A simulated example of the resulting scatter for $T_+ = 50.0\,\mathrm{K} \cdot k_B$ is shown in figure 6.20(b). This procedure is repeated for different drive amplitudes, of which simulated data is shown in figure 6.21. A simple unweighted
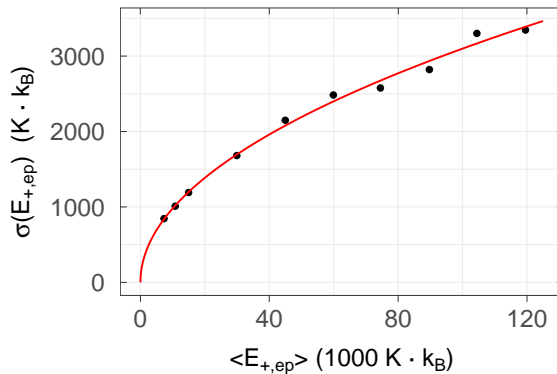
Figure 6.21: Simulated scatter of the cyclotron endpoint energy for different drive amplitudes equivalent to different mean endpoint energies. The red line is a fit from which the initial cyclotron temperature can be derived, in this case 48.4 K. This is in good agreement with the simulation input value of 50.0 K.

least-squares fit yields an initial cyclotron temperature of $T_{+,\text{th}} = 48.4\,\text{K}$. This is in very good agreement with the input parameter of $T_+ = 50.0\,\text{K} \cdot k_B$.

In summary, the simulations provide an independent verification of a temperature measurement method that was employed for a 16 ppt charge-to-mass ratio measurement of the antiproton. The agreement between simulation and theory can also be put into a different light: If one considers the theory of this temperature measurement as established, the results presented here are yet another benchmark case in which simulations of the radial motions and temperature determinations are combined.

6.7   Application IV: Phase methods

The application of phase methods has enabled the most precise cyclotron frequency measurements to date. Two schemes are commonly used, namely the 'pulse and probe' scheme (PnP) [108] and the 'pulse and amplify' scheme (PnA) [55, 109]. In this subchapter, the ability of the simulations to accurately calculate frequencies on the 1×10^{-12} scale will be demonstrated. Since the PnA scheme is the state-of-the-art method for cyclotron frequency measurements, this scheme will be reproduced in the simulations. Note that it is assumed that the reader is familiar with phase methods in general, so that only a brief summary of the PnA method is given here.

A representative example of the energy evolution of one PnA cycle is given in figure 6.22(a). In the first step the modified cyclotron mode is resonantly excited at $\nu_{\text{RF}} = \nu_+$. This causes it to gain energy, but more importantly, the phase of the excitation drive is imprinted on the mode. The second step consists of the free evolution of the cyclotron mode for a certain evolution time T_{evol}. In a full experimental cyclotron frequency measurement, this step is repeated for different evolution times. The cyclotron phase is read out in the third step, where a quadrupolar coupling pulse at the upper sideband $\nu_{\text{RF}} = \nu_z + \nu_+$ is applied. It can be shown that this coupling pulse imprints the phase of the cyclotron frequency on the axial mode [55, 109], i.e. $\phi_z \simeq \phi_+$. The phase of the peak signal of the axial mode can then be read out via the standard image-current techniques. Note the phase can be determined only up to multiples of 2π. Consequently, an initial estimate of the cyclotron frequency is needed, for example from the double-dip technique or from shorter phase evolution times. In order to finally obtain the cyclotron frequency, the accumulated phase as a function of evolution time is measured. The slope of a linear fit directly corresponds to the cyclotron
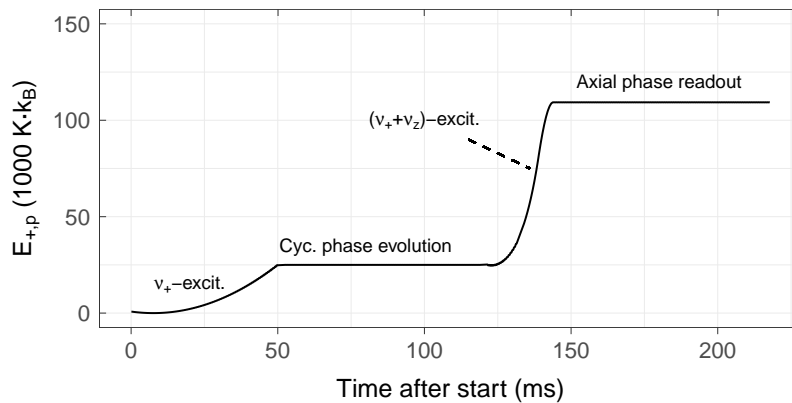
Figure 6.22: Simulated evolution of the cyclotron energy during the 'pulse and amplify' (PNA) scheme. An initial phase is imprinted on the cyclotron motion by exciting it. Afterwards, the cyclotron mode is freely evolved. The evolved phase is then transferred on the axial mode using a $\nu_+ + \nu_z$ excitation. Finally, the axial phase is read out by means of image-current techniques. Note that the subsequent thermalization has been omitted.
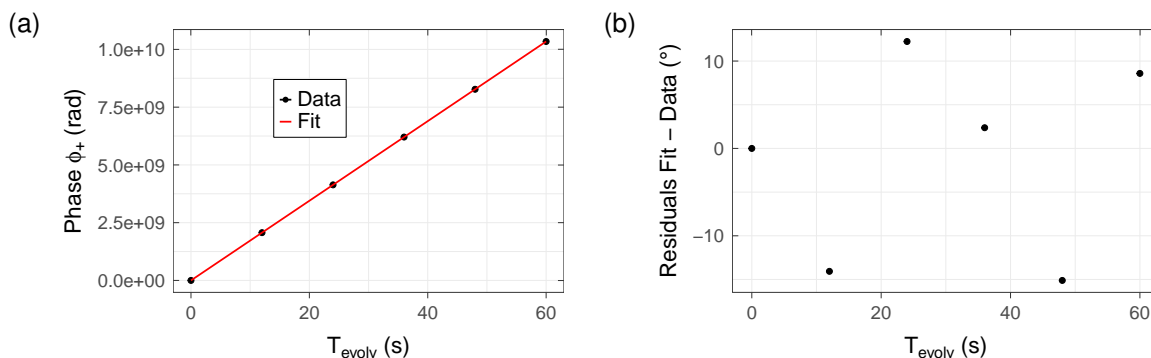
Figure 6.23: Demonstration of the 'pulse and amplify' (PnA) technique with the simulations. The accumulated phase for different cyclotron evolution times is shown in (a). A linear fit yields the cyclotron frequency, in this example with a relative deviation of only 1.6×10^{-12} to the analytical value. In plot (b) the fit residuals are shown.

frequency.

The result of a simulated example of the experimental procedure is shown in figure 6.23. All three modes of a single proton were simulated with a time step of $\Delta t = 1 \times 10^{-10}$ s and a total time of up to 60 s, i.e. up to 6×10^{11} steps. By saving only the phase space data after the $\nu_z + \nu_+$ coupling pulse is turned off, the available memory does not pose a practical issue. To determine the phase, one period of the proton's axial motion was fitted with $z(t) = z_0 \sin(\omega_z t + \phi_z)$ for each evolution time. After unwrapping the phase in terms of multiples of 2π and performing a linear fit, the simulated cyclotron frequency $\nu_{+,\mathrm{p,sim}}$ is obtained. The relative deviation compared to the analytically calculated one $\nu_{+,\mathrm{p,ana}}$ is

$$\left| \frac{\nu_{+,\mathrm{p,sim}} - \nu_{+,\mathrm{p,ana}}}{\nu_{+,\mathrm{p,ana}}} \right| = 1.6 \times 10^{-12}. \tag{6.39}$$

The corresponding fit residuals are shown in figure 6.23(b). Not only is the maximal absolute deviation only $15°$, the fact that no systematic scaling with the evolution time is observed implies that the accumulated phase error over 60 s of simulation time or 6×10^{11} steps is negligible. This result highlights that the simulations are capable of reproducing frequency measurements on the 1×10^{-12} scale. It constitutes a completely different aspect compared to the previous applications that focused on the manipulation of energies

Figure 6.24: Simulated data of the $\nu_z(B_2, E_+)$-shift of a single proton compared to the theoretical shift of equation 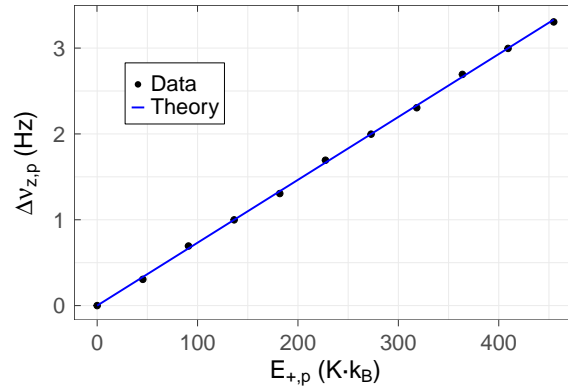(2.28). No difference between simulation and theory is observed, demonstrating the capability of the simulations to study systematic shifts.

and temperatures. The simulations are therefore a valuable tool for the investigation of systematic effects in precision measurements, as will be exemplarily demonstrated in the next subchapter.

6.8   Application V: Systematic frequency shifts

In previous chapters it was argued that simulations can be employed for investigating systematic effects. In this subchapter, this claim will be corroborated exemplarily by studying the axial frequency shift of a proton due to the non-zero cyclotron amplitude in the presence of a quadratic magnetic field coefficient B_2. The B_2-coefficient is defined as

$$\vec{B}_2 = B_2 \left[\left(z^2 - \frac{x^2 + y^2}{2} \right) \vec{e}_z - z \left(x\vec{e}_x + y\vec{e}_y \right) \right] \tag{6.40}$$

and can consequently be incorporated in the simulations by adding the additional forces

$$F_{x,B2}^{(i)} = qB_2 \left[\dot{y} \left(z^2 - \frac{(x^{(i)})^2 + y^2}{2} \right) + \dot{z}zy \right] \tag{6.41}$$

$$F_{y,B2}^{(i)} = qB_2 \left[-\dot{x} \left(z^2 - \frac{x^2 + (y^{(i)})^2}{2} \right) - \dot{z}zx \right] \tag{6.42}$$

$$F_{z,B2}^{(i)} = qB_2 \left[\dot{y}xz^{(i)} - \dot{x}yz^{(i)} \right] \tag{6.43}$$

to the acceleration-term of the integrator.

The simulated axial frequency of the proton is plotted as a function of the cyclotron energy in figure 6.24. The trap parameters of the proton were $\nu_z(E_+ = 0) = 626951.5\,\mathrm{Hz}$, $B_2 = 1.0\,\mathrm{T/m^2}$, $\nu_+ = 27.4\,\mathrm{MHz}$. The simulation parameters were $\Delta t = 1 \times 10^{-10}\,\mathrm{s}$ and $T_{\mathrm{tot}} = 5.0\,\mathrm{s}$. The axial frequency was determined directly via the weighted mean of the FFT of the proton's motion. The blue line is the shift expected from theory, i.e. equation (2.28). Practically no difference between simulation and theory can be observed.

The agreement between simulation and theory demonstrates the novel aspect that the simulations are capable of accurately predicting the particle's behavior even in the presence of electrostatic or magnetostatic inhomogeneities. In fact, although not explicitly shown here, all first-order frequency shifts as a function of C_4 or B_2 have been confirmed in the simulations, i.e. any combination of $\{\Delta\nu_+, \Delta\nu_z, \Delta\nu_-\} * \{B_2, C_4\} * \{\hat{z}, \hat{\rho}_+, \hat{\rho}_-\}$. As a final

note, in the course of this study it was discovered that the $\nu_z - C_4 - \hat{z}$ shift is larger by a factor of 2 if the axial amplitude is not constant but samples a Boltzmann distribution. While this deviation was first considered a programming error in the simulations, it has been subsequently corroborated by experimental data, which will be presented in section 8.

7 | Experiment commissioning and preparatory measurements

In this chapter, the commissioning of the experiment and preparatory measurements towards the sympathetic cooling of a single proton are presented. From this chapter onwards, the data was recorded over two experimental cooldowns, one from January 2022 to May 2022 and the other one from August 2022 that is still ongoing. The only difference between these two cooldowns was the exchange of the proton laser ablation target (section 7.1) and some technical repairs of the cryogenic amplifiers and SiPMs. Notably, the order the data is presented here does not necessarily correspond to the temporal order the data was recorded.

7.1   Preparation of single particles

7.1.1   Adiabatic transport

A crucial ingredient for the operation of a Penning-trap system with six traps is the adiabatic transport of ions between the traps. This transport is performed by a sequence of bipolar voltage ramps of the individual trap electrodes: First, all electrodes towards the target location are biased to usually $+10\,\text{V}$. Initially, the ion is located in the potential well of two electrodes biased to usually $-10\,\text{V}$. For transport, one of the two negatively biased electrodes is ramped up while the next electrode in the other direction is ramped down, thus advancing the ion by one electrode. This procedure is repeated until the target location is reached. The typical ramp speed is $20\,\text{V/s}$. However, some trap electrodes are biased via a $1\,\text{G}\Omega$ resistor. The resistor forms together with the stray capacitance of the electrode an RC-circuit with decay times on the order of seconds, so that a certain waiting time is required. Overall, in this way the particles can be transported with negligible heating rate (see section 7.4.2) along the trap axis.

7.1.2   Cleaning procedures

Any kind of ion source produces not only the ion of interest but also contaminants. For measurements that rely on a single particle, it is thus crucial to apply cleaning procedures and isolate the desired species [26, 54, 61, 74].

HV ramp

One of the most reliable cleaning procedures is the application of a high-voltage (HV) ramp to the ring electrode. This increases the axial frequency, and eventually the Penning-trap stability criterion is not fulfilled anymore:

$$\omega_z < \omega_c/\sqrt{2} \qquad \Longrightarrow \qquad m/q < \frac{B_0^2}{4C_2|U_0|}. \tag{7.1}$$

If $|U_0|$ is increased, species with high m/q start to drop out of trap. Notably, this method is quasi-deterministic in the sense that contamination with high m/q can be removed reproducibly. However, if the ratio between contaminants and ion of interest is unfavourable, also the ion of interest might drop out as well. In practice, $|U_0|$ is limited by the breakdown voltages of the capacitors of the DC lowpass filters. In the LT, a HV ramp to $-350\,\text{V}$ is

commonly used to remove ions with $m/q > 7\,\mathrm{u/e}$. To clean out even higher masses, the clouds are transported to the TMT or AT. These traps have a smaller B_0 due to the ferromagnetic ring electrode and a larger C_2 and hence reach the stability criterion at lower absolute voltages. As a final note, for large ion clouds the radial extend due to space charge causes ions to be lost at significantly lower $|U_0|$ than predicted by the stability criterion.

Evaporative cooling

A simple method to remove ions from the trap is to lower the trapping potential until a fraction of ions is not trapped anymore, i.e. is lost by evaporation. This is especially useful for hot ions directly after loading. In order to discriminate between the ion of interest and contaminants, usually the ion of interest is cooled with the resonator beforehand. However, this method has several disadvantages. First, in order to detect and cool the ion of interest with the resonator, the ratio between contamination and ion of interest must be sufficiently small, since otherwise the contamination prevents detecting the particle signal. Second, this method is non-deterministic since the energies of the contaminants are usually unknown and broadly distributed and can even be sympathetically cooled by collisions with cold ions. Third, one will inevitably also lose a certain fraction of the species of interest, especially for large clouds. In our application, this is disadvantageous if the goal is to prepare a large cloud of beryllium ions for sympathetic cooling experiments.

Magnetron or axial excitations

By exciting the magnetron or axial motion directly, specific charge-to-mass ratios can be addressed. Exciting the cyclotron motion of contaminants is possible too, however, due to the higher frequency it is usually less effective than magnetron or axial excitations. Since species with large m/q are cleaned out reliably by the HV ramp, this method is usually employed for ions with m/q lower than the ion of interest. If the subscript 'ioi' denotes the ion-of-interest frequencies, for excitations with $\nu_{\mathrm{z,ioi}} < \nu_{\mathrm{RF}} < \nu_{+,\mathrm{ioi}}$ the axial frequency of lighter ions is excited. Since the effective excitation strength of the drive decreases once the ion is excited to a large amplitude, this method is usually combined with an evaporative cooling sequence.

Alternatively, one can excite the magnetron motion. For fixed trapping potentials and in the same trap, the magnetron frequency of other species is no more than a few kHz different than the one of the ion of interest. Thus, usually a narrow-band magnetron sweep around $\nu_{-,\mathrm{ioi}}$ is applied to excite the magnetron motion of contaminants. Larger excitation strengths can be used if the species of interest is magnetron-cooled simultaneously. Stored Waveform Inverse Fourier Transform (SWIFT) excitations can be used to exclude the magnetron frequency of the ion of interest, but were not employed during this thesis. Similar to the axial excitation, the magnetron excitation usually does not remove the contaminants directly. Thus, a magnetron excitation can be combined with a transport to a trap with smaller radius.

7.1.3 Preparation of single particles

After the cleaning procedures have been conducted, usually a single particle from a cloud of the species of interest is prepared. To this end, one option is to perform successive evaporative cooling sequences. However, this is very laborious since the trapping voltage at which one out of two particles is retained is not known and an iterative lowering of the trapping potential is required.

A better solution is to perform a W-potential separation, shown schematically in figure 7.1. Assuming a cloud of particles is trapped, the ring electrode is quickly ramped towards
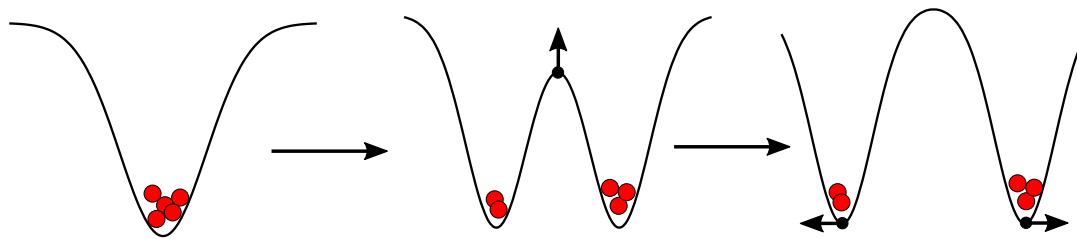
Figure 7.1: Separation scheme to prepare a single particle non-destructively. By ramping up the ring voltage towards positive voltages, a W-potential is created. A slight asymmetry can be applied to adjust the respective fraction of ions in each of the two potential wells.

positive voltages while the correction electrodes remain at their negative potential. This divides the potential well into two symmetric separate ones. By applying a small asymmetric potential to the correction electrodes, it is possible to adjust the relative fraction of particles in each potential well. This separation scheme has several striking advantages. First, the ions are not simply lost. In fact, the efficiency of the separation is close to 100 % if the cloud is initially cold. This is especially useful at the start of a new experimental run, where the transport routines must be tested and ions regularly get lost. Second, once the required asymmetries are established, only few separations must be performed to isolate a single particle. Usually no more than five separations are required to prepare a single particle. Third and finally, this method also constitutes a cleaning procedure since possible contaminants are subject to the separation as well. In our experiment, the W-separation scheme is implemented in the PT, where one of the two resulting clouds is transported to the CT and the other remains in the PT.

The number of ions including a single particle can be determined sufficiently precise based on the dip width (equation (2.42)). However, even after cleaning and separation procedures, particles of the same species can be on high radial orbits such that they do not contribute to the dip width. These are the most challenging to detect and clean. One possibility to determine whether the alleged single particle is indeed not contaminated is by measuring its cyclotron energy distribution with the TMT. A contaminated particle usually has a broader distribution, i.e. one would assign a higher temperature. However, this is a time-intensive process of at least several hours, even when negative feedback is employed.
Another unambiguous sign of contamination is an unexpectedly high Rabi frequency of the cyclotron double dip. A cyclotron double dip spectrum of a single, uncontaminated proton is shown in figure 7.2(a). The Rabi frequency for this PT excitation line is 1.1 Hz for -15 dBm sideband drive amplitude. In contrast, figure 7.2(b) shows two double dip spectra of a contaminated proton. Although the dip width is that of a single proton and the exact same parameters for the cyclotron sideband drive are used, the Rabi frequency is significantly increased. Notably, the Rabi splitting can be changed by exciting the cyclotron mode of the proton with short bursts directly. Even after cooling the cyclotron and magnetron mode of the alleged single proton again, the Rabi splitting of the cyclotron mode is increased in the example of figure 7.2(b) from 3.1 Hz to 16.0 Hz. This suggests that the contamination is one or more protons at higher radial amplitudes and the cyclotron bursts have altered the relative orbits. Although the exact mechanism why the Rabi frequency is enhanced has not been investigated and is arguably also not of relevance, an increased Rabi frequency is a clear sign of contamination. As a final note, having observed the temperature and Rabi splitting of a single proton once beforehand is a prerequisite to be able to identify a contaminated one.
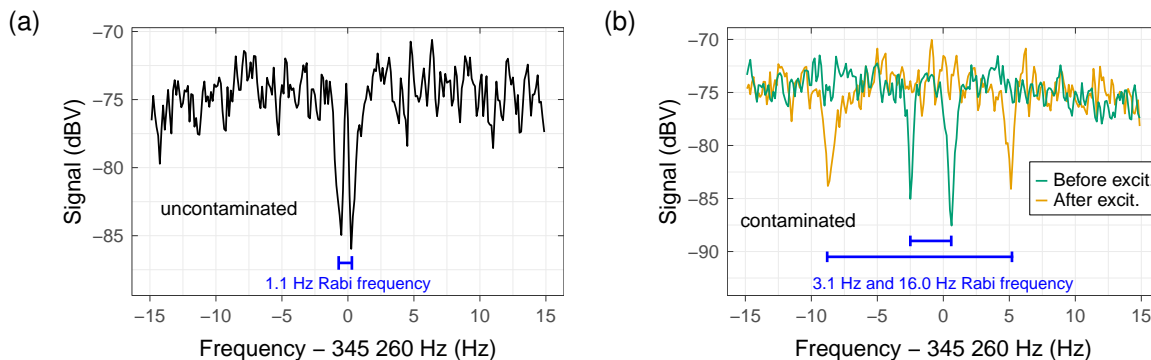
Figure 7.2: Cyclotron double-dip spectrum of a single proton. In (a) the double dip of an uncontaminated proton is shown, while in (b) the double dips of a contaminated proton are shown. Although the same drive parameters were used, due to the contamination the Rabi frequency is higher and can be changed by exciting the particle(s).

7.1.4   Proton and beryllium loading procedures

In this subchapter, 'recipes' for loading beryllium ions and protons will be given. While they might seem very specific, our experiment is special in the sense that we exclusively rely on ion loading via laser ablation. Therefore, these routines might prove useful for the next generation of PhD students at the proton experiment and possibly beyond.

The procedure for loading beryllium ions is:

- Set the LT trap voltages to the nominal beryllium trapping voltages of around $-7.5\,$V. Apply positive voltages of $+13.5\,$V at the LT endcaps and at several other electrodes throughout the trap stack to block hot ions from traversing the trap stack. Avoid applying trapping potentials anywhere but the LT.

- Perform one ablation laser shot of 200–$240\,$µJ on the beryllium target.

- Perform an LT HV ramp to $-250\,$V for preserving large clouds. If the goal is to prepare a single $^9\mathrm{Be}^+$, go to $-280\,$V. This will clean out mass-to-charge ratios of $10\,$u/e and higher.

- If the goal is to prepare a single $^9\mathrm{Be}^+$: Ramp the ring voltage down to $-1.5... - 1.0\,$V such that hot ions will become untrapped.

- Due to the low ionization energy of beryllium ($9.3\,$eV) compared to other species with $m/q \leq 9\,$u/e, the beryllium cloud is usually rather clean. If the goal is a single $^9\mathrm{Be}^+$, transport to the PT and perform the separation schemes. Otherwise, apply the magnetron-excitation in a $\pm 3\,$kHz window around ν_- while the cloud is cooled via another excitation line. Perform additional HV ramps followed by ramping the ring voltage down to $-1.5\,$V as well as a transport to the first BT electrode.

- If available, it is strongly advisable to cool the beryllium cloud with the laser. A large cloud of > 100 ions will take at least hours to cool via the resonator, while it is a matter of minutes or less with a properly adjusted laser.

The procedure for loading a single proton is:

- Set the LT trap voltages to the nominal beryllium trapping voltages of around $-7.5\,$V. Even when loading protons, applying the beryllium trapping voltages has proven to

be more reliable here. Apply positive voltages of $+13.5\,$V at the LT endcaps and at several other electrodes throughout the trap stack to block hot ions from traversing the trap stack. Avoid applying trapping potentials anywhere but the LT.

- Perform one ablation laser shot of 300–$320\,\mu$J on the proton target. The higher energy is needed most likely due to the larger ionization energy of hydrogen ($13.6\,$eV).

- Perform an LT HV ramp to $-350\,$V.

- Transport the ions to the PT.

- (Optional) Perform a mass spectrum in the PT to check for protons and contaminants.

- Transport the ions to the TMT or the AT and perform a HV ramp, $-240\,$V in the TMT or $-160\,$V in the AT (see note below).

- Transport the ions back to the PT and perform the separation schemes.

Note, due to lack of necessity protons have not been observed in the LT yet. One peculiarity of our experiment is that, due to the common-resonator setup, rapidly changing voltages in one trap can mutually affect the trapping potential of the respective other trap. For example, when performing a laser ablation shot in order to load a beryllium cloud in the LT, the single proton in the PT gets lost. However, this can be prevented by transporting the proton in the transport section (T3, compare figure 10.1). Similarly, the PT separation schemes cause ion losses in the LT if the LT trapping potential is not made deeper to e.g. $-100\,$V.

Another note regarding HV ramps for cleaning the proton: In the AT mass-over-charge ratios of $\geq 2\,$amu/e become unstable at $-140\,$V. Thus, an HV ramp to $-160\,$V in the AT is ideally suited to clean out every possible contaminant besides other protons at high radii. However, the transport into the AT inexplicably stopped working a few months after the start of the second experimental run. Despite thorough investigation, no fault could be found. As a result, the following HV ramps were performed in the TMT but only to $-240\,$V corresponding to $\geq 5\,$amu/e.

Finally, it was observed that it is possible to catch large clouds of ions in other traps directly after a laser ablation shot, especially in the PT, even though blocking potentials were applied. This is a strong indication that the ionization process does not solely occur due to the ablation but rather due to collisions, either between neutral atoms or between neutral atoms and electrons. This can also be the reason why the effect of loading-induced patch potentials are still observed in all traps despite the special design of the LT.

7.1.5 Mass spectra proton targets

As mentioned in section 3.7 already, one of the major challenges of the first experimental run was that the old proton target, a PE foil, produced many contaminants. In our experiment, mass spectra can be recorded by applying a $2\nu_z$ drive and sweeping the trap voltages. If an ion species becomes resonant with the $2\nu_z$ drive, it is strongly excited and a peak signal is observable at the resonator frequency ν_z. Since $m/q \propto U_0$, by identifying suitable calibrant species the trap voltages can be converted to ion mass-to-charge ratios. An exemplary mass spectrum in the LT after an ablation laser shot on the old PE target is shown in figure 7.3(a). Six ion species can be identified. The beryllium and berylliumhydride most likely stem from the deposition of neutral beryllium atoms on the PE target in the course of the beryllium loading process. Besides, also doubly-charged carbon as well
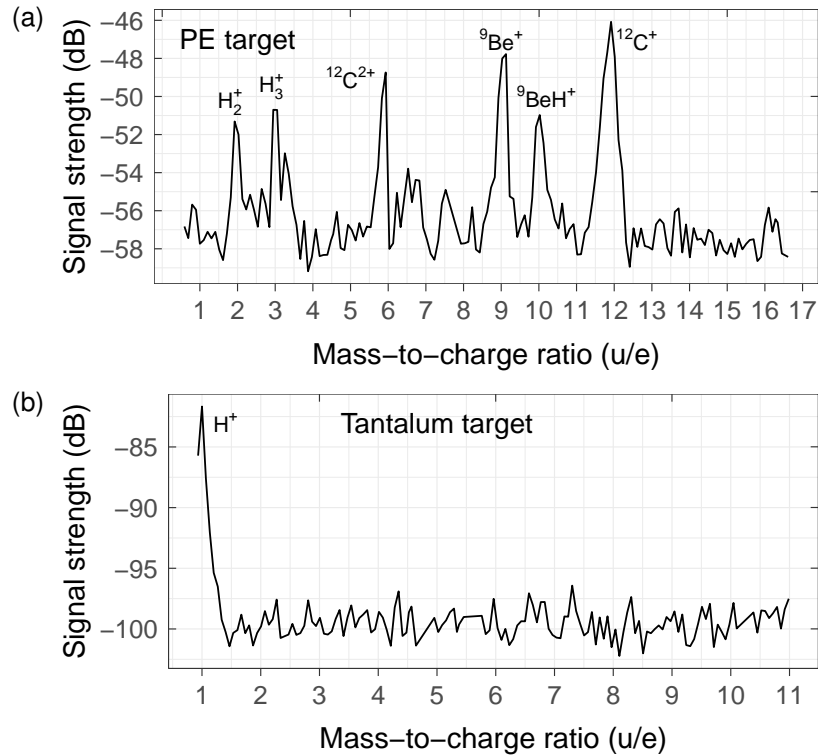
Figure 7.3: Exemplary mass spectra of the proton targets. In a first experimental run, a polyethylene (PE) target was used. The corresponding mass spectrum recorded in the LT is shown in (a). Although this target produced small amounts of protons, the contamination was too severe to reliably detect and isolate a single proton. For the second experimental run a tantalum target was installed. The corresponding mass spectrum recorded in the PT is shown in (b). Note that for this mass spectrum an HV ramp that cleans $m/q > 8\,\mathrm{u/e}$ was performed so that the mass spectra are not directly comparable. Nevertheless, the tantalum target reproducibly yields clean protons with almost no contamination.
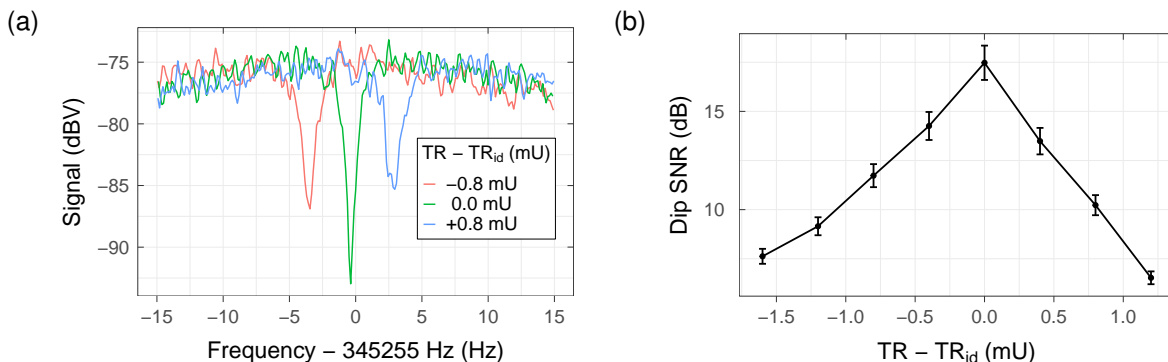
Figure 7.4: Effect of a non-ideal TR for a single proton in the PT. If the TR is not set to the ideal value TR_{id}, the dip loses in SNR. A dip spectrum for optimal TR and two dip spectra for $\pm 0.8\,\mathrm{mU}$ are shown in (a). A full TR scan is shown in (b).

as the hydrogen molecules H_2^+ and H_3^+ are observed in this spectrum. This specific mass spectrum is an example only, in this mass range N^{2+}, O^{2+} and H^+ were observed as well.

In contrast, a mass spectrum of the new tantalum target is shown in figure 7.3(b). Notably, this mass spectrum was recorded in the PT and after a $-350\,\mathrm{V}$ HV ramp in the LT that removes species with mass-to-charge ratios $\geq 8\,\mathrm{u/e}$, i.e. the mass spectra are not directly comparable. However, it is nevertheless evident that the tantalum target produces a clean proton signal. In fact, the only relevant contaminant in this mass-to-charge range has been $^{12}C^{2+}$, which can be easily removed by an HV ramp in the TMT or AT. The clean proton signal has been reproducible for > 20 laser ablation shots over the course of > 7 months.

7.2   Commissioning of the traps

7.2.1   Preparing a single particle dip

One of the most time-intensive tasks at the beginning of an experimental run is finding the particles in the trap. Even small patch potentials cause significant deviations between the theoretical and experimental ring voltage, compare table 1. For example, the experimental ring voltage of the CT for a single proton deviates by about $40\,\mathrm{mV}$ and the ideal TR deviates by about $50\,\mathrm{mU}$ relative to the theoretical values. Since the axial frequency of a proton shifts by about $500\,\mathrm{Hz/mV}$ in the CT and our axial detection system is narrow-band (of order $100\,\mathrm{Hz}$), a ring voltage scan must be performed in $\approx 0.2\,\mathrm{mV}$ steps. Furthermore, the CT is a comparably small trap with correspondingly large D_4, so that the TR must be adjusted to better than $\approx 5\,\mathrm{mU}$. Thus, a TR scan must be performed with smaller than $10\,\mathrm{mU}$ TR steps, corresponding to $5\,\mathrm{mU}$ maximal deviation. Since the ring voltage and TR are independent of each other, a two-dimensional scan must be performed to find the particle. Assuming an FFT averaging of $45\,\mathrm{s}$, in the best-case scenario such a 2D scan for the proton in the CT takes $50\,\mathrm{h}$ of measurement time. In reality, finding the particle usually takes several days.

However, several measures are available to speed up the particle search. First, using a cloud of ions instead of a single particle is beneficial due to the larger dip width. In addition, the SNR loss due to a non-ideal TR is significantly smaller. Second, if a suitable excitation line is available, a $2\nu_z$-drive can be applied. This allows to sweep the ring voltage and narrow down the range in ring voltage and TR. Finally, applying the magnetron sideband drive at the theoretical frequency can broaden the allowed TR deviations at which a particle signal is observable.

Once a particle dip is unambiguously observed, a TR scan is performed with a single particle. Since the measurements presented in this thesis do not necessarily require a perfectly nulled C_4, the TR is only adjusted based on the SNR method. An example is shown in figure 7.4 for a single proton in the PT. More precise adjustments can be done e.g. via magnetron excitations, see e.g. [86, 107]. For traps featuring a magnetic bottle, the situation is further complicated. Not only is the ring voltage range enhanced due to the $\nu_z(B_2, E_+)$-shift, the presence of a non-zero B_4 also makes the ideal TR a function of the cyclotron energy. A measurement of this effect will be presented in section 7.2.4.

7.2.2 Magnetron and cyclotron frequency search

The next time-intensive task is to find the radial frequencies via the sideband method. The magnetron frequency is mainly determined by the axial frequency and the particle properties and can therefore be calculated to a good precision. As a result, the magnetron sideband frequency is usually found manually within several minutes. In contrast, the cyclotron frequency of light particles and especially the proton is laborious to find. Small magnetic field changes between two experimental runs, e.g. due to a slightly different positioning of the traps in the superconducting magnet, cause the magnetic field at the ion position to change significantly.

Finding the cyclotron frequency of the proton in the 'first' trap can be done via the magnetic field calculated based on the trap frequencies of a single beryllium ion. The remaining search must be done by scanning the sideband frequency, similar to the ring voltage and TR scans. A complicating circumstance of this experiment is that the coupling of the rf lines to the proton is comparably weak at the cyclotron frequency of the proton, so that only small Rabi splittings of $\leq 10\,\mathrm{Hz}$ are possible. However, in all further traps the cyclotron sideband can be searched not via a double-dip spectrum, but via the change of the particle's axial frequency in the TMT. For this, the applied sideband drive is modulated. If the cyclotron sideband frequency is within this range, the cyclotron energy change is sufficient to be unambiguously detectable in the TMT. An example of such a scan with $40\,\mathrm{Hz}$ steps and $\pm 40\,\mathrm{Hz}$ modulation range is shown in figure 7.5(a), albeit for illustrative purposes a single beryllium ion instead of a proton was used, since for the latter the axial frequency jump in the TMT is too large to be observed within one spectrum. The standard deviation of the axial frequency stability for a detuned sideband drive is about $900\,\mathrm{mHz}$, i.e. the $18\,\mathrm{Hz}$ jump at around $2.6\,\mathrm{kHz}$ constitutes a $20\,\sigma$-event and therefore unambiguously narrows down the possible range of the cyclotron sideband frequency. Typically, modulation ranges between $\pm 10\,\mathrm{Hz}$ and $\pm 100\,\mathrm{Hz}$ are used so that several kHz can be covered within a few hours, which is significantly faster than a double-dip based search.

7.2.3 TMT B_2 measurement

In order to convert axial frequency shifts to temperatures, the B_2-coefficient of the TMT must be measured. The B_2-coefficient is determined by measuring the magnetic field at different axial ion positions in the TMT. The magnetic field itself is determined by measuring the free cyclotron frequency ν_c, which is given by the quadratic sum of all motional frequencies (equation (2.20)). The axial frequency is given directly by the dip position. However, due to the large B_2, the measured $\nu_z(E_+ > 0)$ is always larger than $\nu_{z,0} \equiv \nu_z(E_+ = 0)$. Hence the distribution of axial frequencies is measured after repeatedly thermalizing the cyclotron mode with a modulated sideband drive with sufficiently large modulation range. $\nu_{z,0}$ is then obtained as the leftmost frequency cut of the resulting axial frequency distribution. A single beryllium ion is employed for this study since for a proton
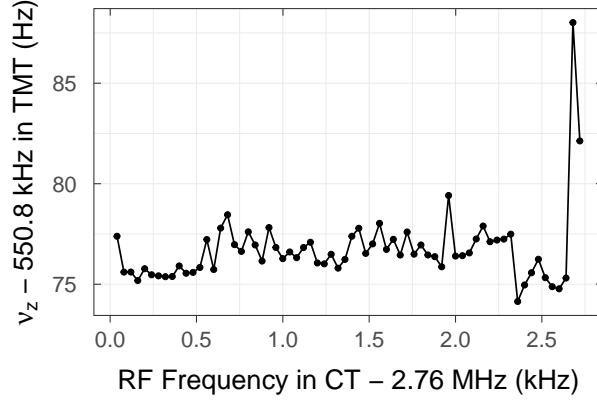
Figure 7.5: Cyclotron sideband frequency search via axial frequency scatter measurements in the TMT. A modulated rf drive of $\pm 40\,\text{Hz}$ is applied at different frequencies in the CT. If the drive is resonant with the cyclotron sideband, the cyclotron energy is altered, which is observable as an axial frequency jump in the TMT. This method speeds up the cyclotron sideband search significantly compared to the double-dip method.
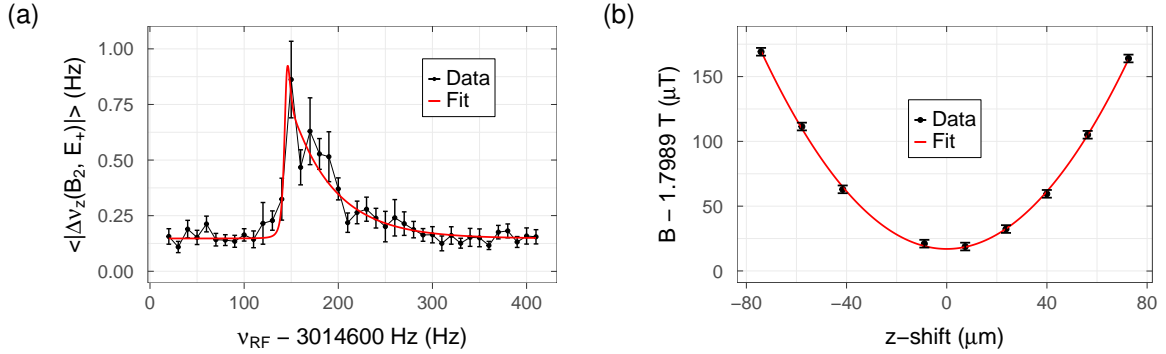

Figure 7.6: (a) Cyclotron frequency measurement of a single beryllium ion in the TMT. Due to the large B_2-coefficient, the cyclotron frequency is measured by exciting the cyclotron mode directly with an rf drive and recording the average axial frequency deviation between two successive measurements. The leftmost cut corresponds to the cyclotron frequency at zero axial energy. (b) The measurement in (a) is repeated for different axial ion positions. The motional frequencies of the ion are used to determine the magnetic field and from a quadratic fit B_2 is derived.

the thermal axial frequency distribution is broader than the resonator width.

The magnetron frequency is obtained from a double dip when applying the corresponding sideband drive. The modified cyclotron frequency cannot be measured by the double-dip technique due to the broadening from the large B_2-coefficient. In addition, since $\nu_+ > \nu_z > \nu_-$, the uncertainty of ν_+ mostly defines the uncertainty of the final magnetic field values. To determine ν_+ precisely, the fact that $\nu_z = \nu_z(E_+)$ is utilized by applying a dipolar rf-excitation at different frequencies close to ν_+. If $\nu_{\text{RF}} \cong \nu_+$, the cyclotron energy changes, which is recorded as a jump in ν_z. The amplitude of the excitation drive is chosen as low as possible, but high enough that the ν_z-jumps are still resolved, in this case about $-100\,\text{dBm}$. An example measurement is shown in figure 7.6(a). The lineshape including the tail towards higher ν_{RF} is well-understood and stems from the non-zero axial amplitude of the ion in the magnetic bottle [39]. More precisely, since $\nu_+ > \nu_z$, the magnetic field that defines ν_+ is a function of the ion's momentary axial position. Furthermore, since our B_2 is positive, the tail extends towards higher ν_{RF}, i.e. higher magnetic fields. The
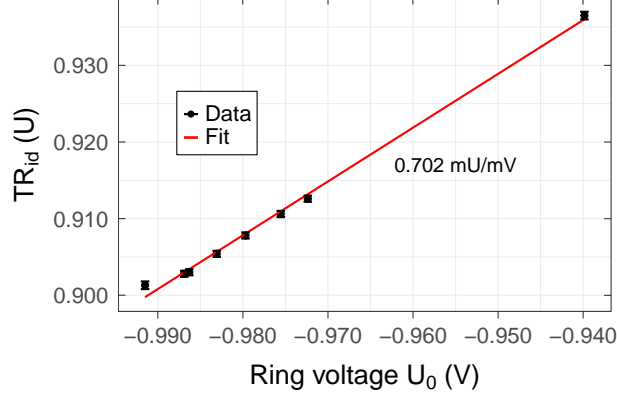
Figure 7.7: Ideal TR as a function of ring voltage U_0 in the TMT. The different ring voltages arise from different cyclotron energies and the $\nu_z(B_2, E_+)$-shift. The linear relationship between TR and U_0 stems from a non-zero B_4-coefficient of the TMT. The different cyclotron energies are prepared via sideband-coupling to an axial temperature of order $10\,\mathrm{K}$.

theoretical lineshape is derived in reference [39] and reads

$$\chi(\nu) = \frac{4}{\pi}\Re \left(\frac{\Delta\omega_1' \Delta\omega_1}{(\Delta\omega_1' + \Delta\omega_1)^2} \cdot \right. \tag{7.2}$$

$$\left. \sum_{n=0}^{\infty} \frac{(\Delta\omega_1' - \Delta\omega_1)^{2n}(\Delta\omega_1' + \Delta\omega_1)^{-2n}}{(n+1/2)\Delta\omega_1' - \Delta\omega_1/2 - 2\pi i(\nu - \nu_{+,0})} \right).$$

Here $\Delta\omega_1$ is the dip width in radians (equation (2.42)) and $\Delta\omega_1' = \sqrt{\Delta\omega_1^2 + 4i\Delta\omega_1\Delta\omega}$ is a modified dip width accounting for a linewidth parameter $\Delta\omega \propto T_z$. The measured lineshape is fitted with equation (7.2) and $\nu_{+,0}$ is extracted for different axial equilibrium positions z_0 of the ion. To change the axial position of the ion a voltage offset to one of the endcap electrodes is applied, which introduces an asymmetry that shifts the electric potential minimum. The shift in position is determined for the given trap geometry with COMSOL™ [48] and amounts to $\Delta z_0/\Delta U_{ec} = 16.3(2)\,\mu\mathrm{m}/(100\,\mathrm{mV})$. The measurement of the magnetic field for different axial positions is shown in figure 7.6(b). A quadratic fit yields

$$B_2 = 27.8(7)\,\mathrm{kT/m}^2. \tag{7.3}$$

The uncertainty of B_2 arises dominantly from the uncertainty of $\Delta z_0/\Delta U_{ec}$. This value is in perfect agreement with the target value of $27.7\,\mathrm{kT/m}^2$ based on COMSOL™ simulations [48].

7.2.4 TMT B_4 measurement

Besides a large B_2-coefficient, the TMT features a significant non-zero B_4. This coefficient causes the ideal tuning ratio $\mathrm{TR_{id}}$ to become a function of the cyclotron energy. While the effect is negligible for temperature measurements with beryllium ions, it is crucial to account for when performing temperature measurements with a single proton, especially for temperatures above $1\,\mathrm{K}$. The B_4-coefficient is given by [110, p. 42]

$$B_4 = -\frac{\partial \mathrm{TR_{id}}}{\partial U_0}\frac{\partial U_0}{\partial \nu_z}\underbrace{\frac{B_2}{2B_0}\frac{\nu_+ + \nu_-}{\nu_-}\nu_z\frac{1}{4\pi^2 m\nu_+^2}}_{=\frac{\partial \nu_z}{\partial E_+}} m2\pi(\nu_+ - \nu_-)|U_0|D_4. \tag{7.4}$$

Here, $\frac{\partial \mathrm{TR_{id}}}{\partial U_0}$ is the relevant parameter that needs to be experimentally determined and of which the measurement is shown in figure 7.7. All other quantities are given by the trap and particle properties. The data is recorded by determining $\mathrm{TR_{id}}$ via a TR scan for different cyclotron energies sampled by sideband coupling to the axial resonator with a temperature of order $10\,\mathrm{K}$. $\frac{\partial \mathrm{TR_{id}}}{\partial U_0}$ is given by the slope of the linear fit and amounts to

$$\frac{\partial \mathrm{TR_{id}}}{\partial U_0} = 0.702\,\mathrm{mU/mV}, \tag{7.5}$$

thus yielding

$$B_4 = (-4.4 \pm 0.5) \times 10^6\,\mathrm{T/m^4}. \tag{7.6}$$

A TR deviation of only 1–$2\,\mathrm{mU}$ causes significant loss in dip SNR already, compare the data in figure 7.4(b) where the SNR loss is even alleviated due to the smaller D_4 of the PT. Since a $10\,\mathrm{K}$ distribution extends over several kHz in axial frequency corresponding to detunings of tens of mV in ring voltage, it is crucial to adjust the TR accordingly. This experimentally obtained value compares to a simulated one of $B_4^{\mathrm{sim}} = -3.8 \times 10^6\,\mathrm{T/m^4}$ [48]. Accounting for the fact that B_4 is already a higher-order coefficient, this can still be considered a good agreement.

7.3   Proton cyclotron frequency drift as a function of fill level

Currently, the trap chamber is mounted on a rather long lever arm which is fixated at the bottom of the liquid helium bath cryostat, compare section 3. This causes the position of the trap stack within the magnet to be a function of the weight of the LHe cryostat, i.e. a function of the liquid helium level. Combined with the fact that the modified cyclotron frequency of a single proton is overwhelmingly determined by the magnetic field, these effects lead to the circumstance that the proton cyclotron frequency is a function of the liquid helium level. The cyclotron frequency of a single proton over about three filling cycles (one week) is shown in figure 7.8. Cyclotron frequency jumps of up to $12\,\mathrm{Hz}$ can be unambiguously attributed to the LHe filling. While this effect is merely an inconvenience for sympathetic cooling measurements, it is a severe issue for the next-generation g-factor measurement of the proton. As a consequence, a new concept for the cryo-mechanical support that is based on mounting the trap relative to the magnet flanges is currently in development.

7.4   Two-trap temperature measurements with the TMT

7.4.1   Inferring temperatures from frequency shifts

In this subchapter, the method and data analysis procedure for the two-trap temperature measurements will be outlined in detail. Assuming the particle is initially trapped in the CT, the cyclotron sideband is irradiated continuously. This thermalizes the cyclotron mode to the axial temperature. After the cyclotron sideband is turned off, the cyclotron energy remains constant again. Thus, applying the cyclotron sideband can be considered sampling a new value of the Boltzmann distribution. Then, the particle is transported into the TMT, where its axial frequency is measured. Invoking equation (2.28), this frequency is the sum of the unshifted axial frequency at $E_+ = 0$, $\nu_{\mathrm{z},0}^{\mathrm{TMT}}$, and the frequency shift due to non-zero E_+. However, since $\nu_{\mathrm{z},0}^{\mathrm{TMT}}$ is unknown initially, a single measurement is not sufficient to determine an energy or temperature. Thus, the particle must be transported back into the
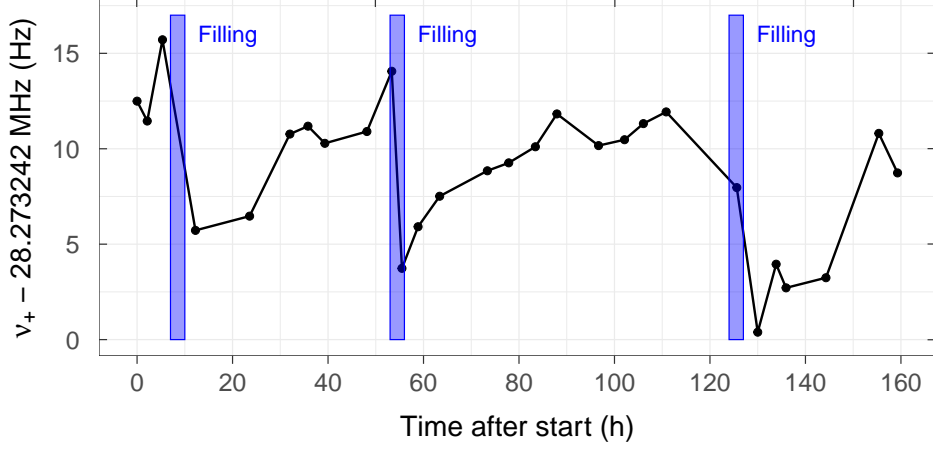
Figure 7.8: Cyclotron frequency of a proton over the course of one week. The refilling of the liquid helium bath cryostat changes the position of the trap stack in the magnet and thus causes frequency jumps of up to $12\,\mathrm{Hz}$.

CT and the whole process must be repeated. In this way a distribution of axial frequencies in the TMT is measured. As a practical example, the axial temperature measurement of a single beryllium ion in the CT will be examined in the following. The sequence of axial frequency measurements in the TMT is shown in figure 7.9(a). The cryogenic amplifier of the CT was turned off for this measurement. To infer a temperature from this frequency distribution, the following effects have to be accounted for: First, since the TMT measures cyclotron energies, the cyclotron temperature is determined via equation (2.28). In general, it can be shown that the mean of the observations of an exponential distribution is equal to the maximum-likelihood estimator of the distribution parameter. Applied to our case, this means that the maximum-likelihood estimator of the cyclotron temperature in the TMT is given by

$$T_+^{\mathrm{TMT}} = \frac{4\pi^2}{k_{\mathrm{B}}} \frac{B_0^{\mathrm{TMT}}}{B_2^{\mathrm{TMT}}} m\, \nu_{\mathrm{z},0}^{\mathrm{TMT}} \left\langle \nu_{\mathrm{z,i}} - \nu_{\mathrm{z},0}^{\mathrm{TMT}} \right\rangle, \tag{7.7}$$

where $\nu_{\mathrm{z,i}}$ are the individual axial frequencies in the TMT, $\left\langle \nu_{\mathrm{z,i}} - \nu_{\mathrm{z},0}^{\mathrm{TMT}} \right\rangle$ is the mean frequency shift, and $\nu_{\mathrm{z},0}^{\mathrm{TMT}} \equiv \nu_{\mathrm{z}}^{\mathrm{TMT}}(E_+ = 0)$ the lower cut of the frequency distribution. Furthermore, compared to equation (2.28), this formula assumes $\nu_{\mathrm{z}}^2 = 2\nu_+\nu_-$ and $(\nu_+ + \nu_-)/\nu_- \approx \nu_+/\nu_-$, which is both fulfilled at our experiment. The next effect that needs to be accounted for is the fact that during the particle transport, the cyclotron quantum number n_+ is the conserved quantity and not the cyclotron energy E_+. Since $E_+ = \hbar\omega_+(n_+ + 1/2)$, the different magnetic field of the TMT due to the ferromagnetic ring electrode changes E_+ and T_+. Consequently, the cyclotron temperature in the CT must be scaled up by

$$T_+^{\mathrm{CT}} = \frac{B_0^{\mathrm{CT}}}{B_0^{\mathrm{TMT}}} T_+^{\mathrm{TMT}}. \tag{7.8}$$

While this effect is a correction of about 5% only, it must be taken into account for accurate temperature determinations. Finally, the cyclotron sideband drive couples the temperatures according to $T_{\mathrm{z}} = \frac{\nu_{\mathrm{z}}}{\nu_+} T_+$, see equation (2.58). In total, the axial temperature of the particle in the CT is determined by

$$T_{\mathrm{z}}^{\mathrm{CT}} = \frac{\nu_{\mathrm{z}}^{\mathrm{CT}}}{\nu_+^{\mathrm{CT}}} \frac{B_0^{\mathrm{CT}}}{B_0^{\mathrm{TMT}}} \frac{4\pi^2}{k_{\mathrm{B}}} \frac{B_0^{\mathrm{TMT}}}{B_2^{\mathrm{TMT}}} m\, \nu_{\mathrm{z},0}^{\mathrm{TMT}} \left\langle \nu_{\mathrm{z,i}} - \nu_{\mathrm{z},0}^{\mathrm{TMT}} \right\rangle. \tag{7.9}$$

Although technically axial energies are not measured, equation (7.9) can be used to define
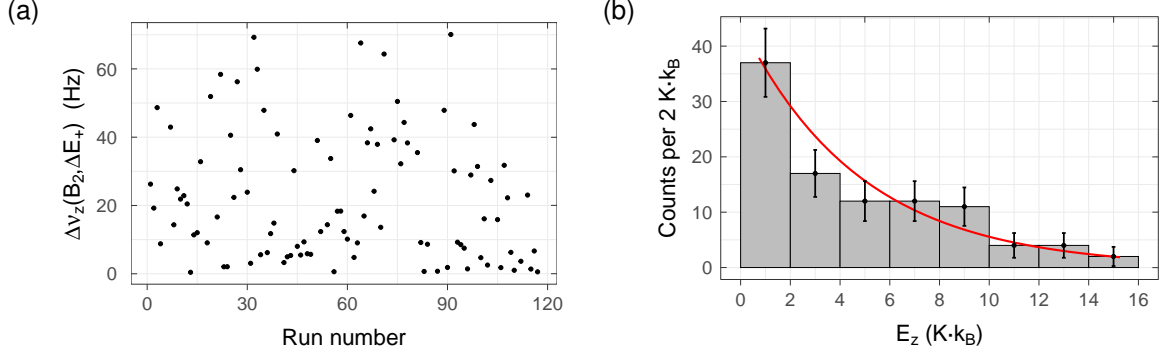
Figure 7.9: Demonstration of a two-trap temperature measurement for a single beryllium ion in the CT and TMT. In (a) the sequence of axial frequency shifts relative to the minimum in the TMT is shown. In between these measurements the cyclotron energy is thermalized to the axial resonator in the CT. In (b) the resulting binned Boltzmann distribution is shown. The red line corresponds to a Boltzmann distribution whose temperature is calculated by the maximum-likelihood method.

individual $E_{\mathrm{z,i}}^{\mathrm{CT}}$ by substituting $\langle \nu_{\mathrm{z,i}} - \nu_{\mathrm{z,0}}^{\mathrm{TMT}} \rangle \to \nu_{\mathrm{z,i}} - \nu_{\mathrm{z,0}}^{\mathrm{TMT}}$, yielding

$$E_{\mathrm{z,i}}^{\mathrm{CT}} = k_{\mathrm{B}} \frac{\nu_{\mathrm{z}}^{\mathrm{CT}}}{\nu_{+}^{\mathrm{CT}}} \frac{B_0^{\mathrm{CT}}}{B_0^{\mathrm{TMT}}} \frac{4\pi^2}{k_{\mathrm{B}}} \frac{B_0^{\mathrm{TMT}}}{B_2^{\mathrm{TMT}}} m\, \nu_{\mathrm{z,0}}^{\mathrm{TMT}} \left(\nu_{\mathrm{z,i}} - \nu_{\mathrm{z,0}}^{\mathrm{TMT}} \right). \tag{7.10}$$

The same principles apply if the proton is trapped in the PT instead of the CT. Due to the different axial frequencies the shifts per Kelvin axial temperature are slightly different between CT and PT, namely

$$T_{\mathrm{z,p}}^{\mathrm{CT}} = 360\,\mathrm{Hz/K} \tag{7.11}$$

$$T_{\mathrm{z,Be}}^{\mathrm{CT}} = 4.5\,\mathrm{Hz/K} \tag{7.12}$$

$$T_{\mathrm{z,p}}^{\mathrm{PT}} = 470\,\mathrm{Hz/K} \tag{7.13}$$

$$T_{\mathrm{z,Be}}^{\mathrm{PT}} = 5.8\,\mathrm{Hz/K}. \tag{7.14}$$

Applying equation (7.9) to the example measurement, the corresponding Boltzmann distribution shown in figure 7.9(b) is obtained. Before calculating a final temperature, it is imperative to note that this method assumes that every possible cyclotron energy is detected. However, depending on the particle dip width, the particles can only be reliably detected $\approx 50 - 150\,\mathrm{Hz}$ off-resonant to the resonator frequency. As a result, for beryllium ions at $T_{\mathrm{z}} \gtrsim 5\,\mathrm{K}$ or protons at $T_{\mathrm{z}} \gtrsim 100\,\mathrm{mK}$ several TMT spectra have to be recorded, where the particle is 'searched' by lowering the ring voltage $|U_0|$. The frequency shift of the particle can then be calculated via the precisely measurable parameters $\frac{\partial \nu_{\mathrm{z}}}{\partial U_0}$ and $\frac{\partial \nu_{\mathrm{z}}}{\partial \mathrm{TR}}$. If this method is employed, for practical reasons a certain threshold for the maximal number of TMT spectra is defined, which is chosen sufficiently high that $> 80\%$ of the cyclotron energies are detected. However, the remaining $< 20\%$ where the axial frequency shift is above the threshold $\Delta\nu_{\mathrm{z,max}}$ have to be accounted for in the data analysis nonetheless. To this end, the mean axial frequency shift $\langle \Delta\nu_{\mathrm{z}} \rangle \equiv \langle \nu_{\mathrm{z,i}} - \nu_{\mathrm{z,0}}^{\mathrm{TMT}} \rangle$ of the normalized, truncated Boltzmann distribution is given by

$$\begin{aligned} \langle \Delta\nu_{\mathrm{z}} \rangle &= \int_0^{\Delta\nu_{\mathrm{z,max}}} \frac{1}{1 - e^{-\Delta\nu_{\mathrm{z,max}}/(\lambda_+ k_B T_+)}} \times \\ &\quad \frac{1}{\lambda_+ k_B T_+} e^{-\frac{\Delta\nu_{\mathrm{z}}}{\lambda_+ k_B T_+}} \Delta\nu_{\mathrm{z}}\, d(\Delta\nu_{\mathrm{z}}) \\ &= \lambda_+ k_B T_+ - \frac{\Delta\nu_{\mathrm{z,max}}}{e^{\frac{\Delta\nu_{\mathrm{z,max}}}{\lambda_+ k_B T_+}} - 1} \end{aligned} \tag{7.15}$$
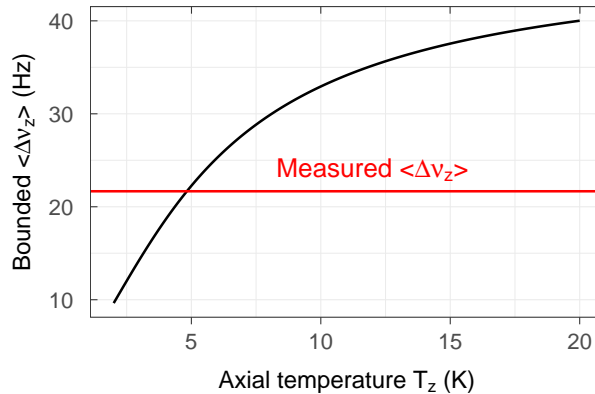
Figure 7.10: Numerical determination of the axial temperature based on the bounded mean shift. The black line corresponds to the theoretical calculation and the red horizontal line to the measured mean frequency shift. The intersection yields the temperature, in this case about 4.8 K.

where for readability $T_+ \equiv T_+^{\mathrm{TMT}}$. In addition, the abbreviation

$$\lambda_+ = \frac{1}{4\pi^2} \frac{B_2^{\mathrm{TMT}}}{2B_0^{\mathrm{TMT}}} \frac{1}{m\nu_{\mathrm{z},0}^{\mathrm{TMT}}} \tag{7.16}$$

is used, compare equation (7.7). Since $\langle \Delta\nu_{\mathrm{z}} \rangle$ is the observable, equation (7.15) is solved numerically for T_+^{TMT}. $T_{\mathrm{z}}^{\mathrm{CT/PT}}$ is then obtained in the same manner as previously. Artificial Boltzmann distributions with known temperature were simulated to backtest this analysis and confirm that this method does not introduce any relevant bias for the obtained temperature. In the case of the example measurement, only one TMT spectrum was recorded deliberately and in 16 of 118 spectra no unambiguous dip signal of the beryllium ion was observed. Accounting for the corresponding cutoff frequency, the numerical solution of equation (7.15) is shown in figure 7.10. The black line depicts the temperature as a function of the observed shift as calculated by equation (7.15) and the horizontal red line corresponds to the measured $\langle \Delta\nu_{\mathrm{z}} \rangle$. In this way, a temperature of $T_{\mathrm{z}}^{\mathrm{CT}} = (4.85 \pm 0.25)\,\mathrm{K}$ is obtained. The uncertainty is assumed to be of statistical nature only and calculated by $T_{\mathrm{z}}^{\mathrm{CT}}/\sqrt{N}$, where N is the number of individual cyclotron energy measurements. This method is applicable as long as the measured mean shift is in the linear range of the black line in figure 7.10, as it is the case here to a good degree. If $\langle \Delta\nu_{\mathrm{z}} \rangle$ were in the saturation region, the associated 'vertical' statistical uncertainty would translate into a significantly larger uncertainty for the final axial temperature.

As a final note, in anticipation of the sympathetic cooling measurements in section 9, the truncated method was not required for the sympathetically cooled proton since here only few axial TMT spectra were required and the proton was detected in every cycle. However, it was required for the measurement of the detector temperature, but the number of TMT spectra was chosen sufficiently large that the mean bounded shift is in the linear region.

7.4.2   TMT temperature resolution and transport heating rate

A crucial ingredient for precise two-trap temperature measurements is that the transport heating rate is sufficiently low. To this end, the exact same sequence for an on-resonance coupling measurement with a proton in the PT and a cloud of beryllium ions in the LT was carried out. The detailed sequence will be described in section 9, however, for now it is sufficient that every step is included in the same order. The only difference to a real
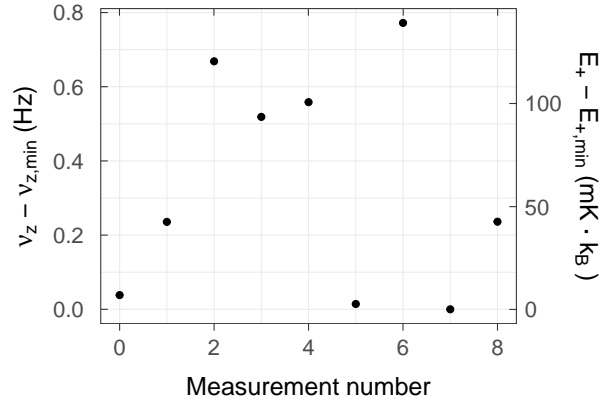
Figure 7.11: Investigation of a possible heating rate via axial frequency measurements of a single proton in the TMT. In between the individual measurements the complete routine for on-resonance cooling is performed. The axial frequency fluctuations of $\leq 800\,\mathrm{mHz}$ translate into cyclotron energy fluctuations of $\leq 140\,\mathrm{mK} \cdot k_B$ or axial energy fluctuations of $1\text{-}2\,\mathrm{mK} \cdot k_B$.

coupling sequence is that the frequency of the cyclotron sideband drive of the proton was detuned by 10 kHz. This detuning ensures that possible heating effects from the drive itself can be detected but the cyclotron mode is not thermalized. This sequence consists not only of transporting the proton, but also shining in the cooling laser at the beryllium ions, applying the magnetron sideband drives for both the proton and beryllium ions, as well as changing the ring voltage of the beryllium ions.

The axial frequency sequence recorded this way is shown in figure 7.11. The maximal deviation within 9 data points is 800 mHz, corresponding to about $140\,\mathrm{mK} \cdot k_B$ in cyclotron energy. Accounting for $T_z = \frac{\nu_z}{\nu_+}T_+$, this constitutes less than $1.5\,\mathrm{mK} \cdot k_B$ uncertainty in axial energy and is thus negligible for the axial temperatures of 140–160 mK reached in this thesis. In other words, the target axial temperature resolution of the TMT of 1-2 mK is achieved. It should be noted that the due to the sideband coupling the cyclotron energy resolving power scales approximately $\propto 1/m^2$, i.e. the resolution is a factor of 81 worse and only $\approx 100\,\mathrm{mK}$ for a beryllium ion. Furthermore, this data is consistent with the absence of any additional heating source on a level of 1 mK per cycle. The observed fluctuations are in agreement with those expected from the combination of the jitter of the power supply, the repeated thermalization of the magnetron mode, and the cyclotron transition rate. Finally, if in future experiments an even better temperature resolution is required, the AT can be employed as temperature measurement trap.

7.5 Laser cooling of beryllium ions

The proper adjustment of the laser cooling parameters is crucial to control large beryllium clouds and comprises several steps. First, the laser beam path is coarsely adjusted based on a photodiode signal. Second, the vanishing dip signal of beryllium ions is recorded. Third, the cooling resonance frequency is determined based on the fluorescence signal. Fourth and finally, an intensity gradient of the laser at the position of the beryllium ions is introduced for efficient magnetron cooling.
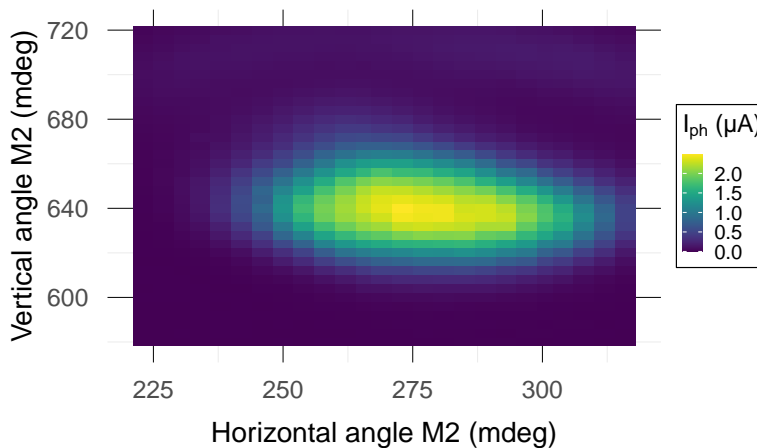
Figure 7.12: Two-dimensional scan of the photodiode current I_{ph} as a function of the vertical and horizontal angle of the second piezo-mirror mount.

7.5.1   Photodiode signal

In a first step, the laser beam path is coarsely adjusted based on the photodiode signal (compare section 3.8). The photodiode is mounted on top of the resonator housing and is operated in zero-bias mode. The piezo-motor mount of the fibre output ('M1', compare figure 3.10) is manually adjusted such that the beam path approximately aligns with the trap stack. Then, a two-dimensional scan of the photo diode signal as a function of the horizontal and vertical angle of the mirror installed on the second piezo-motor mount ('M2') is recorded. These directions will be referred to as M2h and M2v in the following. An example of such a scan is shown in figure 7.12. If no signal is observed over the full range of M2, the offset must be adjusted manually. Note that the absolute position of the photo diode signal in terms of M2h and M2v changes if M1 is changed, however, the width of the signal is to first order the same since it is determined by the size of photodiode. The fact that the vertical width is smaller stems from the fact that the photodiode is tilted downwards to avoid back reflections.

7.5.2   Vanishing dip signal

Since the laser beam width is larger than the ion radius, the laser beam can be adjusted to the maximum photodiode current and it is practically guaranteed that the ions will be illuminated to some degree. Hence, the next step is to observe the laser-cooling of beryllium ions via the characteristic vanishing of the SNR of the dip signal [26]. The SNR loss occurs if the damping rate of the beryllium ions due to the laser is comparable to the dip width, so that the beryllium ions cannot fully short the resonator noise anymore. Therefore it is a distinct signal of laser cooling. A measured example for different laser frequency detunings is shown in figure 7.13. However, at first the detuning to the resonance frequency is not known and has to be searched. While the resonance frequencies from earlier experimental runs are a good starting point, it must be searched again for each cooldown due to slightly different magnetic fields at the position of the ions and possible long-term drifts of the wavemeter. The SNR method can be used natively, as it does not require fluorescence detection and can therefore be employed in any trap. Furthermore, when sweeping the laser frequency up at sufficient laser power, the reduction in dip SNR is observed earlier than a significant rise in fluorescence counts.
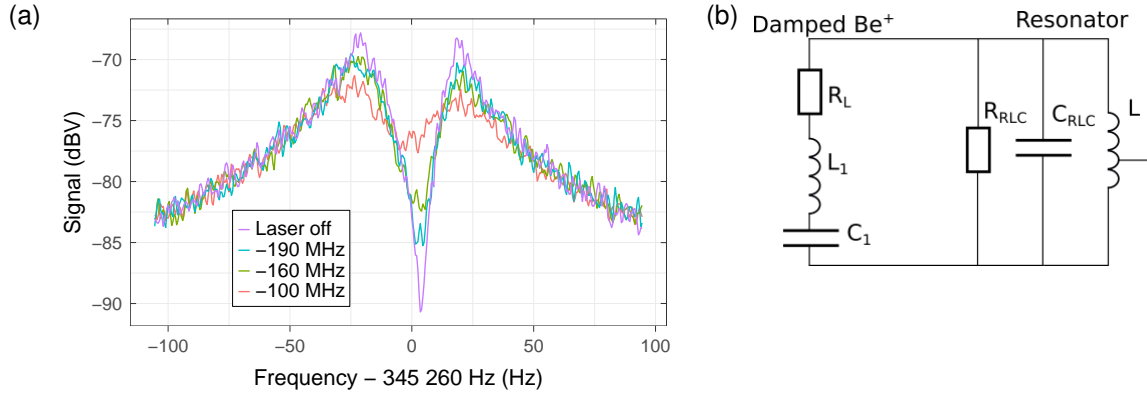
Figure 7.13: The dip of the beryllium ions loses in SNR if the damping rate of the cooling laser becomes comparable to the dip width, as visible in (a). The beryllium ions cannot fully compensate the resonator noise anymore due to the cooling by the laser. This decoupling can be described by an additional laser resistance R_L in the equivalent circuit model, as shown in (b).
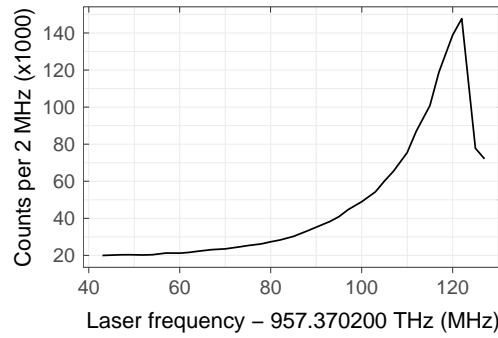

Figure 7.14: Measurement of the resonance frequency of the laser cooling transition by means of fluorescence detection.

Theoretically, the damping by the laser can be modelled as an additional series resistance R_L in the equivalent circuit model, see figure 7.13(b). The impedance is then given by

$$Z_{\mathrm{RLC+ion}}(\omega) = \cfrac{1}{\cfrac{1}{R_L + i\omega L_1 + \frac{1}{i\omega C_1}} + \frac{1}{R_{\mathrm{RLC}}} + \frac{1}{i\omega L} + i\omega C_{\mathrm{RLC}}}. \qquad (7.17)$$

Concrete calculations of the laser damping resistances can be found in refs. [27, 48, 85].

7.5.3 Laser cooling resonance

If available, the loss in dip SNR should be corroborated by fluorescence detection. An exemplary laser frequency scan is shown in figure 7.14. Once the resonance frequency of in our case $957.370\,320\,\mathrm{THz}$ has been found, the laser frequency can be adjusted in terms of detuning to the resonance. Note that due to lack of necessity the wavemeter had not been calibrated for an extended time period so that the absolute value of the transition frequency should only be treated as a coarse estimate. In addition, the polarization of the laser can be optimized by maximizing the fluorescence signal. Furthermore, several quantities such as the temperature of the beryllium cloud can be estimated based on the lineshape of the fluorescence signal, as described in detail in refs. [48, 85].

7.5.4   Gradient adjustment and laser beam width

A crucial ingredient to control large beryllium clouds ($N > 1000$) is the ability to establish the laser setting described theoretically in section 2.7.3 in the experiment. In summary, in order to cool the magnetron and cyclotron motion simultaneously, the ions must be subjected to a laser intensity gradient in radial direction. This setting can be prepared based on the fluorescence signal. An example of the procedure is shown in figure 7.15. The laser frequency is modulated with a smoothed rectangular function ('thimble'), where the upper laser frequency is adjusted to be only several MHz below the resonance frequency, creating the oscillatory peak structure in the observed fluorescence counts. By using a rectangular frequency modulation, the background signal is monitored continuously, which ensures that the peak signals truly stem from fluorescence counts and not merely from beam reflections. The height of the fluorescence peaks is a measure of the relative spatial difference between the intensity maximum of the laser beam and the position of the ions. The annotated numbers above the braces are the angles of the horizontal direction of the second mirror in degree, i.e. M2h. Starting at M2h $= -0.170$ deg, the angle is decreased in steps of 4 mdeg. This increases the fluorescence counts up until the maximum at -0.186 deg is reached. Going beyond this maximum, a continuous loss in fluorescence signal is observed even though the mirror position is not further changed. This is consistent with the theory described in section 2.7.3, as beyond the maximum the gradient changes sign, which then leads to an expansion of the ion cloud. However, the ions can be recovered by adjusting M2h back to the cooling region. The final setting is chosen to be M2h $= -0.178$ deg, since here the fluorescence counts are at about half of the maximal counts. This position thus corresponds to the maximum of the gradient, as outlined in section section 2.7.3. The vertical angle M2v is optimized to its fluorescence maximum and kept at that position. Note that the mirror mounts exhibit a small hysteresis if the sign of subsequent angle changes is swapped.

Furthermore, this data allows to estimate the beam width. The axial distance from the LT ring electrode to M2 is about 60 cm. An angle change of approximately 8 mdeg leads to a reduction of the fluorescence signal by a factor of 2. Thus, assuming the radius of the ions is negligible, trigonometric considerations yield a full width at half maximum (FWHM) of the beam of about 170 μm.

7.5.5   Choice of laser frequency detuning

The choice of laser detuning needs to account for several aspects. First and foremost, the condition for simultaneous magnetron and cyclotron cooling, $\nu_- < \zeta < \nu_+$ (equation (2.78)), described in section section 2.7.3 must be fulfilled. Assuming the beam profile has Gaussian shape, the parameter y_0 describing the local intensity gradient at $I = I_{\max}/2$ can be approximated in terms of the full width at half maximum (FWHM) by $y_0 \cong \frac{1}{2\ln(2)}$FWHM. Thus, apart from the constant wavelength and width of the transition, ζ is a function of the laser detuning and beam width only. Figure 7.16(a) shows ζ for different laser detunings and beam widths. From the scale it is directly apparent that $\zeta < \nu_+$ is automatically fulfilled for all practical settings. In contrast, fulfilling $\nu_- < \zeta$ requires active adjustment. With the previously estimated beam width of 170 μm the condition is fulfilled at a laser detuning of about -130 MHz or larger red detunings. In practice, the sympathetic cooling measurements for the largest beryllium cloud were performed at -200 MHz. Since the on-resonance sympathetic cooling scheme only requires very low damping rates (compare figure 6.16), this detuning is sufficiently large that a convenient laser power of order 100 μW could be used. Smaller laser powers, especially smaller than
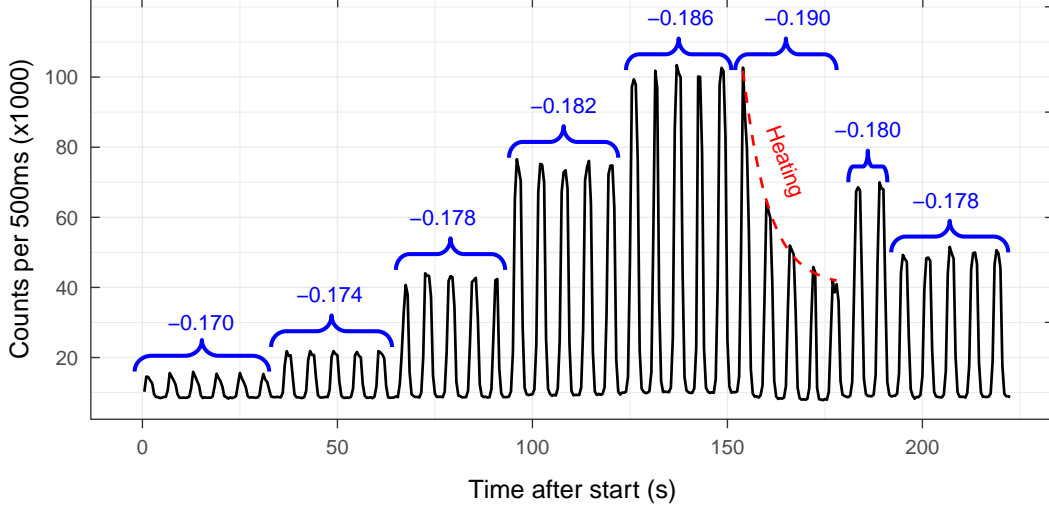
Figure 7.15: Optimization of the beam path of the cooling laser. The laser frequency is modulated with a smoothed rectangular function, where the upper frequency is close to the resonance, thus generating the peak-like fluorescence signal. The annotated numbers are the horizontal angles of the last mirror in the beam path. The ions are only cooled on one flank of the maximal illumination. On the other flank, the ion cloud expands, observable as a loss in fluorescence signal.

$10\,\mu\text{W}$, are difficult to adjust precisely due to the background light in the laboratory. In addition, operating the laser at $10\,\Gamma$ red-detuning also has the advantage that drifts of the wavemeter, which are typically on the order of 2–3 MHz over several hours, do not alter the effective damping rate and improve the relative stability over one sympathetic cooling measurement. On the other hand, even larger red detunings would require more than the currently technically available laser power to achieve the desired laser damping rates.

As a final note, the condition for simultaneous magnetron and cyclotron cooling assumes a single particle. In reality, large clouds of more than 1000 ions are used so that the Coulomb interaction cannot be neglected anymore and applying the magnetron sideband drive is still necessary to keep the cloud cold. Furthermore, plasma effects start to occur, such as axial frequency drifts that depend on the trap harmonicity. These effects will be discussed in section 9.

7.5.6   Determination of the saturation laser power

The remaining quantity to fully characterize the laser cooling is the saturation intensity or saturation power. While it is an intrinsic property of the transition, it is conveniently measurable. To this end, the fluorescence counts were recorded as a function of the laser power. The laser power is measured by scaling up the fraction of the light that is reflected by a laser polarizer as described in section 3.8. The data is shown in figure 7.16(b) and a fit with

$$\gamma_{\text{s,eff}} = \gamma_{\text{bgd}} + \eta \frac{P}{P_{\text{sat}}} \frac{\Gamma/2}{1 + \frac{P}{P_{\text{sat}}} + 4\left(\frac{\omega - \omega_{\text{L0}}}{\Gamma}\right)^2} \tag{7.18}$$

is performed. This equation is a modified version of equation (2.72), where $\frac{I}{I_{\text{sat}}} \to \frac{P}{P_{\text{sat}}}$ was substituted and a background rate γ_{bgd} as well as an effective efficiency η was accounted for. The data was recorded at a fixed laser detuning of $\omega - \omega_{\text{L0}} = 2\pi \cdot 8\,\text{MHz}$. The fit yields a saturation power of $P_{\text{sat}} = 344\,\mu\text{W}$.
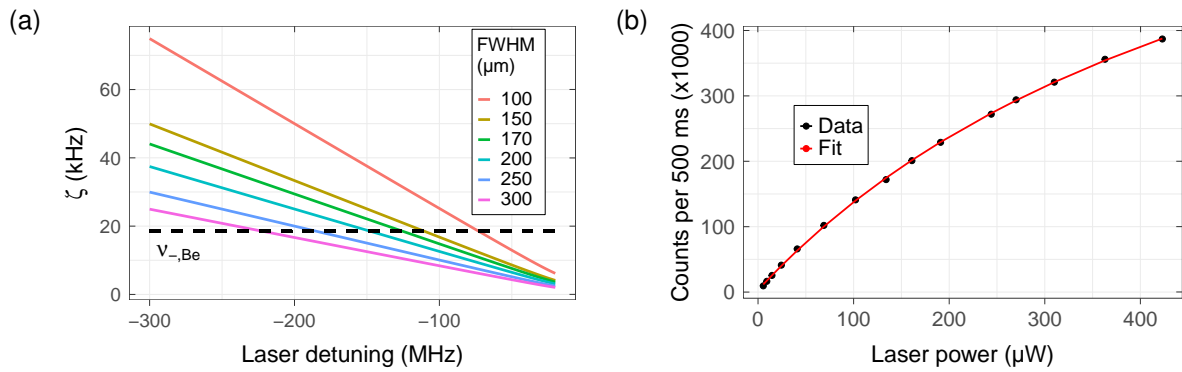
Figure 7.16: (a) Calculation of the rate ζ based on equation (2.78). It is assumed that the beam profile is Gaussian and the position of the ions is at half of the maximum laser intensity. This allows to express the gradient in terms of the full-width at half maximum (FWHM) of the beam. The estimated beam FWHM based on the data of figure 7.15 is $170\,\mu$m. (b) Determination of the saturation laser power via fluorescence detection.

8 | Frequency shift and SNR reduction due to non-zero C_4

As mentioned in section 6 already, in the course of benchmarking the simulations, all first-order magnetostatic and electrostatic frequency shifts, i.e. all combinations of $\{\nu_+, \nu_z, \nu_-\} \star \{C_4, B_2\} \star \{\hat{\rho}_+, \rho_z, \hat{\rho}_-\}$, were cross-checked. All simulated frequency shifts matched the theoretical ones to at maximum a few percent deviation, except the $\nu_z - C_4 - \rho_z$ shift, where the simulated shift was a factor of 2 too large. While this deviation was initially considered a bug in the simulation code, upon further investigation no error could be found. Although the primary goal of the experimental campaign was and still is the sympathetic cooling of a single proton, the comprehensive understanding of frequency shifts is nevertheless a crucial ingredient for the next generation of Penning-trap based precision measurements, see also refs. [41, 111]. Thus, a dedicated experimental investigation was launched as a 'sidequest', which ultimately confirmed the simulation result. Notably, the theoretical shift is not incorrect, but rather its direct application to our experimental setting. The difference lies in the fact that the theoretical shift assumes constant axial energy, whereas in the experiment the energies are Boltzmann-distributed. In the following, all measurements involving a C_4 were conducted with a single beryllium ion in the CT, since the relevant experimental quantities are favourable here. Independent temperature measurements were performed with the TMT.

8.1   Simulating the C_4-shift

The possibility of simulating the C_4-shift is implemented by adding another force that is proportional to $\frac{\partial}{\partial z} z^4$ in the differential equation of the axial motion. Using the definition of equation (2.23), the differential equation of the coupled system then reads:

$$m\ddot{z} + 2qC_2U_0 z + 4qC_4U_0 z^3 - \frac{q}{D}L\dot{I}_L = 0 \tag{8.1}$$

$$LC_{\mathrm{RLC}}\ddot{I}_{\mathrm{L}} + \frac{L}{R_{\mathrm{RLC}}}\dot{I}_L + I_L + I_{\mathrm{noise}} + \frac{q}{D}I_{\mathrm{ind}} = 0, \tag{8.2}$$

where $D \equiv D_{\mathrm{RLC,Be}}$. The simulation of the radial modes are not performed since they do not play a role here. The trap and resonator parameters are set to be the exact same ones as in the experiment.

The $\nu_z(C_4, E_z)$-shift is simulated twofold: First, in order to confirm the theoretical shift, equation (2.25) in section 2.2.1, the frequency shift at constant particle energy $E_z = 15\,k_B\cdot\mathrm{K}$ is simulated by disabling the resonator simulation. The particle frequency is determined directly by calculating the mean frequency of the power spectral density of the axial motion of the particle. The simulated data is shown as rectangles in figure 8.1 and perfect agreement with the theory at constant energy is observed. The numerical value is

$$\frac{\Delta\nu_z(C_4, \rho_z)}{\Delta\mathrm{TR}\,\Delta T_z} = 28.1\,\mathrm{Hz/(K\cdot U)}. \tag{8.3}$$

However, in the experiment the axial energy is not constant but continuously samples a Boltzmann distribution. Therefore, as a second step, Boltzmann-distributed energies are simulated by enabling the resonator simulation with $T_{\mathrm{RLC}} = 15\,\mathrm{K}$ and fitting the resulting dip spectra with equation (2.43) to extract ν_z. The averages of the resulting ν_z-shifts of five independent simulation runs per $\Delta\mathrm{TR}$ are shown as circles in figure 8.1. A linear fit
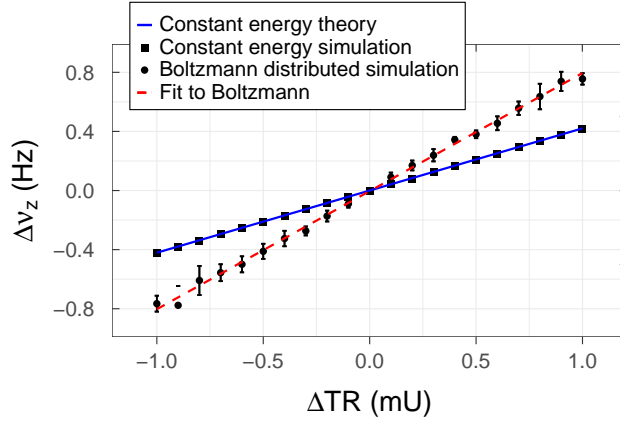
Figure 8.1:   Simulated axial frequency shifts as a function of the anharmonicity $C_4 = D_4 \Delta TR$. The simulations agree perfectly with the constant-energy case (error bars are smaller than the rectangles). However, once the axial energy of the particle samples a Boltzmann distribution, the derived frequency shift is a factor of ≈ 2 larger.

(red line) yields

$$\frac{\Delta \nu_z(C_4)}{\Delta TR \, \Delta T_z} = 53.3 \, \text{Hz}/(\text{K} \cdot \text{U}), \tag{8.4}$$

strongly indicating the existence of an additional factor of 2 in the $\nu_z(C_4, T_z)$-shift. Note that the same result is obtained if the mean frequency is calculated based on the direct FFT of the particle motion, which is however only possible in the simulations.

8.2   Measurement of D_4

As a first step of measuring the C_4-shift, the D_4-coefficient of the trap has to be determined independently. To this end, the axial frequency shift due to non-zero cyclotron energy, equation (2.26) in section 2.2.1, is employed with $C_4 = D_4 \Delta TR$. No factor of 2 is present for this shift since the cyclotron energy is constant over an axial frequency measurement. In particular, ν_z is measured at $\Delta TR = +1 \, \text{mU}$ before and after applying a cyclotron sideband drive. To enhance the shift, positive feedback is applied such that $T_z = 34.0 \, \text{K}$. Note that this is the largest temperature setting employed to measure the $\Delta \nu_z(C_4, T_z)$-shift in the next section. The cyclotron sideband drive changes the cyclotron energy by ΔE_+, thus shifting the frequency by $\Delta \nu_z(C_4, \Delta E_+)$. ΔE_+ is determined by measuring the cyclotron energy for each axial frequency measurement in the CT with the TMT. In this way, $\Delta \nu_z(C_4, \Delta E_+)$ can be related to ΔE_+ as shown in figure 8.2. The scatter of the data points stems from the finite axial frequency stability of about $\delta \nu_z = 40 \, \text{mHz}$. A linear fit yields

$$\begin{aligned} D_4 &= -\frac{\Delta \nu_z(C_4, \Delta E_+)}{\Delta E_+} \frac{C_2 4\pi^2 m \nu_+^2}{3\nu_z \Delta TR} \\ &= 3.32(19) \times 10^{10} \, \text{m}^{-4}. \end{aligned} \tag{8.5}$$

Here $\frac{\Delta \nu_z(C_4, \Delta E_+)}{\Delta E_+}$ is the slope of the linear regression. This measured value is in perfect agreement with the theoretical estimate of $3.27 \times 10^{10} \, \text{m}^{-4}$ based on analytic calculations of the trapping potentials for the given trap geometry [74].
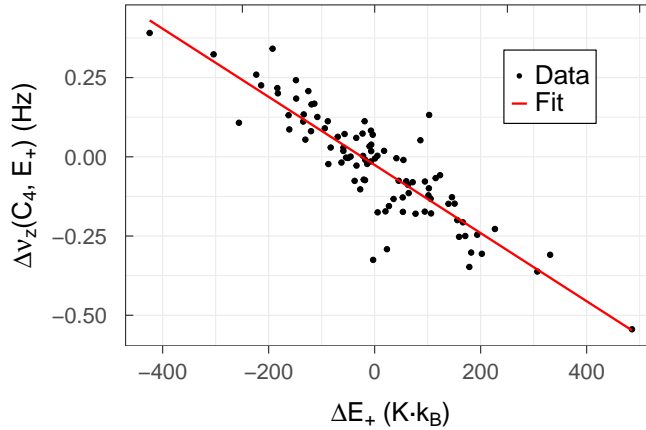
Figure 8.2: Measurement of the D_4-coefficient of the CT based on the $\Delta\nu_z(C_4, E_+)$-shift at $\Delta TR = 1.0\,\text{mU}$ with a single beryllium ion. A change of ν_z is recorded in the CT due to a change in the modified cyclotron energy E_+, where the latter one is measured with the TMT.

8.3   Measurement of the C_4-shift

The measurement of the $\Delta\nu_z(C_4)$-shift was performed for six different values of positive feedback G_{FB} ($0.1 \leq G_{\text{FB}} \leq 1.3$), i.e. the beryllium ion was subjected to six different axial temperatures. The different feedback settings were achieved by means of a voltage-controlled attenuator in the feedback line, compare figure 3.6 in section 3.5. The phase of the feedback was tuned such that the resonator eigenfrequency shifts less than 0.5 Hz at the largest G_{FB} and was kept fixed for all measurements. For clarity, $\Delta\nu_z(C_4, \Delta T_z)$ will notate the axial frequency shift between a certain feedback setting relative to no feedback applied in the following. In order to account for slow drifts of the axial frequency, ν_z-measurements with feedback on and feedback off were interleaved. Consequently, $\Delta\nu_z(C_4, \Delta T_z)$ is calculated as the shift to an interpolated reference:

$$\Delta\nu_{z,i}(C_4, \Delta T_z) = \frac{\nu_{z,2i} + \nu_{z,2i+2}}{2} - \nu_{z,2i+1}. \tag{8.6}$$

Here, ν_z-measurements with feedback on(off) have an odd(even) index on the right-hand side of the equation. An example of two ν_z-measurements with feedback on and feedback off is given in figure 8.3. This measurement cycle was repeated as a function of ΔTR.

In a second step, the axial temperature T_z that corresponds to each feedback setting was measured with the TMT as described in section 7.4.1. A pecularity of temperature measurements of a single beryllium ion in the TMT is that its dip width is comparably small, namely 1.0 Hz. As a consequence, since the 3 dB-width of the detection resonance is $\approx 30\,\text{Hz}$ for the TMT (table 1), only axial frequencies that are $< 70\,\text{Hz}$ off-resonant can be detected reliably. In addition, at high cyclotron energies, the dip signal smears out due to axial frequency instability caused by the cyclotron quantum transitions. These two effects cause an automated dip detection to be difficult. As a result, in order to extend the measurement range of $\Delta\nu_z(B_2)$, for large values of T_z 3 spectra were always recorded in the TMT, where for each additional spectrum $+3\,\text{mV}$ was added to the ring voltage. This shifts the particle frequency by $\Delta\nu_z(+3\,\text{mV}) = -89.1\,\text{Hz}$, which allows to detect particles with $\Delta\nu_z(B_2) \lesssim 250\,\text{Hz}$ corresponding to $E_+ \leq 167\,\text{K} \cdot k_B$. The analysis procedure to determine temperatures from the TMT frequency shifts including the cutoff frequency is performed as described in section 7.4.1. With a temperature value assigned to each feedback setting, $\Delta\nu_z(C_4, \Delta T_z)/\Delta T_z$ is determined for a certain ΔTR by performing a linear fit to the data. An example measurement for ΔTR $= 0.7\,\text{mU}$ is shown in figure 8.4(a).
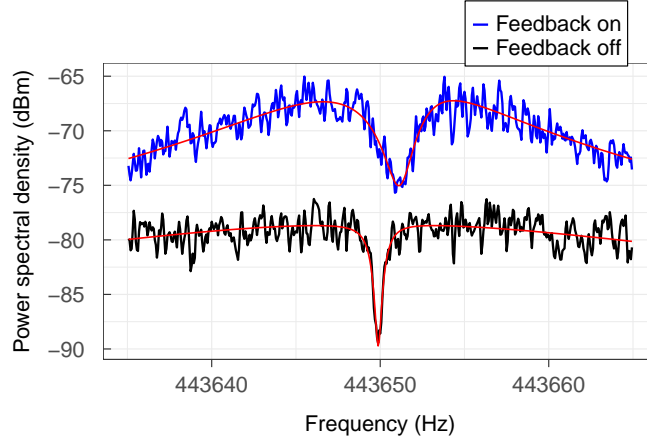
Figure 8.3: Exemplary measurement of $\Delta\nu_z(C_4)$ in the CT at $\Delta\mathrm{TR} = 0.7\,\mathrm{mU}$. The black line depicts a reference measurement with feedback off. The blue line shows a measurement at the largest feedback gain G_{FB}. The red lines are fits using equation (2.43) from which the respective ν_z is extracted.
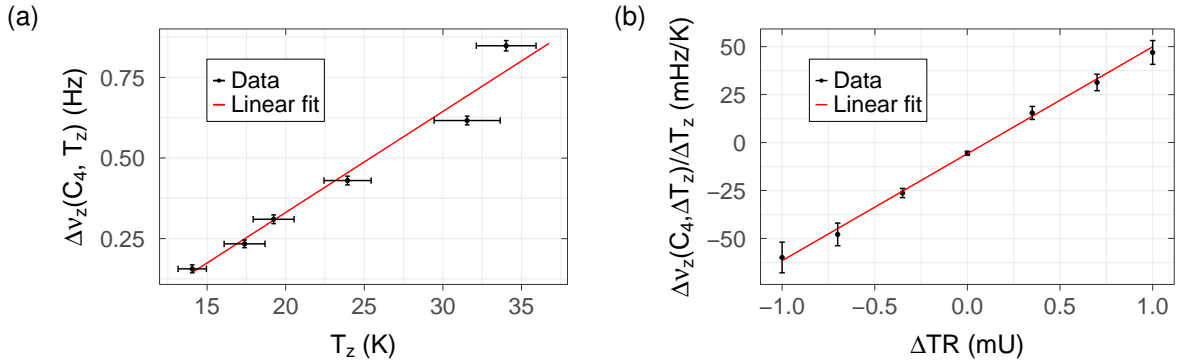
Figure 8.4: (a) Example measurement of the $\Delta\nu_z(C_4)$-shift in the CT at $\Delta\mathrm{TR} = 0.7\,\mathrm{mU}$. The axial temperatures are measured in the TMT. (b) Determination of the final value of $\frac{\Delta\nu_z(C_4,\Delta T_z)}{\Delta\mathrm{TR}\Delta T_z}$. The data points in this graph are the slopes from the measurements of $\Delta\nu_z$ at a given $\Delta\mathrm{TR}$. The uncertainties of each data point are the fit uncertainties from the previous step only, however, since the data points are highly correlated, the true uncertainty is higher (see text).

Next, this procedure was repeated for different ΔTR with data shown in figure 8.4(b). Fitting the measured data points yields a slope of

$$\frac{\Delta\nu_\text{z}(C_4, \Delta T_\text{z})}{\Delta\text{TR}\,\Delta T_\text{z}} = (55.7 \pm 5.3)\text{Hz}/(\text{K} \cdot \text{U}). \tag{8.7}$$

The largest source of uncertainty for $\frac{\Delta\nu_\text{z}(C_4,\Delta T_\text{z})}{\Delta\text{TR}\,\Delta T_\text{z}}$ are the statistical uncertainties of the temperature measurements in the TMT. Hence, the uncertainty is estimated by performing a Monte-Carlo simulation, in which the assumed temperature of each feedback setting is varied based on its statistical uncertainty. Then, the full analysis is repeated. The standard deviation of the resulting $\frac{\Delta\nu_\text{z}(C_4,\Delta T_\text{z})}{\Delta\text{TR}\,\Delta T_\text{z}}$-distribution is used as uncertainty, amounting to $\sigma\left(\frac{\Delta\nu_\text{z}(C_4,\Delta T_\text{z})}{\Delta\text{TR}\,\Delta T_\text{z}}\right) = 5.3\,\text{Hz}/(\text{K} \cdot \text{U})$. Note that this uncertainty is significantly larger than the one expected from figure 8.4(b) because for each data point therein the same temperature values are used, thus the data points are highly correlated. The largest systematic uncertainty for the absolute value of $\frac{\Delta\nu_\text{z}}{\Delta\text{TR}\,\Delta T_\text{z}}$ stems from the uncertainty of the B_2 in the TMT of about 2.5%. However, this uncertainty is already a factor of 4 smaller than the statistical one and is thus negligible in the final uncertainty budget. The uncertainty of the theoretical value for the constant-amplitude case is dominated by the uncertainty of D_4 of about 6%. As a final result, the ratio a between the measured $\frac{\Delta\nu_\text{z}(C_4,\Delta T_\text{z})}{\Delta\text{TR}\,\Delta T_\text{z}}$ and the theoretical one for constant amplitude is determined, yielding

$$a = 1.98 \pm 0.19. \tag{8.8}$$

This ratio agrees within 1σ to the prediction by the simulations that an additional factor of 2 is present if the axial energy samples a Boltzmann distribution and the dip position is derived from frequency power spectra. The constant-amplitude shift ($a = 1$) is rejected by 5.2σ.

8.4   Theory of the C_4-shift for Boltzmann-distributed energies

The remaining ingredient for a comprehensive understanding of the C_4-shift is the theoretical description for Boltzmann-distributed axial energies. This comprises two theoretical cases: First, the case where the FFT of the particle motion can be recorded directly, i.e. 'peak detection'. This case is currently not possible to reconstruct in the experiment. A particle could be detuned and axially excited, however, then its energy does not sample a Boltzmann distribution. The second case is where the particle is tuned on the resonator. Then, it does sample a Boltzmann distribution, but its frequency cannot be recorded faster than one cooling time constant, i.e. only the average frequency and not the time-resolved components can be measured. It bears mentioning that the theoretical description for the latter case could not be fully derived until now. The challenge is that the experimental setting is right between two limits, which are already quite complex but more easily calculable. Nevertheless, in the following the calculation of the two limits will be presented. Furthermore, it will be demonstrated which experimental observable comes out correct for each limit, which will be additionally corroborated by experimental data.

8.4.1   Peak-detection

In the following, the mean particle frequency as derived from the direct FFT of the particle's motion will be calculated. It is crucial to recognize that a particle frequency derived this way is different from the purely time-weighted average particle frequency for the following reason: If the axial energy of the particle samples a Boltzmann distribution, the fraction

at high energies is not only subject to a larger frequency shift, but also contributes a proportionally larger amplitude to the frequency power spectrum. Regardless of whether the FFT is calculated based on the position or velocity of the particle, the observed power is proportional to the energy, $P = Z(\omega)I_{\text{ind}}^2 \propto E_z$. Hence, an additional weighting factor $\propto E_z$ is required when integrating over the Boltzmann distribution. For brevity $\lambda_{C_4} = \frac{3}{2}\frac{C_4}{C_2}\frac{1}{4\pi^2 m\nu_z}$ is introduced such that $\Delta\nu_z(C_4, E_z) = \lambda_{C_4}E_z$. The mean frequency is then given by

$$
\begin{aligned}
\langle\Delta\nu_z(C_4, T_z)\rangle &= \int_0^\infty \lambda_{C_4}E_z\frac{1}{k_BT_z}e^{-\frac{E_z}{k_BT_z}}\frac{E_z}{k_BT_z}dE_z \\
&= 2\lambda_{C_4}k_BT_z,
\end{aligned}
\tag{8.9}
$$

which is a factor of 2 higher compared to the purely time-weighted average with $\langle E_z\rangle = k_BT_z$.

8.4.2   Dip detection

The previous case shall now be applied to the case where the particle frequency is determined via a dip spectrum. In the case of highly harmonic particle motion ($\Delta\text{TR} = 0$), equation (2.43) describes the experimentally observed dip spectra to a high degree. In order to incorporate a non-zero C_4, the substitution $\nu_1 \to \nu_1(C_4) = \nu_1 + \lambda_{C_4}E_z$ must be performed. At this point it should be mentioned that there is already a conflict in existing literature. Ref. [112, eq. (25)] and ref. [113, eq. (D3)] both perform the aforementioned substitution, but arrive at irreconcilable results.

However, in the following I will summarize the findings obtained during this thesis. The fact that the substitution $\nu_1 \to \nu_1(C_4) = \nu_1 + \lambda_{C_4}E_z$ in equation (2.43) must be performed is unquestioned. However, for the step afterwards two options are possible: In equation (2.43), n_1 not only accounts for the coupling and amplification factors, but it is also proportional to the effective resonator temperature T_{RLC}. Thus, the resulting lineshape is also an average over the Boltzmann distribution. The difference between the two options is whether one assumes that the momentary energies of the particle and resonator are fully correlated or completely uncorrelated. In the uncorrelated case, the additional substitution

$$
n_1 \to \frac{n_1}{(k_BT_z)^2}\int_0^\infty \exp\left(\frac{-E_{\text{RLC}}}{k_BT_z}\right)E_{\text{RLC}}dE_{\text{RLC}}
\tag{8.10}
$$

must be performed, where the RLC circuit energy E_{RLC} and the particle energy E_z are independent and therefore uncorrelated. The resulting lineshape is then given by

$$
\langle u_{\text{th, exp}}^2(\nu|C_4)\rangle = n_0 + \frac{n_1}{(k_BT_z)^2}\int_0^\infty \exp\left(\frac{-E_{\text{RLC}}}{k_BT_z}\right)E_{\text{RLC}}\ dE_{\text{RLC}} \times
\tag{8.11}
$$

$$
\int_0^\infty \exp\left(\frac{-E_z}{k_BT_z}\right)\frac{4\left(\frac{\nu-\nu_1-\lambda_{C_4}E_z}{\Delta\nu_1}\right)^2}{4\left(\frac{\nu-\nu_1-\lambda_{C_4}E_z}{\Delta\nu_1}\right)^2 + \left(4\frac{\nu-\nu_0}{\Delta\nu_0}\frac{\nu-\nu_1-\lambda_{C_4}E_z}{\Delta\nu_1} - 1\right)^2}dE_z \qquad \text{(uncor.)}.
$$

The first integral can be easily evaluated, but it is notated this way to demonstrate the difference to the correlated case. In the fully correlated case, $E_{\text{RLC}} = E_z$ at all times, leading to the integral

$$
\langle u_{\text{th, exp}}^2(\nu|C_4)\rangle = n_0 + \frac{n_1}{(k_BT_z)^2}\times
\tag{8.12}
$$

$$
\int_0^\infty \exp\left(\frac{-E_z}{k_BT_z}\right)\frac{4\left(\frac{\nu-\nu_1-\lambda_{C_4}E_z}{\Delta\nu_1}\right)^2 E_z}{4\left(\frac{\nu-\nu_1-\lambda_{C_4}E_z}{\Delta\nu_1}\right)^2 + \left(4\frac{\nu-\nu_0}{\Delta\nu_0}\frac{\nu-\nu_1-\lambda_{C_4}E_z}{\Delta\nu_1} - 1\right)^2}dE_z \qquad \text{(cor.)}.
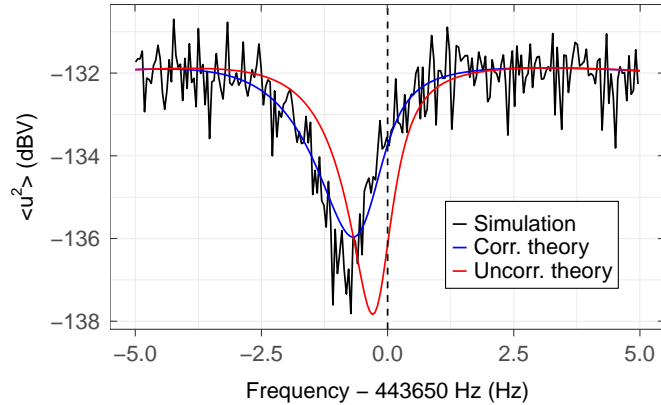$$

Figure 8.5: A simulated high-statistics dip of a single beryllium ion in the CT at $\Delta\text{TR} = -1.2\,\text{mU}$ is compared against the lineshape theory with correlated energies (blue line) and uncorrelated energies (red line). The unshifted particle frequency is indicated by the dashed line. For details, see text.

In both cases, for $\lambda_{C_4} \neq 0$ the numerator of the large fraction will not be 0 at $\nu = \nu_1$, corresponding to the reduction in dip SNR.

However, from experimental observables it is directly clear that neither of these two limit cases corresponds to the real system: Due to the different widths of the RLC resonance and particle dip, the energies cannot be exactly the same for all points in time. In contrast, they also cannot be fully uncorrelated, since then the particle would not create a dip signal in the first place, even for $C_4 = 0$. The true description most probably requires correlation coefficients similar as they have been employed for the calculation of the geonium lineshape in ref. [39].
Nevertheless, both limit cases shall be studied more thoroughly in the following. Figure 8.5 shows simulated data of a single beryllium ion in the CT at $\Delta\text{TR} = -1.2\,\text{mU}$ and $T_z = 15\,\text{K}$. The simulation data is an average of several independent high-statistic runs. In addition, the theoretical dip lineshapes for the fully correlated case (blue) and fully uncorrelated case (red) are plotted. Note that these lineshapes are not fits but direct calculations with equations (8.11, 8.12). The same parameters as in the simulation are used, namely $\nu_0 = \nu_1 = 443\,650\,\text{Hz}$, $n_0 = 0$, and $n_1 = 4k_B T_{\text{RLC}} R_{\text{RLC}}$ with $T_{\text{RLC}} = 15\,\text{K}$ and $R_{\text{RLC}} = 78.4\,\text{M}\Omega$. This exemplary data demonstrates an interesting observation: The theory with correlated energies reproduces the factor of 2 in frequency shift to a good degree, but fails to match the signal-to-noise ratio. The roles are reversed for the theory with uncorrelated energies, where the signal-to-noise ratio is correctly reproduced but the frequency shift is too small. The fact that the uncorrelated theory reproduces the correct dip SNR is of practical interest since this method was employed as temperature measurement method in the latest antiproton g-factor measurement campaign [59]. Thus, a temperature measurement via the SNR-method will be linked to an independent temperature measurement via the B_2-coefficient in the next subchapter.

8.4.3   Temperature measurement via the SNR-method

The first step of confirming the observation that the theory of uncorrelated particle and resonator energies correctly reproduces the SNR of the dip consists of measuring the axial temperature of the ion in the TMT. This is done in the standard way via the TMT as
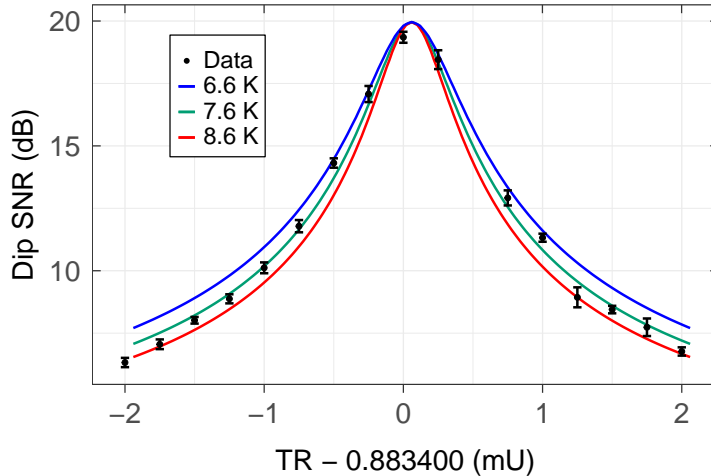
Figure 8.6: The measured dip SNR of a single beryllium ion in the CT as a function of TR. A fit to the data with the theory of uncorrelated energies, equation (8.11), yields an axial temperature of $(7.6 \pm 0.5)\,\mathrm{K}$, which agrees with the one of $(8.2 \pm 0.6)\,\mathrm{K}$ that is independently obtained via a TMT-measurement. The curves at $6.6\,\mathrm{K}$ and $8.6\,\mathrm{K}$ only serve to demonstrate the SNR scaling with temperature.

described in section 7.4.1. This measurement yields an axial temperature of

$$T_{\mathrm{z}}^{(B_2)} = (8.2 \pm 0.6)\,\mathrm{K}. \tag{8.13}$$

Next, the dip SNR has been measured as a function of TR with data shown in figure 8.6. A fit with equation (8.11) is performed to the data, where $n_0, n_1, T_{\mathrm{RLC}}$, and $\mathrm{TR}_{\mathrm{id}}$ are free parameters. The resulting temperature is

$$T_{\mathrm{z}}^{(C_4,\mathrm{SNR})} = (7.6 \pm 0.5)\,\mathrm{K}. \tag{8.14}$$

This temperature agrees well within the combined 1σ-uncertainty to the temperature obtained via the B_2-measurement. To demonstrate the SNR-scaling with temperature, in addition the curves corresponding to $\pm 1.0\,\mathrm{K}$ are plotted in figure 8.6. Thus, the SNR-method, which was previously purely based on simulation and theory only, is now independently cross-checked and confirmed by experimental data.

8.5   Summary of the C_4-shift and SNR

In summary, the theoretical $\nu_{\mathrm{z}}(C_4)$-shift as published in ref. [41] is correct. However, it does not directly apply to the experimental situation, since it assumes that the axial energy is constant. In case of Boltzmann-distributed energies, both simulation and experiment confirm that the shift is larger by a factor of 2. The additional factor of 2 also occurs in theory if the energies of the particle and resonator are assumed to be fully correlated. However, this theory does not reproduce the simulated and measured dip SNR. In contrast, a theory that assumes fully uncorrelated energies reproduces the SNR, but not the factor of 2 shift. The SNR scaling of the uncorrelated theory is confirmed by simulation and experiment via an independent temperature measurement. However, it is clear that neither theory corresponds to the experimental reality and future work is required here. As a final note, the additional factor of 2 in frequency shift was already measured at our experiment in 2016/2017 in ref. [74], but the inconsistency was considered a measurement uncertainty and not a fundamental feature. In particular, regarding the temperature measurement via the AT, ref. [74, p. 45] writes: *"Correcting by the ratios of magnetic fields as introduced in the*

previous section the temperature of the PT axial resonator, $T_z = 5.9(1.0)\,K$, is obtained." Concerning the temperature measurement via the C_4-shift, ref. [74, p. 46] writes: *"This leads to an estimated temperature of $T_z = 13.6(1.4)\,K$ which is in disagreement with the previously measured temperature."* Thus, the presence of the factor of 2 in the C_4-shift is further corroborated by measurements conducted not only with different particles in different traps, but ultimately also by a different PhD student who had no time overlap with myself. The origin of the discrepancy observed in ref. [74] has now been identified and resolved.

9 | Sympathetic cooling measurements

In this chapter measurements with the on-resonance sympathetic cooling technique down to 140 mK are presented. These measurements are the culmination of the previous simulation work and the commissioning of a new experimental apparatus.

9.1   Axial frequency stability of a large beryllium cloud

When working with large beryllium clouds, a critical observation is that the axial frequency drifts after irradiating the magnetron sideband drive. For our application it is essential to null this drift to the best possible degree, since the simulations predict that even for on-resonance coupling the axial frequencies of the proton and beryllium cloud must be matched to a few hundred mHz. It turns out that the drift is related to the TR of the trap, as demonstrated in figure 9.1, where the axial frequency of two beryllium clouds is measured after the magnetron sideband was irradiated. Each individual FFT spectrum corresponds to 45 s measurement time. The cooling laser was constantly on during these measurements, but its power was chosen to be sufficiently weak that no loss of dip SNR occurs. Interestingly, the axial frequency can be reset to its initial value by applying the magnetron sideband drive again. For mid-sized clouds between 100 and 1000 ions, this axial frequency drift is practically linear for relevant time scales and can be nulled sufficiently precise. In contrast, for large clouds of > 1000 ions, a quadratic component of the shift arises. This poses a challenge, since in a cooling measurement, the flat region of the drift must thus be matched to the time of the proton-beryllium coupling, i.e. to the minimum of the parabola. For example, for the specific cloud in figure 9.1(b), the initial drift is weakest for TR = 0.4295. However, if the proton-beryllium coupling is performed at the time-equivalent of 2–3 spectra after applying the magnetron-sideband to the beryllium cloud, it is favourable to adjust the TR to TR = 0.4300 since the axial frequency drift is flat in this region. Admittedly, this then requires a relative offset of the axial frequencies of the proton and beryllium ions, which constitutes another parameter in the already complex parameter space.

It bears mentioning that the reproducibility of the TR is impaired by several effects of which some remain to be identified. For example, in the course of this thesis work, it was observed that the strength of the drift as well as the TR at which it is approximately nulled is a function of the amplitude of the magnetron sideband drive. This has practical consequences, for example the dip and magnetron sideband frequency must be centered in order to measure the TR drift reproducibly. An uncentered dip or magnetron sideband frequency corresponds to an effective different drive amplitude and a TR optimization would thus yield inconclusive results. However, even when accounting for this effect the drifts behave unexpectedly for some TR values, e.g. TR = 0.429 in figure 9.1(a) should be closer to 0 and in figure 9.1(b) the ones of TR = 0.4285 and TR = 0.4290 are inverted compared to the general scaling. An example of a quantity to which the drift was not sensitive is the damping rate by the cooling laser. The laser power was both increased and decreased by a factor of 2 and no significant change of the TR drifts were observed. Although this result might be owed to the weak damping rate and the laser beam geometry, it is nevertheless sufficient for the sympathetic cooling application.

Notably, similar effects as these TR-related drifts have been observed for electron plasmas [114] and laser-cooled beryllium ions [115], but the exact mechanisms remain elusive to this date. As a final remark, this drift is the main contribution to the axial frequency instability of large beryllium clouds. If the drift is subtracted, e.g. by measuring dip spectra interleaved with magnetron cooling, the axial frequency stability of large beryllium clouds is about 200–400 mHz per 30–60 s spectrum, which already includes the fit uncertainty
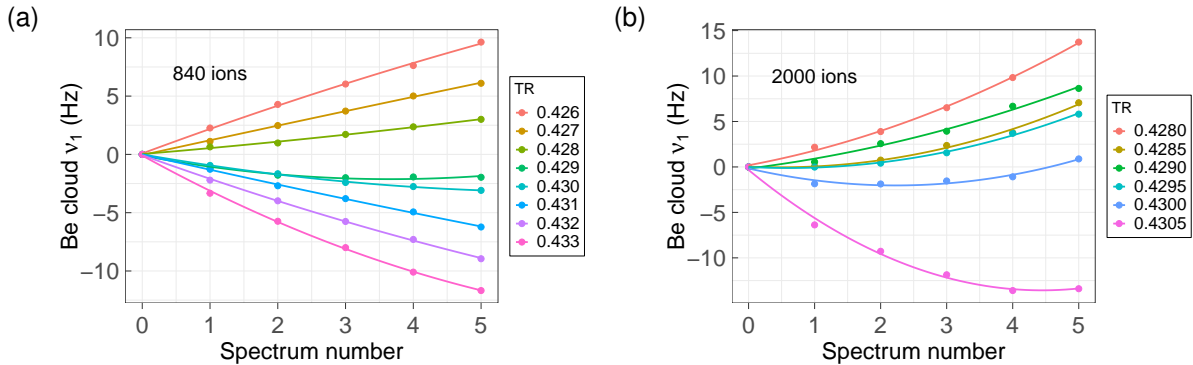
Figure 9.1: Axial frequency drifts of a beryllium cloud after applying the magnetron sideband drive with 840 ions in (a) and 2000 ions in (b). For a cooling measurement the TR must be adjusted such that the drift is ideally nulled.

imposed by the large dip width.

9.2   Temperature measurement of the axial detection system

The last preparatory step before performing the sympathetic cooling measurements consists of determining the temperature of the axial detection system. In the following, if not explicitly stated otherwise, all measurements are performed with a single proton in the PT and with the cryogenic amplifier turned off. This reduces the input noise of the FET and thus lowers the effective noise temperature. Furthermore, all temperature measurements are performed as described in section 7.4.1. Three temperature measurements of the axial detection system with amplifier off are shown in figure 9.2. A weighted average yields a temperature of

$$T_{\mathrm{RLC}} = (8.6 \pm 0.8)\,\mathrm{K}. \tag{9.1}$$

This value will from now on be used as a reference temperature from which the proton is cooled. The three individual measurements are spaced apart by about one week to observe possible temperature changes over time, which is not the case here. The TMT is optimized for measuring axial proton temperatures between $10\,\mathrm{mK}$ and $\approx 1\,\mathrm{K}$. For example, the axial frequency width of the thermal distribution for a $8.6\,\mathrm{K}$ proton is about $4.0\,\mathrm{kHz}$. Nevertheless, higher temperatures can still be measured by recording several axial FFTs at different ring voltages. In this thesis work, steps of $1\,\mathrm{mV}$ corresponding to $256\,\mathrm{Hz}$ axial frequency shift (table 1) are performed. The maximal number of FFTs was chosen to be at least 40, corresponding to $10.2\,\mathrm{kHz}$ or about 2.5 distribution widths of an $8.6\,\mathrm{K}$ proton. This ensures that only $< 10\%$ of the high-energy fraction of the Boltzmann distribution is truncated. This cutoff is accounted for in the data analysis as described in section 7.4.1. An automated dip detection ensures that the axial frequency search of the proton in the TMT is stopped after it has been found. In order to not miss the $E_+ = 0$ cut, a certain buffer is accounted for, i.e. it is a deliberate choice that the first few spectra are always empty.

9.3   Sympathetic cooling measurements down to $140\,\mathrm{mK}$

After the preparation work had been completed, the sympathetic cooling measurements were performed. In the course of this thesis, three differently sized beryllium clouds were
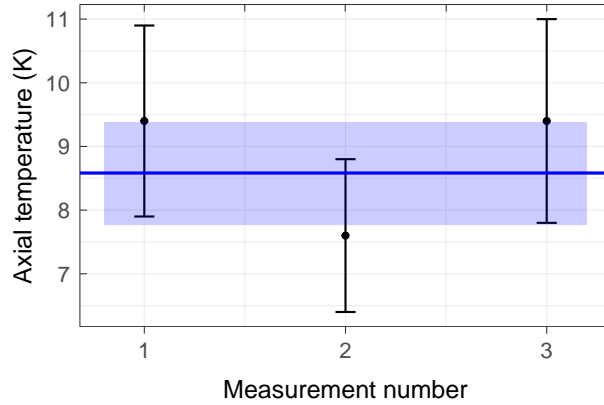
Figure 9.2: Three independent measurements of the axial detection system with the cryo-genic amplifier turned off. The temperatures are determined in preparation of the cooling measurements.

employed for cooling, namely dip widths of 48 Hz, 84 Hz, and 120 Hz. The number of ions is tenfold the dip width in Hz, see table 1. Assuming that initially the magnetron sideband drive is applied to the beryllium cloud and the laser is continuously on, the exact cooling cycle with some comments to the reasoning is the following:

1. Turn off the magnetron sideband drive and detune the beryllium cloud by 100–200 Hz (4–8 mV ring voltage)
   ↪ This allows centering of the proton.

2. Turn on the magnetron sideband drive for the detuned beryllium cloud.
   ↪ The magnetron sideband coupling ensures that the cloud stays in a defined and cold state while the proton is centered. Although the cloud is detuned from the resonator, it is still axially cooled by the laser.

3. Record a PT FFT, fit the proton dip and adjust the PT ring voltage to center the proton to the resonator frequency.
   ↪ This task avoids long-term drifts of the proton's axial frequency. In case cycle time becomes relevant, this sequence and the associated detuning of the beryllium ions can be done e.g. every 10th cycle only.

4. Turn off the detuned magnetron sideband drive and tune the beryllium cloud back on the resonator.

5. Turn on the undetuned magnetron sideband drive for the beryllium cloud.

6. Record an LT FFT (45 s).
   ↪ This FFT serves as magnetron-cooling time and to verify that the beryllium cloud is not magnetron-hot. This step and the following five are required to prepare the beryllium cloud in a defined state.

7. Turn off the magnetron sideband drive for the beryllium ions.

8. Record an LT FFT and center the beryllium cloud on the resonator.

9. Turn on the magnetron sideband drive for the beryllium cloud.

10. Record an LT FFT (45 s).

11. Turn off the magnetron sideband drive for the beryllium cloud.

12. Turn off the PT-LT cryogenic amplifier.
    ↪ By turning off the amplifier, the amplifier's input noise and thus the effective temperatures are reduced.

13. Turn on the cyclotron sideband drive for the proton with ≈ 1 Hz Rabi splitting.
    ↪ A larger Rabi frequency would constitute an effective frequency detuning between the proton and beryllium ions and should therefore be avoided.

14. Wait 90 s.
    ↪ This is the cooling time where the proton and beryllium ions are coupled on-resonant to each other. The cooling time constant has not been explicitly measured, but 90 s is sufficiently long such that the temperatures are converged.

15. Turn off the cyclotron sideband drive for the proton.

16. Briefly turn on the magnetron sideband drive for the proton (15 s).
    ↪ This is only done so that the proton does not get magnetron-hot over several hours of measurement time. If cycle time is crucial, it can be done e.g. every 10th cycle only.

17. Turn on the PT-LT cryogenic amplifier again.

18. Turn on the magnetron sideband drive of the beryllium ions.
    ↪ This keeps the beryllium cloud in a defined and cold state while the cyclotron energy of the proton is measured.

19. Transport the proton into the TMT.

20. Record FFTs in the TMT with successively 1 mV higher ring voltage (lower particle frequencies) until the proton is found on the resonator.
    ↪ 1 mV ring voltage corresponds to about 250 Hz axial frequency shift or a maximum frequency detuning of 125 Hz to the resonator in our case, which is still reproducibly detectable. The measured axial frequency yields the cyclotron energy of the proton.

21. Transport the proton back into the PT.

Short waiting times, e.g. for device communication or stabilization of trap voltages after transport, have been omitted. A graphical summary of the most important steps is given in figure 9.3. It should be noted that this sequence is not optimized for cycle time but rather for reproducibility and long-term stability. Before each cooling measurement, the laser settings are reexamined based on the fluorescence signal as described in section 7.5.4. For the 48 Hz cloud a laser power of $P = 5 - 15\,\mu W$ and $-84\,MHz$ laser frequency detuning were used, which corresponds to $1.5\% - 4.5\%$ of the saturation power and 4 linewidths red detuning. For the other two clouds a laser power of $P = 100\,\mu W$ and $-200\,MHz$ laser frequency detuning were used, which corresponds to $1/3$ of the saturation power and 10 linewidths red detuning. Both settings yield a sufficiently low damping rate, which the simulations predict is necessary for the on-resonance coupling. An exemplary temperature measurement for a proton sympathetically cooled to about 200 mK is shown in figure 9.4. The measured cyclotron energies are converted to axial energies based on equation (7.10). No correlation between two successive energy samples is observable. Furthermore, as visible in the histogram, the energies follow the expected Boltzmann distribution.

The temperature data for all three clouds is summarized in figure 9.5. The individual measurements for each cloud are independent and consist of 25 to 60 cyclotron energy
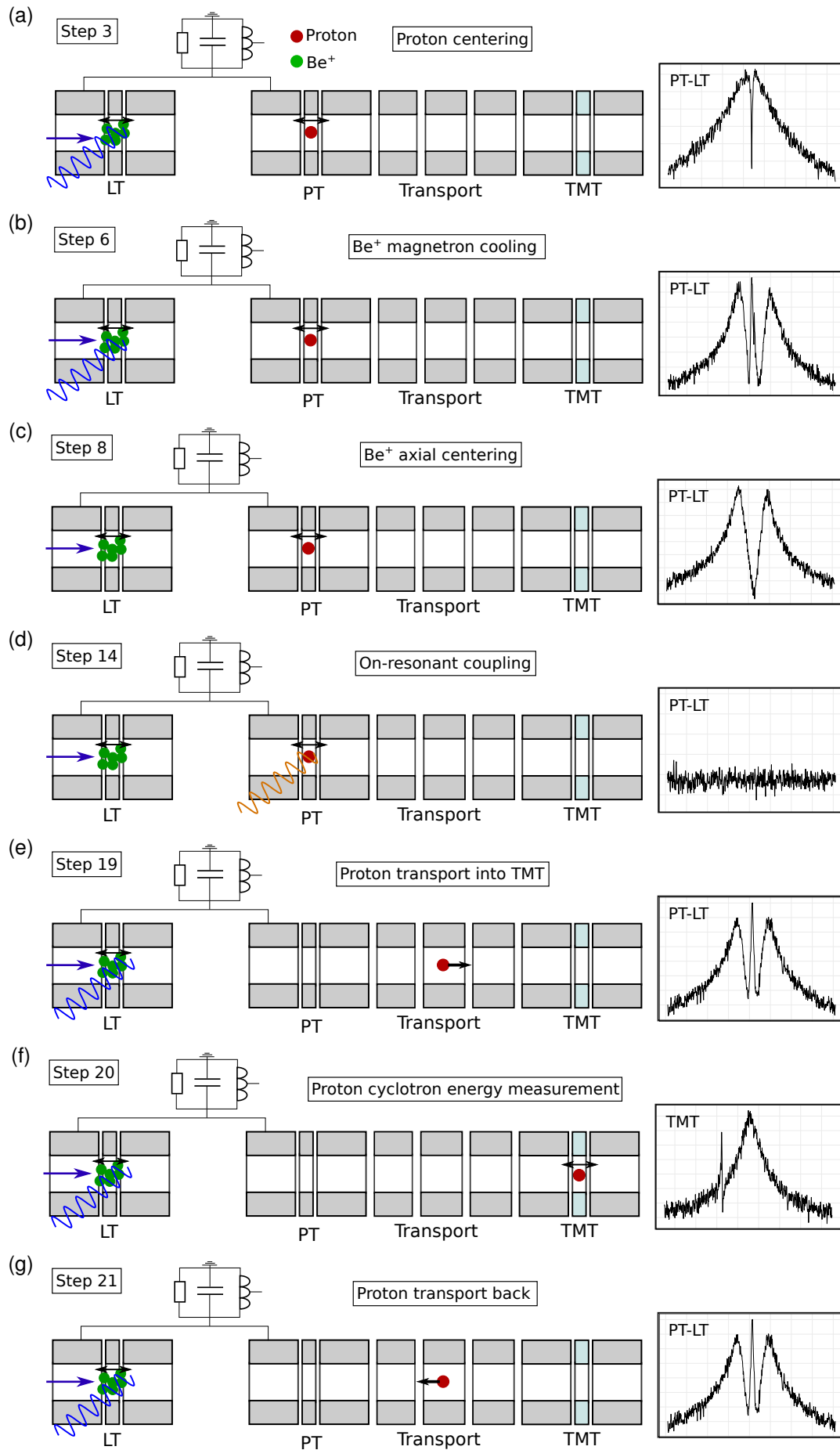
Figure 9.3:   Schematic of a full cooling cycle. For details, see text. Black double arrow: Axial ion motion in trap. Black single arrow: Ion transport direction. Purple arrow: 313 nm cooling laser. Blue wave: Beryllium magnetron sideband. Orange wave: Proton cyclotron sideband.
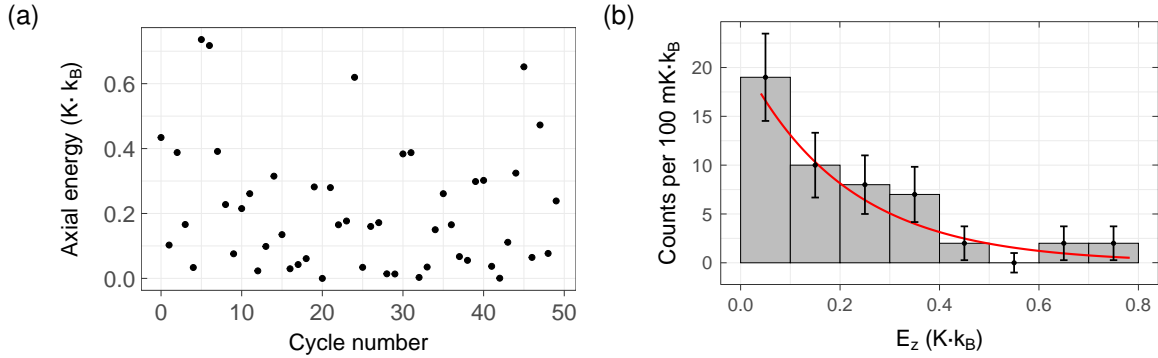
(a)

(b)

Figure 9.4: Example of a sympathetic cooling measurement of a single proton in the PT by laser-cooled beryllium ions in the LT. The individual cyclotron energies measured in the TMT are converted to axial energies and are plotted in (a). A histogram with the corresponding Boltzmann distribution is shown in (b). The red line is a continuous Boltzmann distribution whose temperature is calculated with equation (7.9). This measurement is measurement number 1 of the 84 Hz cloud in figure 9.5.

measurements. The plotted error bars are exclusively the statistical uncertainties. The horizontal red line is the theoretical prediction based on the simulation work,

$$T_{\mathrm{z}} = \frac{T_{\mathrm{RLC}}}{1 + \frac{\Delta\nu_{1,\mathrm{Be}}}{\Delta\nu_{1,\mathrm{p}}}}, \tag{9.2}$$

where T_{RLC} is the previously measured temperature of the axial detection system, see equation (9.1). The shaded red areas are the projected 1σ-uncertainties of the averaged detector temperature measurements. It bears mentioning that the data is not cherry picked. Only measurements where something 'obvious' failed, e.g. the cooling laser drifted out of its frequency lock, were excluded. Furthermore, since the proton is cooled, the frequency distribution is sufficiently narrow so that all individual cyclotron energies are recorded and no high-energy cutoff must be accounted for in the data analysis.

These temperature measurements are a remarkable result for several reasons: First and foremost, the axial temperature of the proton is reduced by a factor of 50–60 compared to the environment temperature. The temperatures achieved with the 120 Hz cloud, about (160 ± 30) mK, constitute a factor of 16 improvement compared to the previous record measurement of (2.6 ± 2.5) K [27]. Moreover, this improvement is achieved reproducibly as it is evident by the individual measurements. The best single-shot measurement of (146 ± 29) mK, measurement number 3 of the 84 Hz cloud, constitutes a factor of 18 improvement. Second, these measurements demonstrate the capability of the newly commissioned TMT to measure temperatures. It is the nature of the method that the temperature uncertainty scales down proportionally with the temperature itself until the frequency stability plays a role, which would be at a few mK in this case. Although the final temperature uncertainty depends on the number of cycles, the resolution of about 30 mK can also be regarded as an improvement by a factor of about 80 compared to the previous measurements in ref. [27]. Third, and for me personally the greatest achievement, nearly all individual measurements agree exceptionally well within the combined 1σ-uncertainty with the prediction made by simulation and theory. One data point deviates by 2.0σ (measurement number 3 of the 84 Hz cloud) to the simulation prediction, but one 2σ-deviation is practically expected within 11 data points from a statistical point of view. Thus, in total the agreement between simulation and experiment is striking. Although the simulations were successfully benchmarked against experimental data already previously, until now the simulation work regarding sympathetic cooling either postdated the experimental data or was generated simultaneously. Here, the simulation prediction was made well before the experiment was
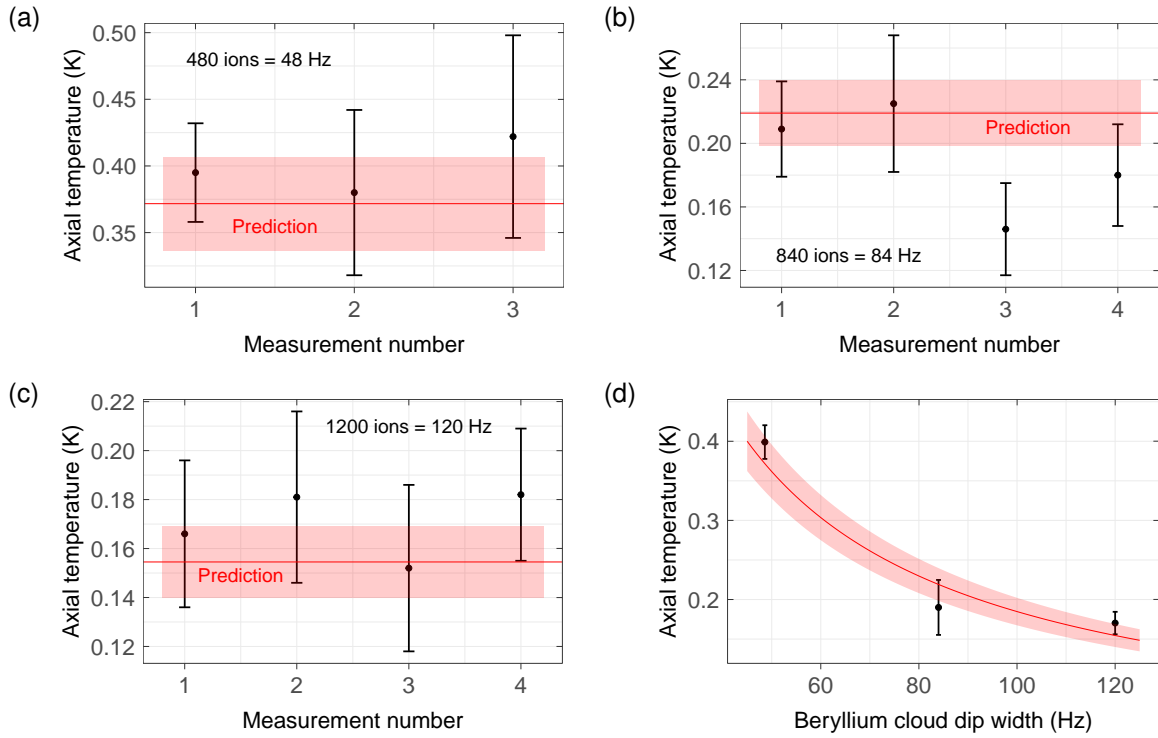
Figure 9.5: Overview of individual sympathetic cooling measurements of a single proton in the PT by laser-cooled beryllium ions in the LT. Three clouds with dip widths of 48 Hz, 84 Hz and 120 Hz were employed, shown in figure (a), (b), and (c), respectively. The red horizontal line corresponds to the theoretical prediction by the simulations, equation (9.2), and the measured temperature of the axial detection system T_{RLC}. The shaded red area is the projected uncertainty of T_{RLC}. In (d) the combined data of (a)–(c) is shown to demonstrate the scaling of the temperature as a function of the dip width of the beryllium cloud. For details, see text.

conducted. Besides, it should be emphasized that not only the result agrees well with the simulation, but also the method: The simulations predict that an unusually weak damping of the beryllium ions is required, which is exactly the laser setting that was used for the cooling measurements. This allowed to collect the sympathetic cooling data within a few weeks only, where otherwise time-intensive systematic studies would have been required. Fourth and finally, in absolute temperature terms this result is in fact better than expected: The simulation work assumed that only 80 beryllium ions can be controlled sufficiently well, albeit in a trap with larger dip width per ion. Nevertheless, the estimated temperature limit of the on-resonance cooling is given as 350 mK [28], and these measurements have surpassed it by a factor of 2. While 80 beryllium ions were certainly a conservative choice, this demonstrates that the simulations are performed with parameters that are also realistic in the experiment. As a result, the agreement between simulation and experiment for the on-resonance coupling scheme constitutes a strong anchor for the claim that a proton temperature of 10 mK is indeed realistically achievable in the experiment with off-resonant schemes as layed out in section 6.5.3.

9.4 Systematic study: Sensitivity to detuning

Due to the simulation work, the predicted temperature minimum has been reached experimentally with practically no need of systematic studies. However, it is nevertheless instructive to perform systematic studies for verification purposes and in order to gain an improved understanding of the experimental processes. One quantity that is of great interest is the sensitivity of the temperature to a relative particle frequency detuning. This quantity can be easily measured by simply introducing a relative frequency detuning between proton and beryllium ions and repeating the sympathetic cooling sequence described in the previous section. This was done for the 120 Hz cloud with data shown in figure 9.6. Note that, since data for nominal 0 Hz detuning was already recorded, it was decided to continue measuring with amplifier off. This comes at the cost of not having recorded the axial frequency of the beryllium cloud at the time of the coupling. As a result, the detunings for each data point in figure 9.6 are projections based on the TR-dependent drift and the two LT FFT spectra that are recorded before the coupling. As such, the horizontal axis should be treated as a coarse estimate only. A small offset of about 1.5 Hz to the nominal detuning is necessary to account for the TR-dependent drift. Nevertheless, this data demonstrates a cooling resonance and the minimum corresponds to the prediction made by the simulations. Other systematic studies, e.g. how the proton temperature changes with laser power, have proven to be challenging as they change the stability of the beryllium cloud. Nonetheless, they will be a subject of future work.

9.5 Limitations

Invoking equation (9.2) again, the temperature limit achieved by the on-resonance coupling scheme is mainly defined by two parameters: The temperature of the axial detection system and the ratio of the beryllium cloud dip width to the proton dip width. Since the dip width per ion is fixed by the trap properties, the ratio can only be enhanced by increasing the number of beryllium ions. At present, the maximum number of beryllium ions is limited by the effect visible in figure 9.7. The data is part of a TR-dependent drift optimization of a cloud of 1800 ions and the spectrum plotted in red is the last one before resetting the 50 Hz frequency drift by turning on the magnetron sideband. However, despite having full dip signal-to-noise before, when irradiating the magnetron sideband again, the cloud gets extremely hot and the image-current signal rises by more than 20 dB. Unfortunately, this
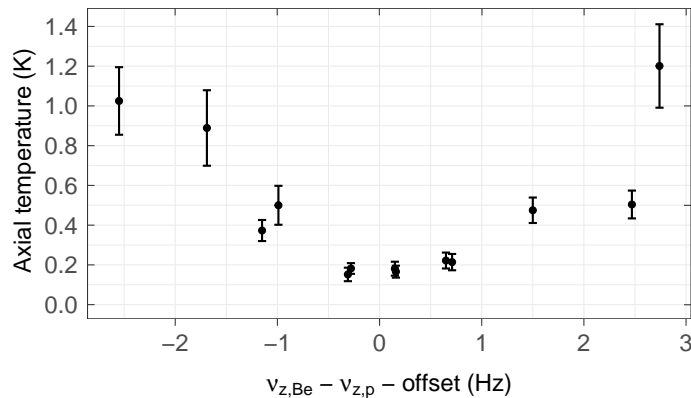
Figure 9.6: Proton temperature as a function of the relative axial frequency difference of the proton and beryllium cloud. An offset is required due to the TR-dependent drift after magnetron cooling the beryllium cloud, see section 9.1. The data was recorded with the 120 Hz cloud and the four data points in the minimum correspond to the ones presented in section 9.3.
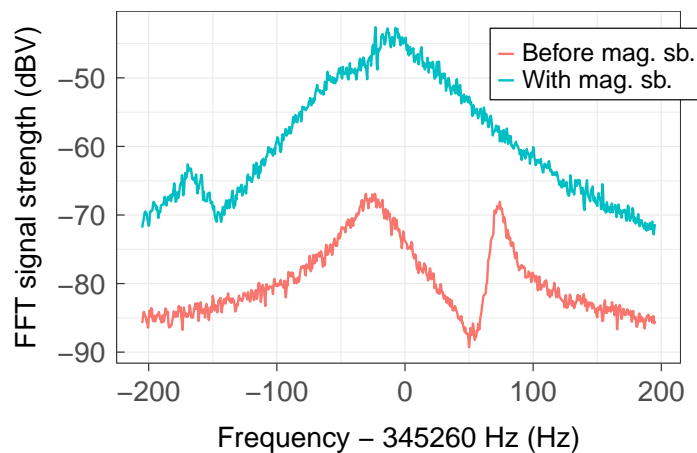

Figure 9.7:   Two successive FFT spectra of a cloud of 1800 ions. The spectrum in red shows the beryllium dip directly before turning on the magnetron sideband drive. With the magnetron sideband applied, the cloud gets extremely hot, as visible in the teal spectrum. This heating effect currently limits the maximum number of beryllium ions.

effect is to date non-deterministic, which further complicates a systematic study. It bears mentioning that the theory of laser cooling the radial modes of ions in a Penning trap as described in section 2.7.3 only refers to a single ion. In contrast, the heating effect here scales with the number of beryllium ions, so that it is most certainly a plasma effect, which will be subject of systematic investigation in the near future.

An alternative way to decrease the proton temperature would be to decrease the temperature of the axial detection system. A readily available technique to achieve this is to apply negative feedback, see section 3.5. The axial temperature with a certain feedback setting has been reduced to $T_{\mathrm{RLC,fb}} = (2.5 \pm 0.3)\,\mathrm{K}$. This temperature was measured with a single proton via the TMT. Although the cryogenic amplifier needs to be turned on for the application of feedback, the temperature reduction by a factor of 3.3 is consistent with the scaling of the resonator width and the dip widths of the particles (equation (3.2)). Several sympathetic cooling measurements were performed with practically the same routine as described in section 9.3. Thus, even with the 48 Hz cloud a temperature of about 110 mK should be achievable. However, the lower limit of the experimentally obtained tempera-
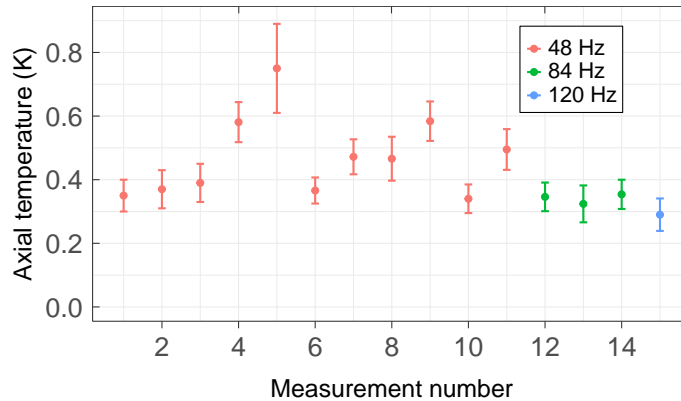
Figure 9.8:   Sympathetic cooling measurements conducted with a reduced resonator temperature of $T_{\mathrm{RLC}}^{\mathrm{fb}} = (2.5 \pm 0.3)\,\mathrm{K}$ by the application of negative feedback. The feedback introduces a noise limit of about 300 mK. Within the measurements for the 48 Hz cloud various different cooling parameters were tested.

tures is about 300 mK, as shown in figure 9.8. The 11 measurements with the 48 Hz cloud include varying parameters such as different laser powers or longer cooling times. However, since these different parameters were only sensitive in the negative sense, they are not resolved on purpose in the figure. This is already a strong hint that the feedback introduces a noise limit of 300 mK in our case. An even more convincing observation for this argument is the lack of scaling of the proton temperature with the number of beryllium ions: If the temperature limit were caused by non-ideal cooling parameters, the proton temperature should nevertheless scale with the number of beryllium ions. Moreover, for the 84 Hz and 120 Hz cloud the temperatures achieved without feedback are lower than with feedback. Notably, the feedback is attenuated by passive components only, i.e. no voltage-controlled attenuator that can be a source of additional noise is installed. However, the fundamental noise limit is nevertheless present. It should be mentioned that a similar limitation is also observed for cyclotron resonators to which negative feedback is applied [59] and the exact mechanism has yet to be understood. In total, the application of negative feedback has not been useful to reduce the temperature of the sympathetically cooled proton further.

10 | Discussion and outlook

In the following, I will summarize the results obtained in the course of this thesis and discuss their impact on not only our experiment specifically but on the whole precision Penning-trap community. In addition, I will comment on which of the possible next steps I deem as the most worthwhile ones.

First of all, the axial temperature of a single proton has been reproducibly reduced to about $T_z = (160 \pm 30)\,\text{mK}$. This temperature constitutes a factor of 16 improvement compared to the previous best-ever value of $T_z = (2.6 \pm 2.5)\,\text{K}$ [27] and is a factor of about 55 below the environment temperature. This improvement could be considered an achievement on its own. However, what is equally important are the means which have enabled this result. On the one hand, a new experimental apparatus was built [48] and commissioned, whose most essential new feature is a dedicated temperature measurement trap that allows to resolve and measure axial temperatures down to a few mK. On the other hand, a simulation framework was developed with which complex Penning-trap physics can be simulated from first principle. These simulations not only predicted the temperature limit correctly, but also the experimental settings to reach it. Most prominently, the finding that, in order to reach the temperature limit with the on-resonance coupling scheme, the laser damping rate must be reduced significantly below a value where the dip signal loses in SNR, was an initially unexpected result. However, the subsequent measurements have confirmed the simulation prediction.

In consideration of the vast amount of experimental parameters that require proper adjustment, the sympathetic cooling measurements are comparable to a precision measurement in terms of preparatory effort (section 7) and the actual measurement sequence (section 9.3). In this respect, the simulations are an invaluable asset since they allow independent systematic studies and therefore save valuable experiment time. The fact that the sympathetic cooling measurements were recorded within a few weeks only was only achievable due to the strong foundation by the preceding simulation work, since otherwise time-intensive systematic studies would have been required. Finally, it should be emphasized that the simulations are not limited to temperature-related studies only, but are also suitable for the quantitative investigation of systematic effects. For example, in this thesis a factor of 2 discrepancy in the systematic frequency shift due to an electrostatic anharmonicity (C_4) to the established theory was first discovered with the simulations and was subsequently verified experimentally.

The excellent consistency between simulation and experiment is also a solid basis for the near-term goals of our experiment: The simulations predict that a resonator-mediated but off-resonant sympathetic cooling scheme allows reaching axial temperatures of $10\,\text{mK}$ for a single proton. Moreover, this prediction assumes a rather conservative cloud of $N = 80$ beryllium ions only, while the on-resonant cooling measurements in this thesis were performed with up to 1200 beryllium ions. Although the Rabi frequency scales with $1/\sqrt{N}$ only, the overall gain is larger since the axial frequency stability does not worsen to the same extent. Consequently the ratio between Rabi frequency and relative particle frequency detuning becomes more favourable. Another prediction by the simulations is that, since the off-resonant cooling schemes rely on coherent energy exchange between the proton and beryllium ions, optimal cooling is achieved with a strong but repeatedly pulsed cooling laser. Notably, the conclusion that even for off-resonant schemes the resonator-mediated version is more feasible is a non-trivial result as well: Both, the first proposal by Heinzen and Wineland [24] as well as the initial proposal by our group [25] envisaged coupling via a common endcap with a far-detuned resonator ($> 100\,\text{kHz}$). However, this concept is abandoned for the experimental campaigns in the near future since the low Rabi

frequencies make it the most difficult scheme to achieve experimentally. Nevertheless, it might experience a revival if temperatures significantly below 10 mK become of interest.

With these considerations in mind, the short-term plans for our experiment are practically set in stone: The sympathetic cooling effort must be transitioned from the PT-LT towards the BT-CT trap combination. At first, a brief on-resonance cooling campaign will be launched in order to gain experience and to discover possible pitfalls for this trap combination. Next, the resonator-mediated off-resonance cooling scheme will be performed by employing the cryogenic switch and pulsed laser cooling. The 10 mK proton will enable quasi-deterministic preparation of the cyclotron energy below the threshold that allows to resolve single spin transitions. As a result, it will significantly boost the sampling rate of the next generation of magnetic moment measurements. Further, considering the cyclotron energy distribution below a certain threshold energy, an overall colder thermal bath also skews the mean of this truncated distribution towards lower cyclotron energies. Thus, not only the sampling rate, but also the spin-state fidelity will be enhanced. Besides spin-readout related improvements, the motional frequency measurements can be conducted at lower cyclotron energy and therefore at reduced systematic shifts. From there on, additional technical upgrades must be installed to the experiment before the next g-factor measurement can be conducted. The pressure stabilization and the shim coil system that were developed throughout this thesis are already part of these upgrades. However, further crucial elements such as the implementation of phase methods are still missing. Nevertheless, these upgrades are relatively minor compared to the implementation of sympathetic cooling and are well-established at other experiments [7, 80, 107]. In total, these developments with the sympathetic cooling as the leading technique will pave the way for the next generation of CPT tests with protons and antiprotons at BASE.

Although to this date there is no evidence that suggests that the off-resonant scheme is unfeasible, it should be kept in mind that also the on-resonant scheme can be improved significantly. One option is to systematically study if different laser settings, especially regarding beam angle and axial offset, can further improve the stability of the beryllium cloud for large number of ions. In the course of an experimental campaign that focused on studying the laser cooling of beryllium ions in our setup [48], several thousands of ions were well under control already. However, these clouds were trapped in the BT and not in the LT. Considering that without a cooling laser, it was significantly easier to cool both the radial modes simultaneously in the BT than it was in the LT, the magnetron heating effect might very well be related to the non-standard trap design of the LT. If the magnetron heating effect is also present in the BT, it might be worthwhile to implement Coulomb interaction between the beryllium ions in the simulations. In fact, the numerical algorithm is predestined for this task as it has been initially developed for solving N-body problems [99]. While hundreds or even thousands of ions might become computationally unfeasible with the current concept, the fundamental effect should still be observable even with a few ions only, which might already be sufficient for a systematic study.

Another experimental approach would be to create a steady state of the beryllium ions by continuously applying the magnetron sideband and matching the cyclotron double dip of the proton in the PT to the magnetron double dip of the beryllium cloud in the LT. Alternatively, if the number of ions is truly limited and the off-resonant scheme is unfeasible due to unforeseen reasons, the on-resonance coupling scheme might also achieve a 10 mK proton with only little technical modifications: If the resonator of the BT is not connected to the endcap electrode but to one of the correction electrodes, the dip width per beryllium ion increases to about 1.0 Hz/ion (table 1). Hence, assuming a cloud of 1200 beryllium ions and a setup where the PT and BT are connected to the same resonator, an axial temperature of about 15 mK could be reached. Moreover, since the on-resonance scheme is independent of the absolute axial frequency and in the end the cyclotron temperature is the parameter of interest, it might be beneficial to increase the resonator frequencies by

a factor of 2-3 such that the ratio ν_+/ν_z becomes smaller, which is ultimately limited by the Penning-trap stability condition of the beryllium ions. Yet another option would be to systematically study the origin of the noise limit imposed by the feedback. If the origin is a device at the 300 K stage, it should be possible to deliberately increase the noise limit by attenuating the resonator signal before the 300 K amplification stage and modifying the feedback attenuation correspondingly. Then, the exact component in the setup that introduces the noise could be identified by iteratively placing this additional attenuation one component further upstream.

Apart from our experiment, the sympathetic cooling is of great interest to the whole Penning-trap community. This becomes most apparent by the fact that nearly every MPIK-related cryogenic Penning-trap experiment relies at least partially on sympathetic cooling for the next generation of precision measurements: The ALPHATRAP-experiment [12] plans to perform the off-resonant resonator-mediated cooling for QED-tests via g-factor measurements of heavy hydrogen-like ions [29, 116]. At this point, it should be mentioned that the methods which were employed in ref. [29] to arrive at the conclusion that the resonator-mediated off-resonant scheme is the preferred tool are completely different. This consistency thus constitutes a cross-check spanning over independent groups and therefore significantly raises the confidence that a 10 mK proton is indeed achievable. Further, the g-factor helium experiment [32] requires sympathetic cooling for the measurement of the g-factor of $^3\mathrm{He}^{2+}$. Although initially similar sympathetic cooling methods were proposed [32, 117], recently the possibility of cooling via direct ion-ion Coulomb interaction has been investigated [118]. Next, due to the lack of laser access, the PENTATRAP-experiment [30] has recently founded the new experiment ELCOTRAP to investigate the possibility of cooling heavy highly-charged ions via radiatively cooled electrons for improved mass measurements [31]. While the technical setups quite differ, the overall concepts regarding sympathetic cooling are very similar. Moreover, even within our collaboration different approaches are pursued: The local BASE group in Hanover works on implementing quantum logic spectroscopy (QLS) techniques by trapping the target ion in close vicinity to beryllium ions such that the Coulomb interaction couples both ions [23]. While not too long ago one or two traps were sufficient to perform a ground-breaking precision measurement, today our trap stack consists of six independent Penning traps. Considering the aforementioned developments, the progression towards highly optimized multi-Penning-trap systems is not exclusive to our experiment but is rather a general trend. On the one hand, this can be considered as a manifestation of the increasing complexity of the experiments and associated techniques. On the other hand, this is also a reflection of the exceptionally innovative Penning-trap community.

Thus, as a final line of thought, I would like to ask the reader to disregard the specific details of the cooling schemes in the following and focus on the situation as a whole. Then it becomes clear that the previously described developments are merely the beginning of transferring temperatures of laser cooled ions to specific target ions. In this regard, the resonator-mediated cooling schemes have two striking advantages: First, the target ion can be an arbitrary trapped charged particle. The only requirement is that it carries a charge and, in case it is unstable, that its lifetime is sufficiently long. Second, the target particle and the laser-coolable species can be separated by macroscopic distances. In particular, since the cooling schemes rely on image currents, they are not inherently limited to Penning traps only. As a result, applications beyond our specific field are conceivable. For example, studies of radioactive ions at online facilities [119, 120], experiments with molecular ions in rf traps [121], or trapped-ion quantum computing [122] might eventually benefit from the general developments here. Moreover, in the long term, cooling techniques that reach temperatures below the Doppler limit, such as resolved sideband cooling [123, 124], may be employed to cool the target ion to even lower temperatures.

With this promising future ahead, I conclude this thesis. I hope the measurements and

concepts presented here prove useful to the reader and I am excited to see where the sympathetic cooling developments lead.

List of publications

The following articles have been published during this PhD thesis until April 2023 with me as (co-)author and part of the `BASE` collaboration:

1. C. Will et al. "Sympathetic cooling schemes for separately trapped ions coupled via image currents". In: *New Journal of Physics* 24.3 (2022), p. 033021
   ↪ The content of this article is fully integrated into this thesis and can be found in section 6. Cited as [28].

2. M. Bohman et al. "Sympathetic cooling of a trapped proton mediated by an LC circuit". In: *Nature* 596.7873 (2021), pp. 514–518.
   ↪ The content of this article is partially used in this thesis. In particular, the simulation work and the experimental signatures of proton-beryllium coupling outlined in section 6.4 are described both in the article and in this thesis. Cited as [27].

3. M. J. Borchert et al. "A 16-parts-per-trillion measurement of the antiproton-to-proton charge–mass ratio". In: *Nature* 601.7891 (Jan. 2022), pp. 53–57.
   ↪ This article uses a temperature measurement method that has been verified with the simulations. However, the specific simulation studies are only described in this thesis, see section 6.6. Cited as [106].

4. J. A. Devlin et al. "Constraints on the Coupling between Axionlike Dark Matter and Photons Using an Antiproton Superconducting Tuned Detection Circuit in a Cryogenic Penning Trap". In: *Phys. Rev. Lett.* 126 (4 2021), p. 041301.
   ↪ The content of this article is not described in this thesis.

5. F. Völksen et al. "A high-Q superconducting toroidal medium frequency detection system with a capacitively adjustable frequency range >180 kHz". In: *Review of Scientific Instruments* 93.9 (2022), p. 093303.
   ↪ The content of this article is not described in this thesis.

Previous work unrelated to this PhD thesis can be found under the following link:
ⓘ https://orcid.org/0000-0003-4622-7799

Bibliography

[1] M. S. Safronova et al. "Search for new physics with atoms and molecules". In: *Rev. Mod. Phys.* 90 (2 2018), p. 025008. DOI: `10.1103/RevModPhys.90.025008`. URL: `https://link.aps.org/doi/10.1103/RevModPhys.90.025008` (↪ cited on p. 12).

[2] P. Micke et al. "Coherent laser spectroscopy of highly charged ions using quantum logic". In: *Nature* 578.7793 (2020), pp. 60–65. DOI: `10.1038/s41586-020-1959-8`. URL: `https://doi.org/10.1038/s41586-020-1959-8` (↪ cited on p. 12).

[3] I. Kozyryev and N. R. Hutzler. "Precision Measurement of Time-Reversal Symmetry Violation with Laser-Cooled Polyatomic Molecules". In: *Phys. Rev. Lett.* 119 (13 Sept. 2017), p. 133002. DOI: `10.1103/PhysRevLett.119.133002`. URL: `https://link.aps.org/doi/10.1103/PhysRevLett.119.133002` (↪ cited on p. 12).

[4] F. Schreck and K. v. Druten. "Laser cooling for quantum gases". In: *Nature Physics* 17.12 (Dec. 2021), pp. 1296–1304. ISSN: 1745-2481. DOI: `10.1038/s41567-021-01379-w`. URL: `https://doi.org/10.1038/s41567-021-01379-w` (↪ cited on p. 12).

[5] C. D. Bruzewicz et al. "Trapped-ion quantum computing: Progress and challenges". In: *Applied Physics Reviews* 6.2 (2019), p. 021314. DOI: `10.1063/1.5088164`. URL: `https://doi.org/10.1063/1.5088164` (↪ cited on p. 12).

[6] G. Schneider et al. "Double-trap measurement of the proton magnetic moment at 0.3 parts per billion precision". In: *Science* 358.6366 (2017), pp. 1081–1084. ISSN: 0036-8075. DOI: `10.1126/science.aan0207`. URL: `https://science.sciencemag.org/content/358/6366/1081` (↪ cited on p. 12, 28, 52, 62).

[7] R. X. Schüssler et al. "Detection of metastable electronic states by Penning trap mass spectrometry". In: *Nature* 581.7806 (2020), pp. 42–46. ISSN: 1476-4687. DOI: `10.1038/s41586-020-2221-0`. URL: `https://doi.org/10.1038/s41586-020-2221-0` (↪ cited on p. 12, 133).

[8] D. Rodríguez. "A quantum sensor for high-performance mass spectrometry". In: *Applied Physics B* 107.4 (2012), pp. 1031–1042. ISSN: 1432-0649. DOI: `10.1007/s00340-011-4824-5`. URL: `https://doi.org/10.1007/s00340-011-4824-5` (↪ cited on p. 12, 38).

[9] N. Madsen, F. Robicheaux, and S. Jonsell. "Antihydrogen trapping assisted by sympathetically cooled positrons". In: *New Journal of Physics* 16.6 (2014), p. 063046. DOI: `10.1088/1367-2630/16/6/063046`. URL: `https://doi.org/10.1088/1367-2630/16/6/063046` (↪ cited on p. 12).

[10] P. Pérez et al. "The GBAR antimatter gravity experiment". In: *Hyperfine Interactions* 233.1 (2015), pp. 21–27. DOI: `10.1007/s10751-015-1154-8`. URL: `https://doi.org/10.1007/s10751-015-1154-8` (↪ cited on p. 12).

[11] C. Amsler et al. "Pulsed production of antihydrogen". In: *Communications Physics* 4.1 (2021), p. 19. ISSN: 2399-3650. DOI: `10.1038/s42005-020-00494-z`. URL: `https://doi.org/10.1038/s42005-020-00494-z` (↪ cited on p. 12).

[12] S. Sturm et al. "The ALPHATRAP experiment". In: *The European Physical Journal Special Topics* 227.13 (2019), pp. 1425–1491. DOI: `10.1140/epjst/e2018-800225-2`. URL: `https://doi.org/10.1140/epjst/e2018-800225-2` (↪ cited on p. 12, 13, 134).

[13] S. M. Brewer et al. "^{27}Al$^+$ Quantum-Logic Clock with a Systematic Uncertainty below 10^{-18}". In: *Phys. Rev. Lett.* 123 (3 2019), p. 033201. DOI: `10.1103/PhysRevLett.123.033201`. URL: `https://link.aps.org/doi/10.1103/PhysRevLett.123.033201` (↪ cited on p. 12).

[14] N. Huntemann et al. "Single-Ion Atomic Clock with 3×10^{-18} Systematic Uncertainty". In: *Phys. Rev. Lett.* 116 (6 Feb. 2016), p. 063001. DOI: `10.1103/PhysRevLett.116.063001`. URL: `https://link.aps.org/doi/10.1103/PhysRevLett.116.063001` (↪ cited on p. 12).

[15] D. J. Larson et al. "Sympathetic cooling of trapped ions: A laser-cooled two-species nonneutral ion plasma". In: *Phys. Rev. Lett.* 57 (1 1986), pp. 70–73. DOI: `10.1103/PhysRevLett.57.70`. URL: `https://link.aps.org/doi/10.1103/PhysRevLett.57.70` (↪ cited on p. 12, 29).

[16] C. J. Baker et al. "Sympathetic cooling of positrons to cryogenic temperatures for antihydrogen production". In: *Nature Communications* 12.1 (2021), p. 6139. ISSN: 2041-1723. DOI: `10.1038/s41467-021-26086-1`. URL: `https://doi.org/10.1038/s41467-021-26086-1` (↪ cited on p. 12).

[17] M. Harlander et al. "Trapped-ion antennae for the transmission of quantum information". In: *Nature* 471.7337 (2011), pp. 200–203. ISSN: 1476-4687. DOI: `10.1038/nature09800`. URL: `https://doi.org/10.1038/nature09800` (↪ cited on p. 12, 29).

[18] K. R. Brown et al. "Coupled quantized mechanical oscillators". In: *Nature* 471.7337 (2011), pp. 196–199. DOI: `10.1038/nature09721`. URL: `https://doi.org/10.1038/nature09721` (↪ cited on p. 12, 29).

[19] C. W. Walter et al. "Candidate for Laser Cooling of a Negative Ion: Observations of Bound-Bound Transitions in La$^-$". In: *Phys. Rev. Lett.* 113 (6 Aug. 2014), p. 063001. DOI: `10.1103/PhysRevLett.113.063001`. URL: `https://link.aps.org/doi/10.1103/PhysRevLett.113.063001` (↪ cited on p. 12, 29).

[20] R. Tang et al. "Candidate for Laser Cooling of a Negative Ion: High-Resolution Photoelectron Imaging of Th$^-$". In: *Phys. Rev. Lett.* 123 (20 Nov. 2019), p. 203002. DOI: `10.1103/PhysRevLett.123.203002`. URL: `https://link.aps.org/doi/10.1103/PhysRevLett.123.203002` (↪ cited on p. 12, 29).

[21] M. Schuh et al. "Image charge shift in high-precision Penning traps". In: *Phys. Rev. A* 100 (2 2019), p. 023411. DOI: `10.1103/PhysRevA.100.023411`. URL: `https://link.aps.org/doi/10.1103/PhysRevA.100.023411` (↪ cited on p. 12, 38).

[22] L. Deslauriers et al. "Scaling and Suppression of Anomalous Heating in Ion Traps". In: *Phys. Rev. Lett.* 97 (10 Sept. 2006), p. 103007. DOI: `10.1103/PhysRevLett.97.103007`. URL: `https://link.aps.org/doi/10.1103/PhysRevLett.97.103007` (↪ cited on p. 12).

[23] J. M. Cornejo et al. "Quantum logic inspired techniques for spacetime-symmetry tests with (anti-) protons". In: *New Journal of Physics* 23.7 (2021), p. 073045 (↪ cited on p. 12, 134).

[24] D. J. Heinzen and D. J. Wineland. "Quantum-limited cooling and detection of radio-frequency oscillations by laser-cooled ions". In: *Physical Review A* 42.5 (1990), p. 2977 (↪ cited on p. 12, 30, 48, 64, 80, 83, 132).

[25] M. Bohman et al. "Sympathetic cooling of protons and antiprotons with a common endcap Penning trap". In: *Journal of Modern Optics* 65.5-6 (2018), pp. 568–576. DOI: `10.1080/09500340.2017.1404656`. URL: `https://doi.org/10.1080/09500340.2017.1404656` (↪ cited on p. 12, 43, 48, 64, 78–80, 132).

[26] M. Bohman. "Sympathetic Cooling of a Proton with Resonant Image Current Coupling". PhD thesis. Ruperto-Carola University of Heidelberg, 2020 ($\hookrightarrow$ cited on p. 12, 33, 36, 45, 52, 64, 77, 93, 108).

[27] M. Bohman et al. "Sympathetic cooling of a trapped proton mediated by an LC circuit". In: *Nature* 596.7873 (2021), pp. 514–518. ISSN: 1476-4687. DOI: `10.1038/s41586-021-03784-w`. URL: `https://doi.org/10.1038/s41586-021-03784-w` ($\hookrightarrow$ cited on p. 12, 13, 48, 64, 72–74, 77, 82–84, 109, 127, 132, 136).

[28] C. Will et al. "Sympathetic cooling schemes for separately trapped ions coupled via image currents". In: *New Journal of Physics* 24.3 (2022), p. 033021 ($\hookrightarrow$ cited on p. 13, 20, 29, 48, 65, 72, 76, 77, 84, 129, 136).

[29] B. Tu et al. "Tank-Circuit Assisted Coupling Method for Sympathetic Laser Cooling". In: *Advanced Quantum Technologies* 4.7 (2021), p. 2100029. DOI: `https://doi.org/10.1002/qute.202100029`. URL: `https://onlinelibrary.wiley.com/doi/abs/10.1002/qute.202100029` ($\hookrightarrow$ cited on p. 13, 78–80, 86, 134).

[30] J. Repp et al. "PENTATRAP: a novel cryogenic multi-Penning-trap experiment for high-precision mass measurements on highly charged ions". In: *Applied Physics B* 107.4 (2012), pp. 983–996. ISSN: 1432-0649. DOI: `10.1007/s00340-011-4823-6`. URL: `https://doi.org/10.1007/s00340-011-4823-6` ($\hookrightarrow$ cited on p. 13, 61, 134).

[31] Max-Planck-Institut für Kernphysik Heidelberg. *Progress Report 2020-2022*. URL: `https://www.mpi-hd.mpg.de/mpi/fileadmin/bilder/Progress_Reports/2020-22/ProgressReport2020-2022.pdf` ($\hookrightarrow$ cited on p. 13, 134).

[32] A. Mooser et al. "A New Experiment for the Measurement of the g-Factors of $^3\text{He}^+$ and $^3\text{He}^{2+}$". In: *Journal of Physics: Conference Series* 1138 (2018), p. 012004. DOI: `10.1088/1742-6596/1138/1/012004` ($\hookrightarrow$ cited on p. 13, 134).

[33] D. J. Wineland and H. G. Dehmelt. "Principles of the stored ion calorimeter". In: *Journal of Applied Physics* 46.2 (1975), pp. 919–930. DOI: `10.1063/1.321602`. URL: `https://doi.org/10.1063/1.321602` ($\hookrightarrow$ cited on p. 14, 22, 65, 73).

[34] F. G. Major, V. N. Gheorghe, and G. Werth. "Charged Particle Traps". In: *Springer Series on Atomic, Optical, and Plasma Physics* (2005). DOI: `10.1007/b137836` ($\hookrightarrow$ cited on p. 14).

[35] G. Werth, V. N. Gheorghe, and F. G. Major. "Charged Particle Traps II". In: *Springer Series on Atomic, Optical, and Plasma Physics* (2009). DOI: `10.1007/978-3-540-92261-2` ($\hookrightarrow$ cited on p. 14).

[36] L. S. Brown and G. Gabrielse. "Geonium theory: Physics of a single electron or ion in a Penning trap". In: *Rev. Mod. Phys.* 58 (1 Jan. 1986), pp. 233–311. DOI: `10.1103/RevModPhys.58.233`. URL: `https://link.aps.org/doi/10.1103/RevModPhys.58.233` ($\hookrightarrow$ cited on p. 14, 17, 25).

[37] G. Gabrielse, L. Haarsma, and S. Rolston. "Open-endcap Penning traps for high precision experiments". In: *International Journal of Mass Spectrometry and Ion Processes* 88.2 (1989), pp. 319–332. ISSN: 0168-1176. DOI: `https://doi.org/10.1016/0168-1176(89)85027-X` ($\hookrightarrow$ cited on p. 14, 17, 18).

[38] J. Dilling et al. "Penning-Trap Mass Measurements in Atomic and Nuclear Physics". In: *Annual Review of Nuclear and Particle Science* 68.1 (2018), pp. 45–74. DOI: `10.1146/annurev-nucl-102711-094939`. URL: `https://doi.org/10.1146/annurev-nucl-102711-094939` ($\hookrightarrow$ cited on p. 14).

[39] L. S. Brown. "Geonium lineshape". In: *Annals of Physics* 159.1 (1985), pp. 62–98. ISSN: 0003-4916. DOI: `https://doi.org/10.1016/0003-4916(85)90192-7`. URL: `http://www.sciencedirect.com/science/article/pii/0003491685901927` ($\hookrightarrow$ cited on p. 18, 101, 102, 119).

[40] F. Köhler. "Bound-Electron g-Factor Measurements for the Determination of the Electron Mass and Isotope Shifts in Highly Charged Ions". PhD thesis. Ruperto-Carola University of Heidelberg, 2015 (↪ cited on p. 18).

[41] J. Ketter et al. "First-order perturbative calculation of the frequency-shifts caused by static cylindrically-symmetric electric and magnetic imperfections of a Penning trap". In: *International Journal of Mass Spectrometry* 358 (2014), pp. 1–16. ISSN: 1387-3806. DOI: `https://doi.org/10.1016/j.ijms.2013.10.005`. URL: `http://www.sciencedirect.com/science/article/pii/S1387380613003722` (↪ cited on p. 18, 74, 113, 120).

[42] H. Dehmelt. "Continuous Stern-Gerlach effect: principle and idealized apparatus". In: *Proceedings of the National Academy of Sciences* 83.8 (1986), pp. 2291–2294 (↪ cited on p. 19).

[43] S. Ulmer et al. "Observation of Spin Flips with a Single Trapped Proton". In: *Phys. Rev. Lett.* 106 (25 June 2011), p. 253001. DOI: `10.1103/PhysRevLett.106.253001`. URL: `https://link.aps.org/doi/10.1103/PhysRevLett.106.253001` (↪ cited on p. 19).

[44] A. Mooser et al. "Demonstration of the double Penning Trap technique with a single proton". In: *Physics Letters B* 723.1 (2013), pp. 78–81. ISSN: 0370-2693. DOI: `https://doi.org/10.1016/j.physletb.2013.05.012`. URL: `https://www.sciencedirect.com/science/article/pii/S0370269313003808` (↪ cited on p. 19, 39).

[45] H. Häffner et al. "Double Penning trap technique for precise g factor determinations in highly charged ions". In: *The European Physical Journal D - Atomic, Molecular, Optical and Plasma Physics* 22.2 (2003), pp. 163–182. ISSN: 1434-6079. DOI: `10.1140/epjd/e2003-00012-2`. URL: `https://doi.org/10.1140/epjd/e2003-00012-2` (↪ cited on p. 19).

[46] C. Smorra et al. "Observation of individual spin quantum transitions of a single antiproton". In: *Physics Letters B* 769 (2017), pp. 1–6. ISSN: 0370-2693. DOI: `https://doi.org/10.1016/j.physletb.2017.03.024`. URL: `https://www.sciencedirect.com/science/article/pii/S0370269317302113` (↪ cited on p. 19).

[47] H. Nyquist. "Thermal Agitation of Electric Charge in Conductors". In: *Phys. Rev.* 32 (1 July 1928), pp. 110–113. DOI: `10.1103/PhysRev.32.110`. URL: `https://link.aps.org/doi/10.1103/PhysRev.32.110` (↪ cited on p. 21).

[48] M. Wiesinger. in preparation. PhD thesis. Ruperto-Carola University of Heidelberg, 2023 (↪ cited on p. 21, 36, 38, 39, 41, 43, 46, 48, 49, 102, 103, 109, 132, 133).

[49] H. Nagahama. "High-Precision Measurements of the Fundamental Properties of the Antiproton ". PhD thesis. University of Tokyo, 2017 (↪ cited on p. 21).

[50] H. Nagahama et al. "Highly sensitive superconducting circuits at ∼ 700 kHz with tunable quality factors for image-current detection of single trapped antiprotons". In: *Review of Scientific Instruments* 87.11 (2016), p. 113305. DOI: `10.1063/1.4967493`. URL: `https://doi.org/10.1063/1.4967493` (↪ cited on p. 21, 42, 77).

[51] W. Shockley. "Currents to Conductors Induced by a Moving Point Charge". In: *Journal of Applied Physics* 9.10 (1938), pp. 635–636. DOI: `10.1063/1.1710367`. URL: `https://doi.org/10.1063/1.1710367` (↪ cited on p. 22).

[52] S. R. Jefferts et al. "Superconducting resonator and a cryogenic GaAs field-effect transistor amplifier as a single-ion detection system". In: *Review of Scientific Instruments* 64.3 (1993), pp. 737–740. DOI: `10.1063/1.1144153`. URL: `https://doi.org/10.1063/1.1144153` (↪ cited on p. 22).

[53] K. Franke. "The BASE Experiment and Analysis Tools for G-Factor Resonances". Master's thesis. Ruperto-Carola University of Heidelberg, 2015 (↪ cited on p. 22, 23).

[54] S. Ulmer. "First Observation of Spin Flips with a Single Proton Stored in a Cryogenic Penning Trap". PhD thesis. Ruperto-Carola University of Heidelberg, July 2011 (↪ cited on p. 22, 29, 36, 38, 42, 93).

[55] S. Sturm. "The g-factor of the electron bound in $^{28}Si^{13+}$: The most stringent test of bound-state quantum electrodynamics". PhD thesis. Johannes Gutenberg-Universität Mainz, 2011 (↪ cited on p. 22, 89).

[56] M. J. Borchert et al. "Measurement of Ultralow Heating Rates of a Single Antiproton in a Cryogenic Penning Trap". In: *Phys. Rev. Lett.* 122 (4 2019), p. 043201. DOI: `10.1103/PhysRevLett.122.043201`. URL: `https://link.aps.org/doi/10.1103/PhysRevLett.122.043201` (↪ cited on p. 27, 73, 81).

[57] D. Budker et al. "Millicharged Dark Matter Detection with Ion Traps". In: *PRX Quantum* 3 (1 Feb. 2022), p. 010330. DOI: `10.1103/PRXQuantum.3.010330`. URL: `https://link.aps.org/doi/10.1103/PRXQuantum.3.010330` (↪ cited on p. 27).

[58] W. Nolting. *Grundkurs Theoretische Physik 5/1*. Springer Spektrum Berlin, Heidelberg, 2013. DOI: `10.1007/978-3-642-25403-1` (↪ cited on p. 28).

[59] C. Smorra et al. "A parts-per-billion measurement of the antiproton magnetic moment". In: *Nature* 550.7676 (2017), pp. 371–374. DOI: `10.1038/nature24048`. URL: `https://doi.org/10.1038/nature24048` (↪ cited on p. 28, 29, 119, 131).

[60] X. Fan et al. "Measurement of the Electron Magnetic Moment". In: *Phys. Rev. Lett.* 130 (7 Feb. 2023), p. 071801. DOI: `10.1103/PhysRevLett.130.071801`. URL: `https://link.aps.org/doi/10.1103/PhysRevLett.130.071801` (↪ cited on p. 28).

[61] A. Mooser. "Der g-Faktor des Protons". PhD thesis. Johannes Gutenberg-Universität Mainz, 2013 (↪ cited on p. 29, 38, 93).

[62] W. D. Phillips. "Nobel Lecture: Laser cooling and trapping of neutral atoms". In: *Rev. Mod. Phys.* 70 (3 July 1998), pp. 721–741. DOI: `10.1103/RevModPhys.70.721`. URL: `https://link.aps.org/doi/10.1103/RevModPhys.70.721` (↪ cited on p. 29, 31).

[63] M. Niemann et al. "Cryogenic 9Be+ Penning trap for precision measurements with (anti-)protons". In: *Measurement Science and Technology* 31.3 (Dec. 2019), p. 035003. DOI: `10.1088/1361-6501/ab5722`. URL: `https://dx.doi.org/10.1088/1361-6501/ab5722` (↪ cited on p. 29).

[64] W. Demtröder. *Laser Spectroscopy: Vol. 1: Basic Principles*. Springer Berlin, Heidelberg, 2008. DOI: `10.1007/978-3-540-73418-5` (↪ cited on p. 30).

[65] A. Corney. *Atomic and Laser Spectroscopy*. Oxford University Press, 2006 (↪ cited on p. 30).

[66] H. J. Metcalf and P. Van der Straten. "Laser cooling and trapping of neutral atoms". In: *The Optics Encyclopedia: Basic Foundations and Practical Applications* (2007) (↪ cited on p. 30, 31, 73).

[67] C. Foot. *Atomic Physics*. Oxford Master Series in Physics. OUP Oxford, 2005. ISBN: 9780198506959 (↪ cited on p. 30, 31).

[68] W. M. Itano and D. J. Wineland. "Laser cooling of ions stored in harmonic and Penning traps". In: *Phys. Rev. A* 25 (1 1982), pp. 35–54. DOI: `10.1103/PhysRevA.25.35`. URL: `https://link.aps.org/doi/10.1103/PhysRevA.25.35` (↪ cited on p. 31, 34, 35, 68).

[69] T. Andersen, K. A. Jessen, and G. Sørensen. "Mean-Life Measurements of Excited Electronic States in Neutral and Ionic Species of Beryllium and Boron". In: *Phys. Rev.* 188 (1 1969), pp. 76–81. DOI: 10.1103/PhysRev.188.76. URL: https://link.aps.org/doi/10.1103/PhysRev.188.76 (↪ cited on p. 31).

[70] K. Nakamura and Particle Data Group. "Review of Particle Physics". In: *Journal of Physics G: Nuclear and Particle Physics* 37.7A (July 2010), p. 075021. DOI: 10.1088/0954-3899/37/7A/075021. URL: https://dx.doi.org/10.1088/0954-3899/37/7A/075021 (↪ cited on p. 32).

[71] S. Kraemer. "Towards Laser Cooling of Beryllium Ions at the ALPHATRAP Experiment". PhD thesis. Ruperto-Carola University of Heidelberg, 2017 (↪ cited on p. 33).

[72] A. Egl. "High-Precision Laser Spectroscopy of the Fine Structure in $^{40}Ar^{13+}$ at ALPHATRAP". PhD thesis. Ruperto-Carola University of Heidelberg, 2020 (↪ cited on p. 33).

[73] G. Z. K. Horvath and R. Thompson. "Laser cooling of ions stored in a Penning trap: A phase-space picture". In: *Physical Review A* 59.6 (1999), p. 4530 (↪ cited on p. 34).

[74] G. Schneider. "300 ppt Measurement of the Proton g-Factor". PhD thesis. Johannes Gutenberg University Mainz, 2017 (↪ cited on p. 36, 38, 39, 52, 68, 77, 93, 114, 120, 121).

[75] Stahl Electronics. *UM - Series Multichannel Precision Voltage Sources*. 2023. URL: https://www.stahl-electronics.com/devices/um/Manual_UM_LN_SW_V2023a.pdf (↪ cited on p. 36).

[76] C. de Carvalho Rodegheri. "Neuartige kryogene Penning-Falle für den Nachweis von Spin-Übergängen eines Protons und Bestimmung seines g-Faktors". ger. PhD thesis. Johannes Gutenberg-Universität Mainz, 2014. DOI: http://doi.org/10.25358/openscience-2864 (↪ cited on p. 38).

[77] S. Sellner et al. "Improved limit on the directly measured antiproton lifetime". In: *New Journal of Physics* 19.8 (2017), p. 083023. DOI: 10.1088/1367-2630/aa7e73. URL: https://doi.org/10.1088%2F1367-2630%2Faa7e73 (↪ cited on p. 40).

[78] S. Ulmer et al. "A cryogenic detection system at 28.9 MHz for the non-destructive observation of a single proton at low particle energy". In: *Nuclear Instruments and Methods in Physics Research Section A: Accelerators, Spectrometers, Detectors and Associated Equipment* 705 (2013), pp. 55–60. ISSN: 0168-9002. DOI: https://doi.org/10.1016/j.nima.2012.12.071. URL: https://www.sciencedirect.com/science/article/pii/S0168900212016087 (↪ cited on p. 42, 43).

[79] B. D'Urso, B. Odom, and G. Gabrielse. "Feedback Cooling of a One-Electron Oscillator". In: *Phys. Rev. Lett.* 90 (4 2003), p. 043001. DOI: 10.1103/PhysRevLett.90.043001. URL: https://link.aps.org/doi/10.1103/PhysRevLett.90.043001 (↪ cited on p. 42).

[80] S. Rau et al. "Penning trap mass measurements of the deuteron and the HD+ molecular ion". In: *Nature* 585.7823 (2020), pp. 43–47. DOI: 10.1038/s41586-020-2628-7. URL: https://doi.org/10.1038/s41586-020-2628-7 (↪ cited on p. 43, 133).

[81] L. Velardi et al. "Proton extraction by laser ablation of transition metals". In: *Nuclear Instruments and Methods in Physics Research Section B: Beam Interactions with Materials and Atoms* 331 (2014). 11th European Conference on Accelerators in Applied Research and Technology, pp. 20–22. ISSN: 0168-583X. DOI: https://doi.org/10.1016/j.nimb.2013.11.029. URL: https://www.sciencedirect.com/science/article/pii/S0168583X1400113X (↪ cited on p. 45).

[82] Thorlabs. *Tunable Diode Laser TA-FHG pro*. Available at `https://www.toptica.com/fileadmin/Editors_English/11_brochures_datasheets/01_brochures/toptica_BR_Scientific_Lasers.pdf`. 2023 (↪ cited on p. 45, 46).

[83] Y. Colombe et al. "Single-mode optical fiber for high-power, low-loss UV transmission". In: *Opt. Express* 22.16 (2014), pp. 19783–19793. DOI: `10.1364/OE.22.019783`. URL: `http://www.opticsexpress.org/abstract.cfm?URI=oe-22-16-19783` (↪ cited on p. 45).

[84] Thorlabs. *alpha-BBO Glan-Laser Polarizers*. Available at `https://www.thorlabs.com/newgrouppage9.cfm?objectgroup_id=5093`. 2023 (↪ cited on p. 46).

[85] M. Wiesinger et al. "Trap-integrated fluorescence detection based on silicon photomultipliers in a cryogenic Penning trap". In: (2023). to be published in Review of Scientific Instruments (↪ cited on p. 46, 109).

[86] S. Rau. "High-precision measurement of the deuteron's atomic mass". PhD thesis. Ruperto-Carola University of Heidelberg, 2020. DOI: `10.11588/heidok.00029010` (↪ cited on p. 50, 100).

[87] S. Erlewein. In preparation. PhD thesis. Ruperto-Carola University of Heidelberg, 2023 (↪ cited on p. 50).

[88] J. A. Devlin et al. "Superconducting Solenoid System with Adjustable Shielding Factor for Precision Measurements of the Properties of the Antiproton". In: *Phys. Rev. Appl.* 12 (4 Oct. 2019), p. 044012. DOI: `10.1103/PhysRevApplied.12.044012` (↪ cited on p. 54).

[89] G. D. Brittles et al. "Persistent current joints between technological superconductors". In: *Superconductor Science and Technology* 28.9 (Aug. 2015), p. 093001. DOI: `10.1088/0953-2048/28/9/093001`. URL: `https://dx.doi.org/10.1088/0953-2048/28/9/093001` (↪ cited on p. 55).

[90] J. J. Hansen. "Active stabilization of magnetic field fluctuations in the BASE antiproton-experiment at CERN". Bachelor's thesis. Christian-Albrechts Universität zu Kiel, 2019 (↪ cited on p. 55).

[91] S. Sturm. Personal communication. 2020 (↪ cited on p. 55).

[92] N. J. Simon, E. S. Drexler, and R. P. Reed. *Properties of Copper and Copper Alloys at Cryogenic Temperatures*. 1992. URL: `https://nvlpubs.nist.gov/nistpubs/Legacy/MONO/nistmonograph177.pdf` (↪ cited on p. 58).

[93] Bosch Sensortec. *BMP390 – Datasheet*. BST-BMP390-DS002-07. 2021. URL: `https://www.bosch-sensortec.com/media/boschsensortec/downloads/datasheets/bst-bmp390-ds002.pdf` (↪ cited on p. 60).

[94] Bronkhorst. *DATASHEET F-201CV*. 2023. URL: `https://www.bronkhorst.com/de-de/produkte/gas-durchfluss/el-flow-select/f-201cv/?pdf=true` (↪ cited on p. 60).

[95] Arduino. *Arduino Nano Product Reference Manual*. 2023. URL: `https://docs.arduino.cc/static/4abeb3b7b8ffa90673c4735bc1bb94d9/A000005-datasheet.pdf` (↪ cited on p. 60).

[96] K. Kromer. "Environmentally-induced systematic effects at the high-precision mass spectrometer PENTATRAP." Master's thesis. Ruperto-Carola University of Heidelberg, 2019. URL: `https://pure.mpg.de/rest/items/item_3117608_1/component/file_3117609/content` (↪ cited on p. 61).

[97] M. Door. Personal communication. 2023 (↪ cited on p. 61).

[98] S. Streubel. "Kontrolle der Umwelteinflüsse auf THe-Trap am Beispiel der Bestimmung des Massenverhältnisses von Kohlenstoff-12 zu Sauerstoff-16". PhD thesis. Ruperto-Carola University of Heidelberg, 2014 (↪ cited on p. 61).

[99] H. Yoshida. "Construction of higher order symplectic integrators". In: *Physics Letters A* 150.5 (1990), pp. 262–268. ISSN: 0375-9601. DOI: `https://doi.org/10.1016/0375-9601(90)90092-3`. URL: `http://www.sciencedirect.com/science/article/pii/0375960190900923` (↪ cited on p. 66, 133).

[100] R. W. Hockney and J. W. Eastwood. *Computer Simulation Using Particles*. IOP Publishing Ltd, 1988 (↪ cited on p. 67).

[101] D. Eddelbuettel and R. François. "Rcpp: Seamless R and C++ Integration". In: *Journal of Statistical Software* 40.8 (2011), pp. 1–18. DOI: `10.18637/jss.v040.i08`. URL: `http://www.jstatsoft.org/v40/i08/` (↪ cited on p. 69).

[102] *Using the GNU Compiler Collection (GCC)*. Accessed: 2023-02-21. URL: `https://gcc.gnu.org/onlinedocs/gcc/Optimize-Options.html#index-O3` (↪ cited on p. 69).

[103] Microsoft and S. Weston. *foreach: Provides Foreach Looping Construct*. R package version 1.5.1. 2020. URL: `https://CRAN.R-project.org/package=foreach` (↪ cited on p. 69).

[104] Microsoft Corporation and S. Weston. *doParallel: Foreach Parallel Adaptor for the 'parallel' Package*. R package version 1.0.16. 2020. URL: `https://CRAN.R-project.org/package=doParallel` (↪ cited on p. 69).

[105] S. Ulmer et al. "The quality factor of a superconducting rf resonator in a magnetic field". In: *Review of Scientific Instruments* 80.12 (2009), p. 123302. DOI: `10.1063/1.3271537`. URL: `https://doi.org/10.1063/1.3271537` (↪ cited on p. 77).

[106] M. J. Borchert et al. "A 16-parts-per-trillion measurement of the antiproton-to-proton charge–mass ratio". In: *Nature* 601.7891 (Jan. 2022), pp. 53–57. ISSN: 1476-4687. DOI: `10.1038/s41586-021-04203-w`. URL: `https://doi.org/10.1038/s41586-021-04203-w` (↪ cited on p. 87, 88, 136).

[107] M. J. Borchert. "Challenging the Standard Model by high precision comparisons of the fundamental properties of antiprotons and protons". PhD thesis. Gottfried Wilhelm Leibniz Universität Hannover, 2021. DOI: `10.15488/11564` (↪ cited on p. 88, 100, 133).

[108] E. A. Cornell et al. "Single-ion cyclotron resonance measurement of M(CO+)/M(N 2+)". In: *Physical Review Letters* 63.16 (1989), p. 1674 (↪ cited on p. 89).

[109] S. Sturm et al. "Phase-Sensitive Cyclotron Frequency Measurements at Ultralow Energies". In: *Phys. Rev. Lett.* 107 (14 2011), p. 143003. DOI: `10.1103/PhysRevLett.107.143003`. URL: `https://link.aps.org/doi/10.1103/PhysRevLett.107.143003` (↪ cited on p. 89).

[110] J. L. V. Galiana. "Ultrapräzise Messung des elektronischen g-Faktors in wasserstoffähnlichem Sauerstoff". ger. PhD thesis. Johannes Gutenberg-Universität Mainz, 2003. URL: `https://openscience.ub.uni-mainz.de/bitstream/20.500.12030/7327/1/ultrapr%C3%A4zise_messung_des_elek-20220705140323995.pdf` (↪ cited on p. 102).

[111] J. Ketter et al. "Classical calculation of relativistic frequency-shifts in an ideal Penning trap". In: *International Journal of Mass Spectrometry* 361 (2014), pp. 34–40. ISSN: 1387-3806. DOI: `https://doi.org/10.1016/j.ijms.2014.01.028`. URL: `https://www.sciencedirect.com/science/article/pii/S1387380614000426` (↪ cited on p. 113).

[112] S. Djekic et al. "Temperature measurement of a single ion in a Penning trap". In: *The European Physical Journal D - Atomic, Molecular, Optical and Plasma Physics* 31.3 (Dec. 2004), pp. 451–457. ISSN: 1434-6079. DOI: `10.1140/epjd/e2004-00168-1`. URL: `https://doi.org/10.1140/epjd/e2004-00168-1` (↪ cited on p. 118).

[113] F. Heiße et al. "High-precision mass spectrometer for light ions". In: *Phys. Rev. A* 100 (2 Aug. 2019), p. 022518. DOI: 10.1103/PhysRevA.100.022518. URL: https://link.aps.org/doi/10.1103/PhysRevA.100.022518 (↪ cited on p. 118).

[114] C. S. Weimer et al. "Electrostatic modes as a diagnostic in Penning-trap experiments". In: *Phys. Rev. A* 49 (5 May 1994), pp. 3842–3853. DOI: 10.1103/PhysRevA.49.3842. URL: https://link.aps.org/doi/10.1103/PhysRevA.49.3842 (↪ cited on p. 122).

[115] J. J. Bollinger et al. "Electrostatic modes of ion-trap plasmas". In: *Phys. Rev. A* 48 (1 July 1993), pp. 525–545. DOI: 10.1103/PhysRevA.48.525. URL: https://link.aps.org/doi/10.1103/PhysRevA.48.525 (↪ cited on p. 122).

[116] F. Hahne. "Investigation of a Novel Method for Sympathetic Laser Cooling of Highly Charged Ions in a Penning Trap". Master's thesis. Ruperto-Carola University of Heidelberg, 2020. URL: https://pure.mpg.de/rest/items/item_3249695_2/component/file_3249696/content (↪ cited on p. 134).

[117] A. V. Bock. "Characterization of an ultra-stable voltage supply and implementation of sympathetic laser cooling for the $^3\mathrm{He}^{2+}$ g-factor measurement". Master's thesis. Ruprecht-Karls-Universität Heidelberg, 2022 (↪ cited on p. 134).

[118] N. V. Bock. "Theoretische Modellierung einer Penning-Falle zur Nutzung sympathetischer Laserkühlung und Charakterisierung einer dafür vorgesehenen Präzisionsspannungsquelle". Bachelor's thesis. Ruprecht-Karls-Universität Heidelberg, 2022 (↪ cited on p. 134).

[119] K. Blaum. "High-accuracy mass spectrometry with stored ions". In: *Physics Reports* 425.1 (2006), pp. 1–78. ISSN: 0370-1573. DOI: https://doi.org/10.1016/j.physrep.2005.10.011. URL: https://www.sciencedirect.com/science/article/pii/S0370157305004643 (↪ cited on p. 134).

[120] T. Eronen and A. Jokinen. "High-precision atomic mass measurements for a CKM unitarity test". In: *International Journal of Mass Spectrometry* 349-350 (2013). 100 years of Mass Spectrometry, pp. 69–73. ISSN: 1387-3806. DOI: https://doi.org/10.1016/j.ijms.2013.03.003. URL: https://www.sciencedirect.com/science/article/pii/S1387380613000791 (↪ cited on p. 134).

[121] W. B. Cairncross et al. "Precision Measurement of the Electron's Electric Dipole Moment Using Trapped Molecular Ions". In: *Phys. Rev. Lett.* 119 (15 2017), p. 153001. DOI: 10.1103/PhysRevLett.119.153001. URL: https://link.aps.org/doi/10.1103/PhysRevLett.119.153001 (↪ cited on p. 134).

[122] C. D. Bruzewicz et al. "Trapped-ion quantum computing: Progress and challenges". In: *Applied Physics Reviews* 6.2 (2019), p. 021314. DOI: 10.1063/1.5088164. URL: https://doi.org/10.1063/1.5088164 (↪ cited on p. 134).

[123] J. F. Goodwin et al. "Resolved-Sideband Laser Cooling in a Penning Trap". In: *Phys. Rev. Lett.* 116 (14 2016), p. 143002. DOI: 10.1103/PhysRevLett.116.143002. URL: https://link.aps.org/doi/10.1103/PhysRevLett.116.143002 (↪ cited on p. 134).

[124] P. Hrmo et al. "Sideband cooling of the radial modes of motion of a single ion in a Penning trap". In: *Phys. Rev. A* 100 (4 2019), p. 043414. DOI: 10.1103/PhysRevA.100.043414. URL: https://link.aps.org/doi/10.1103/PhysRevA.100.043414 (↪ cited on p. 134).

Appendix

Parameter	PT	TMT	CT	BT	AT	LT
r (mm)	4.5	2.5	2.0	2.0	1.8	3.6 / 10.0
D_c (mm)	10.0(*)	5.7(*)	4.6(*)	4.6	4.2	-
D_e (mm)	25.6	14.1	10.9	10.9(*)	9.7(*)	14.4(*)
D_{c+e}(mm)	7.2	4.1	3.2	3.2	2.9	-
C_2 (m^{-2})	18 510	59 900	93 500	93 500	115 360	29 400
D_4^{theo} (m^{-4})	1.28×10^9	1.34×10^{10}	3.27×10^{10}	3.27×10^{10}	4.98×10^{10}	-1.76×10^9
D_4^{exp} (m^{-4})	-	-	$3.32(19) \times 10^{10}$			
$\nu_0 \equiv \nu_{\mathrm{RLC}}$ (Hz)	345 260	550 875	443 650	443 650	550 875	345 260
Q	9500	20 000	9500	9500	20 000	9500
$\Delta\nu_{1,\mathrm{p}}$/ion (Hz)	2.1	9.0	9.0	1.6	3.1	0.95
$\Delta\nu_{1,\mathrm{Be}}$/ion (Hz)	0.22	1.0	1.0	0.18	0.35	0.10
$U_{0,\mathrm{p}}^{\mathrm{theo}}$ (V)	-1.298	-1.032	-0.433	-0.433	-0.547	-0.833
$U_{0,\mathrm{p}}^{\mathrm{exp}}$ (V)	-1.296	-0.995	-0.477	-	-	-
$U_{0,\mathrm{Be}}^{\mathrm{theo}}$ (V)	-11.615	-9.234	-3.880	-3.880	-4.897	-7.457
$U_{0,\mathrm{Be}}^{\mathrm{exp}}$ (V)	-11.574	-9.243	-3.989	-4.110	-	-7.447
$\mathrm{TR}_{\mathrm{id,p/Be}}^{\mathrm{theo}}$	0.881	0.881	0.881	0.881	0.881	0.442
$\mathrm{TR}_{\mathrm{id,p}}^{\mathrm{exp}}$	0.903	0.912	0.933	-	-	0.428
$\mathrm{TR}_{\mathrm{id,Be}}^{\mathrm{exp}}$	0.885	0.887	0.883	0.844	-	-
$(\partial\nu_z/\partial U_0)_{\mathrm{p}}^{\mathrm{exp}}$ (Hz/mV)	-133	-256	-504	-	-	-
$(\partial\nu_z/\partial U_0)_{\mathrm{Be}}^{\mathrm{exp}}$ (Hz/mV)	-14.5	-29.1	-57.3	-64.4	-	-22.9
$(\partial\nu_z/\partial\mathrm{TR})_{\mathrm{p}}^{\mathrm{exp}}$ (Hz/mU)	-4.1	-17	-13	-	-	-
$(\partial\nu_z/\partial\mathrm{TR})_{\mathrm{Be}}^{\mathrm{exp}}$ (Hz/mU)	5.6	-20.5	-12.7	11.2	-	-
B_0^{exp} (T)	1.900126	1.79817	1.899733	1.898719	-	1.89427
$\nu_{+,\mathrm{p}}^{\mathrm{exp}}$ (Hz)	28 963 753	-	28 954 826	-	-	-
$\nu_{-,\mathrm{p}}^{\mathrm{exp}}$ (Hz)	2057	5546	3500	-	-	-
$\nu_{+,\mathrm{Be}}^{\mathrm{exp}}$ (Hz)	3 219 374	3 014 750	3 206 515	3 204 770	-	3 209 200
$\nu_{-,\mathrm{Be}}^{\mathrm{exp}}$ (Hz)	18 505	50 335	30 695	30 730	-	18 535

Table 1: Overview of the experimental parameters relevant for this thesis work. Entries that are not filled out have not been determined. For the effective electrode distances, $D_{\mathrm{c/e/c+e}}$, the resonator connection that is actually used in the experiment is marked with (*), where the indices c,e,c+e represent a resonator connected to the correction electrode, the endcap electrode, and both together, respectively.
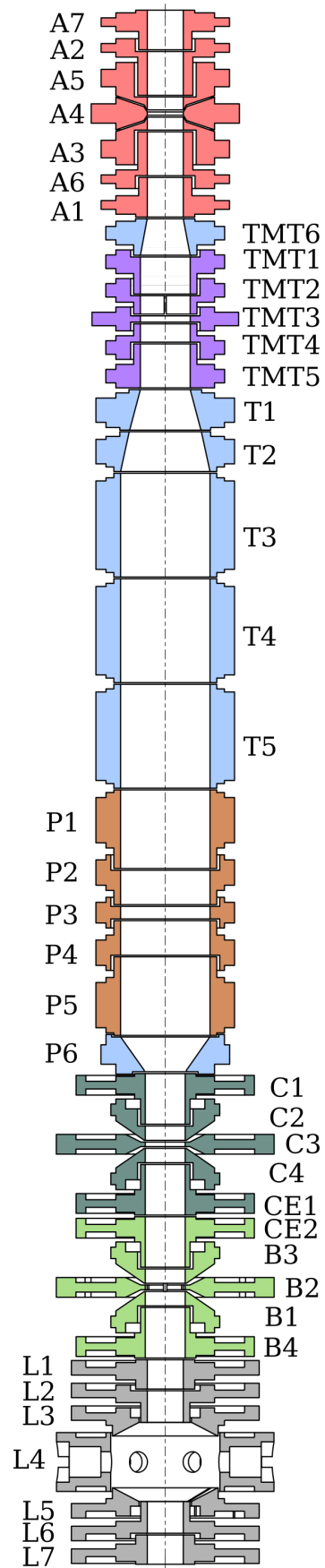
Figure 10.1: Trap stack consisting of six traps and a transport section. The numbering of the AT and BT is not in order since the electrodes were swapped for technical reasons but the names were kept for unambiguous identification.
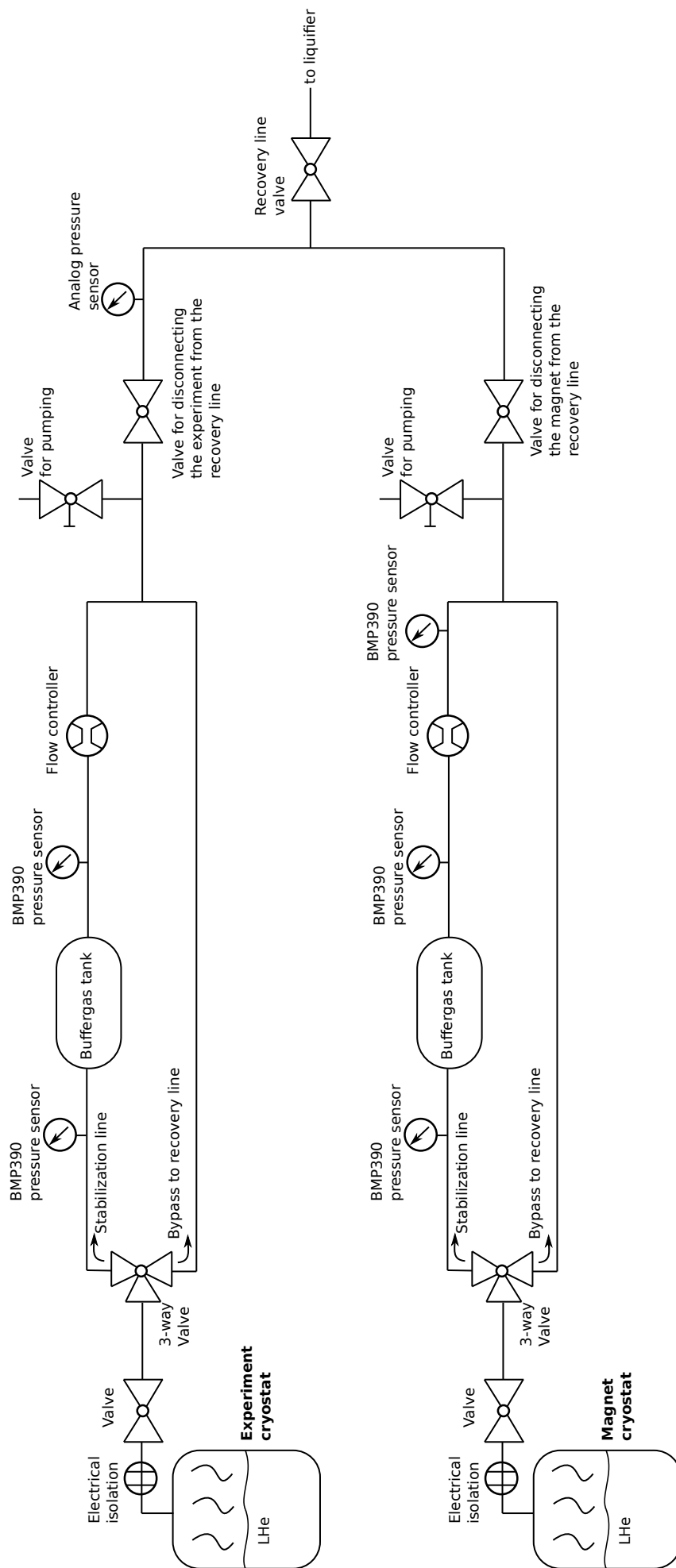
Figure 10.2: Schematic of the helium pressure stabilization system. This figure is a larger version of figure 5.2.

Acknowledgments

It takes a village to raise a child.
While PhD students are usually not children anymore, the thought behind this proverb still applies to a PhD project. Even the best students can only succeed in a thriving environment. Therefore, I have to thank several people: First and foremost **Klaus Blaum**, who warmly welcomed me in his group as an 'outsider' and continued to support me to this day. The fact that one receives an answer to any e-mail request within less than 24 hours is probably unmatched. It is only one example which demonstrates that, even as vice president of the MPG, your PhD students are still important to you, which simply shows in every regard of the day-to-day interactions.
Next, I would like to thank **Markus Oberthaler** for agreeing to be the second referee of this thesis. I do know how much time and effort such a job takes and therefore appreciate it very much.
Our local group has comparably few members. For this reason it is even more important to thank the people who put in all the extra effort to make things happen nonetheless:

- **Christian Smorra**, who, despite his double job as PI of this experiment and the new experiment `BASE-STEP`, has always found the time to discuss any matter. Also, thank you for proofreading this thesis.

- **Markus Wiesinger**, from whom I 'inherited' the apparatus and from whose technical thoroughness the measurements presented in this thesis greatly benefitted.

- **Matthew Bohman**, who introduced me to the experiment and recorded the first coupling measurements that allowed benchmarking the simulations.

- **Stefan Ulmer**, who, during our virtual group meetings, regularly provided the decisive idea to solve any issue we were currently facing.

- **Peter Micke**, who, as a postdoc, grew into the role of the local laboratory supervisor. Based on this experience I am certain your own group at GSI/Jena will face nothing but success. Also, thank you for proofreading this thesis.

- **Hüseyin Yildiz**, who will take over the experiment now. I am certain that the temperature records of this thesis will not hold for very long.

Further, thanks to the people working at the other two Penning-trap experiments in Mainz for interesting conversations during lunch and short-term help. This includes **Sven Sturm**, **Sascha Rau**, **Fabian Heiße**, **Sangeetha Sasidharan**, and **Olesia Bezrodnova** as members of the `LIONTRAP` group as well as **Fatma Abbass** and **Daniel Popper** as members of the `BASE-STEP` group.

Besides the scientific support, such an experiment requires immense infrastructure to function efficiently. Therefore I want to thank the people running the secretariat as well as the helium liquifier and the mechanical workshop of the University of Mainz.

Zu guter Letzt gilt allen aus meinem privaten Umfeld Dank, die mich auf dem Weg unterstützt haben: Dies sind einerseits meine Freunde und meine Freundin Lisa, die sich die ein oder andere Physik-Story anhören mussten und dabei geduldig zugehört haben. Andererseits waren es aber insbesondere auch meine Eltern und Großeltern, die mir zu jeder Zeit den Rücken freigehalten haben.